

# **Design and the Modeling of Wind-Driven Self-Excited Synchronous Reluctance Generator and its Applications**

A

*Thesis Submitted*

*in Partial Fulfilment of the Requirements*

*for the Degree of*

**DOCTOR OF PHILOSOPHY**

By

**Tefera Kitaba Tolesa**



Department of Electronics and Electrical Engineering

Indian Institute of Technology Guwahati

Guwahati - 781 039, INDIA.

July, 2021



---

## Certificate

This is to certify that the thesis “**Design and the Modeling of Wind-Driven Self-Excited Synchronous Reluctance Generator and its Applications**”, submitted by **Tefera Kitaba Tolesa** (156102022) are research scholar in the *Department of Electronics and Electrical Engineering, Indian Institute of Technology Guwahati*, for the award of the degree of **Doctor of Philosophy**, is a record of an original research work carried out by him under our supervision and guidance. The thesis has fulfilled all requirements as per the regulation of the institute and in our opinion has reached the standard needed for submission. The results embodied in this thesis have not been submitted to any other University or Institute for the award of any degree or diploma.

Dated:  
Guwahati.

Prof. Praveen Tripathy  
Dept. of Electronics & Electrical Engg.  
Indian Institute of Technology Guwahati  
Guwahati - 781039, Assam, India.

Dated:  
Guwahati.

Prof. Ravindranath Adda  
Dept. of Electronics & Electrical Engg.  
Indian Institute of Technology Guwahati  
Guwahati - 781039, Assam, India.



---

*To my family...*





---

## Acknowledgements

I would like to express my gratitude heartily to my supervisors, Dr. Praveen Tripathy and Dr. Ravindranath Adda, for their excellent guidance and constant motivation during the thesis work. They give me strength to overcome the difficulties faced during the work. I am grateful to them for their constant monitoring of my thesis work. And without their help, the work/thesis might not have reached to its current form.

I also thank my doctoral committee members Dr. Sisir Kumar Nayak, Dr. Tony Jacob and Dr. Sanjib Ganguly for their continuous scrutiny of my thesis work and suggestion to improve the thesis. The support provided by the current Head of the Department, and other faculty members during the course is commendable. I thank specially to all the members of the Power and control lab for providing necessary lab facilities required for the research work.

I am grateful to my family for their love, care and support me during the course. I had immense pleasure spending great time with friends during my stay at IIT Guwahati including all friends in Power and control, Electrical power system and Electrical machines lab. They stood by me during my difficult times. Their support and encouragement gave me immense strength.

I am thankful to Ministry of National Defence of Ethiopia (MOND) for providing assistantship during the course. The good weather of the city of Guwahati made my stay pleasant. The stay at this place also gave me an opportunity to know the rich diversity of the north-east state.

Finally, I thank those invisible hands of the Almighty, which always shower blessings on me and my work.

( *Tefera Kitaba Tolesa* )



## Abstract

The use of fossil fuels for power generation over a long period is one of the major cause for the global warming, which has now become a serious environmental concern. An attempt to reduce the effects of climate change due to carbon dioxide production and to meet the future energy requirement has resulted in significant research in renewable energy sources for power generation. The present thesis is mainly focus towards the design and development of generator suitable for low power wind conversion systems.

The machine specifications have been obtained from the wind turbine model, such as torque, speed, and power. Based on these specifications, the design of a synchronous reluctance generator (SRG) with a rating of  $2.1kW$  is proposed in the thesis. Due to its ruggedness, and good efficiency, its potential application may be towards the electrification of the rural area of a country. In SRG, the design of the rotor is the most challenging part of the design. Here, the thickness of the axial and tangential ribs plays a significant role in its performance. The design procedure presented in the work includes the effect of stator resistance, as it cannot be neglected in the design of SRG with low power ratings. Various parameters of the designed machine are analyzed through an analytical model and cross-verified through Ansys Electronics Desktop software. Further, the thesis includes experimental validation of the results. The formulae to approximate the minimum values of the excitation capacitor requirement, for a self-excited SRG with inductive load, are developed. Further analysis of the generator's performance under different conditions of wind speed and loads is evaluated.

The effects of placing the ferrite magnet into the rotor air barrier of synchronous reluctance generators (FM-SRG) on its electromagnetic performance have been analyzed. The difference between average electromagnetic torque and ripple torque is used as a measure of the perfor-

---

mance index. Here, in the analysis, a magnetic material is placed in the middle of each air barrier, and its size is symmetrically increased on both sides to increase the percentage of the volume of the magnetic material. The effect of an increase in the volume of the magnetic material on its performance is presented. Moreover, the variation in electromagnetic features such as the  $d$ - and  $q$  - axes inductance and flux linkage is also explored and compared for different volumes and ferrite material.

Design and analysis of electromagnetic performance in itself are not enough to secure the durability and reliability of the machine. The mechanical and thermal modeling of the machine also plays a significant role in machine design. Hence, the thesis also includes the mechanical and thermal analysis of SRG.

The mechanical analysis consists of the analysis of the change in the mechanical stress due to the presence of centripetal force, wind speed, and rotor speed on the tangential and radial ribs with different thicknesses. Moreover, the variation in the electromagnetic feature such as the  $q$ - and  $d$  - axes flux, reactance ratio, inductance, torque, and torque ripple are discussed for different thicknesses of tangential and radial ribs. Increasing both tangential and radial rib thickness has an effect on the electromagnetic performance, but it is observed that the effect is significantly more with the variation of tangential rib thickness. Similarly, the mechanical stress analysis for rotor design has been explored in this work. It is observed that a high concentration of peak stress on the rotor ribs, which limits the range of rotor speed.

The study focused on the thermal analysis of the synchronous reluctance generator (SRG) with a rating of 2.1 kW, mainly uses explicit, and implicit finite difference methods for the thermal analysis to reduce the complexity of thermal calculation for the machine's components. It compares the results with the results obtained using a finite element analysis (FEA) and includes the experimental verification of the obtained results. The explicit, and implicit finite difference thermal analysis is relatively simple and computationally fast. Once the design parameters are known, the electric losses and iron losses of the SRG are evaluated. These machine parameters are utilized in developing the explicit finite difference (EFD), the implicit finite difference (IFD), and the 3D FEA model for thermal analysis. It is observed that the obtained results from

---

the EFD, IFD, FEA, and experiments are very close to each other, and the temperature rise for the designed machine is within the desired and acceptable range.





# Contents

<b>List of Figures</b>	<b>xvii</b>
<b>List of Tables</b>	<b>xxiii</b>
Nomenclature . . . . .	xxv
<b>List of Acronyms</b>	<b>xxv</b>
Nomenclature . . . . .	xxvii
<b>List of Symbols</b>	<b>xxvii</b>
<b>1 INTRODUCTION</b>	<b>1</b>
1.1 Literature Review . . . . .	4
1.1.1 Self-excited Synchronous Reluctance Generator . . . . .	5
1.1.2 Self-excited Ferrite-magnet Synchronous Reluctance Generator . . . . .	6
1.1.3 Mechanical stress and thermal analysis of Self-excited SRG . . . . .	7
1.1.3.1 Mechanical stress of Self-excited SRG . . . . .	7
1.1.3.2 Thermal Analysis of SRG for Wind Energy Application . . . . .	8
1.2 Motivation . . . . .	8
1.3 Scope and objectives . . . . .	9
1.4 Thesis Organization . . . . .	10
<b>2 DESIGN AND MODELING OF SELF EXCITED SRG FOR WIND ENERGY GENERATION</b>	<b>15</b>
2.1 Introduction . . . . .	16
2.2 Wind turbine model . . . . .	18
2.3 Design and analytical modeling of SRG . . . . .	21
2.3.1 Design algorithm . . . . .	21

## Contents

---

2.3.2	Analytical model of SRG . . . . .	22
2.3.2.1	Copper and core loss . . . . .	27
2.3.2.2	Excitation capacitance and load modeling . . . . .	28
2.3.3	Experimental and finite element analysis of SRG . . . . .	29
2.3.4	Technical performance of SRG . . . . .	38
2.4	Steady-state performance analysis . . . . .	40
2.4.1	Performance analysis of SRG with resistive load . . . . .	45
2.4.2	Residual flux linkage for self-excitation . . . . .	47
2.4.3	Effects of wind speed, and load on the system performance . . . . .	50
2.5	Summary . . . . .	53
<b>3</b>	<b>ELECTROMAGNETIC TORQUE ANALYSIS OF SRG WITH FERRITE MAGNET FOR WIND ENERGY GENERATION</b>	<b>57</b>
3.1	Introduction . . . . .	58
3.2	Impact of placing Ferrite magnet and analytical modeling of FM-SRG . . . . .	59
3.3	Construction troubles of the FM-SRG . . . . .	65
3.4	Structure and performance evaluations . . . . .	67
3.4.1	Finite element analysis of FM-SRG for $V_{fm} = 30\%$ . . . . .	73
3.4.2	Technical performance of FM-SRG . . . . .	82
3.4.3	Effects of wind speed, and load on the system performance of FM-SRG . . . . .	85
3.4.4	Performance comparison of SRG and FM-SRG . . . . .	88
3.5	Summary . . . . .	92
<b>4</b>	<b>ELECTROMAGNETIC-MECHANICAL STRESS ANALYSIS OF SRG FOR WIND ENERGY APPLICATION</b>	<b>95</b>
4.1	Introduction . . . . .	96
4.2	Machine design parameters and problem statement . . . . .	97
4.2.1	Design specification and parameters . . . . .	97
4.2.2	Rotor parameterizations . . . . .	98
4.3	Analysis of electromagnetic performance . . . . .	99

4.4	Analysis of mechanical performance . . . . .	106
4.4.1	Centripetal force on flux barriers . . . . .	106
4.4.2	Tangential and radial rib thickness . . . . .	107
4.5	Summary . . . . .	111
<b>5</b>	<b>EFD AND IFD THERMAL MODELING OF SELF-EXCITED SRG FOR WIND ENERGY APPLICATION</b>	<b>115</b>
5.1	Introduction . . . . .	116
5.2	Heat sources calculation of SRG . . . . .	117
5.3	Lumped parameter model, and the use of EFD and IFD to estimate the temperature rise. . . . .	118
5.3.1	Analytical solution of thermal conductance, capacitance, EFD and IFD methods . . . . .	122
5.3.1.1	Estimation of temperature rise using calculated thermal conductance and capacitance . . . . .	123
5.3.1.2	Solution of the developed lumped parameter based thermal model using explicit and implicit methods . . . . .	137
5.4	Thermal analysis of SRG using 3D FEA . . . . .	141
5.5	Experimental verification of the results . . . . .	143
5.5.1	Comparison of EFD, IFD, 3D FEA with the experimental results . . . . .	144
5.6	Summary . . . . .	149
<b>6</b>	<b>CONCLUSION AND FUTURE WORK</b>	<b>151</b>
6.1	Conclusions . . . . .	152
6.1.1	Scope for further work . . . . .	154
<b>A</b>	<b>SUPPLEMENTARY MATERIALS</b>	<b>157</b>
A.1	Some important design equations are placed as: . . . . .	158
A.2	Stator and Rotor Details: . . . . .	158
A.2.1	Stator and slot details design: . . . . .	158
A.2.2	Complete rotor lamination: . . . . .	159

## Contents

---

A.3	The Impedance load detail derivation . . . . .	159
A.3.1	Excitation Capacitors Modeling . . . . .	161
A.3.2	Resistive and Inductive loads Modeling . . . . .	164
A.4	The steady state torque derivation of SRG . . . . .	168
A.4.1	Effects of ferrite-magnet on $q$ – axis flux . . . . .	170
<b>References</b>		<b>173</b>
<b>List of Publications</b>		<b>179</b>
<b>Bio-Data</b>		<b>181</b>



## List of Figures

1.1	Wind energy conversion without power converter interface for fixed speed . . . .	2
1.2	Variable speed configuration with reduced-capacity converters . . . . .	3
1.3	Variable speed configuration with full-capacity converters . . . . .	4
2.1	(a) Cross-section and $dq$ axes rotor reference frame of the SRG. (b) Stand-alone generating system for rural area applications. . . . .	17
2.2	(b) Analytical approximation of $C_p - \lambda$ characteristics. (a) Turbine power characteristics at pitch angle $\alpha = 0$ . . . . .	20
2.3	(a) Rotor ribs structure modeling . (b) Typical geometry of stator slot and rotor dimensions. . . . .	24
2.4	(a) The drive motor and SRG set up. (b) Rotor core lamination and assemble. (c) Schematic diagram of the test bench. . . . .	30
2.5	(a) Machine emf at given frequency. (b) emf curves as a function of current. . .	31
2.6	(a) Torque verses power angle curves. (b) Torque verses current curves of the machine. . . . .	33
2.7	Variation of SRG electromagnetic torque with power angle, for $R_s \neq 0$ . . . . .	34
2.8	(a) $d$ - and $q$ -axes flux linkages magnetizing of the machines. (b) $d$ and $q$ -axes magnetizing inductance. . . . .	36
2.9	(a) Magnetic flux density distribution and flux lines of the machines . (b) Size of the machine. . . . .	39
2.10	Circuit of the synchronous reluctance generator with capacitor $C$ , resistive $R_L$ and inductive $X_L$ loads ( $V = V_d + jV_q, I = I_d + jI_q, \Lambda = \lambda_d + j\lambda_q$ ) . . . . .	40

**List of Figures**

---

2.11 (a) Capacitor, voltage and speed curves ( $R_L = 18 \Omega, L = 80 \text{ mH}$ ), ( $R_L = 250 \Omega, L = 30 \text{ mH}$ ). (b) Reactive power map at the speed of 1500 rpm with different currents ( $R_L = 50 \Omega, L = 3 \text{ mH}$ ). . . . . 43

2.12 The generated voltage verses speed for  $C = 240 \mu \text{ F}$  and  $R_L = 71 \Omega$ . . . . . 45

2.13 The out put power verses speed for  $C = 240 \mu \text{ F}$  and  $R_L = 71 \Omega$ . . . . . 46

2.14 Efficiency at resistive load and different speed conditions of the 2.1 kW SRG . 46

2.15 (a) Voltage collapse with out magnetizing voltage. (b) Self-excitation/voltage build up after magnetizing with voltage). . . . . 48

2.16 Wind-driven SRG at constant of  $v_\omega = 10 \text{ m/s}$  with  $R_L = 250 \Omega, L = 30 \text{ mH}$  for  $C = 190 \mu \text{ F}$ . . . . . 50

2.17 Wind-driven SRG for falls in speed from  $v_\omega = 10 \text{ m/s}$  to  $v_\omega = 4.98 \text{ m/s}$  with  $R_L = 250 \Omega, L = 30 \text{ mH}$  for  $C = 190 \mu \text{ F}$ . . . . . 51

2.18 Wind-driven SRG at constant of  $v_\omega = 10 \text{ m/s}$  with  $Z_L = 258 \Omega$  to  $150 \Omega$  for  $C = 190 \mu \text{ F}$ . . . . . 52

2.19 Wind-driven SRG for variable speed with  $R_L = 250 \Omega, L = 30 \text{ mH}$  for  $C = 190 \mu \text{ F}$ . . . . . 52

3.1 Cross-section and  $dq$  axes rotor reference frame of the FM-SRG. . . . . 59

3.2 (a) Maximum permissible ferrite compositions FM-SRG. (b) Rotor of the reference SRG. . . . . 62

3.3 Illustration schematic for the ferrite magnet-increment arrangements of a 2.1 kW, 4 poles FM-SRG. . . . . 63

3.4 (a) Efficiency enhancement as amount of ferrite magnet increments.(b) Performance index as the amounts of ferrite magnet increments. . . . . 64

3.5 Design parameters/variables for rectangular ferrite magnet shape . . . . . 66

3.6	Stator and rotor structure and field density distribution of 2.1 kW generators. (a) Stator and rotor of reference SRG (for $V_{fm} = 0\%$ ). (b) Stator and rotor of FM-SRG (for $V_{fm} = 30\%$ ). (c) Stator and rotor of FM-SRG ( $V_{fm} = 40\%$ ). (d) Stator and rotor of FM-SRG (for $V_{fm} = 58\%$ ). . . . .	68
3.7	(a) Summarized stator yoke, rotor and teeth losses. (b) Entire core and resistive losses. . . . .	69
3.8	(a) $d$ -and $q$ - axes inductance with generator volumes at $V_{fm} = 0\%$ . (b) $d$ -and $q$ - axes flux with generator volumes at $V_{fm} = 0\%$ . . . . .	71
3.9	(a) $d$ -and $q$ - axes inductance with generator volumes and at $V_{fm} = 30\%$ . (b) $d$ -and $q$ - axes flux with generator volumes and at $V_{fm} = 30\%$ . . . . .	72
3.10	(a) $d$ -and $q$ - axes inductance with generator volumes and at $V_{fm} = 40\%$ . (b) $d$ -and $q$ - axes flux with generator volumes and at $V_{fm} = 40\%$ . . . . .	74
3.11	(a) $d$ -and $q$ - axes inductance with generator volumes and at $V_{fm} = 58\%$ . (b) $d$ -and $q$ - axes flux with generator volumes and at $V_{fm} = 58\%$ . . . . .	75
3.12	Volume of ferrite magnet-increment verses volume of machine for 2.1 kW, 4 poles PM-SRG. . . . .	76
3.13	(a) Machines emf at given frequency. (b) Machine emf curves as a function of current. . . . .	78
3.14	(a) Torque verses power angle curves. (b) Cogging torque of FM-SRG (without excitation). . . . .	79
3.15	(a) Torque verses current curves of the machine. (b) Variation of FM-SRG electromagnetic torque with power angle. . . . .	81
3.16	Linkage flux of FM-SRG (without excitation). . . . .	82
3.17	(a) $d$ - and $q$ -axes flux linkages magnetizing of the machine. (b) $d$ and $q$ -axes magnetizing inductances of FM-SRG. . . . .	83
3.18	(a) Magnetic flux density distribution and flux lines of the machine. (b) Size of the machine. . . . .	85

**List of Figures**

---

3.19	Wind-driven FM-SRG at constant of $v_\omega = 10 \text{ m/s}$ with $R_L = 250 \Omega$ , $L = 30 \text{ mH}$ for $C = 190 \mu \text{ F}$ . . . . .	86
3.20	Wind-driven FM-SRG for falls in speed from $v_\omega = 10 \text{ m/s}$ to $v_\omega = 4.98 \text{ m/s}$ with $R_L = 250 \Omega$ , $L = 30 \text{ mH}$ for $C = 190 \mu \text{ F}$ . . . . .	87
3.21	Wind-driven FM-SRG at constant of $v_\omega = 10 \text{ m/s}$ with $Z_L = 258 \Omega$ to $150 \Omega$ for $C = 190 \mu \text{ F}$ . . . . .	87
3.22	Wind-driven FM-SRG for variable speed with $R_L = 250 \Omega$ , $L = 30 \text{ mH}$ for $C = 190 \mu \text{ F}$ . . . . .	88
4.1	Structural, cross-section and $dq - axes$ rotor reference frame of SRG. . . . .	97
4.2	Rotor cross section view: radial and tangential ribs thickness. . . . .	100
4.3	Magnetic field density and flux lines plot showing ribs saturation. . . . .	100
4.4	(a) $d$ - and $q$ -axes flux linkages magnetizing curve with tangential rib widths. (b) $d$ - and $q$ -reactance ratio with tangential rib widths. . . . .	101
4.5	(a) $d$ - and $q$ -inductances with tangential rib widths. (b) $d$ - and $q$ -axes flux linkages magnetizing curve with radial rib widths. . . . .	102
4.6	(a) $d$ - and $q$ -reactance ratio with radial rib widths. (b) $d$ - and $q$ -inductances with radial rib widths. . . . .	103
4.7	(a) Average torque-current profile of SRG curve with tangential rib widths. (b) Average torque-current profile of SRG curve with radial rib widths. . . . .	104
4.8	(a) Torque ripple percentage curve with tangential rib widths. (b) Torque ripple percentage curve with radial rib widths. . . . .	105
4.9	Von Mises stress distributions (Mpa) of designed rotor with ribs widths variation (minimum=0.1 mm to maximum=1.2 mm) . . . . .	109
4.10	(a) Stress at tangential rib with different widths vs centripetal force. (b) Stress at radial rib with different widths vs centripetal force. . . . .	110
4.11	(a) Stress at tangential rib with different widths vs rotor speed. (b) Safety factor of tangential rib with different widths vs rotor speed . . . . .	111

4.12 (a) Stress at radial rib with different widths vs rotor speed. (b) Safety factor of radial rib with different widths vs rotor speed . . . . .	112
5.1 Rotor and stator structure of SRG. . . . .	118
5.2 Thermal network model of SRG . . . . .	120
5.3 Air circulation, combined forced and free convection between end winding and end cap in a SRG. . . . .	133
5.4 (a) Temperature rise curve using explicit method. (b) Temperature rise curve using implicit method. . . . .	140
5.5 Three-dimensional mesh analysis and thermal distribution rise ( $^{\circ}\text{C}$ ) of SRG for $t = 3600 \text{ sec}$ . . . . .	142
5.6 Three-dimensional stator core and stator end winding thermal distribution ( $^{\circ}\text{C}$ ) of SRG for $t = 3600 \text{ sec}$ . . . . .	143
5.7 TEFC SRG: (a) Thermal experimental setup. (b) Schematic diagram of the test bench. . . . .	145
5.8 (a) Stator outer yoke temperature rise comparisons using 3D-FEA, IFD, EFD and Experimental. (b) Frame temperature rise comparisons using IFD, EFD and Experimental. . . . .	146
5.9 (a) Stator inner yoke temperature rise comparisons using 3D FEA, explicit, implicit, and Experimental. (b) End winding temperature rise comparisons using 3D FEA, explicit, implicit, and Experimental. . . . .	147
A.1 Stator structure design . . . . .	159
A.2 Rotor structure design view . . . . .	160
A.3 Circuit of the synchronous reluctance generator with capacitor $C$ , resistive $R_L$ and inductive $X_L$ loads . . . . .	160
A.4 Synchronous reluctance generator with required capacitor $C$ . . . . .	161

**List of Figures**

---

A.5 (a) Rotor reference frame equivalent circuit of a self excited reluctance generator (d-axis). (b) Rotor reference frame equivalent circuit of a self excited reluctance generator (q-axis). . . . . 168

A.6 The vector diagram of SRG (motor convection) . . . . . 169

A.7 The vector diagram of FM-SRG (motor convection) . . . . . 171



## List of Tables

2.1	Initial data and calculated values of the wind turbine parameters . . . . .	19
2.2	Assigned Parameters . . . . .	23
2.3	Parameters expression . . . . .	26
2.4	Evaluated performance parameters and approximated quantity of 2.1 kW of SRG	29
2.5	Variation of torque ripple with phase currents . . . . .	34
2.6	Values of polynomial coefficients evaluated from curve fit. The unit of equation (2.33) is in $mWb$ . . . . .	35
2.7	Values of polynomial coefficients evaluated from curve fit. The unit of equation (2.34) is in $mH$ . . . . .	37
2.8	Technical achievements of the SRG . . . . .	38
2.9	Analytical, FEA and experimental results of the machines . . . . .	39
2.10	Charged voltage and measured peak phase voltage (at $C = 240 \mu F$ and $R_L = 71 \Omega$ )	48
3.1	Parameters expression . . . . .	60
3.2	Optimal design variables of FM-SRG . . . . .	66
3.3	Torque ripples and electromagnetic torque of the FM-SRG structures . . . . .	67
3.4	Evaluated performance and design parameters for $V_{fm} = 30\%$ of 2.1 kW of FM-SRG . . . . .	76
3.5	Values of polynomial coefficients evaluated from curve fit. The unit of equations (3.15) are in $mWb$ . . . . .	80
3.6	Variation of torque ripple with phase currents . . . . .	80
3.7	Values of polynomial coefficients evaluated from curve fit. The unit of equation (3.16) is in $mH$ . . . . .	84

## List of Tables

---

3.8	Technical performance of FM-SRG . . . . .	84
3.9	Analytical, FEA and experimental achievements of the machine . . . . .	84
3.10	Evaluated performance parameters of SRG and FM-SRG for 2.1 kW Generators . . . . .	89
3.11	Variation of torque ripple with phase currents for SRG and FM-SRG . . . . .	90
3.12	Performance comparison of existing machines with up to date SRG, and FM-SRG . . . . .	91
4.1	Mechanical performance (Von Mises stress, centripetal force, stress factor) of peak stress and Electromagnetic performance (torque and ripple) of the designed rotor speed of 1500 rpm . . . . .	108
4.2	Mechanical performance (Von Mises stress, centripetal force and stress factor) of peak stress and Electromagnetic performance (torque and ripple) of the designed rotor speed of 2500 rpm . . . . .	108
5.1	Limits of temperature for different insulation class in ( $^{\circ}C$ ) [1–3] . . . . .	117
5.2	Loss analysis of the 2.1 kW SRG for rated wind speed . . . . .	118
5.3	Thermal properties for thermal capacitance and resistance calculation at room temperature [1,2] . . . . .	121
5.4	Generator physical dimension data . . . . .	122
5.5	Calculated thermal capacitance and resistance . . . . .	141
5.6	Instruments used in the Experimental setup . . . . .	144
5.7	Explicit, implicit, FEA calculated and Experimental temperature at steady state . . . . .	149

## Nomenclature

<i>ALV</i>	Axially Laminated Variant
<i>DFIG</i>	Doubly Fed Induction Generator
<i>EFD</i>	Explicit Finite Difference
<i>FEA</i>	Finite Element Analysis
<i>FM</i>	Ferrite Magnet
<i>FM – SRG</i>	Ferrite Magnet Synchronous Reluctance Generator
<i>IFD</i>	Implicit Finite Difference
<i>PMSG</i>	Permanent Magnet Synchronous Generator
<i>RR</i>	Radial Ribs
<i>SCIG</i>	Squirrel Cage Induction Generator
<i>SEIG</i>	Self-Excited Induction Generator
<i>SRG</i>	Synchronous Reluctance Generator
<i>TLV</i>	Transversely Laminated Variant
<i>TR</i>	Tangential Ribs
<i>TSR</i>	Tip Speed Ratio
<i>WECS</i>	Wind Energy Conversion System
<i>WRSG</i>	Wound Rotor Synchronous Generator



## Mathematical Notations

$T_\rho$	Torque density SRG
$T_{\rho m}$	Torque density FM-SRG
$\omega$	Generator rated speed (mechanical)
$\omega_e$	Generator rated speed (electrical)
$T_{sp}$	Specific torque SRG
$T_{spm}$	Specific torque FM-SRG
$R_t$	Turbine blade radius
$P_{spm}$	Specific power FM-SRG
$P_{sp}$	Specific power SRG
$k_u$	Stator fill factor
$B_m$	Maximum air gap flux density
$k_d$	Ratio of $d$ – axis inductance to magnetizing inductance
$k_q$	Ratio of $q$ – axis inductance to magnetizing inductance
$L_s/\tau$	Stack aspect ratio
$v_w$	Mean wind speed
$J$	Current density
$\rho_a$	Air density
$c_a$	Air specific heat capacity
$P$	Number of pole pairs
$\Omega$	Turbine tip speed
$P_\rho$	Power density of SRG
$P_{\rho m}$	Power density of FM-SRG

## List of Symbols

---

$\Lambda_m$	Maximum flux linkage of ferrite magnet
$\rho$	Differential operator
$Q_s$	Number of stator slot
$\mu_o$	Air Permeability ( $\mu_o = 4\pi \times 10^{-7}$ )
$b_{ts}$	Stator tooth width
$E_{ph}$	Emf induced per phase
$\Lambda_{resi}$	Residual flux linkage require for SRG
$\Lambda_{resm}$	Residual flux linkage require for FM-SRG
$Q_g$	Generator net reactive power
$Q_c$	Capacitor reactive power
$Q_\omega$	Winding reactive power
$P_g$	Generator active power
$P_{iron}$	Stator core losses
$R_{sc}$	Stator core resistance
$P_{cu-s}$	Stator copper losses
$C_{a...l}$	Thermal capacitance
$c_i$	Specific heat of iron lamination
$\rho_i$	Mass density of iron
$r_{sh}$	Shaft radius
$L_{sh}$	Shaft length
$r_{ewo}$	End winding outer radius
$r_{ewi}$	End winding inner radius
$\delta$	Boltzman constant [ $K^4w/m^2$ ]
$\phi_p$	Tooth pitch
$V_{element}$	Volume of the material
$\phi_e$	Tooth arc
$r_{si}$	Stator inner radius
$P_{core}$	Core losses

$\mathcal{R}_{a...r}$	Thermal resistance
$c_c$	Copper specific heat
$I_{max}$	Maximum current
$I_{rate}$	Rated current
$\rho_c$	Mass density of copper
$A_{air}$	Air ribs area
$A_{sh}$	Shaft area
$A_c$	Copper cross section in slot
$\chi$	Hot spot to average rate temperature
$\beta$	Slot to end winding volume ratio
$L_f$	Fins axial length
$Q_h$	Hydraulic diameter
$\vartheta_f$	Velocity of air in the fin channels
$v_c$	End winding volume
$\rho_{al}$	Mass density of aluminum
$c_{al}$	Specific heat of aluminum
$r_{cap}$	Outer radius of end cap
$L_{air}$	Air end length
$\tau_o$	Pole pitch
$R_t$	Wind turbine radius
$L_{ls}$	Stator leakage inductance
$\xi_1$	Saliency ratio
$G_r$	Gear ratio
$\lambda$	Tip speed ratio
$D_o$	Stator air gap diameter
$D_{in}$	Stator yoke diameter
$D_r$	Rotor outer diameter
$R_s$	Phase resistance

## List of Symbols

---

$\mathfrak{J}_d$	$d$ -axis reluctance
$\mathfrak{J}_q$	$q$ -axis reluctance
$I_d$	$d$ -axis current
$I_q$	$q$ -axis current
$X_d$	$d$ -axis reactance
$X_q$	$q$ -axis reactance
$m$	Number of conductor turns per phase
$I_{ph}$	RMS phase current
$l_g$	Air gap length
$M_a$	Flux line lamination mass
$P_{rated}$	Machine rated power
$T_{rated}$	Machine rated torque
$\lambda_q$	$q$ -axis flux
$\lambda_d$	$d$ -axis flux
$L_q$	$q$ -axis inductance
$L_d$	$d$ -axis inductance
$SF$	Stress intensity factor
$f$	Centripetal force
$T_{ave}$	Average torque
$T_{rip}$	Torque ripple
$L_s$	Active stack length







# 1

## INTRODUCTION

### Contents

---

<b>1.1 Literature Review</b> . . . . .	<b>4</b>
<b>1.2 Motivation</b> . . . . .	<b>8</b>
<b>1.3 Scope and objectives</b> . . . . .	<b>9</b>
<b>1.4 Thesis Organization</b> . . . . .	<b>10</b>

---

## 1. INTRODUCTION

---

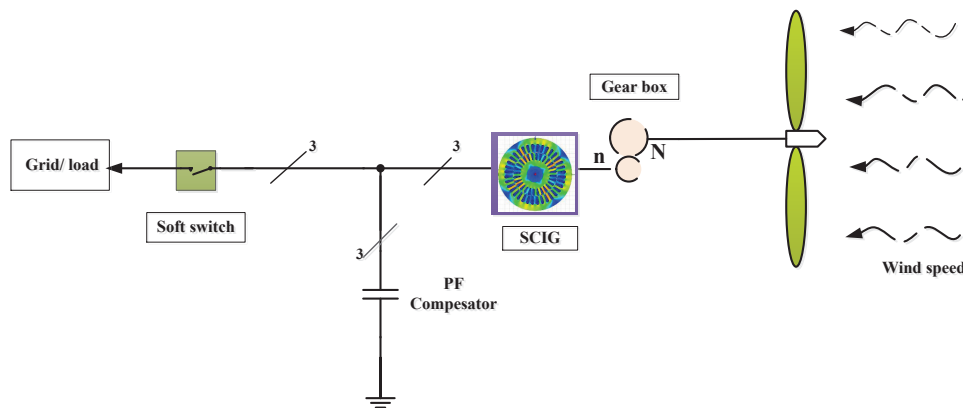


**Figure 1.1:** Wind energy conversion without power converter interface for fixed speed

In recent times, there is a significant focus on the development of green and sustainable grids to meet the future energy demand. The world is witnessing rapid growth in the generation of electricity with large wind farms and solar power plants, etc [4, 5]. These large wind farms are located mainly in the places where high-speed wind i.e., in the range of 10-15 m/s is observed for most of the years. In many parts of the globe, the average wind speed is not very high and the large wind turbine may not be suitable to extract wind power, thus by having a large number of a small power rating wind turbines, it may be possible to harness power from wind energy at low wind speed which may be suitable for providing the electricity to rural areas of the country.

The generators normally used for wind energy conversion are the squirrel cage induction generator (SCIG), doubly fed induction generator (DFIG), wound rotor synchronous generators (WRSGs), and permanent magnet synchronous generators (PMSGs), etc. The power ratings of these generators vary from a few kW to several MWs [6, 7]. The SCIG is rugged and simple in construction. It is comparatively inexpensive and requires minimum maintenance. The SCIG can operate as fixed-speed wind turbines. The SCIGs are also employed in variable-speed wind energy systems. The main drawback of fixed speed wind energy conversion system (WECS) is their low energy conversion efficiency for the variable wind speed. Fig.1.1 shows a typical schematic of a wind energy conversion system with SCIG.

In recent times, there is wide use of DFIG as the generator in WECS. This is mainly for its good performance with the wind at variable speed. In DFIG, the stator of the generator is connected to the grid directly, while the rotor is interfaced with the grid through the converter with

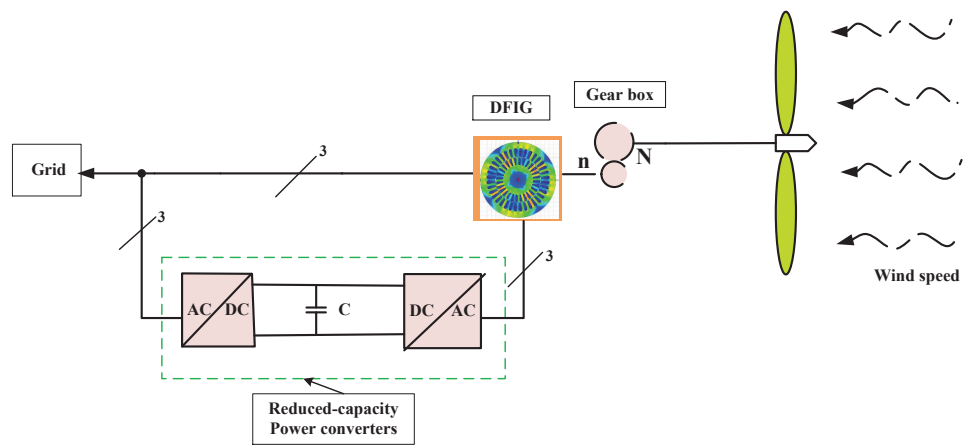


**Figure 1.2:** Variable speed configuration with reduced-capacity converters

reduced power capacity. The use of a rotor side converter with reduces capacity significantly reduces the cost and the requirement of space. Fig. 1.2 shows the DFIG based wind energy system with a reduced capacity converter. Using the power converters, the system power factor can also be adjusted. The converters process the slip power in the rotor circuits, which is approximately 30% of the rated power of the generator. The use of a converter also allows bidirectional power flow in the rotor circuit and increases the speed range of the generator. The DFIG improves overall power conversion efficiency, extends generator speed range  $\pm 30\%$ , and increases dynamic performance as compared to fixed speed SCIG.

The Wound Rotor Synchronous Generator (WRSG) is very well suitable for direct-drive wind turbines with a high power rating. The rotor field winding of the WRSG requires DC excitation. The rotor current can be supplied directly by brushes in contact with a slip ring attached to the shaft and electrically connected to the rotor winding. It is simple but it needs regular maintenance of brushes and slip ring.

In the Permanent Magnet Synchronous Generator (PMSG), the rotor magnetic flux is generated by permanent magnets. Thus, the PMSGs are brushless. Due to the absence of the rotor windings, it has a high power density, thus reducing the size and weight of the generator. Moreover, there are no rotor winding losses and result in reducing the thermal stress on the rotor. The main drawbacks of PMSGs are their high cost and are prone to demagnetization. For all generators, the performance of the wind energy conversion system can be enhanced with the

## 1. INTRODUCTION

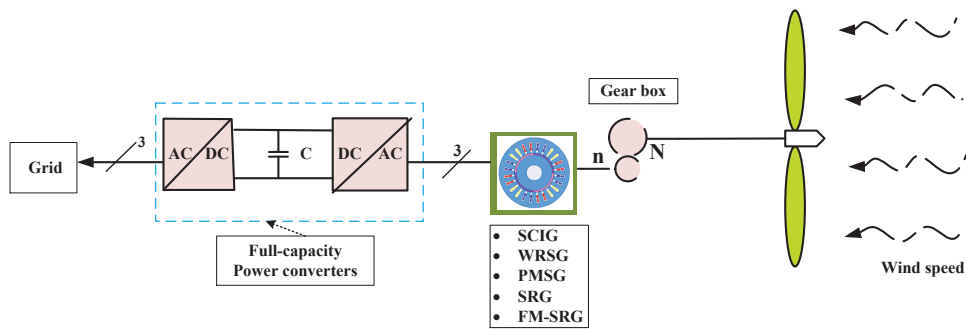


**Figure 1.3:** Variable speed configuration with full-capacity converters

use of a full capacity power converter as shown in Fig.1.3.

Out of these, SCIG is rugged but less efficient, whereas DFIG and WRSG are costly and requires frequent maintenance. The cost of PMSG is also quite high and hence is not much suitable for rural electrification. In recent times, there is some focus on the use of synchronous reluctance generators (SRGs). They are rugged, less costly, and has better efficiency.

The distribution generation (DG) of three phases AC/DC grid-tied system is also getting higher attention than a centralized generation because of transmission cost, mainly for rural areas which are distant and away from the urban. The critical issues included in the distributed generation of DC grid-tied involves machine design, energy conversion, control, and integration. A lot of electrical machines can be used and designed for electromechanical energy conversion, each with its own advantages and disadvantages [8,9].

Motivated by these ideas, the present thesis is towards the design and development of a synchronous reluctance generator (SRG) of a low-power suitable for wind power conversion systems operating at low power.

### 1.1 Literature Review

The advantages of self-excited induction generators (SEIGs) in stand-alone wind energy generation has gained attention in recent days. This is mostly due to its merits over the ac synchronous generator, such as robustness, rugged, brushless, simple, and relatively low maintenance cost [10]. Moreover, self-excited induction generators do not require a DC supply circuit for their excitation [11]. However, the main drawbacks of SEIG are its poor regulation of the voltage and frequency under varying loading conditions. The generated voltage and frequency

are highly dependent on the speed of the prime mover, and the loading condition due to the presence of slip. As a result, it requires a very sophisticated voltage and frequency stabilizer, which significantly increases the cost of installations [12, 13].

There are other generators such as Doubly Fed Induction Generator (DFIG) and permanent magnet synchronous generator which are used as generator in wind energy conversion systems (WECS). Compared to them, the suggestions or use of synchronous reluctance generator (SRG)/ ferrite-magnet synchronous reluctance generator (FM-SRG) as a potential generator of WECS is relatively new, and the availability of the literature is also less. Moreover, it is difficult to find the literature associated with the design and modeling of SRG with a low power rating. Most of the models available in the literature have neglected the effect of stator resistance, which normally will lead to an inaccurate model, especially for a low power generator. The SRG has many advantages as mentioned below [14–16].

- There is no copper winding in the rotor. Thus, the SRG is less costly and has no copper losses in the rotor.
- It reduces the risk of frequency and phase voltage variation in case of load change/ fault.
- It still exhibits high torque density and efficiency even without the need of using a ferrite magnet.
- It is more compact compared to other machines [12, 13].

### 1.1.1 Self-excited Synchronous Reluctance Generator

Wang L. et al. [17] and Sullivan R. et al. [18] reported the key technology behind the design and development of robust, efficient and small scale generator. A few mathematical models have been built to analyze the performance of a self-excited synchronous reluctance generator. Abdel-Kader et al. [19] attempted to develop an equivalent circuit for the SRG in the same manner as the SEIG. Yawei Wang et al. [20] also presented the analysis and modeling of self-excited synchronous reluctance generators with and without load, but, they used only resistive load in the model. Moreover, the effects of core losses and saturation effects are neglected,

## 1. INTRODUCTION

---

despite the losses and saturation have a significant effect on the performance of the machine with low power ratings. Rahim H. et al. [12, 21], investigated  $dq$  axes transformation-based model and demonstrated its validity. T. F. Chan. et al. [22], suggested a two-axis theory to model and analyze a three-phase self-excited reluctance generator that supplies power to an isolated inductive load. However, in these surveys, the estimation of the ratings of the excitation capacitor is not included. Nevertheless, these researches are mostly based on conventional salient rotor synchronous reluctance generators, i.e., no magnetic material or bridges in the rotor. Syede Sara M. and Pragasen P. [23] presented the conditions for self-excitation in terms of minimum residual flux and maximum start-up acceleration to trigger up self-excitation. Bianchi N et al. [24] reported the detailed design of rotor flux barrier design for torque ripple reduction in synchronous reluctance machine. Maged I. and Pilly P. [25] have presented that the conditions to achieve successful self-excitation of SRG for operating in a stand-alone system. i.e., build up of the terminal voltage, and rotor core residual flux is the primary conditions for self-excitation of SRG. Thus advancements in the design and modeling of SRG are required for its practical implementation and cost reduction. Hence, it is important to consider the saturation effects, stator core loss, compactness, and estimation of minimum excitation capacitor in its design, modeling, and implementation.

### 1.1.2 Self-excited Ferrite-magnet Synchronous Reluctance Generator

Yawi W. and Nicola B. [26] analyze the steady-state performance of self-excited Permanent-magnet (PM) assisted reluctance generator. Nicola B. et al. [27] reported the performance comparison between the PM-assisted reluctance motor and synchronous reluctance motor. The geometry analysis and optimization of PM-assisted reluctance motors are reported by Y.Wang, G. Bacco, and N. Bianchi [28]. The rotor saturation of PM-assisted reluctance and synchronous reluctance motors have been analyzed by Emanuele F. et al. [29]. Camara M. et al. [30] presented the merits of PM-assisted synchronous generator such as the compactness in size, no additional  $DC$  supply for magnetic field excitation, and robustness in construction. The main problem with this generator is the cost particularly when neodymium material is used. Latoufis et al. [31] suggested to use low-cost PMs such as ferrites and alnico. Aissaoui et al. [32] reported

the performance of the generators with low-cost PMs is low compare to the same generators using a neodymium magnet. In order to keep the generator with low-cost PM feasible, attention should be paid to the optimization and design. Therefore, the challenge for small-scale and micro-scale wind power generation is to find a solution to the development of the lower costs generator with good efficiency and reliability.

This is one of the motivations for this research work. For that, two configurations of low-cost SRG and FM-SRG suitable for wind power applications have been studied.

### 1.1.3 Mechanical stress and thermal analysis of Self-excited SRG

For all types of electrical generators, mechanical stress, and heat flow analysis is very important for their reliability and performance. In general, thermal analysis and mechanical analysis is quite complex, as it involves solving equations related to heat flows and mechanical stresses. Moreover, these analyses require the generator parameters along with the properties of the material in detail.

#### 1.1.3.1 Mechanical stress of Self-excited SRG

The design of SRG rotors usually uses the rotor topology that can be either transversely laminated variant (TLV) or axially laminated variant (ALV) [14]. The TLV being the most common anisotropic [15]. During the designing of TLV, flux barriers number and their shape insulation ratio are investigated in most cases [16, 33].

According to the survey, it is observed that the large size gearbox may damage wind turbines during large disturbances. Bang D. et al. [34] proposed that it is advantageous to have a small gearbox with a small gear ratio or direct drive wind turbine. Klaus G. et al. [35] and Rouhollah S. et al. [1] reported that it is important that to make the small size generators with high power density, high torque, and coupled with turbine directly or through the gearbox with a small gear ratio.

Park *et al.*, Mohammadi *et al.* [36] and Di Nardo *et al.* [37] have investigated different computational and analytical barriers optimization methods. The suitable selection of material grade is also one of the promising areas of investigation along with its impact on wind-driven SRG [38–40]. A very few and rare studies have been carried out on the analysis and design of

## 1. INTRODUCTION

---

mechanical stress, and electromagnetic performance on the design and thickness of radial and tangential ribs that link the flux lines.

An SRG with a high power factor requires a high  $d$ - to  $q$  - axis reactance ratio, which can be achieved through the high-quality design of the rotor. This comprises not only the design of the number of barriers, shape, and the number of poles but also the design of tangential and radial ribs to ensure good performance. The effect of centripetal or centrifugal force on radial and tangential ribs for a wind turbine operating at a steady-state needs to be studied.

### 1.1.3.2 Thermal Analysis of SRG for Wind Energy Application

Even though SRG has many advantages, some failure is observed due to thermal overloading and insulation breakdown. O' Donnell P. Part I [41] reported that a significant number of machine failures are due to the temperature overloading of the various machine components. O' Donnell P. Part II [42], Albrecht P. F. et al. [43] and Firoz A., Narayan C. [2] reported that nearly, 45% of the induction generator failures are associated with failure of insulation of copper winding and iron core. Tallam R.M. and Lee S.B. [44] reported the rise in temperature slowly degrades the quality of insulation, which is the main cause of generator failures.

The thermal overloading and insulation breakdown failures can severely affect the generation capability. Moreover, it also increases the financial cost associated with the maintenance and replacement of the machine. Staton D.A. and Cavagnino A. [45] identified that the thermal analysis of the generator is as vital as the magnetic design, and it plays an important role in the design of overload thermal protection system.

## 1.2 Motivation

In literature, many designs along with their performance are presented for the synchronous reluctance motors. Almost all the surveys are based on the performance improvement of the machine such as ripple torque reduction, optimization of rotor design, power factor, and efficiency improvement. Different types of rotors shape such as trapezoid, U-curve, circular and multi-bridge are used as per the requirements. Mostly, the trapezoid shape is used as it involves less complexity along with high mechanical stability compared to others.

Research on electric machines driven by wind turbine systems has drawn extensive attention

over the past few years. The electric machine for wind turbines should have high power density, maintenance-free operation, long durability, and high efficiency. Hence, the design of the electric generator must be based on the wind turbine performance, such as power, mechanical torque, and speed.

There is a lack of literature related to the design of an electrical generator considering the coupling of it with a wind turbine. There is also a need to have a better analytical model of SRG and FM-SRG developed using  $dq$  rotor reference frame. Moreover, many authors in their reported literature have neglected core losses,  $q$  – axis saturation, effects of stator resistance on torque. In addition to this, there is a gap in the literature associated with the compactness analysis of SRG and FM-SRG, and estimation of minimum capacitance required for the self-excitation stand-alone SRG and FM-SRG with inductive load.

The thermal and mechanical stress analysis is required to ensure the long durability and stability of the electric machine. The available research works on thermal and mechanical stress analysis are mostly related to induction generators and AC synchronous generators. It is observed from the literature review that the thermal and mechanical analysis of the SRG in self-excited mode is not covered widely, and has no simple and fast method for its analysis. Therefore, it is important to provide the thermal and mechanical stress analysis of SRG in detail to fill the gap in the available literature.

The above are the main motivations behind the design, development, and modeling of SRG and FM-SRG.

### 1.3 Scope and objectives

This section mainly discusses the scope and objective of this thesis. The author observes that there is a significant gap in the available literature on the design, development, and modeling of SRG/ FM-SRG. Thus, this thesis tries to fill these gap with the following contributions:

- (i) **Design and modeling of Self-excited Synchronous Reluctance and Ferrite-magnet Synchronous Reluctance Generators for suitable for Wind Energy Application:**

This includes wind turbine modeling, design, and analytical modeling of the self-excited

## 1. INTRODUCTION

---

SRG and FM-SRG in the  $q$  and  $d$ -axes rotor reference frame. The developed model includes  $q$  and  $d$ -axes saturation of inductances saturation and stator core losses. While designing, more attention is paid towards the increase in its efficiency, compactness, and its performance in the presence of inductive load. Further, the effects of stator winding resistance on electromagnetic torque is analyzed.

The finite element method, analytical calculations, experimental setup, are used to validate the analytical results. Simple formulae is developed to approximately the minimum values of excitation capacitor for self-excitation of SRG/ FM-SRG. It also includes the generator's performances under different conditions of wind speed and loads are presented and analyzed.

### (ii) **Electromagnetic-Mechanical Stress Analysis of Wind-Driven Self Excited Synchronous Reluctance Generator:**

It includes the mechanical stress analysis on the different sizes of tangential and radial ribs due to the centripetal force. The calculation of the centripetal force is based on the wind speed and rotor speed of the generator. It also includes an analysis of the variation in the electromagnetic feature such as the  $q$ - and  $d$  - axes flux, reactance ratio, inductance, and torque ripple for different sizes of tangential and radial ribs thickness. Similarly, the mechanical stress analysis of the rotor shows that a high concentration of peak stress is observed on the rotor ribs which limits the range of rotor speed.

### (iii) **Implicit and explicit thermal analysis of SRG for wind energy application:**

Explicit and implicit has to be used for solving proposed finite-difference modeling for thermal analysis to accurately estimate temperature rise at hot spots, such as end winding, stator windings, and the end region of SRG. It is observed that the temperature rise for the designed machine is good and within the desired and acceptable range.

## 1.4 Thesis Organization

In this section, a brief description of each section of the thesis is presented. The thesis consists of six chapters:

- **Chapter 2:** This chapter includes the design and analytical modeling of the synchronous reluctance generator. The performance of the machine includes both  $d$  and  $q$ -axes saturation effects. Further, the compactness, reliability, and efficiency of this generator are analyzed. The performance of the machine for change of load, constant speed, and variable speed is also analyzed. This also includes the effects of stator winding resistance on electromagnetic torque.
- **Chapter 3:** This chapter includes the design and analytical modeling of the ferrite magnet synchronous reluctance generator. The performance of the machine includes both  $d$  and  $q$ -axes saturation effects. Further, the compactness, reliability, and efficiency of this generator are analyzed. The performance of the machine for change of load, constant speed, and variable speed is also analyzed. This also includes a detailed comparison of SRG and FM-SRG.
- **Chapter 4:** This chapter includes mechanical stress and electromagnetic analysis of an SRG with a transversely laminated variant of the rotor. Mostly, this chapter focuses on issues related to mechanical stress and the electromagnetic design of an SRG rotor. The effects on the  $d$  – axis and  $q$  – axis inductances are analyzed with varying the radial and tangential ribs thickness. In a similar way, the effects of mechanical stress on the radial and tangential ribs are evaluated by varying the radial and tangential ribs thickness. It is observed that  $d$  – axis and  $q$  – axis inductances are affected by increasing/decreasing the thickness of radial and tangential ribs. The thickness of these ribs is chosen based on mechanical and electromagnetic analysis.
- **Chapter 5:** This chapter is focused on the thermal analysis of the self-excited synchronous reluctance generator. The thermal analysis is for the machine designed in Chapter 2 of this thesis. The losses of different components of the generator including electrical loss and core loss are included in the model as the heat source. Three techniques are used to perform overload thermal analysis. Mainly, the explicit, implicit, and FEA-based thermal analysis. The analysis includes the thermal response of different components of SRG.

## 1. INTRODUCTION

---

- **Chapter 6:** In chapter 6, the general conclusions from the research work and the scope for future work are presented.





## 1. INTRODUCTION

---



# 2

## DESIGN AND MODELING OF SELF EXCITED SRG FOR WIND ENERGY GENERATION

### Contents

---

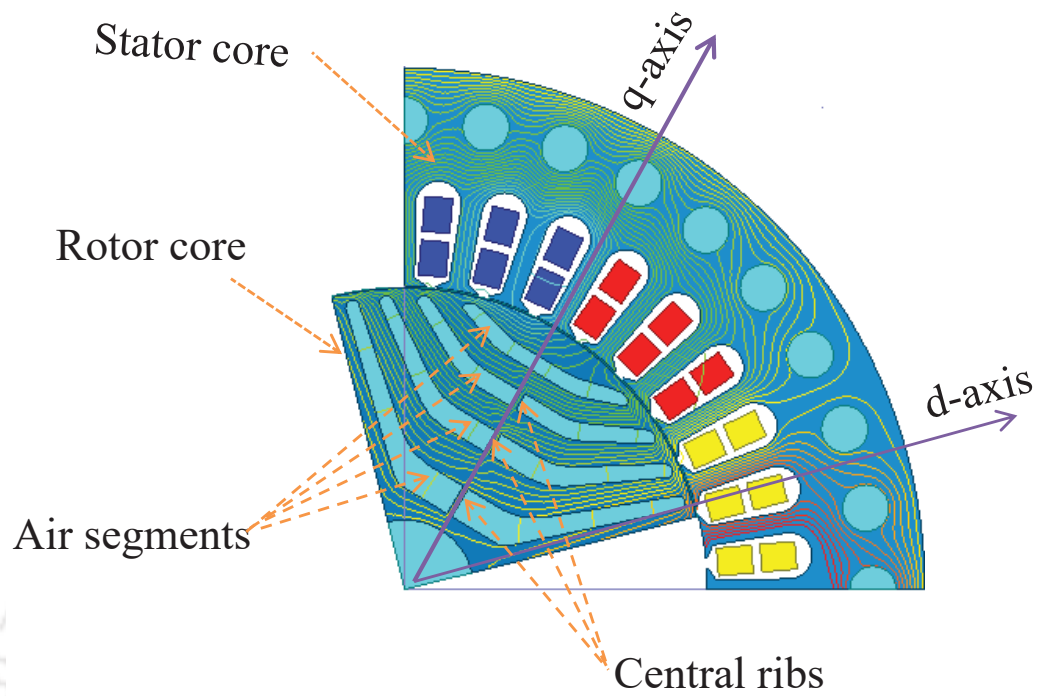
2.1	Introduction . . . . .	16
2.2	Wind turbine model . . . . .	18
2.3	Design and analytical modeling of SRG . . . . .	21
2.4	Steady-state performance analysis . . . . .	40
2.5	Summary . . . . .	53

---

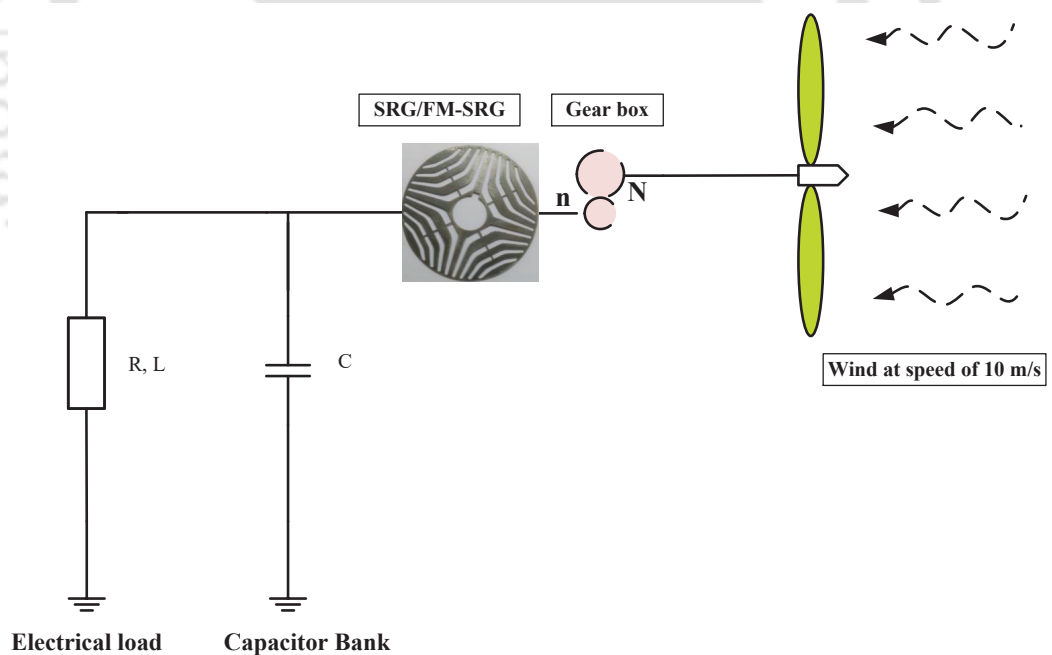
### 2.1 Introduction

In recent years, the evolution of renewable energy sources such as solar, hydroelectric, wind energy, biogas and geothermal energies have gained global attention. Rahim et al. [12] reported that an isolated self-stand generating strategy is desired to achieve electrification in distant areas. The conventional stand alone energy generation system utilizes a synchronous generator that requires a direct current field excitation. Nagria et al. [46] identified that the conventional energy generating methods are not suitable for rural electrification. Instead, a self-stand and self-excited generating system will be more convenient for such applications, as depicted in Fig.2.1(b). For machines like synchronous reluctance machines and induction machine, self-excitation can be realized by the interconnection of excitation capacitors in star or delta across the stator terminals, allowing them to be used as a self-stand generators [47], [48], [20]. The self-excited induction generator (SEIG) offers certain advantages over a conventional synchronous generator as a source of isolated power supply, such as low cost, rugged structure, reduced size, the absence of a direct current source for field excitation and low maintenance requirements [20, 23, 49]. However, the frequency of the generated voltage is influenced by the connected loads and excitation capacitor bank. A self-excited synchronous reluctance generator (SRG) has almost all the advantages of a self-excited induction generator. In addition, its rotor copper losses and the output frequency are not much influenced by the load, i.e., the load variations do not significantly affect the rotor speed and frequency of output voltage [22, 50].

In literature, only few mathematical models have been built to determine the performance of a self-excited synchronous reluctance generator. Abdel-Kader et al. [19] attempted to develop an equivalent circuit for the SRG in the same manner as the SEIG. Yawei Wang et al. [20] also attempted analysis and modeling of self-excited synchronous reluctance generators. But, the load is limited to no load and resistive load conditions. Moreover, the effects of core losses and saturation effects are neglected, although the losses and saturation have significant effect on the performance of the machine. Rahim H. et al. [21, 22, 24], [51], investigated  $dq$  axes transformation based model and demonstrated its validity. T. F. Chan. et al. [22], develops



(a)



(b)

**Figure 2.1:** (a) Cross-section and  $dq$  axes rotor reference frame of the SRG. (b) Stand-alone generating system for rural area applications.

a two-axis theory to model and analyze a three-phase self-excited reluctance generator which supplies to an isolated inductive load. However, in this survey, simple method to estimate the excitation capacitor is not included. Nevertheless, these research papers are mostly based

## 2. DESIGN AND MODELING OF SELF EXCITED SRG FOR WIND ENERGY GENERATION

on conventional salient rotor synchronous reluctance generators, i.e., no magnetic material or bridges in the rotor.

In this Chapter, wind turbine modeling, design and an analytical model in the  $dq$  rotor reference frame is developed as shown in Fig.2.1(a). In addition, the inductive load is considered to estimate the performance of the SRG. A new and simple method to estimate the minimum capacitance requirement for the inductive load is applied. Electromagnetic torque equations are developed in terms of stator winding resistance.

### 2.2 Wind turbine model

Among renewable energy sources on the earth, the generation of electricity from wind energy is more economical and environmentally friendly. Nowadays, there is a significant expansion in the use of wind for power generation. It results in the need for developing turbines and a generator of higher power ratings. Since the present work is more focused on the development of low cost, high-efficiency generators for rural applications. The rating of the turbine is in the range of kilo watts. The performance coefficient of the turbine in terms of the tip speed ratio (TSR) and blade pitch angle is given in equation (2.1) [52]:

$$C_p(\lambda, \alpha) = C_1 \left( \frac{C_2}{\lambda_1} - C_3 \alpha - C_4 \right) \exp \frac{-C_5}{\lambda_1} + C_6 \lambda \quad (2.1)$$

where;

$$\lambda_1 = \frac{(\alpha^3 + 1)(\lambda + 0.08\alpha)}{\alpha^3 - 0.0028\alpha - 0.035\lambda + 1} \quad (2.2)$$

For various types of wind turbine, the values of  $C_1 \sim C_6$  are different. Fig.2.2(a) depicts the group power coefficient curves and tip speed ratio for  $C_1, C_2, C_3, C_4, C_5$  and  $C_6$  as 0.219, 119, 0.4, 6, 12.5, and 0, respectively. The turbine output power is given in (watts)

$$P_m = \frac{R_t^5 \pi \rho_a C_p(\lambda, \alpha) \Omega^3}{2\lambda^3} \quad (2.3)$$

The value of  $\lambda$  has been selected for optimal point of  $C_p$  at  $\alpha = 0$  as shown in Fig.2.2(a). Once the values of  $\lambda$  and  $C_p$  are found, the turbine speed and the radius are calculated from (2.3) and

(2.4). The tip speed ratio can be expressed as:

$$\lambda = \frac{R_t \Omega}{v_\omega} \quad (2.4)$$

The torque causing the rotation of the wind turbine shafts depends on the turbine rated power output and angular velocity. It can be expressed as:

$$T_m = \frac{P_m}{\Omega} = \frac{R_t^5 \pi \rho_a C_p(\lambda, \alpha) \Omega^2}{2\lambda^3} \quad (2.5)$$

The gearbox used in wind turbine is utilized to transfer torque to the generator shaft rotating at a higher speed. The gear ratio is expressed as:

$$G_r = \frac{\omega}{\Omega} \quad (2.6)$$

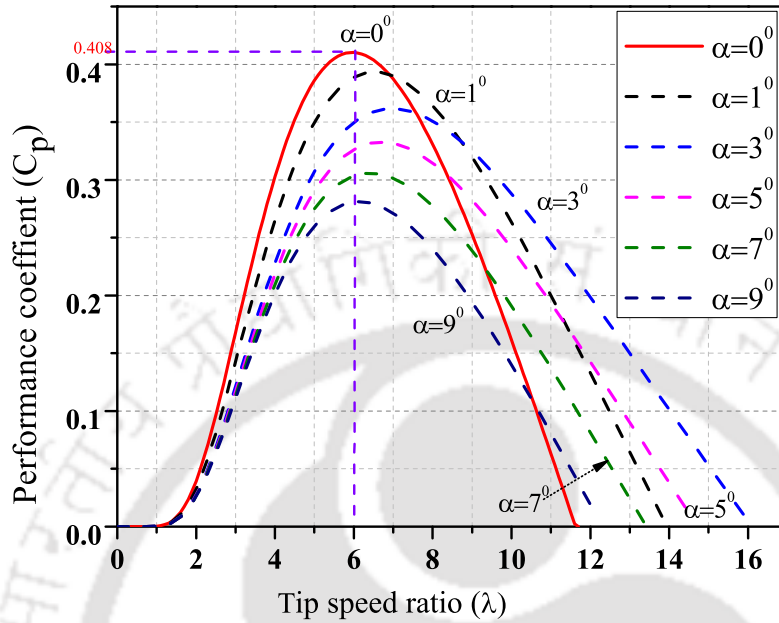
where,  $\omega$  and  $\Omega$  are the rotational speed of the generator and turbine, respectively. Equations (2.1) to (2.6) are used to design a wind turbine that can produce an output shaft power of 2.1 kW at a rated mean wind speed of 10 m/s. Table 2.1 summarizes the designed parameters of the wind turbine. The variation of power coefficient of the wind turbine for different blade pitch

**Table 2.1:** Initial data and calculated values of the wind turbine parameters

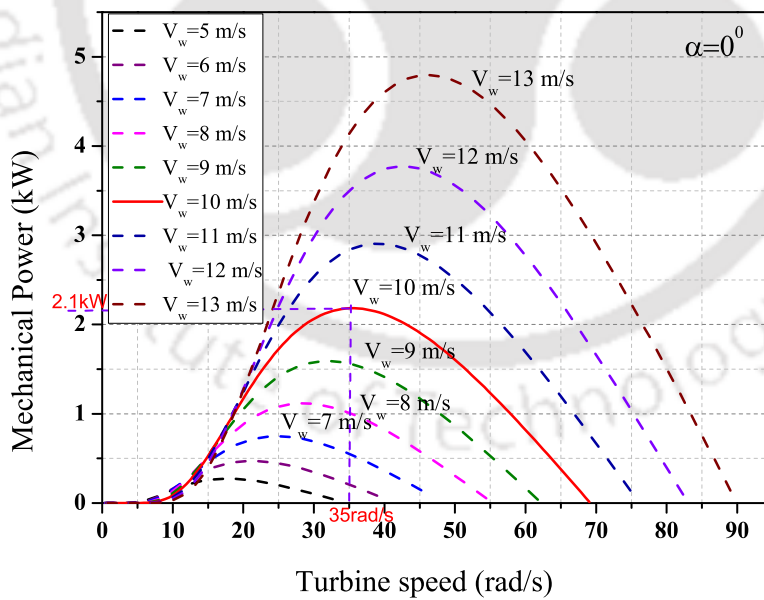
Parameters	Optimal values	units
<i>TSR(<math>\lambda</math>)</i>	6	–
<i>Mean wind speed</i>	10	m/s
<i>Gearing ratio</i>	4.488	–
<i>Blade speed</i>	35	rad/s
<i>Performance coefficient limit</i>	0.408	–
<i>Mechanical transmission efficiency</i>	90	%
<i>Mechanical power</i>	2.1	kW
<i>Mechanical torque of turbine rotor</i>	68.94	Nm
<i>Mechanical torque of generator shaft</i>	12.75	Nm
<i>Generator rated speed</i>	157.08	rad/s
<i>Turbine blade radius</i>	1.68	m

angle  $\alpha$  is shown in Fig. 2.2(a). Fig. 2.2(b), shows the generated mechanical power at different wind velocity. From Fig. 2.2(b), it is observed that as the wind speed increases, the rotational speed of the turbine also needs to be increased to extract maximum power out of the turbine. It

## 2. DESIGN AND MODELING OF SELF EXCITED SRG FOR WIND ENERGY GENERATION



(a)



(b)

**Figure 2.2:** (b) Analytical approximation of  $C_p - \lambda$  characteristics. (a) Turbine power characteristics at pitch angle  $\alpha = 0$ .

is also observed that for the designed wind turbine, the maximum power attains near  $35 \text{ rad/s}$  for the average wind speed of  $10 \text{ m/s}$ .

## **2.3 Design and analytical modeling of SRG**

The subsection below presents the algorithms used to design the SRG.

### **2.3.1 Design algorithm**

The sizing procedure of the generator starts with assigning the initial critical parameters of a wind turbine, such as speed, power, and maximum torque. These assigned parameters are used in the calculations of magnetic, geometric, and electric parameters together with the analytical model of the generator.

The design of the generator starts with the desired range of the output parameters, such as stator geometry, outer rotor diameter, etc. If any of the output parameters after the initial design is not in the desired range, the designed procedure is repeated with some modification, and this process is continued until the objectives of the design are satisfied. The analysis of the designed SRG is done using Finite element (Ansys Electronics Desktop) software. It is used to analyze the generator's performance related to the output functions such as torque ripple, electromagnetic torque, and the magnetic properties such as magnetic field  $H$  and magnetic field density  $B$ . The process ends if results obtained from the Ansys Electronic Desktop software satisfy the design requirements. Otherwise, the process is repeated by updating the assigned parameters such as current and magnetic loading, pole pitch to air gap ratio, and stack aspect ratio to obtain the proper size (see Table 2.2).

The sequence of how the algorithm is executed for the design of the SRG is summarized as follows:

- Step 1. The initial data (i.e., power, torque, and speed, etc.) required for the design is obtained from the assigned and the calculated value of wind turbine parameters, as given in Table 2.1. Initial data is fed to an analytical model to get an estimate of the initial design parameters of the machine.
- Step 2. Fix/assign parameters: some parameters can be fixed during calculations, and some of them should be revised during the design process. The summary of the assigned data parameter is shown in Table 2.2.

## 2. DESIGN AND MODELING OF SELF EXCITED SRG FOR WIND ENERGY GENERATION

Step 3. Choose the rotor's design parameter based on power, torque, size of the generator, and torque ripple. Equations (2.7) and (2.8) are used to get the rotor design parameters such as pole pitch, the outer diameter of the rotor, and stack length.

Step 4. Approximately assign the number of poles. Then search appropriate global and local points to design the rotor flux barrier, and interpolate the points to get a smooth ribs curve. Fig.2.3(a) shows the step involved in the design process.

Step 5. Evaluate the performance of the generator and compare the results with the desired values.

Step 6. If the performance of the generator is close to the desired values, go to step 9, else go to step 7.

Step 7. Optimizing the performance of the generator (i.e., flux noise, smoothen the emf, and reduction of ripple ) by updating the assigned design parameters.

Step 8. Go to step 6

Step 9. The design process is completed.

The design objectives for SRG which need to be satisfied are given as:

- The power rated 2.1 kW, with electromagnetic torque  $\geq 12.75 Nm$ , maximum torque ripple  $\leq 12\%$ , maximum back-emf  $\geq 145 V$ .

### **2.3.2 Analytical model of SRG**

For the developed analytical model, the following simplifying assumptions are considered:

- The time harmonics in current and space harmonics in air gap flux are neglected
- The core loss resistance is assumed to be constant and has no effect on excitation.

**Table 2.2:** Assigned Parameters

Parameters	values	units
$B_m$	[0.5, 1]	$T$
$k_d$	[0.6, 1]	–
$k_q$	(0, 0.4]	–
$L_s/\tau$	[0.6, 3]	–
$v_w$	[5, 25]	$m/s$
$J$	[4.5, 9]	$A/mm^2$
$k_u$	[0.4, 0.7]	–
$\rho_a$	1.2	$kg/m^3$
$Q_s$	36	–
$P$	2	–

Pole pitch  $\tau$ , as given in the equation below, is the prime parameter to obtain the outer rotor diameter of the generator.

$$\tau = \sqrt{\frac{T_m k_d^2 \mu_o}{B_m^2 P^2 (k_d - k_q) \sqrt{L_d/L_q} k_c (1 + k_s) l_g (L_s/\tau)}} \quad (2.7)$$

The outer rotor diameter,  $D_r$  and stack length,  $L_s$  could be:

$$\begin{cases} D_r = 2P\tau/\pi \\ L_s = \tau(L_s/\tau) \end{cases} \quad (2.8)$$

where,  $T_m$ ,  $L_s/\tau$ ,  $k_c = 1.03$ ,  $k_s = 1.2$ ,  $P$ ,  $k_d$ , and  $k_q$  are generator torque from the wind turbine, stack aspect ratio, Carter factor, saturation factor, number of pole pairs, the ratio of  $d$ - and  $q$ -axes inductance to magnetizing inductance, respectively. The parameters are defined in Table 2.2, while the saliency ratio defined as  $L_d/L_q = (k_d - k_q)/2k_q$ .

The design of the stator core geometry, i.e., the stator slot dimensions are shown in Fig.2.3(b). Fig.2.3(a) and Fig.2.3(b) show in details the structure of rotor ribs and stator. The distance of the rotor air gap ribs from the shaft radius is shown in the Fig.2.3(a). It also shows the separation of the edge of the ribs along the inner core radius of the rotor with an angle of  $\alpha_m$ . The segments/points are selected and are interpolated to get the structure of the 4-poles rotor (Fig.2.3(a)).

## 2. DESIGN AND MODELING OF SELF EXCITED SRG FOR WIND ENERGY GENERATION

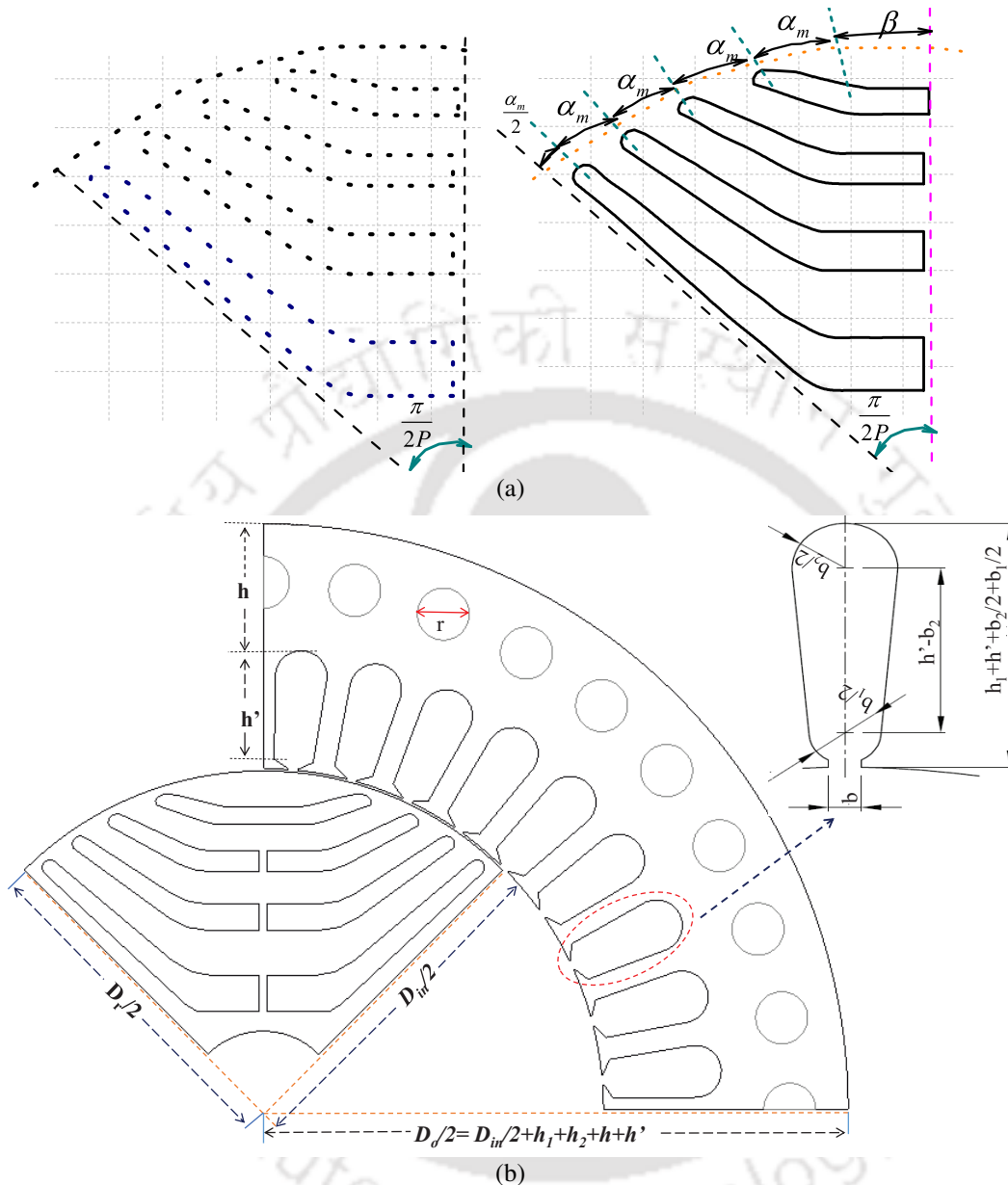


**Figure 2.3:** (a) Rotor ribs structure modeling . (b) Typical geometry of stator slot and rotor dimensions.

Every air, and flux barrier consists of trapezoid shape segments with a tangential thickness, radial thickness, and the endpoint angle of the air gap,  $\alpha_m$ . These parameters are designed in such a way as to ensure the structural stability at the high-speed and required electromagnetic performance.

The expression for maximum rotor tips mechanical end point angle  $\alpha_m$ , in terms of number of flux barriers ( $k_i$ ), poles pair (P) and floating angle ( $\beta$ ) is given as (2.9):

$$\alpha_m = \frac{\left(\pi/(2P) - \beta\right)}{\left(k_i + 1/2\right)} \quad (2.9)$$

Here, the floating angle  $\beta$  assumed to be in between 0 to 10° (0 to  $\pi/18$  rad).

The total slot,  $d$ - and  $q$ - axes components of ampere turns can be expressed as:

$$mI_m = \sqrt{(mI_d)^2 + (mI_q)^2} \quad (2.10)$$

Here,

$$mI_d = \frac{B_m \pi (1 + k_s) k_c l_g}{3 \sqrt{2} (q k_w k_d \mu_o)} \quad (2.11)$$

$$mI_q = mI_d \sqrt{L_d/L_q} \quad (2.12)$$

where,  $I_m = I_{max}$ , and  $k_w$  is stator slot winding factor,  $k_w=0.9598$ . The conductor per slot turns  $m$  is one of the key parameter in the design such as stator resistance, leakage inductance and machine inductances. The resistance per phase  $R_s$ , is:

$$R_s = \frac{2(L_s + L_e) P q J m \rho_r}{I_m} \quad (2.13)$$

where,  $L_e$  is end winding length,  $L_e = \pi \tau/2$ ,  $J$  is current density, and  $\rho_r$  is copper resistivity at temperature of 120°C. The leakage inductance  $L_{ls}$  is given as:

$$L_{ls} = (e_s + e_a + e_e) 2 L_s P q m^2 \mu_o \quad (2.14)$$

Here, the calculated slot permeance,  $e_s = 1.7564$ , air gap coefficient,  $e_a = 0.25$  and the end winding length coefficient,  $e_e = 0.0011685$ . The magnetizing inductance  $L_m$ , for uniform air gap can be presented as:

$$L_m = \frac{6 \mu_o \tau L_s P \left( q k_w m \right)^2}{\pi^2 l_g k_c (1 + k_s)} \quad (2.15)$$

## 2. DESIGN AND MODELING OF SELF EXCITED SRG FOR WIND ENERGY GENERATION

Therefore, for double layer winding, the stator resistance, leakage inductance, magnetizing inductance,  $d$ -, and  $q$  - axes inductances are the function of  $m$ . By simplifying the calculation, they are expressed as in Table 2.3:

**Table 2.3:** Parameters expression

Parameters	SRG	Units
$R_s$	$1.597 \times 10^{-3} (m)^2$	$\Omega$
$L_{ls}$	$2.001 \times 10^{-6} (m)^2$	$H$
$L_m$	$1.308 \times 10^{-4} (m)^2$	$H$
$L_d$	$1.39 \times 10^{-4} (m)^2$	$H$
$L_q$	$0.2616 \times 10^{-4} (m)^2$	$H$

Using the  $d$ - $q$  - axes rotor reference frame in Fig. 2.1(a), equations of the SRG in the transient state are written as below.

$$\begin{cases} V_d = R_s I_d + \rho \lambda_d - \omega P \lambda_q \\ V_q = R_s I_q + \rho \lambda_q + \omega P \lambda_d \\ V_{ph} = \sqrt{V_d^2 + V_q^2} \end{cases} \quad (2.16)$$

Whereas at steady state, the equation can be represented as:

$$V_{ph} = \sqrt{40} \times m \quad (2.17)$$

$$\begin{cases} \lambda_d = L_d I_d + \Lambda_{resi} \\ \lambda_q = L_q I_q \end{cases} \quad (2.18)$$

The above equations (2.16) are written utilizing the motor convention for the reluctance machine. When the machine work in generator mode, they convert mechanical power into electric active power, but requires reactive power to magnetize their magnetic field paths for self-excitation. In motoring mode,  $I_d$  and  $I_q$  are of the same sign, while in generating mode they

are of opposite sign. Referring to the current  $q$  and  $d$ -axes frame, motoring operations are in the first and third quadrants, in other words the motoring mode is when  $I_d$  and  $I_q < 0$  or  $I_d$  and  $I_q > 0$ ,  $T_e > 0$ , generating operations are in the second and fourth quadrants which means  $I_d > 0$  and  $I_q < 0$  or  $I_d < 0$  and  $I_q > 0$ ,  $T_e < 0$ . Fig. 2.6(a) and 2.7, show the reluctance torque developed by the SRG. Neglecting the effect of stator resistance, the torque equation is given as:

$$T_e = \frac{3P}{2}(\lambda_d I_q - \lambda_q I_d) = \frac{3P}{2}(L_d - L_q)I_d I_q \quad (2.19)$$

Since, the wind turbine rotates at low speed, gearbox are utilized to increase the speed of rotation of generator shaft. The swing-equation corresponding to the combined turbine - generator system is given as:

$$\rho \omega_e = \frac{P}{2J_t}(T_m - T_e - \frac{2B\omega_e}{P}) \quad (2.20)$$

### 2.3.2.1 Copper and core loss

The copper loss for SRG can be calculated as follows,

$$P_{cop} = 3R_s I_{ph}^2 \quad (2.21)$$

For machine with low power ratings, the core losses can be determined based on machine parameters. Therefore, for the calculation of iron loss, it is important to know the mass of stator yoke ( $w_y$ ), rotor ( $w_r$ ), and teeth ( $w_t$ ), which are given by the equations as given below [48].

$$\begin{cases} w_t = Q_s [b_{ts} h' + h_2 (\tau_s - (\frac{b_1 + b_2}{2})) + h_1 (\tau_s - b)] L_s \rho_i \\ w_y = \pi [(\frac{D_r}{2} + h_1 + h_2 + h')^2 - (D_r/2 + h_1 + h_2 + h')^2] L_s \rho_i \\ w_r = [\pi (\frac{D_r}{2})^2 - (A_{air} + A_{sh})] L \rho_i \end{cases} \quad (2.22)$$

Thus, the total iron core mass is the sum of stator yoke ( $w_y$ ), rotor ( $w_r$ ) and teeth ( $w_t$ ) masses, i.e.,  $w_{iron} = w_t + w_y + w_r$ . For this machine, the value taken for the machine parameters are,

## 2. DESIGN AND MODELING OF SELF EXCITED SRG FOR WIND ENERGY GENERATION

$h_1 = 1.2 \text{ mm}$ ,  $h_2 = 1.3 \text{ mm}$ ,  $b = 1.6 \text{ mm}$ ,  $h = 13 \text{ mm}$ ,  $h' = 11.81$ ,  $\rho_i = 7600 \text{ kg/m}^3$ , which represents slot opening height, wedge height, opening width, yoke height, height of slot and iron density, respectively. In the equation the stack length ( $L_s$ ) taken as  $65 \text{ mm}$ .

Thus, the core losses can be estimated as follows:

$$\begin{cases} P_{iron} = w_t(P_{B_{maxt}})_{50 \text{ Hz}} + w_y(P_{B_{maxy}})_{50 \text{ Hz}} + w_r(P_{B_{maxr}})_{50 \text{ Hz}} \\ P_{B_{maxt}} = (P_{1.5})_{50 \text{ Hz}}(B_{maxt}/1.5)^2(f/50)^2 \\ P_{B_{maxy}} = (P_{1.5})_{50 \text{ Hz}}(B_{maxy}/1.5)^2(f/50)^2 \\ P_{B_{maxr}} = (P_{1.5})_{50 \text{ Hz}}(B_{maxr}/1.5)^2(f/50)^2 \end{cases} \quad (2.23)$$

where,  $B_{maxt}$ ,  $B_{maxr}$  and  $B_{maxy}$  are stator teeth, rotor and yoke calculated maximum flux density at rated speed.

Since, the rated speed is  $1500 \text{ rpm}$  at  $50 \text{ Hz}$ , utilizing the manufacturer data for  $M - 19$  specifications, i.e.,  $(P_{1.5})_{50 \text{ Hz}} = 2.75 \text{ W/kg}$ . For the designed machine, the results obtained are  $(P_{1.4y})_{50 \text{ Hz}} = 2.4 \text{ W/kg}$ ,  $(P_{1.76r})_{50 \text{ Hz}} = 3.8 \text{ W/kg}$ , and  $(P_{1.1r})_{50 \text{ Hz}} = 1.48 \text{ W/kg}$ . Neglecting a percentage increase for the field harmonics in stator, rotor and mechanical losses percentage of rated power, the result related to the calculated copper and core losses are tabulated in Table 5.2.

### 2.3.2.2 Excitation capacitance and load modeling

The inductive load  $R_L$ ,  $X_L$  is connected to a capacitor bank in shunt at the stator terminals. The equation which relates the stator current, load current, and terminal voltages are presented as follow:

$$\begin{cases} I_{dc} = -I_d - I_{dL} \\ I_{qc} = -I_q - I_{qL} \end{cases} \quad (2.24)$$

The excitation capacitance in rotor reference frame is as follows (2.25)

$$\begin{bmatrix} I_{dc} \\ I_{qc} \end{bmatrix} = \begin{bmatrix} \rho C & \omega PC \\ -\omega PC & \rho C \end{bmatrix} \begin{bmatrix} V_{dL} \\ V_{qL} \end{bmatrix} \quad (2.25)$$

Where as the voltages in rotor reference frame are given as:

$$\begin{cases} \rho V_{qL} = \omega P V_{dL} + (-I_q - I_{qL})C \\ \rho V_{dL} = -\omega P V_{qL} + (-I_d - I_{dL})C \end{cases} \quad (2.26)$$

The R-L load model are obtained as (2.27)

$$\begin{cases} I_{qL} = \int \frac{1}{L} (V_{qL} - I_{qL} R_L + \omega P L I_{dL}) dt \\ I_{dL} = \int \frac{1}{L} (V_{dL} - I_{dL} R_L - \omega P L I_{qL}) dt \end{cases} \quad (2.27)$$

Equation (2.27) is obtained using a general balanced  $RL$  load model ( $V = R_L I + L \frac{dI}{dt}$ ). Table 2.4 summarizes the calculated parameters, the designed parameters of the generator, and their performance.

**Table 2.4:** Evaluated performance parameters and approximated quantity of 2.1 kW of SRG

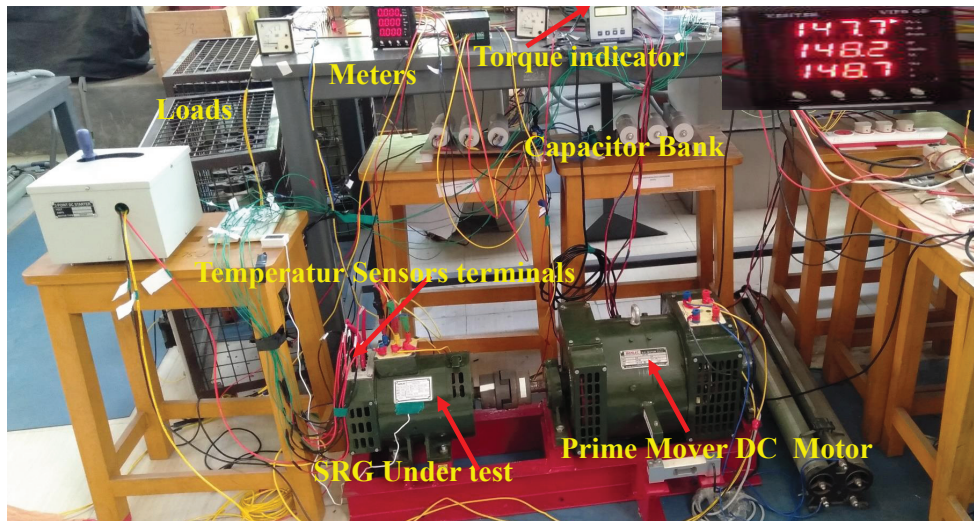
Parameters	Quantity	Parameters	Quantity
$L_m$	76 mH	$D_r$	104 mm
$L_d$	80.5 mH	$D_{in}$	105 mm
$L_q$	15 mH	$D_o$	165 mm
$L_{ls}$	1.15 mH	$h'$	11.811 mm
$I_m$	13.5 A	$m$	24
$P_{cop}$	274 W	$mI_q$	305.819 A.turns
$P_{iron}$	13.868 W	$mI_d$	132.84 A.turns
$L_s$	65 mm	$E_{ph}$	150 V
$l_g$	0.5 mm	$\eta$	86.95%
$k_u$	0.5	$P$	2
$W_r$	2.45 kg	$W_t$	0.99 kg
$R_s$	1.00 $\Omega$	$W_y$	2.7 kg

### 2.3.3 Experimental and finite element analysis of SRG

The present section includes the experimental validation of the proposed design of the SRG on a prototype of the SRG, as shown in Fig.2.4(a). The prototype is developed as per the proposed design specifications, where Fig.2.4(b) shows the core lamination and Fig. 2.4(c), shows the schematic diagram of the experimental setup.

The performance of the designed SRG is evaluated using FEA. The maximum induced

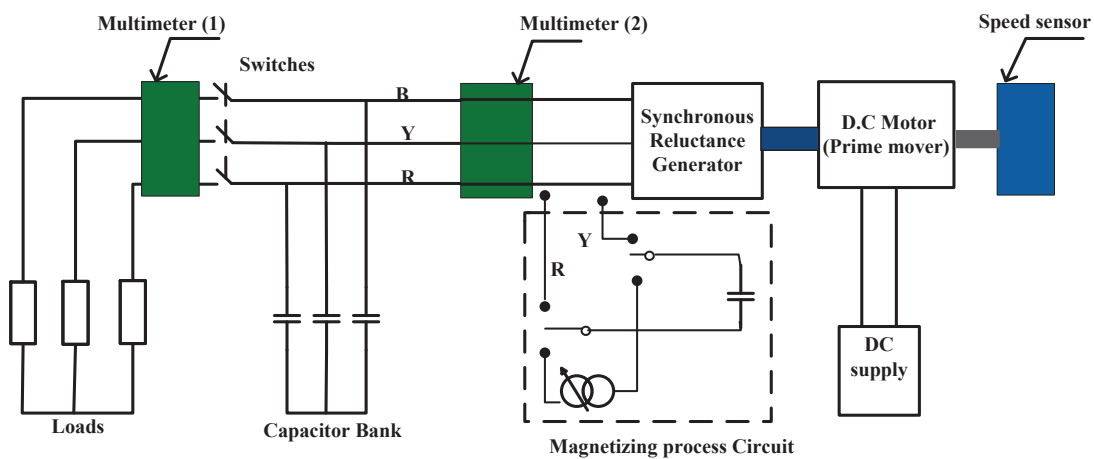
## 2. DESIGN AND MODELING OF SELF EXCITED SRG FOR WIND ENERGY GENERATION



(a)



(b)



(c)

**Figure 2.4:** (a) The drive motor and SRG set up. (b) Rotor core lamination and assemble. (c) Schematic diagram of the test bench.

electromotive forces (emfs) in the stator winding of the 2.1 kW SRG with symmetric design are shown in Fig. 2.5(a). The induced voltage in the machine is given by equation (2.16),

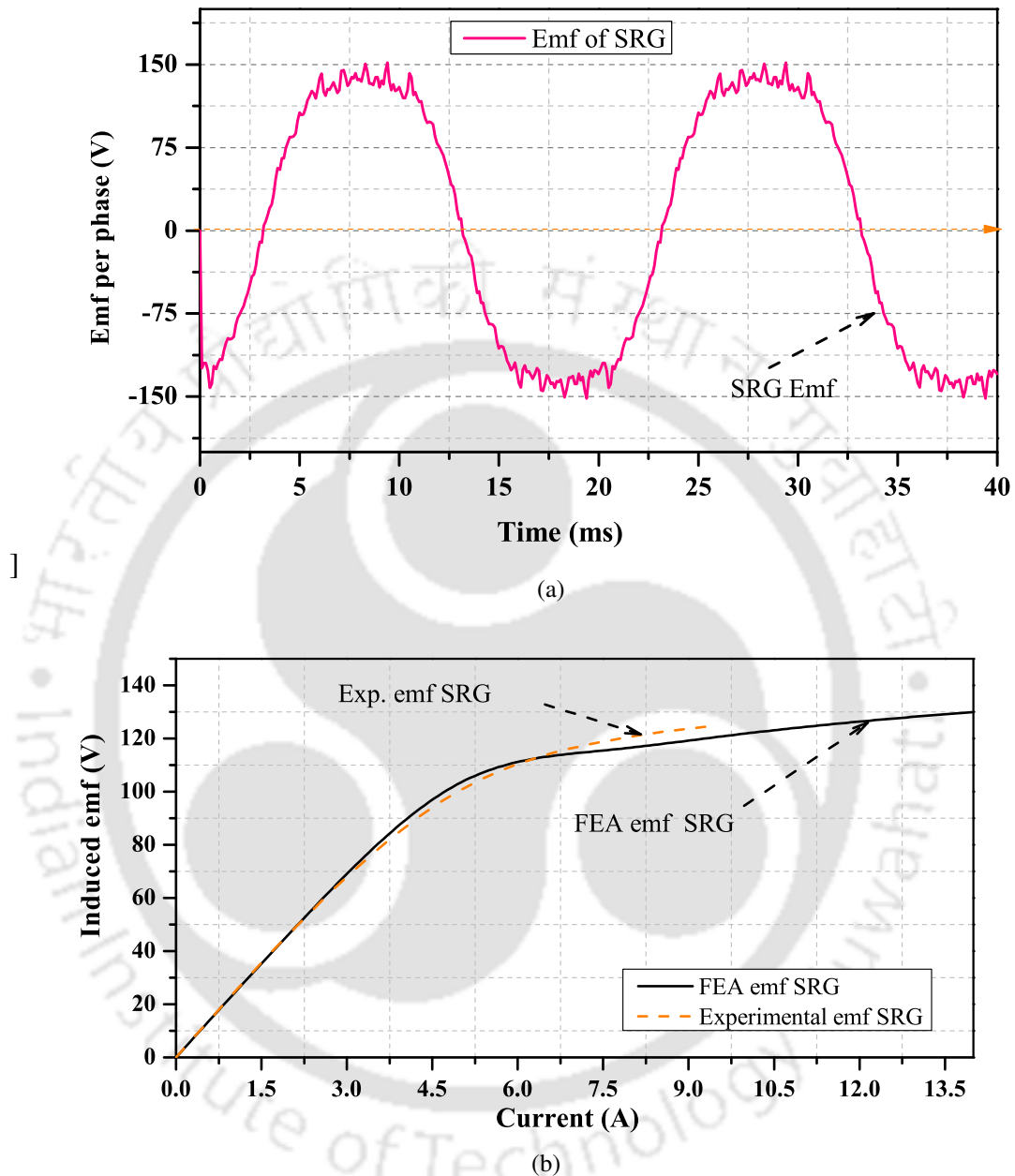


**Figure 2.5:** (a) Machine emf at given frequency. (b) emf curves as a function of current.

which clearly shows that if the effective  $q$  – axis flux is reduced, it leads to a decrease in induced voltage. The results obtained through FEA simulation with the excitation current of the machine is shown in Fig. 2.5(a).

The peak values of the back emf produced at 1500 *rpm* corresponding to different magnetizing currents for the machine is shown in Fig. 2.5(b). It is observed that, emf starts with zero voltage and the experimental result distinguished by dashed line. Fig.2.5(b) shows experimen-

## 2. DESIGN AND MODELING OF SELF EXCITED SRG FOR WIND ENERGY GENERATION

tally obtained emf by SRG, which is very close to the simulated (FEA) results.

The analytical equation of electromagnetic torque of SRG for  $R_s \neq 0$  is given as

$$T_e = \frac{3P}{2(P\omega)^2 L_d (\varphi + \beta^2)^2} V_{max}^2 (1 - \varphi) \left[ (\varphi - \beta^2) \sin(2\gamma) - 2\beta(1 + \varphi) \sin^2(\gamma) + 2\varphi\beta \right] \quad (2.28)$$

where,  $\beta = R_s / (P\omega L_d)$ ,  $\varphi = L_q / L_d$ .

The torque versus power angle curves as shown in Fig. 2.6(a) is obtained using FEA, it is observed that the torque at zero power angle (i.e.,  $\gamma = 0^\circ$ ) is positive. This can also be observed using the analytical equation of torque as given by (2.28) i.e.,  $T_e(\text{at } \gamma = 0) = 3PV_{max}^2(1 - \varphi)\varphi\beta / [(P\omega)^2 L_d (\varphi + \beta^2)^2]$ . It is also observed that the maximum torque angle decreases due to the presence of stator resistance, which cannot be neglected for machine with small ratings. The peak torque in generating mode is achieved at an angle close to  $94^\circ$  of power angle as shown in Fig.2.6(a). It is also observed that for  $R_s \neq 0$ , the torques do not attain their maximum values at power angle of  $45^\circ$  (i.e.,  $\gamma = 45^\circ$ ) for the machine.

If the effect of stator resistance is neglected i.e.,  $R_s = 0$  equation (2.28) is given as

$$T_e = \frac{3P}{2(P\omega)^2 L_d (\varphi)^2} V_{max}^2 (1 - \varphi) \left[ (\varphi) \sin(2\gamma) \right] \quad (2.29)$$

The above equation i.e., (2.29) can be rewritten as:

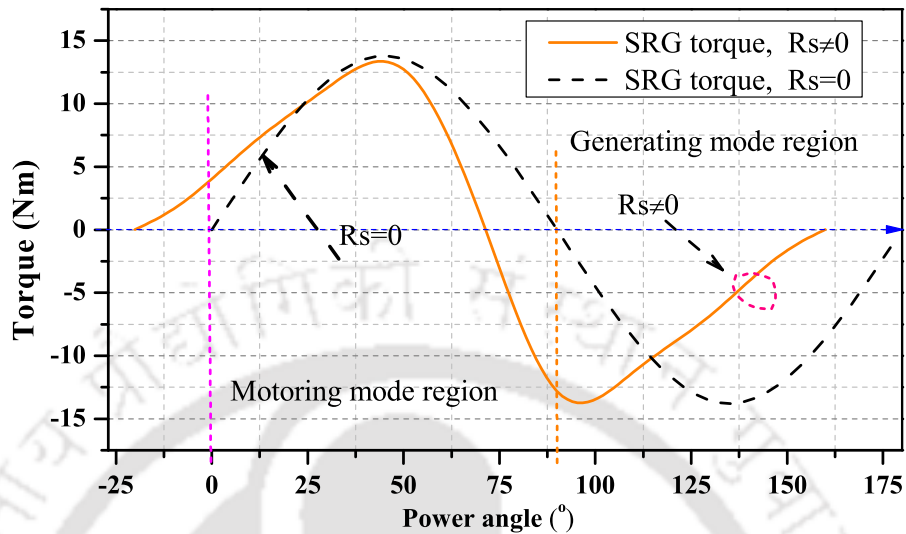
$$T_e = \frac{3P}{2(P\omega)^2 (L_d L_q)} V_{max}^2 (L_d - L_q) \sin(2\gamma) \quad (2.30)$$

Since,  $V_{max} / (P\omega L_d) = I_d$ , and  $V_{max} / (P\omega L_q) = I_q$ , the torque equation is rewritten as

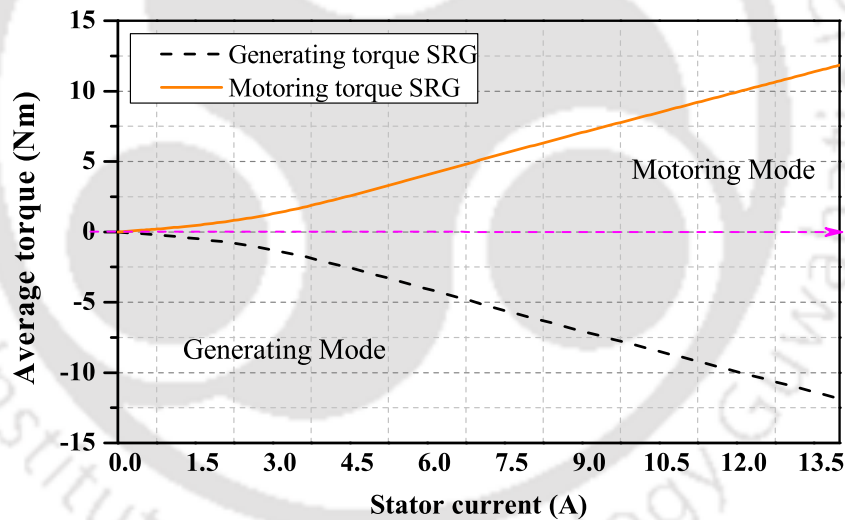
$$T_e = \frac{3P}{2} (L_d - L_q) I_d I_q \sin(2\gamma) \quad (2.31)$$

The maximum torque power angle,  $\gamma_m$  is obtained from equation given below

$$\begin{cases} \frac{dT_e}{d\gamma} = 0 \\ 2\cos(2\gamma) = 0 \end{cases} \quad (2.32)$$



(a)



(b)

**Figure 2.6:** (a) Torque versus power angle curves. (b) Torque versus current curves of the machine.

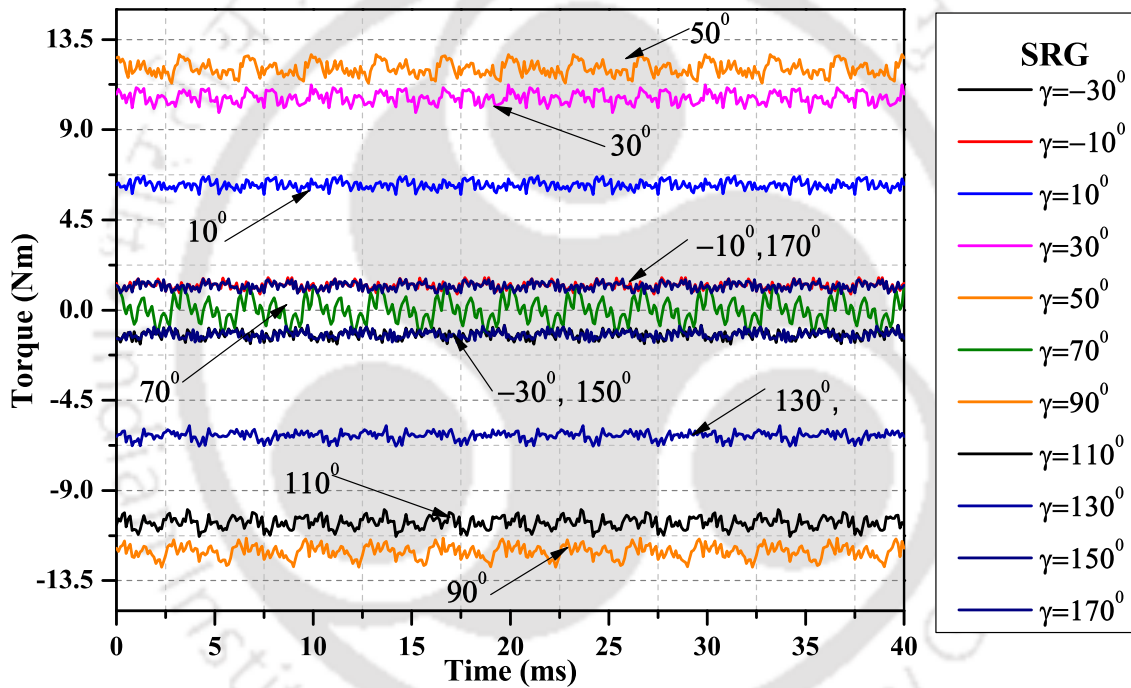
This implies that the maximum torque is obtained at  $\gamma_m = 45^\circ$  Or  $135^\circ$ . From equation (2.29) it can be seen that the torque tends to zero at  $\gamma = 0^\circ$  and  $\gamma = 90^\circ$ .

Fig. 2.6(b) represents that the performance of the machine in motoring and generating mode. From Fig. 2.6(b), it is observed that the average torque is as a function of square of stator current till the current of the machine is 5A. However, after 5 A the difference between  $(L_d - L_q)$  is approximately constant, hence, the variation of average torque is observed to be linear. Table 2.5, provides a comparative analysis of the presence of ripple torque in SRG with

## 2. DESIGN AND MODELING OF SELF EXCITED SRG FOR WIND ENERGY GENERATION

**Table 2.5:** Variation of torque ripple with phase currents

Maximum currents (A)	Ripple values
0	0
2.5	0.155
5	0.430
7.5	0.668
10	0.918
12.5	1.044
13.5	1.260



**Figure 2.7:** Variation of SRG electromagnetic torque with power angle, for  $R_s \neq 0$

increase of stator current.

Fig.2.7 represents the electromagnetic torque of the machine with variations of  $\gamma$ . Moreover, as the magnitude of average torque increases, the torque ripple also increases and viva-versa.

Fig. 2.8(a) depict the  $q$  and  $d$ -axes flux linkages versus the  $q$ -and  $d$ -axes currents. The curves are obtained from finite element analysis (FEA), and are verified through experimental tests, which estimates the  $q$  and  $d$ -axes flux linkage,  $\lambda_q$  and  $\lambda_d$ . From Fig. 2.8(a), it is observed that  $\lambda_d$  and  $\lambda_q$  increase linearly when  $I_d$  and  $I_q$  are less than 6 A. After that,  $\lambda_d$  and  $\lambda_q$  become almost constant due to saturation. It is also observed that simulated results are very close to the

**Table 2.6:** Values of polynomial coefficients evaluated from curve fit. The unit of equation (2.33) is in *mWb*

Poly.coefficient (c,d)	values
$c_0$	0.5
$c_1$	-96.7
$c_2$	104.1
$c_3$	-22.1
$c_4$	2.1
$c_5$	-0.1
$c_6$	0.002
$d_0$	2.2
$d_1$	57
$d_2$	-4.3
$d_3$	0.1
$d_4$	–
$d_5$	–
$d_6$	–

experimental results as shown in Fig.2.8(a). In order to account for the iron saturation effects, the relationship between the  $q$  and  $d$ -axes flux linkages is expressed as the function of armature current. Hence,  $\lambda_d$  and  $\lambda_q$  in (*mWb*) are represented by:

$$\begin{cases} \lambda_d = c_6 I_d^6 + c_5 I_d^5 + c_4 I_d^4 + c_3 I_d^3 + c_2 I_d^2 + c_1 I_d + c_0 \\ \lambda_q = d_3 I_q^3 + d_2 I_q^2 + d_1 I_q + d_0 \end{cases} \quad (2.33)$$

The polynomial coefficients  $c_0 - c_6$ , and  $d_0 - d_3$  are obtained from a curve fit of the actual  $q$  and  $d$ -axes flux linkages as obtained from Ansys Electronic Desktop software FEA. The estimated coefficients are shown in Table 2.6. These equations are utilized to estimated the requirement of minimum residual flux for generator to produce terminal voltage. Further analysis of self-excited synchronous reluctance generator has been carried out, with the presence of inductive load.

Similarly, the empirical expressions for the inductance along the  $d$ - and  $q$ -axes i.e.,  $L_d$ ,  $L_q$

## 2. DESIGN AND MODELING OF SELF EXCITED SRG FOR WIND ENERGY GENERATION

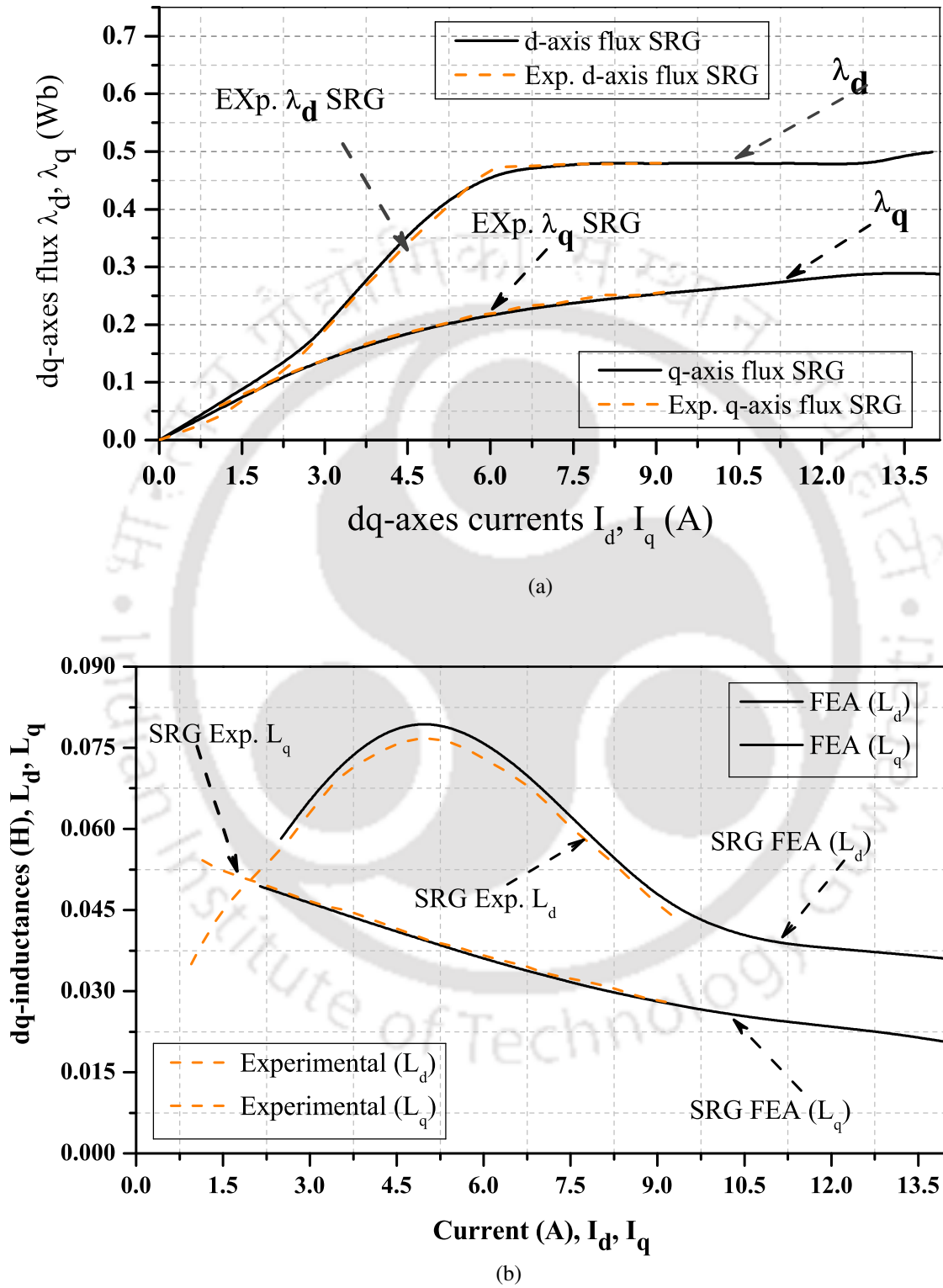


**Figure 2.8:** (a)  $d$ - and  $q$ -axes flux linkages magnetizing of the machines. (b)  $d$  and  $q$ -axes magnetizing inductance.

**Table 2.7:** Values of polynomial coefficients evaluated from curve fit.  
The unit of equation (2.34) is in  $mH$

Poly.coefficient (g,h) for SRG	values
$g_0$	15
$g_1$	9
$g_2$	8.3
$g_3$	-2.5
$g_4$	0.3
$g_5$	-0.01
$g_6$	0.0001
$h_0$	59.5
$h_1$	-4.8
$h_2$	0.1
$h_3$	-
$h_4$	-
$h_5$	-
$h_6$	-

in  $mH$  which are obtained through curve fitting are given below:

$$\begin{cases} L_d = g_6 I_d^6 + g_5 I_d^5 + g_4 I_d^4 + g_3 I_d^3 + g_2 I_d^2 + g_1 I_d + g_0 \\ L_q = h_2 I_q^2 + h_1 I_q + h_0 \end{cases} \quad (2.34)$$

The polynomial coefficients  $g_0 - g_6$ , and  $h_0 - h_2$ , are obtained from a curve fit of the actual  $d$ - and  $q$ -axes inductances.

Fig. 2.8(b) depict the  $d$  and  $q$ -axes inductances verses the  $q$  and  $d$  - axes currents, for SRG. The curves obtained from experiment test bench and FEA are distinguished by dashed and solid line, respectively. Equation (2.34) and Table 2.7 show the variation of saturations as the function of  $q$  and  $d$ -axes currents.

The  $L_d$  of the SRG keeps increasing for low values of current. However, as the current becomes approximately more than 5 A, the value of  $L_d$  starts decreasing and attains a constant value because of the steel saturation. While the  $L_q$  of SRG is high for the low value of current due to the presence of bridge in  $q$  - axis, it decreases gradually with the increase of current and subsequently becomes constant. For no cross-saturation, the  $L_d$  would depends on  $I_d$  only, however, increasing  $I_q$  causes the  $L_d$  to drop. Similarly,  $L_q$  drops when the current,  $I_d$  grows as

## 2. DESIGN AND MODELING OF SELF EXCITED SRG FOR WIND ENERGY GENERATION

**Table 2.8:** Technical achievements of the SRG

SRG			
Parameters	Initial	Final (optimal)	Increase (%)
$P_\rho$	1.22	1.5	19.9
$P_{sp}$	0.20	0.25	20.2
$T_\rho$	7.46	9.10	19.8
$T_{sp}$	1.24	1.49	18.3

shown in Fig. 2.8(b).

### 2.3.4 Technical performance of SRG

The compactness, reliability and efficiency are the important issues related to the power generation at remote locations. The compactness of the machine helps in many ways, such as, easy to transport, reduce installation cost, reduce weight, and reduced cost of other parts of the structure. To develop a low power rating machine with high power density and high efficiency is a very challenging work, but in this work we design a low power rating machine with high power density using FEA. To design the machine, the key parameters such as volume, mass, rated power, and torque of the machines are utilized. Where the volume of the machine  $V_{ml}$ , can be expressed as:

$$V_{ml} = \frac{D_o^2 L_s \pi}{4} \quad (2.35)$$

There are inherent advantages in utilizing synchronous reluctance generator in term of machine performance and manufacturing. It also has high efficiency and high power density. In this Chapter, SRG is designed for a power rating of 2.1 kW. By optimizing the design parameters for the machine, the final design has the stack length of 65 mm for SRG. The other initial and final ( i.e., the optimal one) such as power density ( $P_\rho$ ), specific power density ( $P_{sp}$ ), torque density ( $T_\rho$ ), and specific torque ( $T_{sp}$ ) are provided in Table. 2.8. It can be note that the performance in term of torque density ( $T_\rho$ ), and specific torque ( $T_{sp}$ ) can be evaluated for the machine. Moreover, SRG is more robust and its manufacturing cost is less as compared with SEIG. Table 2.9 provides the performance of self-excited SRG generator. From Tables 2.9 and Fig. 2.9(b), the compactness/size of SRG is observed. Overall, it can be said that the design of SRG is

**Table 2.9:** Analytical, FEA and experimental results of the machines

SRG			
Parameters	Analytical	FEA	Experimental
$V_{ml}$	1.4 L	--	-
$L_d$	80.2 mH	80 mH	79 mH
$L_q$	15 mH	15.2 mH	17.5 mH
$T_e$	12.75 Nm	12.23 Nm	12.17 Nm
$T_{rp}$	-	9.7%	-

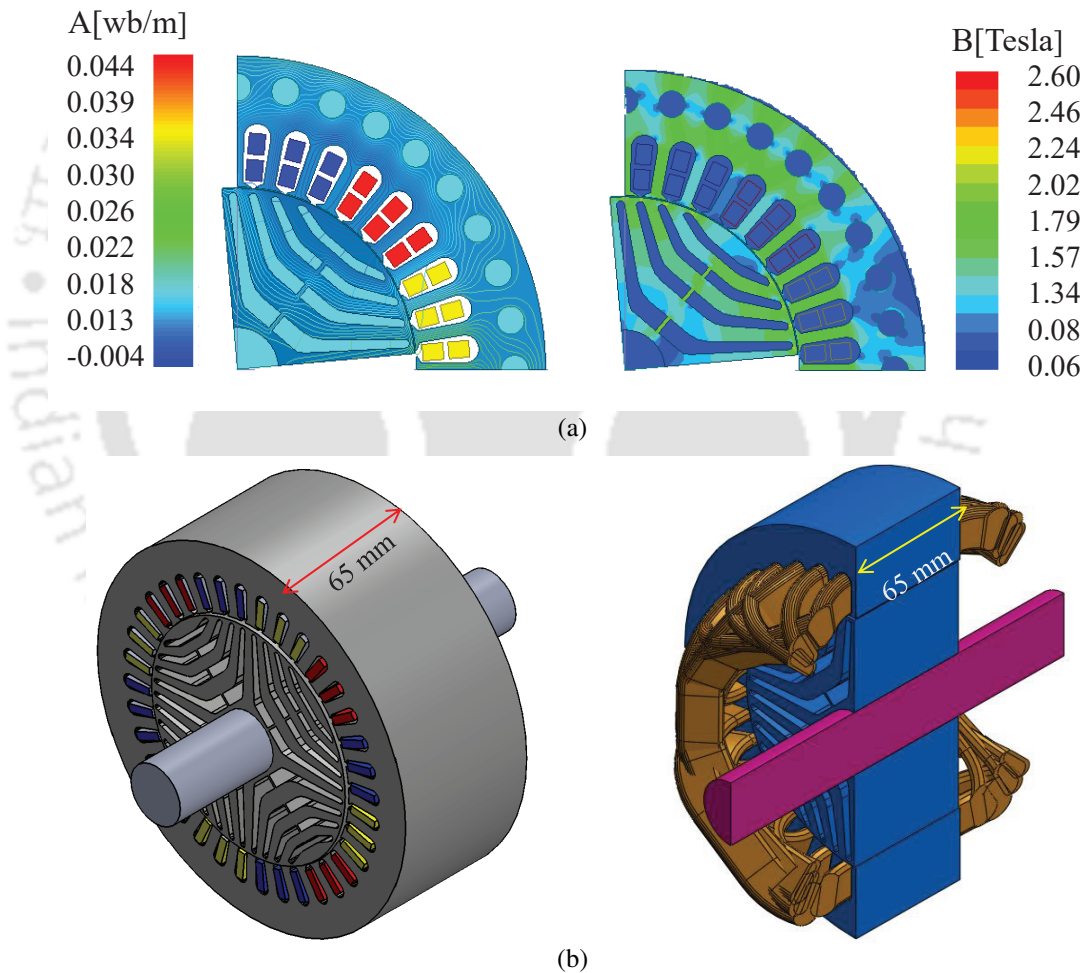


**Figure 2.9:** (a) Magnetic flux density distribution and flux lines of the machines . (b) Size of the machine.

more robust and less costly. Since, cost effectiveness and robustness are major criteria for the suitability of generator for rural electrification application, SRG is more suitable for rural electrification. Fig. 2.9(a) provides magnetic field density distribution and flux lines of SRG

## 2. DESIGN AND MODELING OF SELF EXCITED SRG FOR WIND ENERGY GENERATION

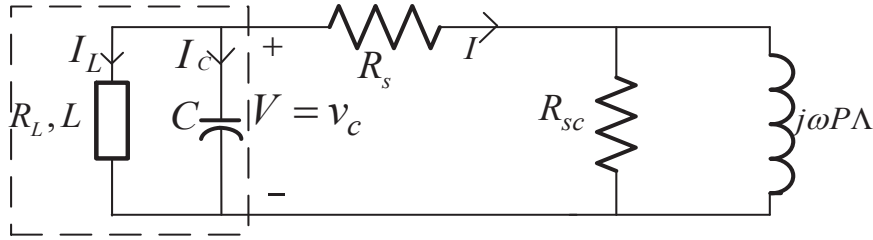


**Figure 2.10:** Circuit of the synchronous reluctance generator with capacitor  $C$ , resistive  $R_L$  and inductive  $X_L$  loads ( $V = V_d + jV_q, I = I_d + jI_q, \Lambda = \lambda_d + j\lambda_q$ )

generator. While Fig. 2.9(b), shows the compactness/volume of the machine.

### 2.4 Steady-state performance analysis

Self-excitation of the SRG is required to build up their emfs and residual flux in the field poles at a given rotor speed. Thus, a suitable excitation capacitance must be selected with some critical value. The detail impedance load analysis of the SRG is carried out in the following section. For the inductive load, the terminals of the SRG are connected to a bank of capacitors  $C$  and the load  $R_L, L$  in parallel as shown in Fig. 2.10. Consequently, the equivalent impedance can be expressed as:

$$Z_{eq} = \frac{-jX_c(R_L + jX_L)}{(R_L + j(X_L - X_c))} \quad (2.36)$$

Rationalization of the denominator yields,

$$Z_{eq} = \frac{X_c R_L X_L}{(R_L)^2 + (X_L - X_c)^2} - \frac{jX_c X_L (X_L - X_c)}{(R_L)^2 + (X_L - X_c)^2} - \frac{jX_c (R_L)^2}{(R_L)^2 + (X_L - X_c)^2} - \frac{X_c R_L (X_L - X_c)}{(R_L)^2 + (X_L - X_c)^2} \quad (2.37)$$

Letting,

$$\Upsilon = \frac{X_c}{(R_L^2 + (X_L - X_c)^2)} \quad (2.38)$$

then,  $Z_{eq} = \Upsilon R_L X_c + j\Upsilon X_L X_c - j\Upsilon R_L^2 - j\Upsilon X_L^2$ . The voltage of impedance (loads) is:

$$\begin{aligned} V = -Z_{eq}I &= (-\Upsilon R_L X_L + j\Upsilon X_L(X_L + X_c) + j\Upsilon R_L^2 \\ &+ \Upsilon R_L(X_L - X_c))(I_d + jI_q) \\ &= -\Upsilon(R_L X_c I_d + I_q R_L^2 + I_q X_L^2 - I_q X_L X_c) \\ &- j\Upsilon(R_L X_c I_q - I_d R_L^2 - I_d X_L^2 + I_d X_L X_c) \end{aligned} \quad (2.39)$$

Therefore, the voltage equations are figure out to:

$$\begin{cases} V_d = R_s I_d - X_q I_q = -\Upsilon(R_L X_c I_d + R_L^2 I_q + X_L^2 I_q - X_L X_c I_q) \\ V_q = R_s I_q + X_d I_d = -\Upsilon(-R_L^2 I_d - X_L^2 I_d + X_L X_c I_d + R_L X_c I_q) \end{cases} \quad (2.40)$$

By elimination of  $I_d$  and  $I_q$  from equations (2.40) and rearrangement of terms yield the following quadratic equation.

$$\begin{aligned} (\Upsilon R_L X_c + R_s)^2 &= (-\Upsilon(R_L^2 + X_L^2 - X_L X_c) + X_q)(\Upsilon(-R_L^2 \\ &- X_L^2 + X_L X_c) + X_d) \end{aligned} \quad (2.41)$$

The condition required for the self-excitation of SRG is obtained by maintaining the active power balanced and equating the reactive power to zero i.e.,  $P_g = P_{cop} + P_{iron} + P_{load}$  and  $Q_c - Q_l - Q_\omega = 0$ . The following equation obtained by substituting equation (2.38) in equation (2.41)

$$\begin{aligned} &\frac{X_L^2(X_c - X_q) - X_c X_L(X_c - 2X_q) + R_L^2(X_c - X_q) - X_c^2 X_q}{R_s(R_L^2 + X_L^2 - 2X_L X_c + X_c^2) + R_L X_c^2} \\ &+ \frac{R_s(R_L^2 + X_L^2 - 2X_L X_c + X_c^2) + X_c^2 R_L}{-X_c^2(X_L + X_d) + (R_L^2 + X_L^2 + 2X_L X_d)X_c - X_d(R_L^2 + X_L^2)} = 0 \end{aligned} \quad (2.42)$$

Solving (2.42), for  $X_c$ , the minimum value of the capacitor for self excitation can be achieved at different speeds. Which gives four resonant points in the self excitation of SRG. (With  $X_d = \omega_e L_d$ ,  $X_q = \omega_e L_q$  and  $X_c = 1/\omega_e C$ ). The solutions are given as:

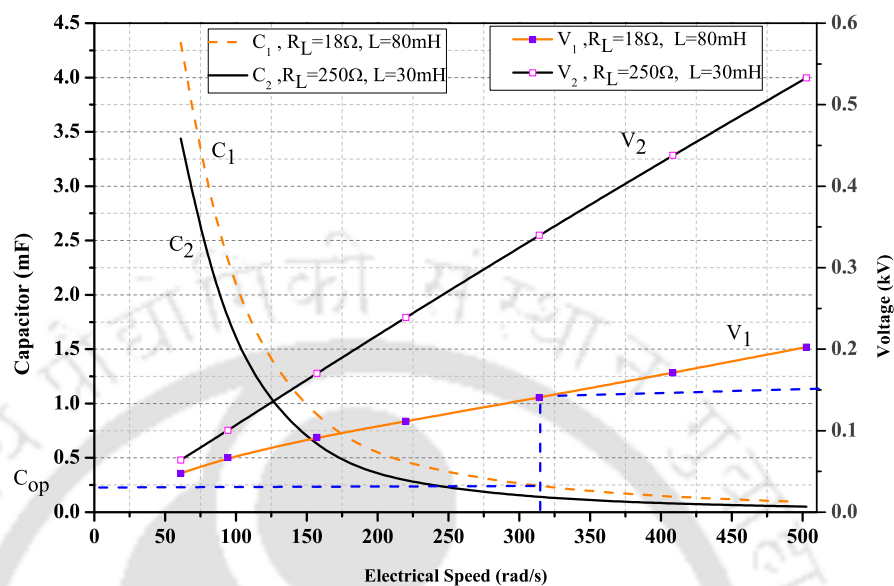
## 2. DESIGN AND MODELING OF SELF EXCITED SRG FOR WIND ENERGY GENERATION

$$\begin{cases} X_c = \frac{1}{\omega_e C} = X_L + jR_L \\ X_c = \frac{1}{\omega_e C} = X_L - jR_L \end{cases} \quad (2.43)$$

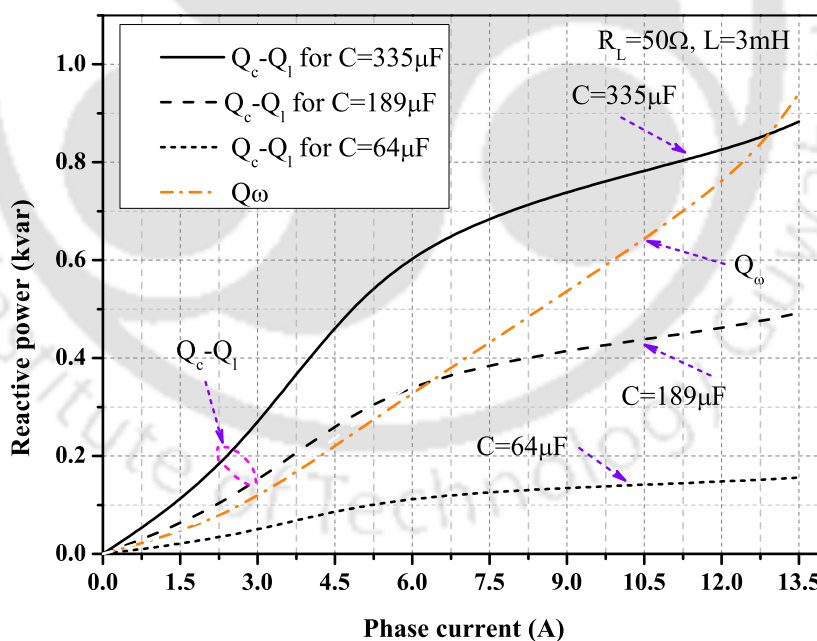
$$\begin{cases} X_c = \frac{1}{\omega_e C} = 1 \left/ \left[ 2 \left( R_L^2 - 2R_L R_s + R_s^2 + X_L^2 + X_L X_d + X_L X_q + X_d X_q \right) \right] \right. \\ \left. \left( R_L^2 X_d + R_L^2 X_q + 2R_s^2 X_L + X_L^2 X_d + X_L^2 X_q + 2X_d X_L X_q \right) \right. \\ \left. + \left( R_L^4 (-4R_s^2 + X_d^2 + 2X_d X_q + X_q^2) + 8R_L^3 (R_s^3 + R_s X_d X_q) + \right. \right. \\ \left. \left. 2R_L^2 (-2R_s^4 - 4X_d^2 X_q^2 - 4R_s^2 X_d X_q + X_L^2 X_q^2 - 2X_L^2 X_d X_q + X_L^2 X_q^2 - 2X_d^2 X_q^2) \right. \right. \\ \left. \left. + 8R_L R_s X_L^2 (R_s^2 + X_d X_q) + X_L^4 (-4R_s^2 + X_d^2 - 2X_d X_q + X_q^2) \right)^{1/2} \right. \end{cases} \quad (2.44)$$

$$\begin{cases} X_c = \frac{1}{\omega_e C} = 1 \left/ \left[ 2 \left( R_L^2 - 2R_L R_s + R_s^2 + X_L^2 + X_L X_d + X_L X_q + X_d X_q \right) \right] \right. \\ \left. \left( -R_L^2 X_d - R_L^2 X_q - 2R_s^2 X_L - X_L^2 X_d - X_L^2 X_q - 2X_d X_L X_q \right) \right. \\ \left. + \left( R_L^4 (-4R_s^2 + X_d^2 + 2X_d X_q + X_q^2) + 8R_L^3 (R_s^3 + R_s X_d X_q) + \right. \right. \\ \left. \left. 2R_L^2 (-2R_s^4 - 4X_d^2 X_q^2 - 4R_s^2 X_d X_q + X_L^2 X_q^2 - 2X_L^2 X_d X_q + X_L^2 X_q^2 - 2X_d^2 X_q^2) \right. \right. \\ \left. \left. + 8R_L R_s X_L^2 (R_s^2 + X_d X_q) + X_L^4 (-4R_s^2 + X_d^2 - 2X_d X_q + X_q^2) \right)^{1/2} \right. \end{cases} \quad (2.45)$$

Since, the  $L_d$ ,  $L_q$  and  $R_s$  are parameters of the generator that have been obtained from the designed machine as shown in (Table 2.4 and equation (2.34)). Therefore, solving (2.42) gives the minimum value of the capacitive reluctance required for self-excitation of the SRG generator. It is observed that while solving equation (2.42) four solutions with two real roots and two imaginary roots are found (see equations (2.43), (2.44), and (2.45)). In case of imaginary roots, no excitation is possible and the generator can not achieve the rated voltages (equations (2.43)), while in case real roots, we calculate the capacitive reluctance given by the roots ((2.44), and (2.45)). Since, we are interested in minimum value of the capacitor, the root which provides maximum reactance is considered. The plots of the estimated capacitor as function of speed corresponding to the two real roots for a load of  $R_L = 18 \Omega$ ,  $L = 30 \text{ mH}$  and  $R_L = 250 \Omega$ ,



(a)



(b)

**Figure 2.11:** (a) Capacitor, voltage and speed curves ( $R_L = 18 \Omega, L = 80 \text{ mH}$ ), ( $R_L = 250 \Omega, L = 30 \text{ mH}$ ). (b) Reactive power map at the speed of  $1500 \text{ rpm}$  with different currents ( $R_L = 50 \Omega, L = 3 \text{ mH}$ ).

$L = 30 \text{ mH}$  is provided in Fig.2.11(a).

## 2. DESIGN AND MODELING OF SELF EXCITED SRG FOR WIND ENERGY GENERATION

From Fig. 2.11(a) it is also observed that the curves are more focused on the solution which give minimum capacitance value with the variation of the speed. Since we are interested in finding the minimum requirement of the capacitor, hence, we have discarded the other solution and use a solution with a minimum capacitor. At approximately 62.5 rad/s, the value of the capacitor used is 0.00425 F, and for 500 rad/s, it is about to 0.00018 F.

Fig. 2.11(a) also provides a comparison of the terminal voltage versus speed with the value of minimum capacitance. It is also observed that the minimum capacitance required at a particular speed is also a function of the inductive load. This is shown by two different curves of minimum capacitance corresponding to the loads  $R_L = 18 \Omega$ ,  $L = 80 \text{ mH}$ , and  $R_L = 250 \Omega$ ,  $L = 30 \text{ mH}$ .

It can also be observed that the terminal voltage depends on the value of capacitor and speed, i.e., by increasing the capacitor or the speed, the terminal voltage increases or vice versa. For the effective use of SRG to generate power, it is important to have some ways of varying the capacitor to maintain the magnitude of the terminal voltage. An economical way, is to design an algorithm that picks the turbine speed and the value of the capacitor to improve the overall efficiency of the system.

In a self-excited system, the reactive power is provided by the capacitor's bank. For inductive load, a reactive power balance is achieved between the generators, capacitors, and inductive load, as shown in the following equations.

$$\begin{cases} Q_g = Q_c - Q_l - Q_\omega \\ P_g = P_{cop} + P_{iron} + P_{load} \end{cases} \quad (2.46)$$

where  $P_g$ ,  $P_{cop}$ ,  $P_{iron}$  and  $Q_g$  are obtained from the FEA simulation.  $P_{load}$  and  $Q_c$  are calculated from the generated voltage, which is also derived from the analytical model and FEA simulation. Fig. 2.11(b) provides the net reactive power supplied to the generator ( i.e.,  $Q_c - Q_l$ ), and the reactive power drawn by the windings of the generator (i.e.,  $Q_\omega$ ) with increasing load current  $i_L$ . For obtaining the plots, it is considered that the generator is rotating at 1500 rpm, connected with an inductive load of  $R_L = 250 \Omega$ ,  $L = 3 \text{ mH}$ . From Fig. 2.11(b), the SRG is

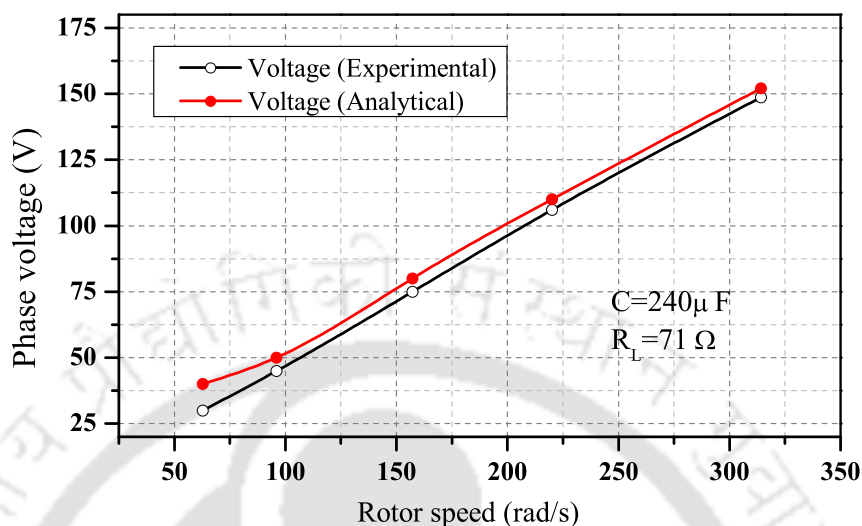


**Figure 2.12:** The generated voltage versus speed for  $C = 240 \mu F$  and  $R_L = 71 \Omega$

able to generate power, provided  $(Q_c - Q_l) \geq Q_\omega$ , thus from the plot it can be observed that for the capacitor with a capacitance of  $64 \mu F$ , the SRG will not be able to produce active power, whereas, with capacitor with capacitance  $335 \mu F$ , it will generate active power till the load current is less than approximately 13.5 A. Similarly, for  $C = 189 \mu F$ , it will generate power until the load current is less than 6 A.

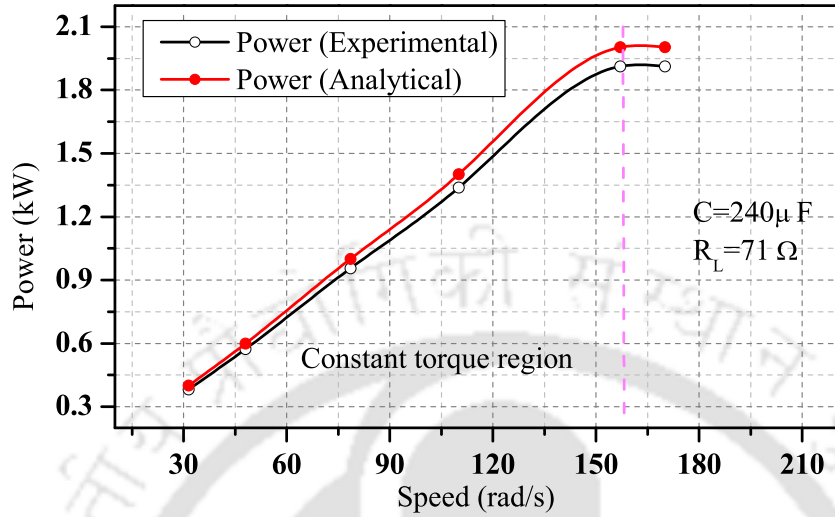
#### 2.4.1 Performance analysis of SRG with resistive load

The present subsection provides the performance analysis of SRG with the presence of constant resistive load ( $R_L$ ). In the present steady state analysis the value of the capacitor connected at the terminal of the generator is kept constant.

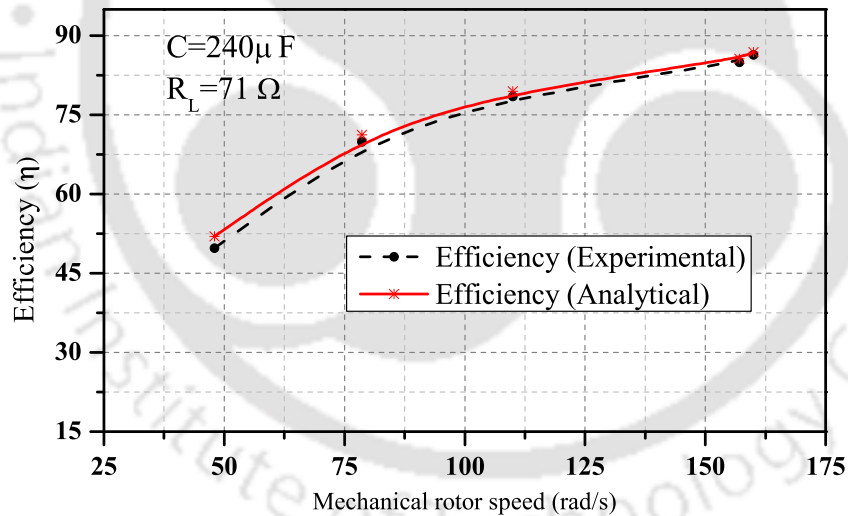
Fig. 2.12 Shows the resistive load generated voltage versus speed for  $C = 240 \mu F$  and  $R_L = 71 \Omega$ . The peak value of phase voltage is increasing with the rotor speed. The solid red line represents the analytical result, while the circles and black lines indicate the experimental result. It is verified that analytical values have a small deviation from the experimental results.

Fig. 2.12 Shows the resistive load generated voltage versus speed for  $C = 240 \mu F$  and  $R_L = 71 \Omega$ . The peak value of phase voltage is increasing with the rotor speed. The solid red line represents the analytical result, while the circles and black lines indicate the experimental result. It is verified that analytical values have a small deviation from the experimental results.

## 2. DESIGN AND MODELING OF SELF EXCITED SRG FOR WIND ENERGY GENERATION



**Figure 2.13:** The out put power verses speed for  $C = 240 \mu F$  and  $R_L = 71 \Omega$



**Figure 2.14:** Efficiency at resistive load and different speed conditions of the 2.1 kW SRG

At the constant resistive load condition ( $R_L = 71 \Omega$ ), the variations of output power with speed for the constant capacitor ( $C = 240 \mu F$ ) are shown in Fig. 2.13. The solid red line represents the analytical result, while the solid black line indicate the experimental result. With the increase of speed, the output power increases. The value of the capacitor helps to increase the generated voltage and power. In case the rotor speed exceeded the rated speed the power becomes constant and the torque will be decrease.

The efficiency of the 2.1 kW SRG for the wind power generation is calculated at different

speed and resistive load condition as shown in Fig. 2.14. The efficiency that is calculated for the generator in the given power range at the rated speed of 157.08 rad/s is above 86.7%. The efficiency is the main feature that makes the SRG generator attractive as it can compute with other types of generators that are used in wind turbines. The solid red line represents the analytical result, while the dotted black line indicate the experimental result.

The similar analysis can be done for ferrite magnet synchronous reluctance generator (FM-SRG), only the voltage equation (2.40) get slightly modified as shown below:

$$\begin{cases} V_d = R_s I_d - X_q I_q + \Lambda_m P \omega = -\Upsilon(R_L X_c I_d + R_L^2 I_q + X_L^2 I_q - X_L X_c I_q) \\ V_q = R_s I_q + X_d I_d = -\Upsilon(-R_L^2 I_d - X_L^2 I_d + X_L X_c I_d + R_L X_c I_q) \end{cases} \quad (2.47)$$

The design and the modeling of FM-SRG have been discussed in Chapter 3.

#### 2.4.2 Residual flux linkage for self-excitation

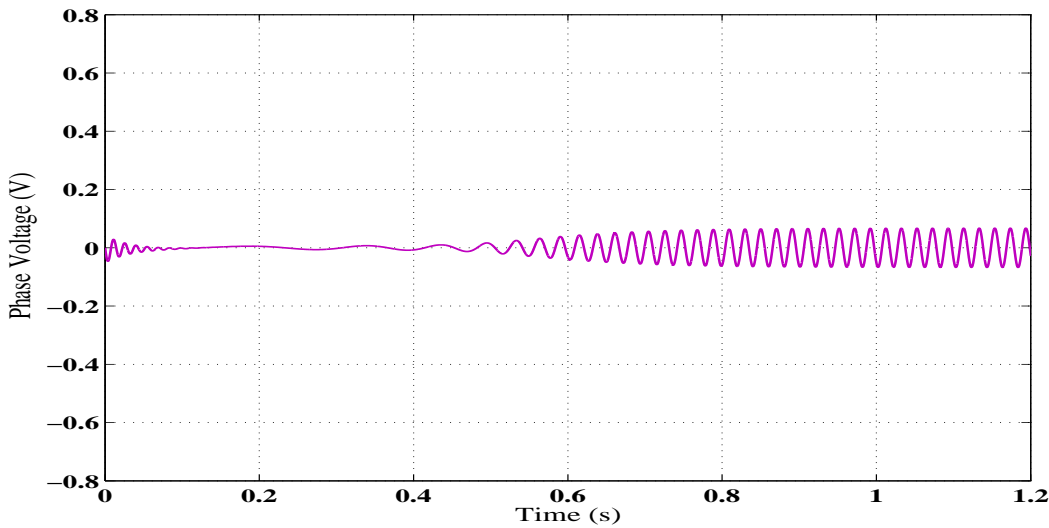
The rating of the excitation capacitor is a function of the operating speed range. It is important to have some residual voltage along with the capacitor to generate voltage to its required value. The developed prototype of SRG, fails to generate a voltage in its first run, due to absence of the residual flux in the rotor core, hence, in case if there is no residual flux, it is important to magnetize the core with the magnetizing circuit. In the experimental setup, the magnetizing circuit consists of a charged capacitor, which is connected temporarily to the terminal of the machine, and immediately disconnected, as shown in Fig.2.4(c). Consequently, the residual flux linkages  $\Lambda_{resi}$  in the rotor core are one of the crucial factors to determine self-excitation in the generators.

To show the excitation voltage build up and collapse for capacitor charged at different voltage levels ( $C = 120 \mu F$  at the speed of 1500 rpm) is given in Table below and in Figs. 2.15(a) and 2.15(b). The experiments were carried out with a voltage charge capacitor (magnetization),  $C = 120 \mu F$ , excitation capacitors,  $C = 240 \mu F$ , resistive load,  $R_L = 71 \Omega$ , and the results are shown in Table 2.10. The generator can be self-excited only if the voltages are high enough. As expected, if the charged voltage of the capacitor is zero, no self-excitation will occur in the

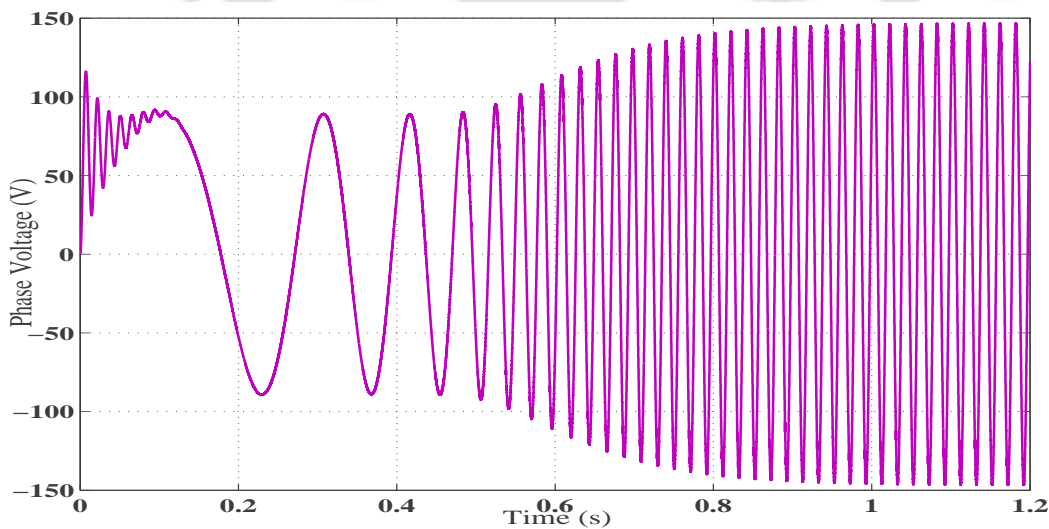
## 2. DESIGN AND MODELING OF SELF EXCITED SRG FOR WIND ENERGY GENERATION

**Table 2.10:** Charged voltage and measured peak phase voltage (at  $C = 240 \mu\text{F}$  and  $R_L = 71 \Omega$ )

Charged Voltage (Auto transformer voltage) in the capacitor ( $C = 120 \mu\text{F}$ ) (Phase, a,b,c)	Measured phase Voltage (V) $C = 240 \mu\text{F}$ and $R_L = 71 \Omega$
+0, 0, 0	0.0
+70, 0, -70	78 to 147.7
+100, 0, -100	90 to 148.2
+110, 0, -110	94 to 148.7
+120, 0, -120	94 to 148.7



(a)



(b)

**Figure 2.15:** (a) Voltage collapse with out magnetizing voltage. (b) Self-excitation/voltage build up after magnetizing with voltage).

generator or it fails to generate voltage.

Figs. 2.15(a) and 2.15(b) shows the two examples representing the same speed value of 1500 rpm, which is machine rated speed, with two different levels of magnetization voltage. In Fig.2.15(a), the SRG is magnetized with zero/lower charge capacitor voltage to starting. When, the rotor is rotated using the prime mover with rated speed. It can be seen that when the generator is magnetized below a certain value of voltage, which is showed in Table 2.10 and Fig.2.15(a), self-excitation does not occur and the terminal voltage collapses (zero experimentally and 0.06 V for simulation at steady state). Fig. 2.15(b), shows a simulation result with the same speed value, but a higher magnetizing charge capacitor voltage. The effect of low magnetizing charge voltage can be clearly seen in these two figures, which shows the effect of the amount of residual flux on the self-excitation condition.

The residual flux linkage in air gap can be expressed as:

$$\Lambda_{resi} = \frac{E_f}{\omega P} \quad (2.48)$$

where  $\omega P$  is electrical speed, and  $E_f$  is an emf required to magnetize the SRG core at electric speed. The residual flux linkage  $\Lambda_{resi}$  can be determined from the emfs at a given speed.

The capacity of the SRG with residual rotor magnetism can be examined. In the analysis, a 190  $\mu F$  capacitors bank, without load, was used at the terminals of the SRG. The voltage/current was used to produce residual magnetism. The rotor speed was slowly changed during the analysis. It is observed that the current has the maximum value at the resonance point (i.e.,  $X_c = X_s$ ), which gives maximum residual flux. The current is increased until the process of self-excitation/resonance point then after it starts decreasing. The equation of the excitation current,  $I_{ex}$  can be expressed as:

$$I_{ex} = \frac{\omega P \Lambda_{resi}}{(R_s + j(X_{ss} - X_c))} \quad (2.49)$$

From equation (2.49) the current at resonance ( $X_c = X_{ss}$ ),  $I_r$  define as:

$$I_r = \frac{\Lambda_{resi}}{R_s \sqrt{L_{ss} C}} \quad (2.50)$$

where,  $X_s$  is generator reactance,  $\omega P = 2\pi f$  and at resonance point  $f = 1/2\pi \sqrt{L_{ss} C}$ , that gives

## 2. DESIGN AND MODELING OF SELF EXCITED SRG FOR WIND ENERGY GENERATION

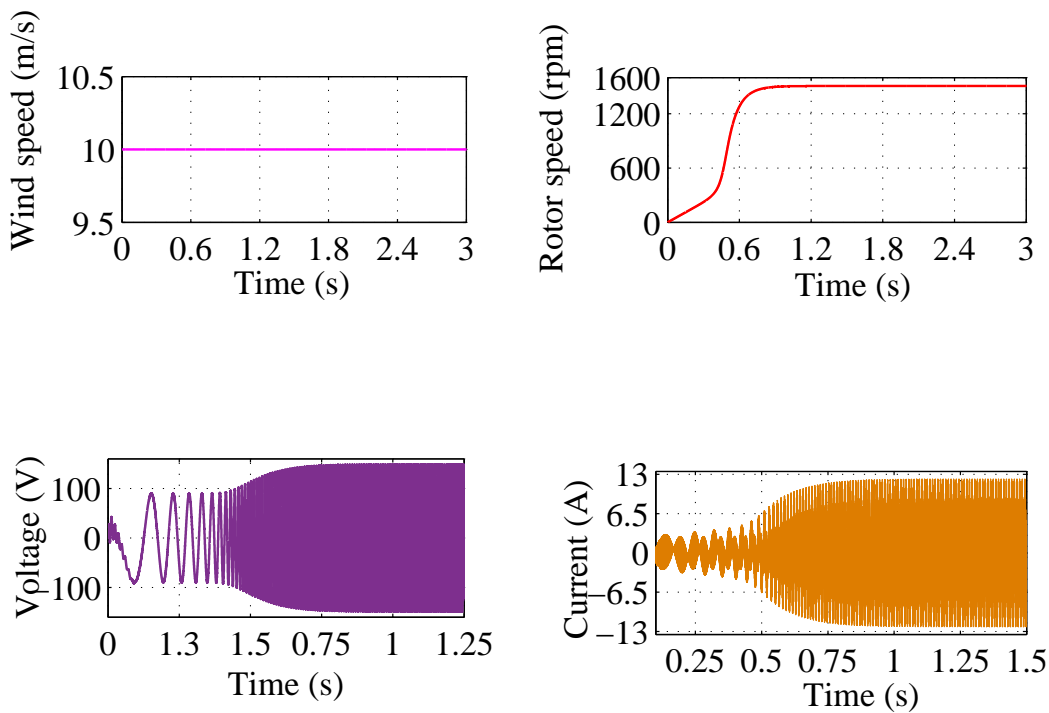


**Figure 2.16:** Wind-driven SRG at constant of  $v_w = 10 \text{ m/s}$  with  $R_L = 250 \Omega$ ,  $L = 30 \text{ mH}$  for  $C = 190 \mu\text{F}$ .

$$\omega P = 1 / \sqrt{L_{ss}C}.$$

The current at resonance value can be used to decide whether the SRG with certain residual flux can be self-excited or not. In fact, the current  $I_r$ , produces the minimum air gap flux linkage required for self-excitation.

### 2.4.3 Effects of wind speed, and load on the system performance

In this section, the simulation has been carried out in Matlab using the design parameters to observe the dynamic behavior of the system under various conditions such as variation of wind speed, constant wind speed, and variation of the load for SRG.

The performance of the SRG under a fixed wind speed of  $10 \text{ m/s}$  and an inductive load ( $R_L = 250 \Omega$ ,  $L = 30 \text{ mH}$  and excitation capacitor of  $190 \mu\text{F}$ ) are shown in Fig. 2.16. As the mechanical torque from wind turbine is applied, the rotor speed of the generator increases to the rated speed of  $1500 \text{ rpm}$ . For constant wind speed, the voltage and current plot of SRG are shown in Fig. 2.16. It is observed that the steady state is reached in about  $1 \text{ s}$  for the machine. To simulate the effect of sudden change in wind speed on the dynamic response of the SRG,

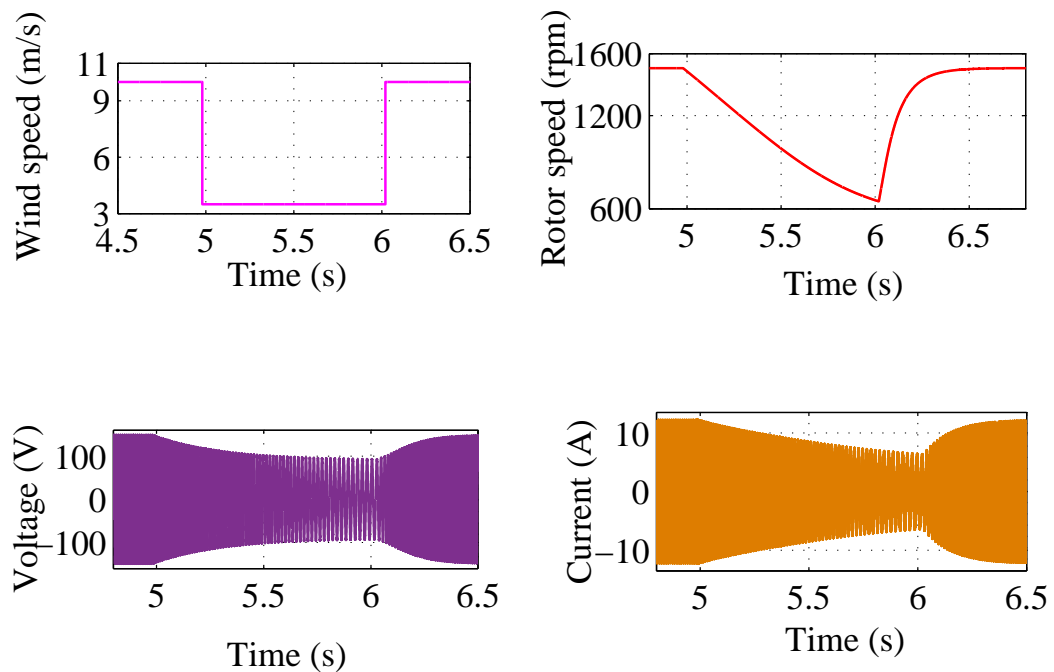


**Figure 2.17:** Wind-driven SRG for falls in speed from  $v_w = 10 \text{ m/s}$  to  $v_w = 4.98 \text{ m/s}$  with  $R_L = 250 \Omega$ ,  $L = 30 \text{ mH}$  for  $C = 190 \mu \text{F}$ .

here, the wind speed is suddenly drop to 4.98 meters per sec. This results into the falls of the generator rotor speed from the rated values of  $157.08 \text{ rad/s}$  (1500 rpm) to  $67.54 \text{ rad/s}$  (645 rpm) as shown in Fig. 2.17. Under this condition, the generated voltage and current decrease from an initial value of  $149.1 \text{ V}$  to a new value of  $92.8 \text{ V}$  for the machine (SRG). The current supplied by the machine also decreases. At  $t=6.5 \text{ s}$ , again the wind speed is increase to its previous value. The performance of the SRG under step change of load are presented in Fig. 2.18. The inductive loads instantly decrease from  $258 \Omega$ ,  $30 \text{ mH}$  to  $150 \Omega$ ,  $10 \text{ mH}$  at  $5 \text{ sec}$ , and then increases back to the initial impedance load values at  $t = 7 \text{ sec}$ . At  $5 \text{ sec}$ , the reduction in both the stator currents and voltages is observed i.e., the voltage slightly change from a steady state value of  $149.1 \text{ V}$ . Similarly, the stator current decreases from  $16.5 \text{ A}$  to  $15.2 \text{ A}$ . When the impedance load value is changed at  $t = 7 \text{ s}$  to its previous value, the current and voltage increase to the initial stable value. As the speed of the SRG kept fixed at  $1500 \text{ rpm}$ , and thus the frequency remains same despite the change in load. This is one of the advantage over self-excited induction generator, whose frequency and voltage are highly influenced by changing load condition. From Fig. 2.18, it is observed that the change in load for SRG, slightly changes

## 2. DESIGN AND MODELING OF SELF EXCITED SRG FOR WIND ENERGY GENERATION

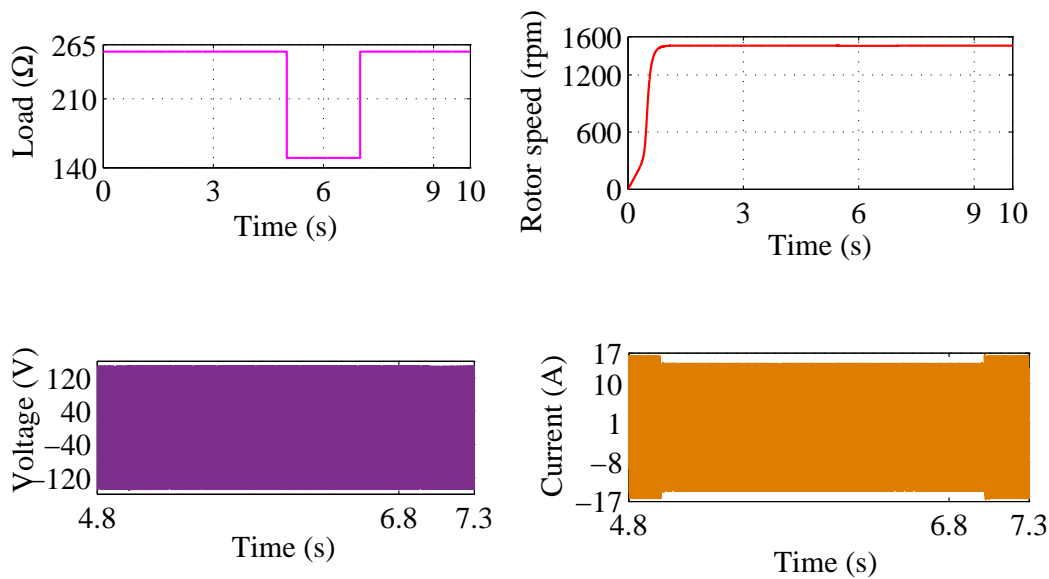


**Figure 2.18:** Wind-driven SRG at constant of  $v_w = 10 \text{ m/s}$  with  $Z_L = 258 \Omega$  to  $150 \Omega$  for  $C = 190 \mu \text{F}$ .

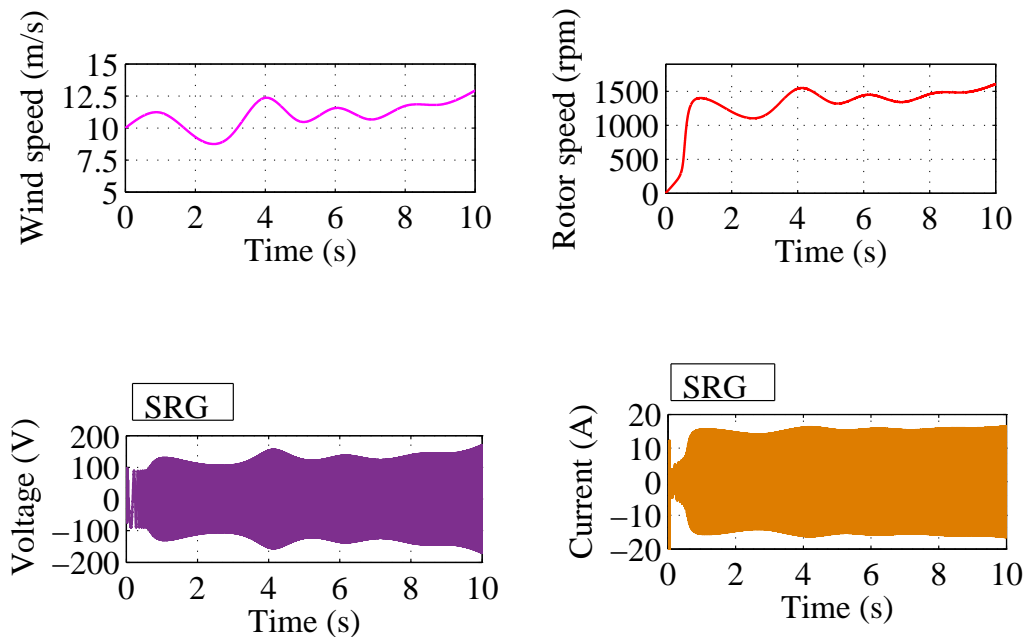


**Figure 2.19:** Wind-driven SRG for variable speed with  $R_L = 250 \Omega$ ,  $L = 30 \text{ mH}$  for  $C = 190 \mu \text{F}$ .

the current and voltage as compared to the self-excited induction generator. The performance of the SRG under the variable wind speed is shown in Fig. 2.19. The inductive load is kept constant at  $250 \Omega$ ,  $30 \text{ mH}$ , and the wind speed is varied, as shown in Fig. 2.19. This variation of wind speed was observed from a location in India over a period of one hour, forty minutes. But to show the effect of wind variation on the machine's performance, the duration of variation

was mapped to a time of 10 *sec* purely for simulation. Fig. 2.19, shows the variation in the stator current, voltage, and rotor speed. However, as the practical generator will have a speed controller, which will regulate the rotor speed, this kind of voltage and current fluctuations will not be observed for a practical SRG.

## **2.5 Summary**

The design and an analytical modeling of synchronous reluctance generator, from wind turbine modeling specifications, are presented. The  $d$  and  $q$ -axes flux and inductance saturation effects has been evaluated. The compactness, reliable and efficiency of this generator have been evaluated. Using inductive load condition, formulae to select the required minimum capacitance are developed. The relationship between generated voltage with the change of capacitor is evaluated. The effects of stator resistance on electromagnetic torque with variation of power angle have been considered. It also verified that if the value of capacitor is less than minimum value of the capacitor, the generator is not able to generate the voltage. The effects of residual flux linkage on the excitation of reluctance generator are analyzed. Using Matlab, the performances of the machine for change of load, and variable wind speed are also determined. With decrease in load impedance the performance of generated current and voltage have been presented. The advantage of continuously varying reactive power to keep the voltage constant, with change of load, has been observed i.e., to dynamically vary the capacitance of the capacitor. It is observed that if the wind-driven SRG operate at constant speed, the frequency remains constant despite the change in load.

## 2. DESIGN AND MODELING OF SELF EXCITED SRG FOR WIND ENERGY GENERATION





## 2. DESIGN AND MODELING OF SELF EXCITED SRG FOR WIND ENERGY GENERATION



# 3

## **ELECTROMAGNETIC TORQUE ANALYSIS OF SRG WITH FERRITE MAGNET FOR WIND ENERGY GENERATION**

### **Contents**

---

<b>3.1</b>	<b>Introduction . . . . .</b>	<b>58</b>
<b>3.2</b>	<b>Impact of placing Ferrite magnet and analytical modeling of FM-SRG . .</b>	<b>59</b>
<b>3.3</b>	<b>Construction troubles of the FM-SRG . . . . .</b>	<b>65</b>
<b>3.4</b>	<b>Structure and performance evaluations . . . . .</b>	<b>67</b>
<b>3.5</b>	<b>Summary . . . . .</b>	<b>92</b>

---

### 3. ELECTROMAGNETIC TORQUE ANALYSIS OF SRG WITH FERRITE MAGNET FOR WIND ENERGY GENERATION

---

#### 3.1 Introduction

Synchronous reluctance generator (SRG) is one of the suitable generator to generate electric power from wind energy conversion systems. It is compact, robust, and it can operate in a self-excited mode using the input mechanical power from the rotating wind turbine. It is reliable, simple in construction, small in weight and size, efficient, and with a reduced cost of maintenance.

To enhance the operating performance of SRG, a small percentage of low-cost ferrite magnets (FMs) are placed into the generator rotor air barrier to form an FM-assisted SRG (FM-SRG) [53–55], [53, 56, 57]. It is observed that by filling the air barrier with a suitable volume of the magnetic material, it is possible to improve the average torque, efficiencies, and power factor of the FM-SRG [55, 58, 59]. The design of the shape of the air barrier has a significant impact on the performance of the SRG. A rectangular shape is preferred while designing the shape of the ferrite magnet, as it reduces the cost and is easy to place them into the air barriers. Hence, significantly reducing the cost of its mass production [59–61]. In some designs, additional ribs are provided between the magnets to increase the mechanical strength of the rotor during its operation [62–65].

Here, for comparison purposes, only the length of the FM-SRG is reduced with an increasing percentage of the volume of ferrite magnet while keeping the rating of the FM-SRG constant i.e., 2.1 kW. The analysis of the performance of the machine is done using the FEA, and the results are also compared with the experimental result obtained by an SRG. The parameters and the rating of the machines i.e., FM-SRG (30% ferrite magnet volume of the total air barrier volume) are similar to the parameters ( $D_{in}$ ,  $D_o$ ,  $D_r$ , rated current and output power, wind turbine modeling) of SRG except for the stack length of 50 mm. In this Chapter, design and an analytical model in the  $dq$  rotor reference frame is developed as shown in Fig.3.1. In addition, the inductive load is considered to estimate the performance of the FM-SRG.

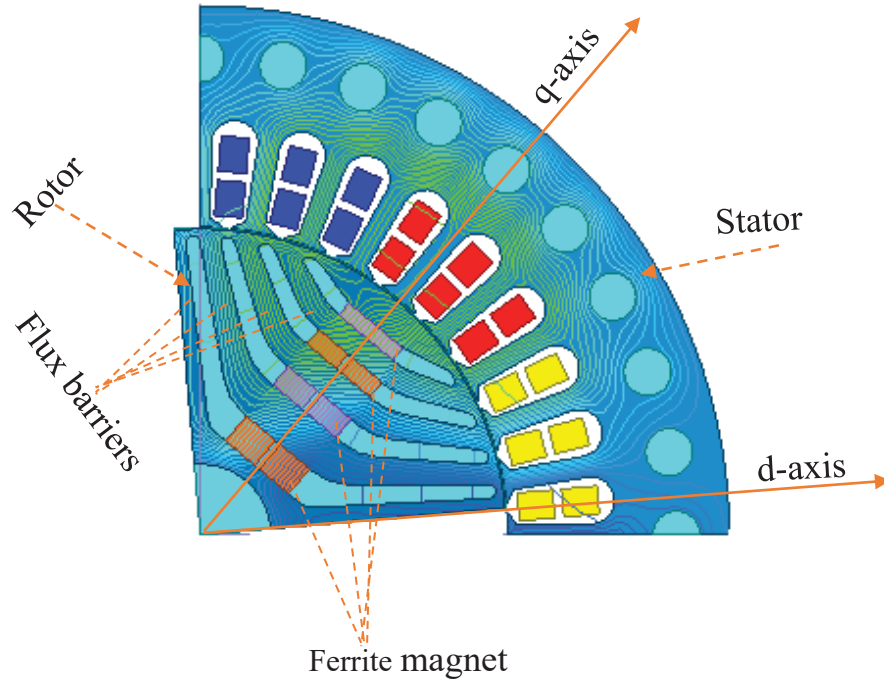


**Figure 3.1:** Cross-section and  $dq$  axes rotor reference frame of the FM-SRG.

### 3.2 Impact of placing Ferrite magnet and analytical modeling of FM-SRG

Using the design procedures as given in Chapter 2, the designed rotor for a 2.1 kW, 4-poles, 1500 rpm SRG is shown in Fig.3.2. Thus, the electromagnetic torque of a FM-SRG without neglecting stator resistance effects, can be expressed as:

$$T_{em} = \frac{3P}{2} \left[ I_d \Lambda_m + \frac{1}{(P\omega)^2 L_d (\varphi + \beta^2)^2} V_{max}^2 (1 - \varphi) \left[ (\varphi - \beta^2) \sin(2\gamma) - 2\beta(1 + \varphi) \sin^2(\gamma) + 2\varphi\beta \right] \right] \quad (3.1)$$

If,  $R_s = 0$ , equation 3.1, yields

$$T_{em} = \frac{3P}{2} \left[ I_d \Lambda_m + \frac{1}{((P\omega)^2 L_d L_q)} V_{max}^2 (L_d - L_q) \sin(2\gamma) \right] \quad (3.2)$$

Since,  $V_{max}/(P\omega L_d) = I_d$ , and  $V_{max}/(P\omega L_q) = I_q$ , the torque equation is rewritten as:

$$T_{em} = \frac{3P}{2} \left[ I_d \Lambda_m + (L_d - L_q) I_d I_q \sin(2\gamma) \right] \quad (3.3)$$

where,  $\beta = R_s/\omega L_d$ ,  $\varphi = L_q/L_d$ ,  $P$  is the number of poles pairs,  $\lambda_q$ ,  $\lambda_d$ ,  $L_q$ ,  $L_d$ ,  $I_q$  and  $I_d$  are stators flux linkages, inductances, and currents referred to the rotor reference frame in  $q$ - and

### 3. ELECTROMAGNETIC TORQUE ANALYSIS OF SRG WITH FERRITE MAGNET FOR WIND ENERGY GENERATION

**Table 3.1:** Parameters expression

Parameters	FM-SRG	Units
$R_s$	$1.362 \times 10^{-3} \left(m\right)^2$	$\Omega$
$L_{ls}$	$1.514 \times 10^{-6} \left(m\right)^2$	$H$
$L_m$	$1.006 \times 10^{-4} \left(m\right)^2$	$H$
$L_d$	$1.205 \times 10^{-4} \left(m\right)^2$	$H$
$L_q$	$0.2006 \times 10^{-4} \left(m\right)^2$	$H$

$d$  – axis, respectively. The conductor per slot turns  $m$ , is one of the key parameter in the design of stator resistance, leakage inductance, and magnetizing inductance. The resistance per phase  $R_s$ , is:

$$R_s = \frac{2(L_s + L_e)PqJm\rho_r}{I_m} \quad (3.4)$$

where,  $L_e$  is end winding length,  $L_e = \pi\tau/2$ ,  $J$  is current density, and  $\rho_r$  is copper resistivity at temperature of 120°C. The leakage inductance  $L_{ls}$  is expressed as;

$$L_{ls} = (e_s + e_a + e_e)2L_sPqm^2\mu_o \quad (3.5)$$

Here, calculated slot permeance,  $e_s = 1.7564$ , air gap coefficient,  $e_a = 0.25$  and the end winding length coefficient,  $e_e = 0.001519$ . The magnetizing inductance  $L_m$ , for uniform air gap is given as:

$$L_m = \frac{6\mu_o\tau L_s P \left(qk_w m\right)^2}{\pi^2 l_g k_c (1 + k_s)} \quad (3.6)$$

Therefore, for double layer windings, the stator resistance, leakage inductance, magnetizing inductance,  $d$ –, and  $q$  – axes inductances are the function of  $m$ . By simplifying the calculation, they are expressed as in Table 3.1:

### 3.2 Impact of placing Ferrite magnet and analytical modeling of FM-SRG

Using the  $d$ - $q$ -axes rotor reference frame as shown in Fig. 3.1, the voltage equations of the FM-SRG in the transient state is written as below.

$$\begin{cases} V_d = R_s I_d + \rho \lambda_d - \omega P \lambda_q + \omega P \Lambda_m \\ V_q = R_s I_q + \rho \lambda_q + \omega P \lambda_d \end{cases} \quad (3.7)$$

whereas, the steady state voltage equation is given as,

$$V_{ph} = \sqrt{\left(-1.73 \times m + 31.416\right)^2 + \left(5.20 \times m\right)^2} \quad (3.8)$$

The above equations (3.7) are written utilizing the motor convention of the reluctance machine. When the machine work in generator mode, they convert mechanical power into active power, but requires reactive power to magnetize their magnetic field paths for self-excitation. Motoring operations are carried out when  $I_d$  and  $I_q$  exhibit the same sign, while generating operations when they exhibit opposite sign. Referring to the current  $q$  and  $d$ -axes frame, motoring operations are in the first and third quadrants. In other words the motoring mode is when  $I_d, I_q < 0$  or  $I_d, I_q > 0$ , which implies  $T_e > 0$ . Similarly, the generating mode are in the second and fourth quadrants, which means  $I_d > 0, I_q < 0$  or  $I_d < 0, I_q > 0$ ,  $\implies T_e < 0$ . The same is shown in Figs. 3.14(a), and 3.15(b). The equation for FM-SRG may be determined from those of the synchronous reluctance machine with the magnetic flux terms included in the equation according to the arrangements of ferrite material.

The electromagnetic torque for SRG depends on location (i.e., along  $q$ - axis or  $d$ -axis) and flux direction (i.e., in the direction of stator flux or opposite to stator flux ) of the magnets. It also depends on the type of magnet, i.e., permanent magnet or ferrites magnetic . In this design, the ferrites magnet are placed to decrease the  $q$ -axis flux from stator as shown in Fig. 3.1. Therefore, the voltage increase by  $\omega P \Lambda_m$ , whereas the produced torque increase by  $\frac{3}{2} P I_d \lambda_m$ . Since, the objective of placing the ferrite magnets into the air barriers is to increase the torque, it is important to place them in an air barrier in such an orientation, which reduces the flux linkage along the  $q$  - axis, i.e.,  $\Lambda'_m$  with FMs is expressed as:

### 3. ELECTROMAGNETIC TORQUE ANALYSIS OF SRG WITH FERRITE MAGNET FOR WIND ENERGY GENERATION

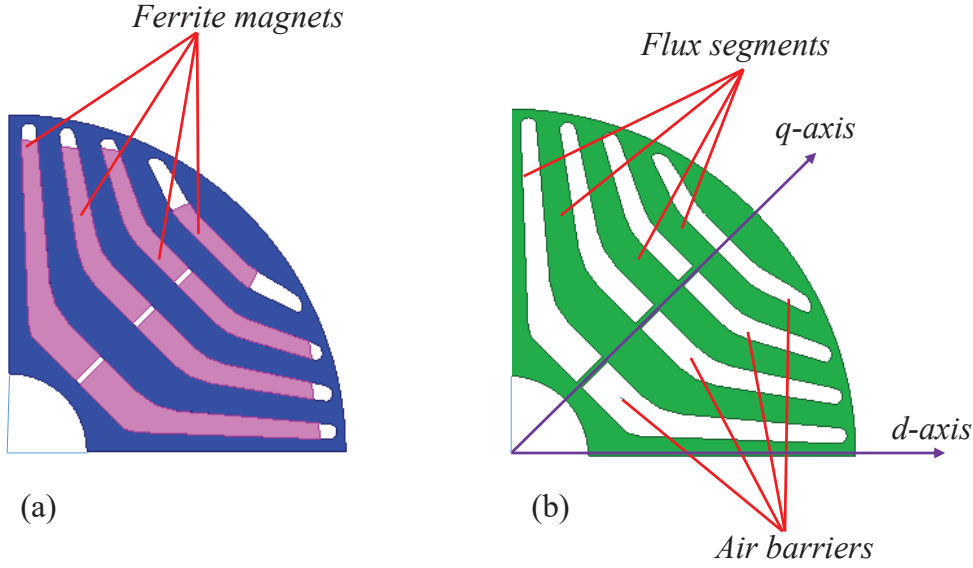


**Figure 3.2:** (a) Maximum permissible ferrite compositions FM-SRG. (b) Rotor of the reference SRG.

$$\Lambda'_m = \lambda_q - \Lambda_m = L_q I_q - \Lambda_m \quad (3.9)$$

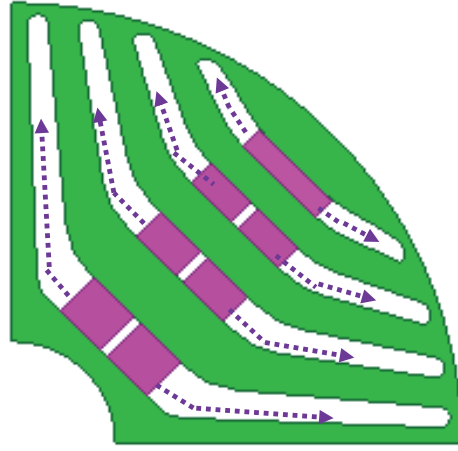
Here,  $\Lambda_m$  is the flux linkage of ferrite magnet oriented along the negative  $q$  – axis.

The electromagnetic torque  $T_{em}$ , that can be produced from such FM-SRG, neglecting stator resistance effects is expressed as

$$T_{em} = \frac{3P}{2} [\Lambda_m I_d + (L_d - L_q) I_d I_q] = T_e + \frac{3P}{2} (\Lambda_m I_d) \quad (3.10)$$

From (3.9), and (3.10), it could be inferred that by placing the ferrite magnet with the correct orientation, the electromagnetic torque of the FM-SRG gets increased, but at the cost of increased torque ripples. This leads to the development of a performance index that uses the combination of average electromagnetic torque, and the ripple torque. Moreover, the increase in the volume of the ferrite magnet in the air barrier also has an effect on the reduction of the  $d$  – axis flux linkage, thus reducing the average torque [51, 64, 66]. If the ferrite magnet of an FM-SRG loses its magnetic strength, still the machine continues to operate as an SRG. This is one of its important advantages. Fig. 3.2(a), and Fig. 3.2(b) shows rotor air barriers of FM-SRG with ferrite magnet, and FM-SRG without ferrite magnet (i.e., SRG), respectively.

Fig. 3.2(a) shows the placement of a ferrite magnet in four air barriers. For increasing the



-----> Direction of ferrite magnet increments

**Figure 3.3:** Illustration schematic for the ferrite magnet-increment arrangements of a 2.1 kW, 4 poles FM-SRG.

percentage volume of the ferrite magnet, the size of the magnet is increased in the direction as given by the arrow in Fig. 3.3. The percentage volume is calculated as the ratio of ferrite volume to that of the total volume of the air barrier, i.e.,  $V_{fm} = 0\%$  FM-SRG without magnet and  $V_{fm} = 100\%$  when the whole air barrier is filled with the ferrite magnet. To quantify the performance, a performance indexes,  $\hbar$ , which represent the difference between torque ripple performance ratio  $R$  and the produced electromagnetic torque performance ratio  $T$  at corresponding  $V_{fm}$  is defined as:

$$T = \frac{\Psi T_{em}}{\left( V_{fm}(T_{fm} - T_e) + T_e \right)} \quad (3.11)$$

$$R = \frac{\Psi_p T_{emrp}}{\left( V_{fm}(T_{fmp} - T_{ep}) + T_{ep} \right)} \quad (3.12)$$

Hence, based on the equations (3.11), and (3.12) the performance index  $\hbar$  can be expressed as:

$$\hbar = T - R \quad (3.13)$$

Here,  $T_{emrp}$  is peak-peak torque ripple of FM-SRG, and  $\Psi$  and  $\Psi_p$  are weight factors of torque and peak to peak torque ripple, respectively. Here,  $T_{em}$  and  $T_{emrp}$  are the average electromagnetic torque, and the ripple torque, which obtained  $T_{em} \simeq T_e$  and  $T_{emrp} \simeq T_{ep}$  when  $V_{fm} = 30\%$ . The

### 3. ELECTROMAGNETIC TORQUE ANALYSIS OF SRG WITH FERRITE MAGNET FOR WIND ENERGY GENERATION

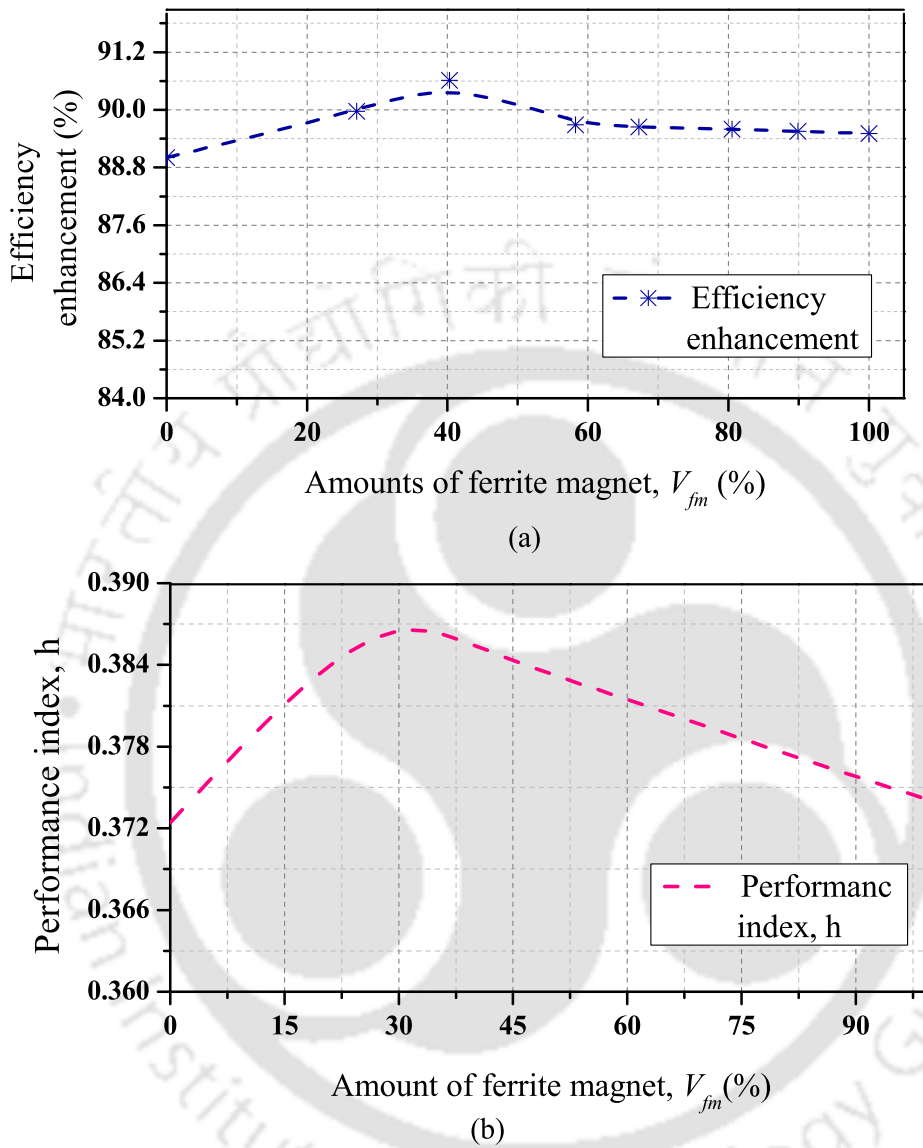


**Figure 3.4:** (a) Efficiency enhancement as amount of ferrite magnet increments.(b) Performance index as the amounts of ferrite magnet increments.

factor  $\Psi$  and  $\Psi_p$  are adjusted to get the actual average and ripple torque for a different volume of ferrite magnet.

The plot of the variation of the operational efficiency is shown in Fig. 3.4(a). However, the efficiency seems high at the ferrite volume of  $V_{fm} = 40\%$ , the performance index start decreasing after this point. It is observed from Fig. 3.4(b) that initially, with the increase in the volume of the ferrite magnet  $V_{fm}$ , the performance index increase, but for  $V_{fm} > 30\%$ , a decreasing in the performance index is observed. This is mainly due to the demagnetization

along the  $d$  – axis and increase in the ripple torque.

### 3.3 Construction troubles of the FM-SRG

The main advantage of FM-SRG as compared with the SRG is in terms of increased power factor and efficiency [58,67]. The design of FM-SRG is similar to that of SRG, except for a few minor changes. The changes are mainly in the shape of the air barriers; typically, the trapezoid shape rotor air barrier is preferred to host low-cost rectangular ferrite magnet, as shown in Fig. 3.3. Moreover, here some additional ribs may also be provided to fit the magnet in the air barrier securely. While designing the tangential and bridge ribs, the additional safety margin is provided to withstand the mechanical stress induced with the rotation of the FM-SRG machine. The sequence/step of how the algorithm is executed for the design of the FM-SRG is similar to that of SRG as summarized in Chapter 2 section 2.3. The design objectives for FM-SRG which need to be satisfied are given as:

- The rating of the machine should be 2.1 kW, with electromagnetic torque  $\geq 12.75 Nm$ , maximum torque ripple  $\leq 12\%$ .
- Ferrite magnet volume is  $\leq 30\%$  of total of air barriers, maximum back-emf  $\geq 120 V$  for FM-SRG .

The results of design parameter/variables for ferrite magnets of rectangular shape as shown in Fig.3.5 are given in Table 3.2 . To reduce the ripple and achieve the objectives the design variables can be adjusted by using the following parameters.

- The adjacent distance between the ferrite magnet  $X$ , length of the ferrite  $X'$ , and  $X_4$ .
- Vertical distance of the ferrite and height of the ferrite,  $X_1 \sim X_3$  and  $Y_1 \sim Y_4$ , respectively.

From Fig. 3.4(b), it could be observed that the maximum performance index is obtained at  $V_{fm} = 30\%$ , i.e., the percentage ratio of the volume of ferrite magnet to that of the total air barrier volume is 30%. The rotor structure and the diameter of the stator of the two machines are the same, only the volume of the FM-SRG is decreased so that the ratings of the two machine

### 3. ELECTROMAGNETIC TORQUE ANALYSIS OF SRG WITH FERRITE MAGNET FOR WIND ENERGY GENERATION

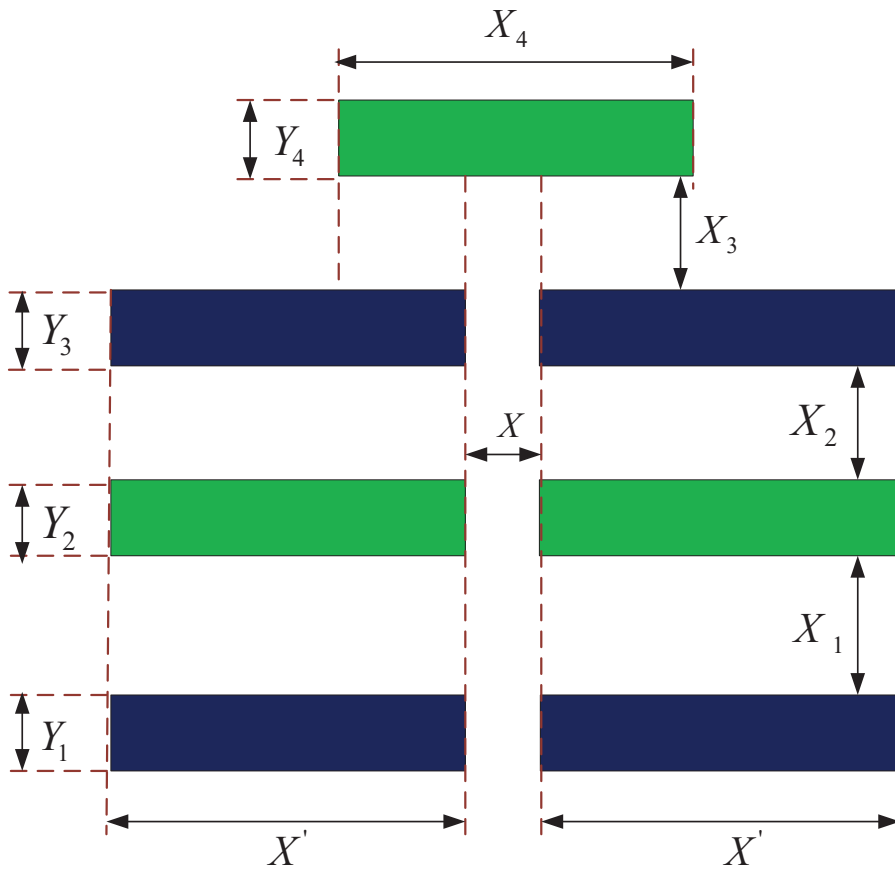


**Figure 3.5:** Design parameters/variables for rectangular ferrite magnet shape

**Table 3.2:** Optimal design variables of FM-SRG

Intervals (mm)	Optimal values (mm)
$5 \leq X_1 \leq 8$	7
$3 \leq X_2 \leq 5$	4.98
$3 \leq X_3 \leq 6.8$	4.74
$10 \leq X_4 \leq 13$	12.7
$1 \leq X_2 \leq 1.3$	1.2
$6 \leq X' \leq 7$	6.5
$4 \leq Y_1 \leq 6$	5.5
$4 \leq Y_2 \leq 4.5$	4.05
$4 \leq Y_3 \leq 4.5$	4
$4.5 \leq Y_4 \leq 5$	4.5

could be kept at a constant value of 2.1 kW (3.14). Due to the presence of flux barriers, the direct axis inductance is higher than the quadrature axis inductance in SRG.

The mathematical expression which relates  $d$  – axis inductance,  $L_d$  or magnetizing inductance  $L_m$  to that of the volume of the SRG is given below:

$$L_m \simeq L_d = \frac{12\mu_o}{\pi^2} \left( \frac{k_w m}{2P} \right)^2 \left( \frac{V_{ml}}{k_c k_s l_g} \right) \left( \frac{D_{in}}{D_o^2} \right) \quad (3.14)$$

where,  $k_w$  is the winding factor, and  $k_c$  and  $k_s$  are Carter factor and saturation factor, respectively. Here, the selected factors are  $k_c = 1.03$ ,  $k_s = 1.2$ . Based on the finite element analysis, the desired electromagnetic-torque and torque-ripple of FM-SRG structures for different volumetric amounts are summarized in Table 3.3.

**Table 3.3:** Torque ripples and electromagnetic torque of the FM-SRG structures

Performance	SRG ( $V_{fm} = 0\%$ )	( $V_{fm} = 30\%$ )	( $V_{fm} = 40\%$ )	( $V_{fm} = 58\%$ )
Average torque (Nm)	12.23	12.28	13.70	13.16
Experimental (Nm)	12.17	-	-	-
Torque ripples (%)	9.7	11	17	17.9

### 3.4 Structure and performance evaluations

The arrangement of the ferrite magnets and the design of rotor flux segments/barriers of an FM-SRG is explained in the previous sections. Figure 3.6 shows the distribution of the magnetic field ( $B$ ) with the change in volume of ferrite magnets using the FEA simulation. Figure 3.6(a) show the magnetic flux distribution without magnet i.e., the initial reference SRG ( $V_{fm} = 0\%$ ). Similarly, Fig. 3.6(b, c, d), shows the distribution of magnetic flux in the presence of ferrite magnet with  $V_{fm} = 30\%$ ,  $40\%$ , and  $58\%$ , respectively. Since with the increase in the volume of the magnet, the core length is also reduced to maintain the same rating of the machine as that of reference SRG, it is observed from Figs. 3.6(a, b, c, d) that the magnitude of flux density distributions is nearly constant. The performance index of the two machines i.e., FM-SRG and SRG of the same ratings, are mainly compared using the data obtained through FEA simulations. Both the machines are of  $2.1 \text{ kW}$ , and has identical stator.

From Table 3.3, it can be observed that the average torque as estimated by FEA is  $12.23 \text{ Nm}$ , and average torque as obtained from the designed prototype of initial reference SRG is  $12.17 \text{ Nm}$ .

### 3. ELECTROMAGNETIC TORQUE ANALYSIS OF SRG WITH FERRITE MAGNET FOR WIND ENERGY GENERATION

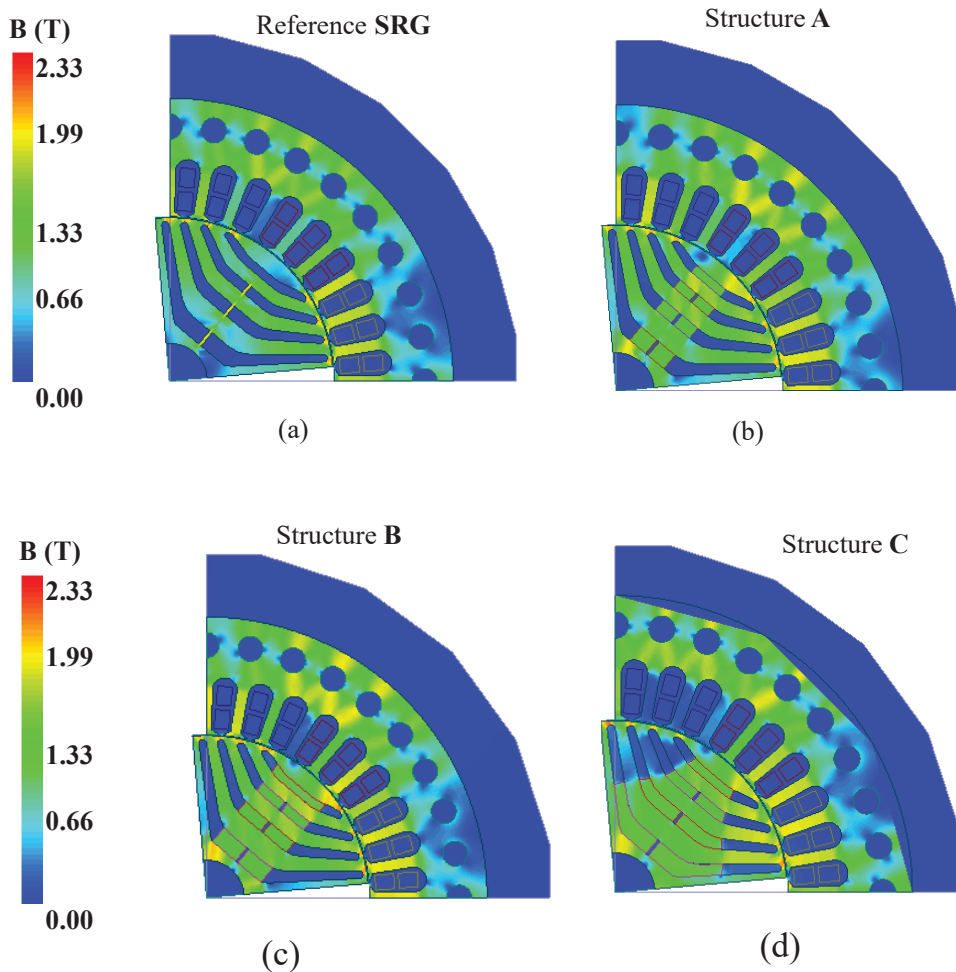
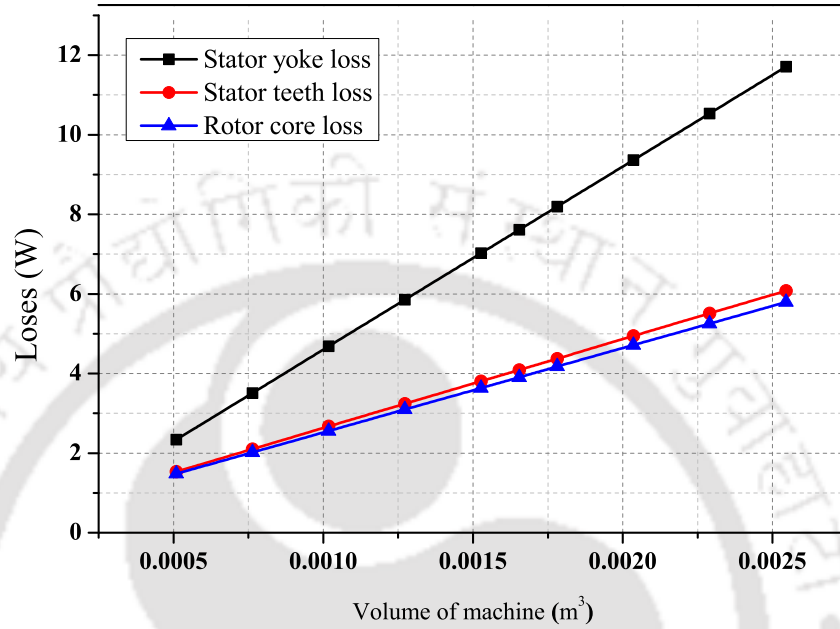


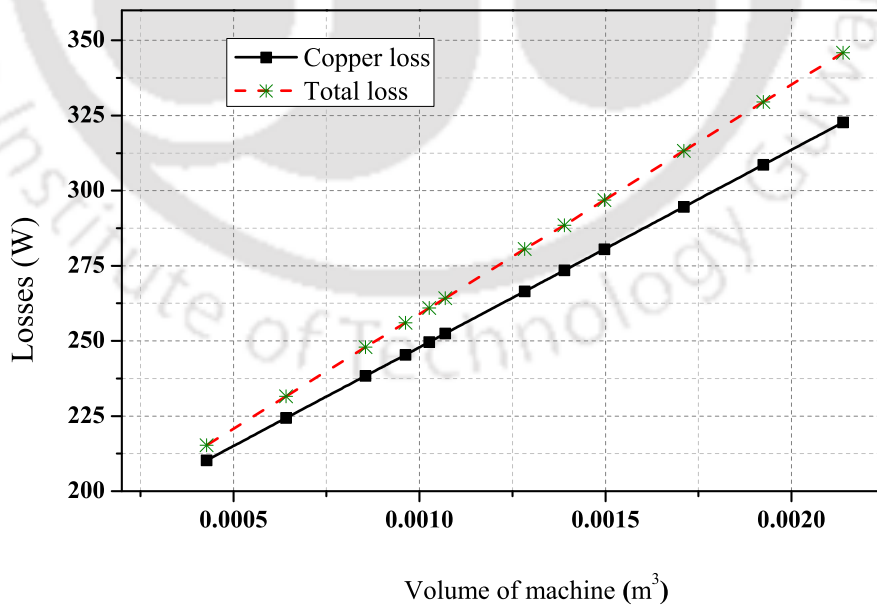
**Figure 3.6:** Stator and rotor structure and field density distribution of 2.1 kW generators. (a) Stator and rotor of reference SRG (for  $V_{fm} = 0\%$ ). (b) Stator and rotor of FM-SRG (for  $V_{fm} = 30\%$ ). (c) Stator and rotor of FM-SRG ( $V_{fm} = 40\%$ ). (d) Stator and rotor of FM-SRG (for  $V_{fm} = 58\%$ ).

Hence, it can be concluded that experimental, and FEA results are very close to each other. This also validates results as obtained from FEA. Fig. 3.7, shows the estimated losses of the stator yoke, rotor core, stator teeth, and copper with the increasing volume of the machine. It is required to get the operational efficiency of the generator with different volumes. Fig. 3.7(a) shows the plot corresponding to the stator yoke, rotor core, and stator teeth losses. It is observed that these losses increase linearly with an increase in the volume of the machine. Similarly, copper loss, and the total losses of the machine is shown in Fig. 3.7(b). It is observed that for the designed SRG core, the total losses and the copper losses are increasing as the volume of the machine increases (i.e., for the machine with  $V_{fm} = 0\%$ ).

The electromagnetic performance of initial reference SRG improves with minimizing the  
[TH-2546\\_156102022](#)



(a)



(b)

**Figure 3.7:** (a) Summarized stator yoke, rotor and teeth losses. (b) Entire core and resistive losses.

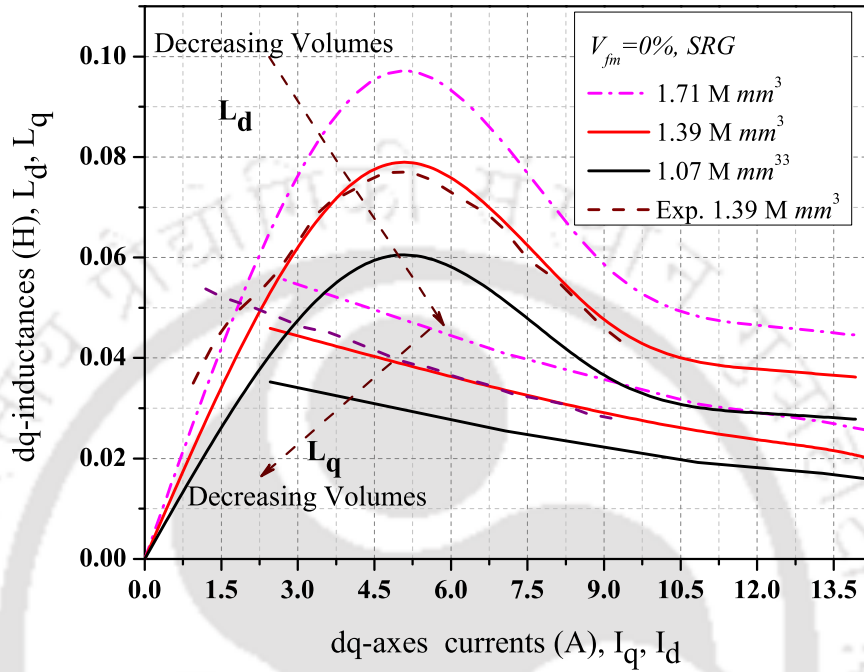
### 3. ELECTROMAGNETIC TORQUE ANALYSIS OF SRG WITH FERRITE MAGNET FOR WIND ENERGY GENERATION

---

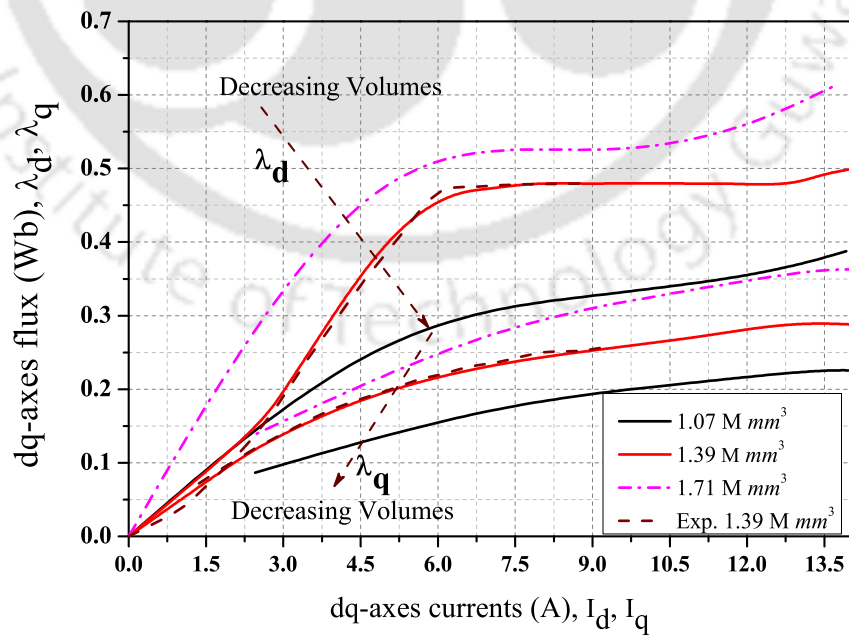
inductance of the  $q$ -axis,  $L_q$ , and maximizing the inductance of  $d$ -axis,  $L_d$ . This also increases the power factor of the machine, which is defined as the ratio of  $(L_d/L_q - 1)$  to the  $(L_d/L_q + 1)$ . It is seen that by increasing the volume of the generator axially, as indicated in Fig. 3.8(a), the inductances  $L_d$  and  $L_q$  is increased, but the increase of  $L_d$  is comparative more as compared to  $L_q$  i.e., the ratio of  $(L_d/L_q - 1)$  to  $(L_d/L_q + 1)$  tends to increase, but torque ripple also tends to increase. Thus, the design selects a suitable axially volume, which gives better performance between these two contradictory objectives. Hence, the design choice made for reference SRG is with a volume of  $1.39M (mm)^3$ , as shown in Fig. 3.8(a). In this Figure, the red-colored curve represents the  $d$ - and  $q$ -axes inductances as estimated using FEA at the axial designed volume, and the dashed line is the one obtained experimentally from the fabricated reference SRG.

Similarly, the variation of the flux along the  $d$ - and  $q$  axes with the change of axial volume is shown in Fig. 3.8(b). It is observed that as the volume of the generator is reduced, the values of  $\lambda_d$  and  $\lambda_q$  reduces (see Fig. 3.8(b)). In Fig. 3.8(b), the red-colored curve represents the  $d$ - and  $q$ -axes as obtained using FEA, and the dashed line curve is experimentally obtained flux values. It can be observed that the result obtained through the experiment are very close to the one obtained through FEA. It is observed that by increasing the volume of the FM-SRG axially, as indicated in Fig. 3.9(a), for  $V_{fm} = 30\%$ , the inductances  $L_d$  and  $L_q$  is increased, but the increase of  $L_d$  is significantly more as compared to  $L_q$  i.e., the ratio of  $(L_d/L_q - 1)$  to  $(L_d/L_q + 1)$  tends to increase significantly, but at the same time torque ripple also tends to increase. Therefore, the design selects a suitable axially volume, which gives better performance between these two conflicting objectives. Hence, the design choice made for FM-SRG is with a volume of  $1.07M (mm)^3$ , as shown in Fig. 3.9(a). In this Figure, the red-colored curve represents the selected  $d$ - and  $q$  - axes inductances as estimated using FEA.

In the same way, the variation of the flux along the  $d$ - and  $q$  axes with the change of axial volume is shown in Fig. 3.9(b), for  $V_{fm} = 30\%$ . It is seen that as the volume of the FM-SRG is reduced, the values of  $\lambda_d$  and  $\lambda_q$  reduces (see Fig. 3.9(b)). In Fig. 3.9(b), the red-colored curve represents the selected  $d$ - and  $q$  - axes flux as obtained using FEA. From Fig. 3.9(b), it is clear that  $\lambda_d$  and  $\lambda_q$  increase, for low values of  $I_d$  and  $I_q$  (i.e., less than 6A). After this,  $\lambda_d$



(a)



(b)

**Figure 3.8:** (a)  $d$ - and  $q$ - axes inductance with generator volumes at  $V_{fm} = 0\%$ . (b)  $d$ - and  $q$ - axes flux with generator volumes at  $V_{fm} = 0\%$ .

### 3. ELECTROMAGNETIC TORQUE ANALYSIS OF SRG WITH FERRITE MAGNET FOR WIND ENERGY GENERATION

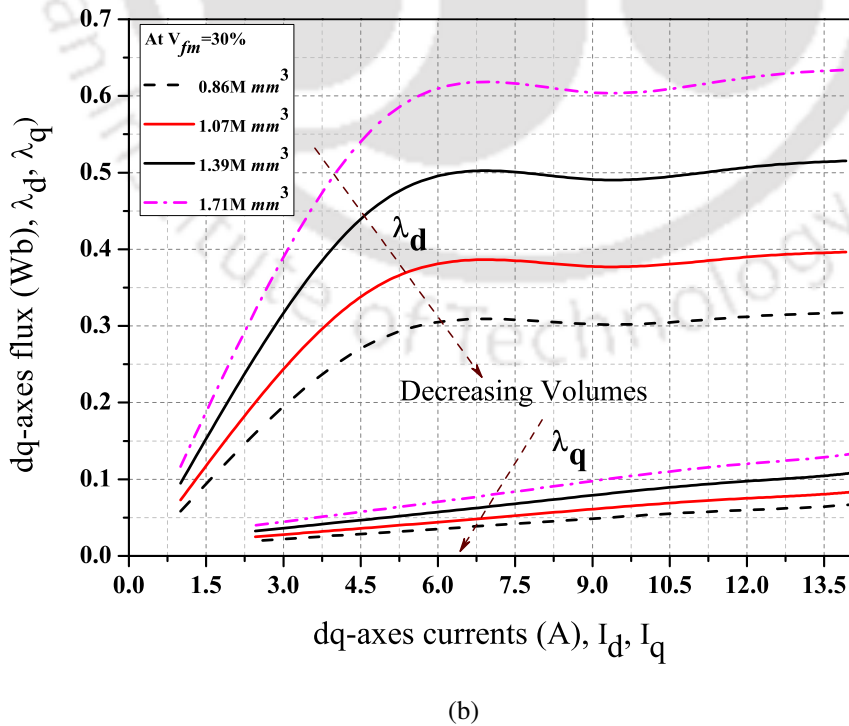
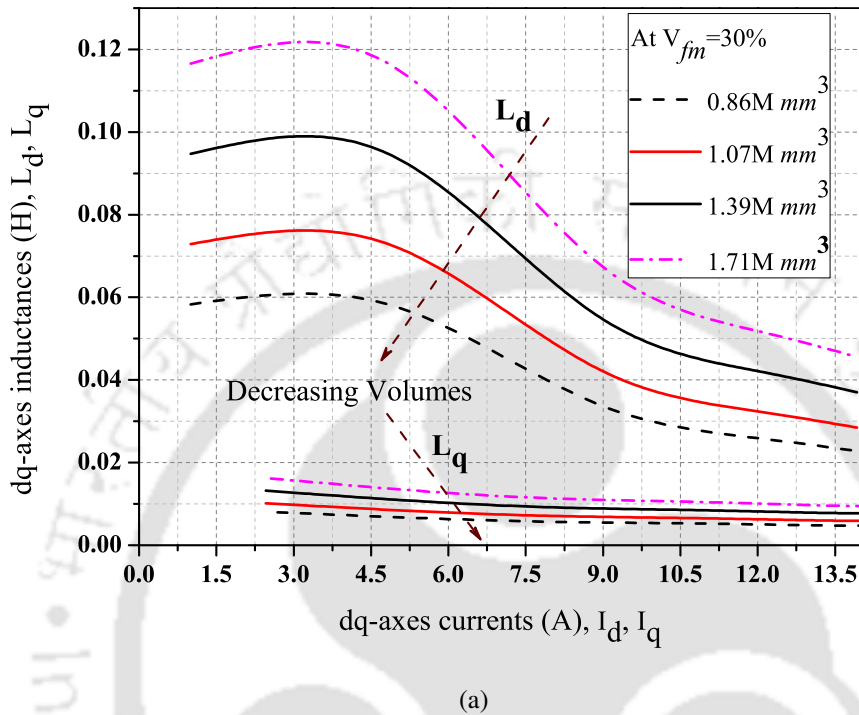


**Figure 3.9:** (a)  $d$ - and  $q$ -axes inductance with generator volumes and at  $V_{fm} = 30\%$ . (b)  $d$ - and  $q$ -axes flux with generator volumes and at  $V_{fm} = 30\%$ .

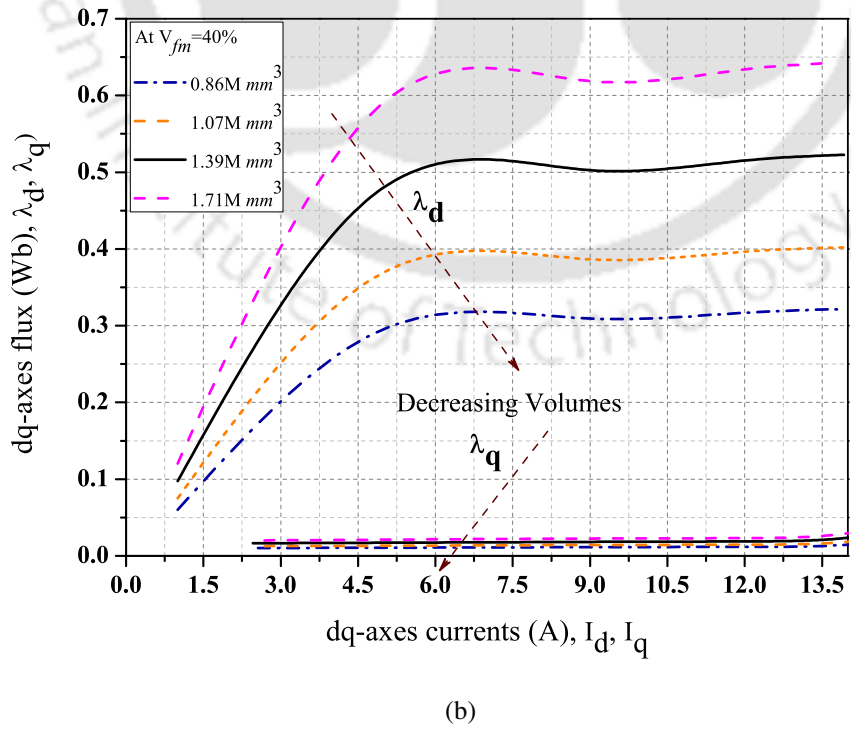
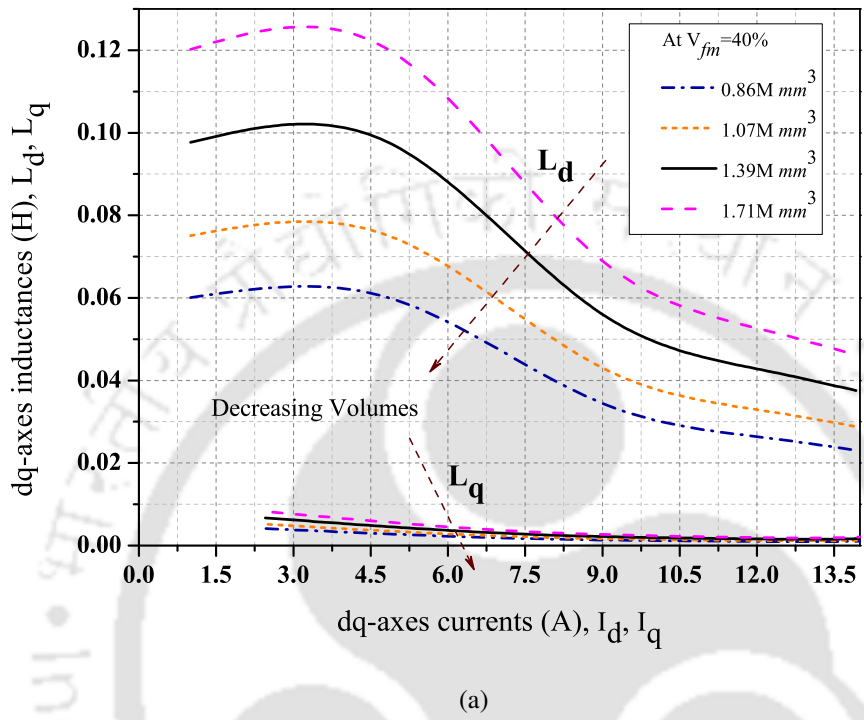
and  $\lambda_q$  become almost constant due to saturation. It is observed that for FM-SRG, the  $q$ -axis flux gradually increases as the current increase. In Fig. 3.10(a), it is seen that by increasing the volume of the FM-SRG axially, at  $V_{fm} = 40\%$ , the inductances  $L_d$  and  $L_q$  is increased, but the increase of  $L_d$  is far more as compared to  $L_q$  i.e., the ratio of  $(L_d/L_q - 1)$  to  $(L_d/L_q + 1)$  is significantly large, but at the same time torque ripple also tends to increase. Hence, the design choice is made for FM-SRG with a volume of nearly  $1.07M (mm)^3$ , as shown in Fig. 3.10(a). Similarly, the variation of the flux along the  $d$ - and  $q$  axes with the change of axial volume is shown in Fig. 3.10(b), for  $V_{fm} = 40\%$ . It is observed that as the volume of the FM-SRG is reduced, the values of  $\lambda_d$  and  $\lambda_q$  reduces (see Fig. 3.10(b)). In Fig. 3.10(b), the  $d$ - and  $q$  - axes group of flux curves are obtained using FEA. Similar observation about the variation of  $d$ - and  $q$  - axes inductances and flux linkage for the FM-SRG with  $V_{fm} = 58\%$  are shown in Figs. 3.11(a) and 3.11(b), respectively. These curves are obtained for different volume i.e.,  $0.86M mm^3$ ,  $1.07M mm^3$ ,  $1.39M mm^3$ , and  $1.71M mm^3$ . In Fig. 3.11(a), it is seen that by increasing the volume of the FM-SRG axially, at  $V_{fm} = 58\%$ , the inductances  $L_d$  and  $L_q$  is increased, but the increase of  $L_d$  is slightly more as compared to  $L_q$  i.e., the ratio of  $(L_d/L_q - 1)$  to  $(L_d/L_q + 1)$  is slightly more, but at the same time torque ripple also tends to increase significantly. Hence, the overall performance of the machine reduces. Similarly, the corresponding variation of the flux is shown in Fig. 3.11(b). Fig. 3.12 represents the decrease in machine volume versus the increase of percentage volume of ferrite magnet while keeping the rating of the machine as  $2.1 kW$ . It is observed that as the volume of ferrite magnet increases, the volume of the machine decrease.

Table 3.4 summarizes the evaluated performance and design parameters for  $V_{fm} = 30\%$  of  $2.1 kW$  of FM-SRG using analytical design.

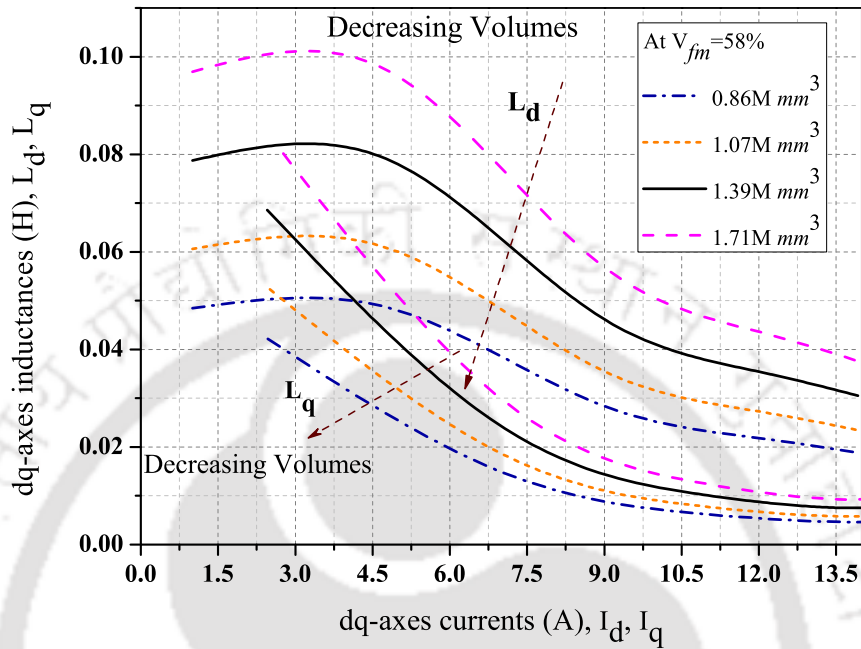
#### 3.4.1 Finite element analysis of FM-SRG for $V_{fm} = 30\%$

Using FEA the performances of the designed FM-SRG have been evaluated. The maximum induced electromotive forces (emfs) in the stator winding of the  $2.1 kW$  FM-SRG with symmetric design are shown in Fig. 3.13(a). The induced voltage in the machine is given by equation (3.7), which clearly shows that if the effective  $q$  - axis flux is reduced, it leads to a decrease in

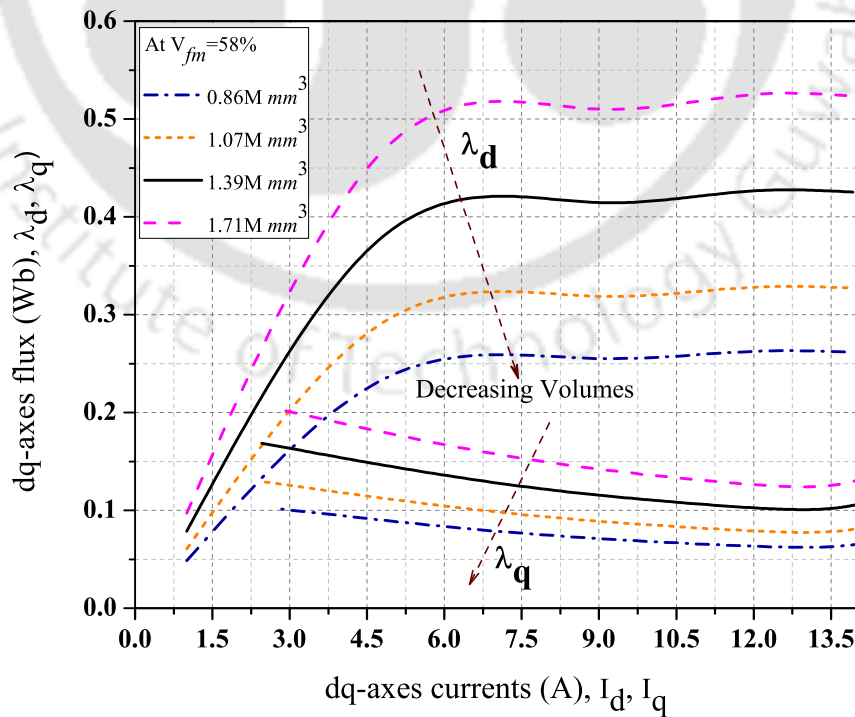
### 3. ELECTROMAGNETIC TORQUE ANALYSIS OF SRG WITH FERRITE MAGNET FOR WIND ENERGY GENERATION



**Figure 3.10:** (a)  $d$ - and  $q$ - axes inductance with generator volumes and at  $V_{fm} = 40\%$ . (b)  $d$ - and  $q$ - axes flux with generator volumes and at  $V_{fm} = 40\%$ .



(a)



(b)

**Figure 3.11:** (a)  $d$ - and  $q$ - axes inductance with generator volumes and at  $V_{fm} = 58\%$ . (b)  $d$ - and  $q$ - axes flux with generator volumes and at  $V_{fm} = 58\%$ .

### 3. ELECTROMAGNETIC TORQUE ANALYSIS OF SRG WITH FERRITE MAGNET FOR WIND ENERGY GENERATION

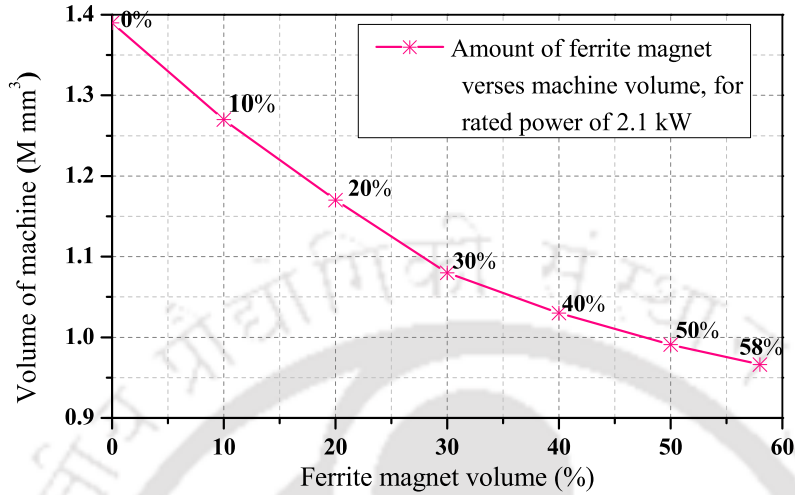


**Figure 3.12:** Volume of ferrite magnet-increment verses volume of machine for 2.1 kW, 4 poles PM-SRG.

**Table 3.4:** Evaluated performance and design parameters for  $V_{fm} = 30\%$  of 2.1 kW of FM-SRG

Parameters	Quantity	Parameters	Quantity
$L_m$	58 mH	$D_r$	104 mm
$L_d$	69.4 mH	$D_{in}$	105 mm
$L_q$	11.55 mH	$D_o$	165 mm
$L_{ls}$	0.87 mH	$h'$	11.811 mm
$I_m$	13.5 A	$m$	24
$mI_q$	305.819 A.turns	$mI_d$	132.84 A.turns
$L_s$	50 mm	$E_{ph}$	125 V
$l_g$	0.5 mm	$\eta$	90.49%
$k_u$	0.5	$W_t$	0.80 kg
$R_s$	0.70 $\Omega$	$W_y$	2.07 kg

induced voltage. The result obtained through FEA simulation with the rated excitation current of the machine is shown in Fig. 3.13(a).

The peak values of back emf produced at 1500 rpm corresponding to different magnetizing currents for the machine is shown in Fig. 3.13(b). It is observed that, the starting emf with zero magnetizing current is approximately 42 volts (peak) due to the presence of magnet. But for FM-SRG, the voltage at saturation is approximately 20 volts less than SRG.

The torque versus power angle curves have been analyzed for the generator. From Fig. 3.14(a), it can be observed that the torque at zero power angle (i.e.,  $\gamma = 0^\circ$ ) is positive. This can

also be observed using the analytical equation of torque as given by (3.1) i.e.,  $T_{em}(\text{at } \gamma = 0) = 3P[\Lambda_m I_d + V_{ph}^2(1 - \varphi)\varphi\beta] / [(P\omega)^2 L_d(\varphi + \beta^2)^2]$ . Similar to SRG, it is observed that the maximum torque angle decreases due to the presence of stator resistance, which cannot be neglected for machine with small ratings. The peak torque in generating mode is achieved at an angle close to  $100^\circ$  of power angle. (see Fig.3.14(a)). It is also observed that for  $R_s \neq 0$ , the torques do not attain their maximum values at power angle of  $45^\circ$  (i.e.,  $\gamma = 45^\circ$ ) for the machine.

If the effect of stator resistance is neglected i.e.,  $R_s = 0$  (see equation 3.3, for  $\gamma = 0^\circ$ , the torque tends to  $\frac{3P}{2}\Lambda_m I_d$ . In order to further evaluate the performance of the FM-SRG for the wind power generation, the cogging torque curves are provided in Fig. 3.14(b). It can be noted that this cogging torque has a negative role in the power generation, while SRG do not experience the presence of cogging torque. The machine with less cogging torque are more suitable for wind power application. Fig. 3.15(a) represents that the performance of the machine in motoring and generating mode. From Fig. 3.15(a), it is observed that the average torque is a function of square of stator current till the current of the machine is 5A. However, after 5A the difference between  $(L_d - L_q)$  is approximately constant, hence, the variation of average torque is observed to be linear. To achieve a higher maximum average torque per ampere, it is suitable to have a ferrite assisted SRG. However, the strength of the ferrite magnetic is limited by the permissible ripple torque in its design (i.e., nearly  $< 12\%$  of rated torque ripple is considered for the design). Fig. 3.15(b) represent the electromagnetic torque of the machine with variations of  $\gamma$ . In Fig. 3.15(b) comparing the torque magnitudes, it can be seen that the torque of machine with ferrite magnet is about 1% higher than the machine without ferrite magnet. Moreover, as the magnitude of average torque increases the ripple increasing for the machine. Table 3.6, provides a comparative analysis of the presence of ripple torque in FM-SRG with increase of stator current.

Fig. 3.17(a) depict the  $q$  and  $d$ -axes flux linkages versus the  $q$ -and  $d$ -axes current. The curves are obtained from finite element analysis (FEA), which gives the  $q$  and  $d$  - axes flux linkage,  $\lambda_d$  and  $\lambda_q$ . From Fig. 3.17(a), it is observed that  $\lambda_d$  and  $\lambda_q$  increase linearly when the current,  $I_d$   $I_q$  are less than 6 A. After that,  $\lambda_d$  and  $\lambda_q$  become almost constant due to saturation.

### 3. ELECTROMAGNETIC TORQUE ANALYSIS OF SRG WITH FERRITE MAGNET FOR WIND ENERGY GENERATION

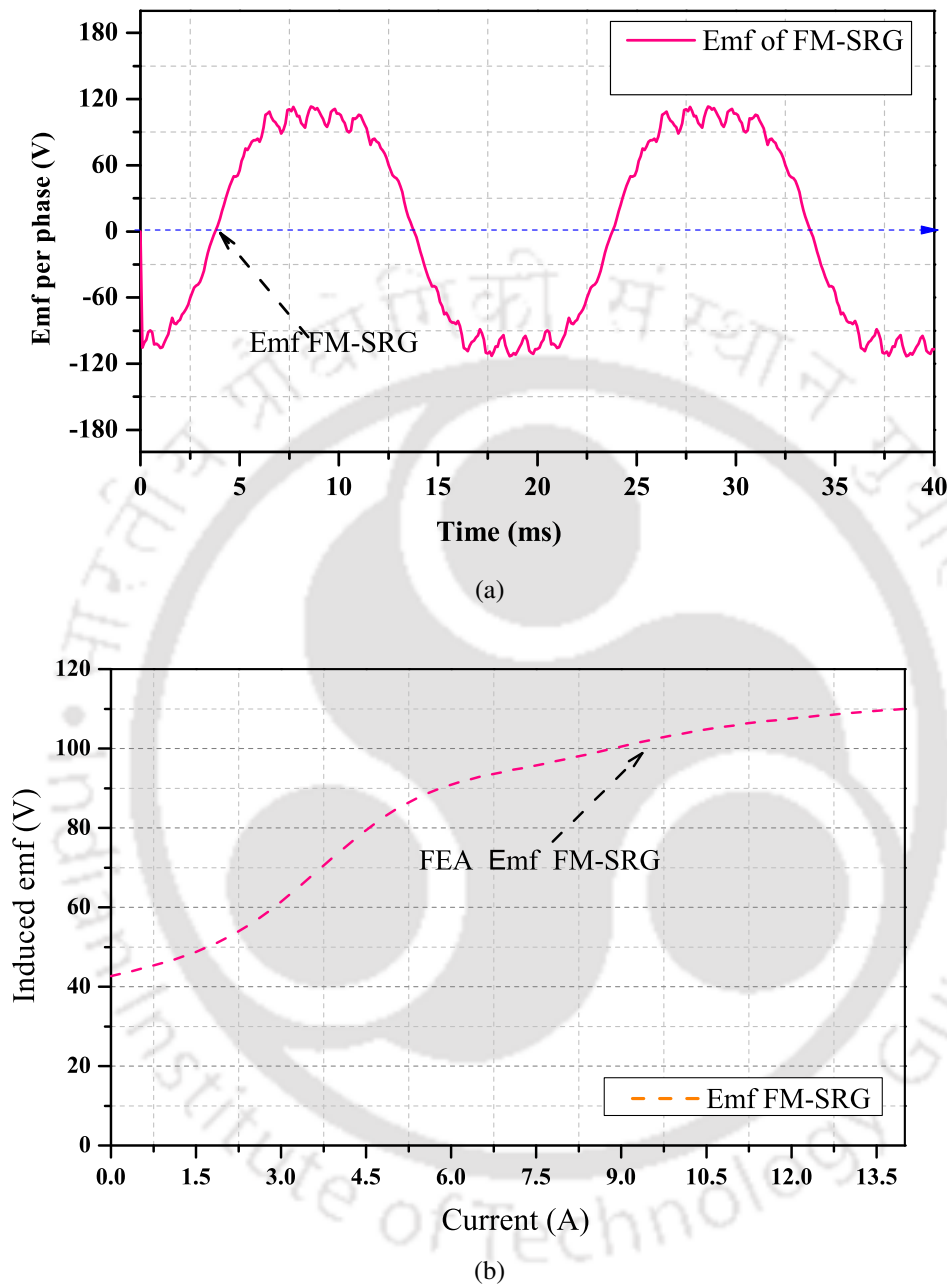


**Figure 3.13:** (a) Machines emf at given frequency. (b) Machine emf curves as a function of current.

It is also observed that for FM-SRG, due to the presence of magnet along the  $q$  – axis (i.e., the magnet produce a flux of 0.1 wb, see Fig. 3.16) get saturated at lower flux as compared with SRG. In order to account for the saturation effects, the  $q$  and  $d$ -axes flux linkages are allowed

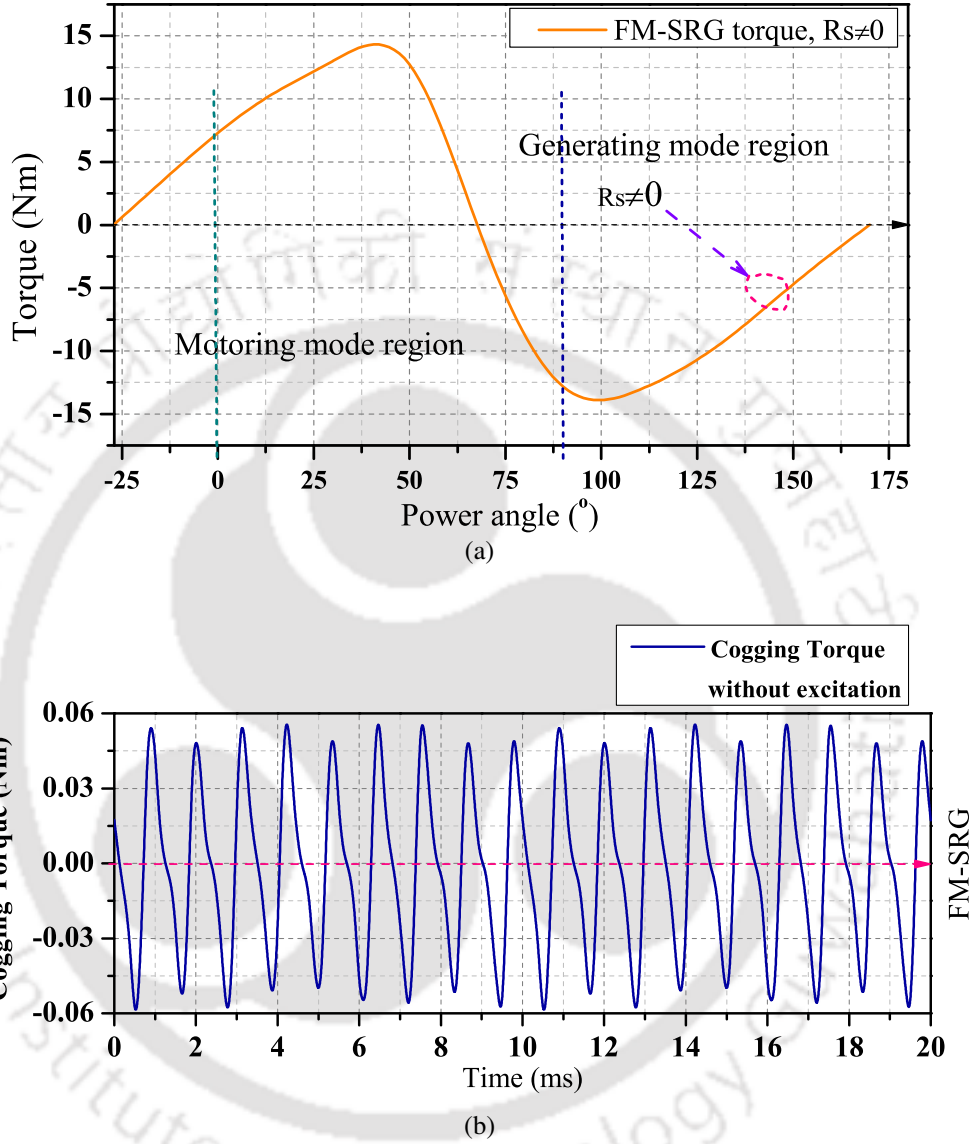


**Figure 3.14:** (a) Torque versus power angle curves. (b) Cogging torque of FM-SRG (without excitation).

to vary with the armature current, as  $\lambda_d$  and  $\lambda_q$  in (mWb) are represented by:

$$\begin{cases} \lambda_d = a_6 I_d^6 + a_5 I_d^5 + a_4 I_d^4 + a_3 I_d^3 + a_2 I_d^2 + a_1 I_d + a_0 \\ \lambda_q = b_6 I_q^6 + b_5 I_q^5 + b_4 I_q^4 + b_3 I_q^3 + b_2 I_q^2 + b_1 I_q + b_0 \end{cases} \quad (3.15)$$

For low or near zero value of currents ( $I_d, I_q$ ), the flux linkage  $\lambda_d$  is near zero, whereas,  $\lambda_q$  is slightly negative due to the presence of  $q$ -axis magnets. The polynomial coefficients  $a_0 - a_6$  and  $b_0 - b_6$  are obtained from a curve fit of the actual  $q$  and  $d$ -axes flux linkages as obtained from

### 3. ELECTROMAGNETIC TORQUE ANALYSIS OF SRG WITH FERRITE MAGNET FOR WIND ENERGY GENERATION

**Table 3.5:** Values of polynomial coefficients evaluated from curve fit.  
The unit of equations (3.15) are in  $mWb$

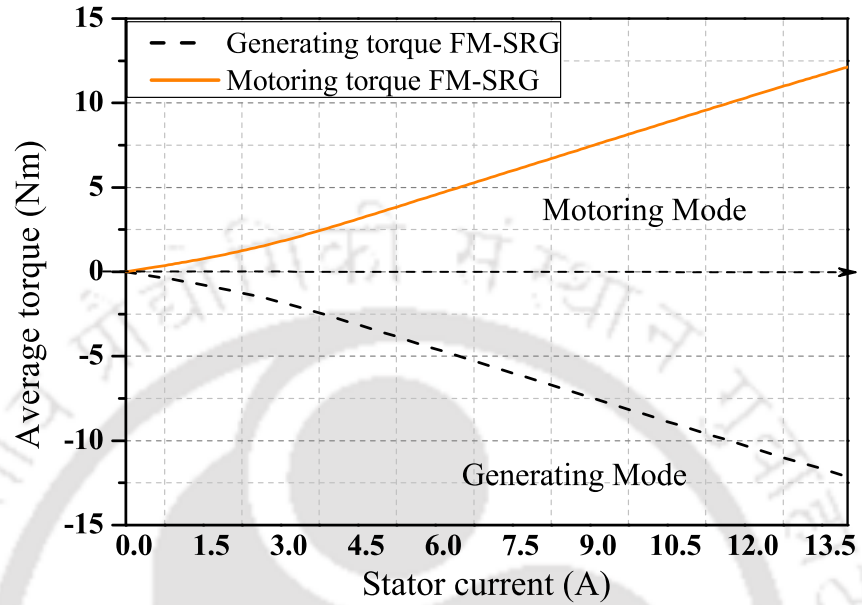
Poly.coefficient (a,b)	values
$a_0$	0.005
$a_1$	29.3
$a_2$	42.8
$a_3$	-11.7
$a_4$	7.2
$a_5$	-0.06
$a_6$	0.001
$b_0$	-0.4
$b_1$	1.5
$b_2$	6.4
$b_3$	-1.5
$b_4$	-7.2
$b_5$	0.1
$b_6$	-0.004

**Table 3.6:** Variation of torque ripple with phase currents

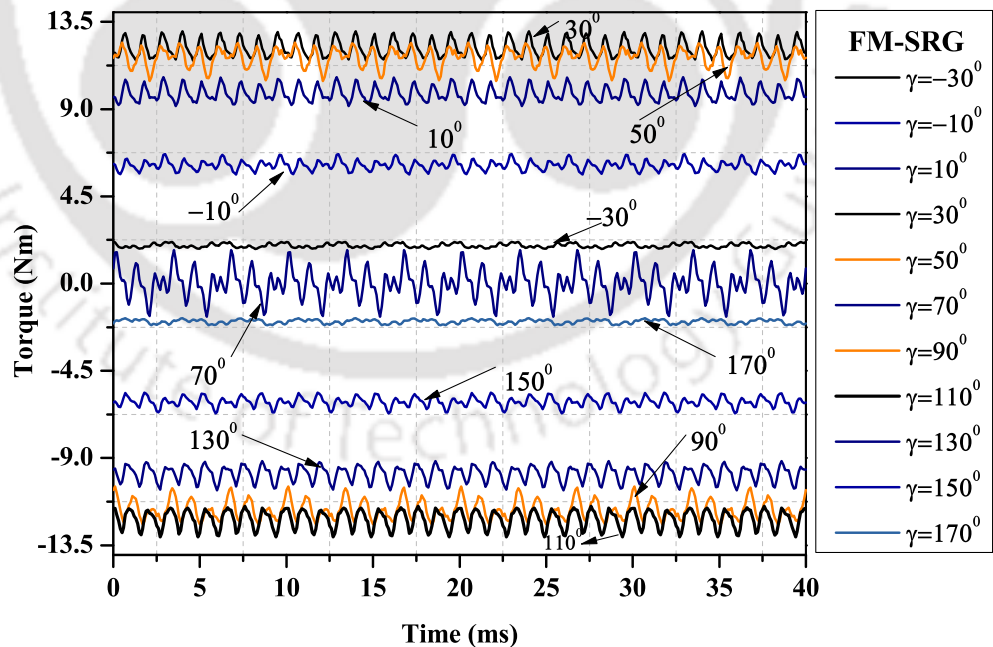
Maximum currents (A)	Ripple values
0	0.126
2.5	0.307
5	0.503
7.5	0.830
10	1.150
12.5	1.390
13.5	1.600

Ansys Electronic Desktop software FEA. The estimated coefficients are shown in Table 3.5. These equations are utilized to estimated the requirement of minimum residual flux for generator to produce terminal voltage. Further analysis of self-excited FM-SRG has been carried out with the presence of inductive load. Similarly, the empirical expressions for the inductance along the  $d$ - and  $q$ -axes i.e.,  $L_d$ ,  $L_q$  in  $mH$  which are obtained through curve fitting are given below:

$$\begin{cases} L_d = e_6 I_d^6 + e_5 I_d^5 + e_4 I_d^4 + e_3 I_d^3 + e_2 I_d^2 + e_1 I_d + e_0 \\ L_q = f_6 I_q^6 + f_5 I_q^5 + f_4 I_q^4 + f_3 I_q^3 + f_2 I_q^2 + f_1 I_q + f_0 \end{cases} \quad (3.16)$$



(a)



(b)

**Figure 3.15:** (a) Torque versus current curves of the machine. (b) Variation of FM-SRG electromagnetic torque with power angle.

The polynomial coefficients  $e_0 - e_6$ , and  $f_0 - f_6$  are obtained from a curve fit of the actual  $d$ - and  $q$ -axes inductances. Fig. 3.17(b) depict the  $d$  and  $q$ -axes inductance verses the  $q$  and

### 3. ELECTROMAGNETIC TORQUE ANALYSIS OF SRG WITH FERRITE MAGNET FOR WIND ENERGY GENERATION

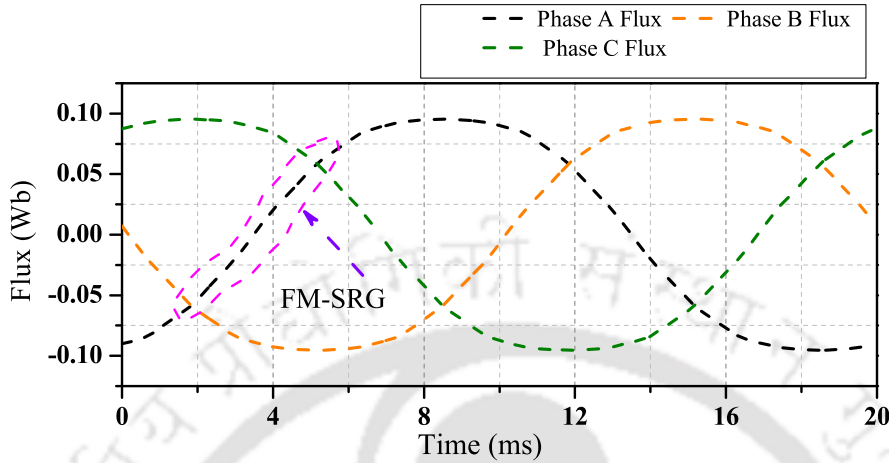
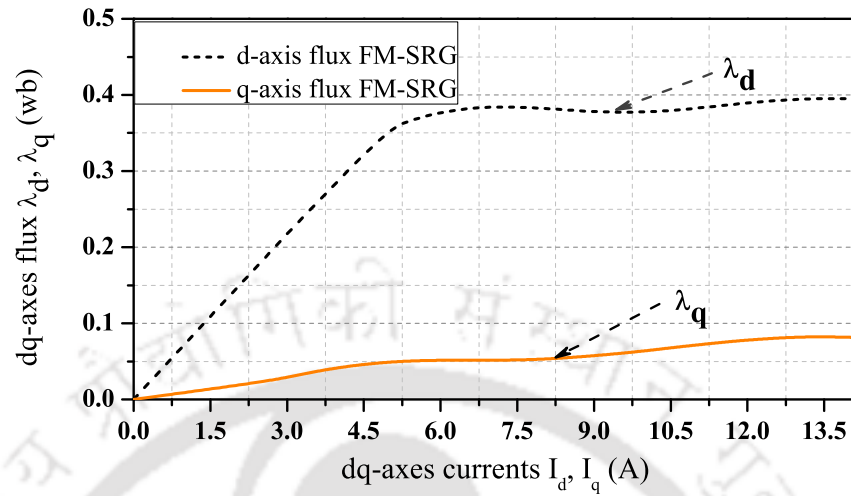


**Figure 3.16:** Linkage flux of FM-SRG (without excitation).

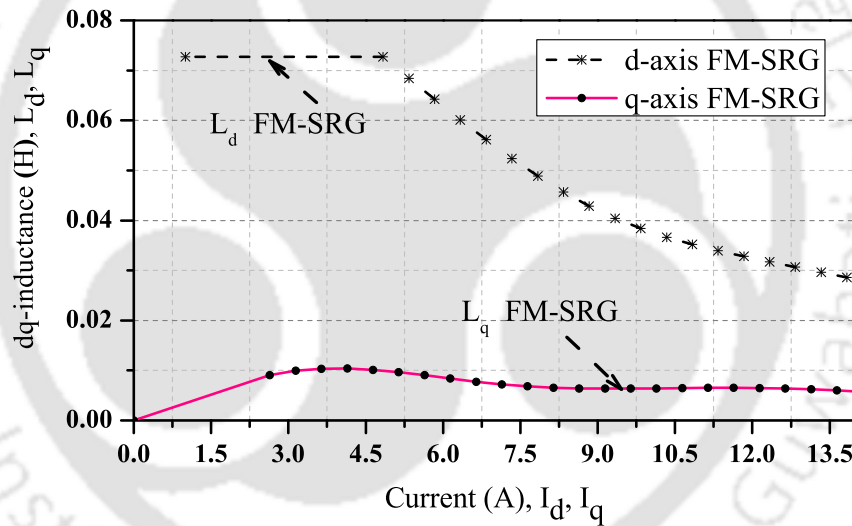
$d$ -axis current for FM-SRG. Equation (3.16), and Table 3.7, shows the variation of saturations as the function of  $q$  and  $d$ -axes currents. The  $L_q$  of the FM-SRG keeps increasing for low values of current. However, as the current increase to a certain value, it starts decreasing and subsequently reaches to a constant value because of the iron saturation. The  $L_d$  of FM-SRG remains constant at low value of current, whereas it start decreasing gradually when current is more than 4 A. Because of the existence of ferrite orientation in the  $q$ -axis, there is no flux linkage in  $d$ -axis without excitation current. But, the  $d$ -axis inductance is of high value at low current and start decreasing as current increases. It remains almost constant when the current is more than 13.5 A.

#### 3.4.2 Technical performance of FM-SRG

Similar to SRG the compactness, reliability, and efficiency are important issues related to power generation at remote locations. To design the machine, the key parameters such as volume, mass, rated power, and torque of the machine are utilized. The specific power and torque densities are calculated from mass and volume of each machine components. There are inherent advantages in utilizing synchronous reluctance generators in terms of machine performance and manufacturing. It also has high efficiency and high power density. In this chapter, FM-SRG are designed for a power rating of 2.1 kW. By optimizing the design parameters for the machine, the final design has the stack length of 50 mm. The other initial and final ( i.e., the optimal one)



(a)



(b)

**Figure 3.17:** (a)  $d$ - and  $q$ -axes flux linkages magnetizing of the machine. (b)  $d$  and  $q$ -axes magnetizing inductances of FM-SRG.

such as power density  $P_{\rho m}$ , specific power density  $P_{spm}$ , torque density  $T_{\rho m}$ , and specific torque  $T_{spm}$  are provided in Table 3.8. Table 3.9 provides performance of self-excited FM-SRG. From Table 3.9, and Fig. 3.18(b), it is observed that FM-SRG is more compact as compared with SRG, but their efficiency and torque/ power densities are comparable. In terms of torque ripple, SRG is better than FM-SRG. Fig. 3.18(a) provides magnetic field density distributions and flux lines of FM-SRG. Similarly, the Fig. 3.18(b), shows the compactness/volume of the machines. From Fig. 3.18(b), it is observed that FM-SRG is more compact as compared with SRG.

### 3. ELECTROMAGNETIC TORQUE ANALYSIS OF SRG WITH FERRITE MAGNET FOR WIND ENERGY GENERATION

**Table 3.7:** Values of polynomial coefficients evaluated from curve fit.  
The unit of equation (3.16) is in  $mH$

Poly.coefficient (e,f)	values
$e_0$	105.3
$e_1$	-50
$e_2$	25.3
$e_3$	-5.7
$e_4$	0.6
$e_5$	-0.03
$e_6$	0.0001
$f_0$	-0.9
$f_1$	2
$f_2$	1.8
$f_3$	-0.8
$f_4$	0.1
$f_5$	0.006
$f_6$	-0.0001

**Table 3.8:** Technical performance of FM-SRG

FM-SRG			
Parameters	Initial	Final (optimal)	Increase (%)
$P_{\rho m}$	1.5	2.10	33
$P_{spm}$	0.25	0.33	27
$T_{\rho m}$	9.10	12.75	33
$T_{spm}$	1.49	1.98	28

**Table 3.9:** Analytical, FEA and experimental achievements of the machine

FM-SRG			
Parameters	Analytical	FEA	
$V_{ml}$	1.07 L	-	-
$L_d$	69.4 mH	70.3 mH	-
$L_q$	11.5 mH	10 mH	-
$T_{em}$	12.68 Nm	12.28 Nm	-
$T_{rp}$	-	11%	-

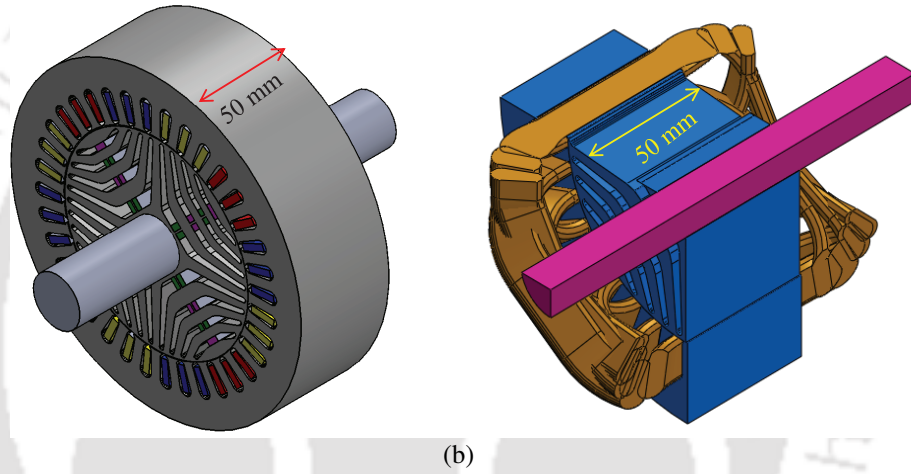
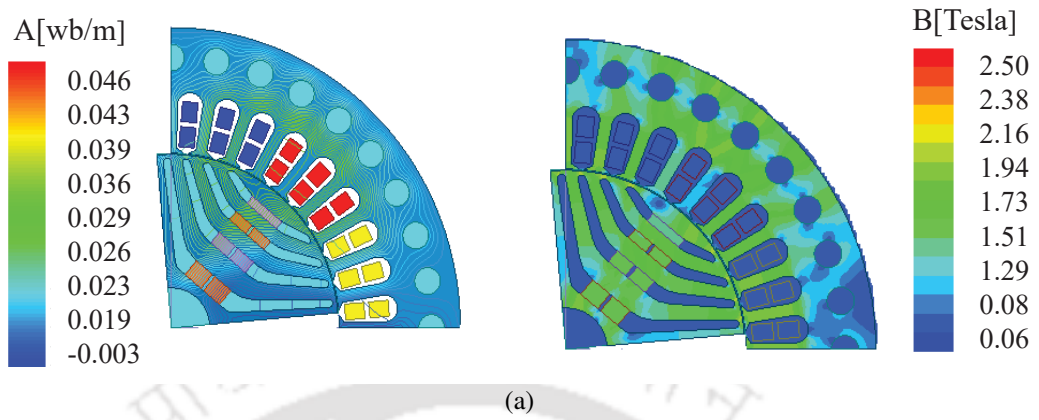


**Figure 3.18:** (a) Magnetic flux density distribution and flux lines of the machine. (b) Size of the machine.

### 3.4.3 Effects of wind speed, and load on the system performance of FM-SRG

In this section, the simulation has been carried out in Matlab using the design parameters to observe the dynamic behavior of the system under various conditions such as variation of wind speed, constant wind speed, and variation of the load for FM-SRG.

The performance of the FM-SRG under fixed wind speed of  $10 \text{ m/s}$  and an inductive load ( $R_L = 250 \Omega$ ,  $L = 30 \text{ mH}$  with an excitation capacitor of  $190 \mu\text{F}$ ) are shown in Fig. 3.19. As the mechanical torque from the wind turbine is applied, the rotor speed of the generator increases to the rated speed of  $1500 \text{ rpm}$ . For constant wind speed, the voltage and current plot of FM-SRG are shown in Fig. 3.19. It is observed that the steady-state is reached in about  $1 \text{ s}$  for the machine. The effect of a sudden change in wind speed is simulated to get the dynamic response of the FM-SRG. Here, the wind speed suddenly drops to  $4.98 \text{ m/s}$ . This results in the falls

### 3. ELECTROMAGNETIC TORQUE ANALYSIS OF SRG WITH FERRITE MAGNET FOR WIND ENERGY GENERATION

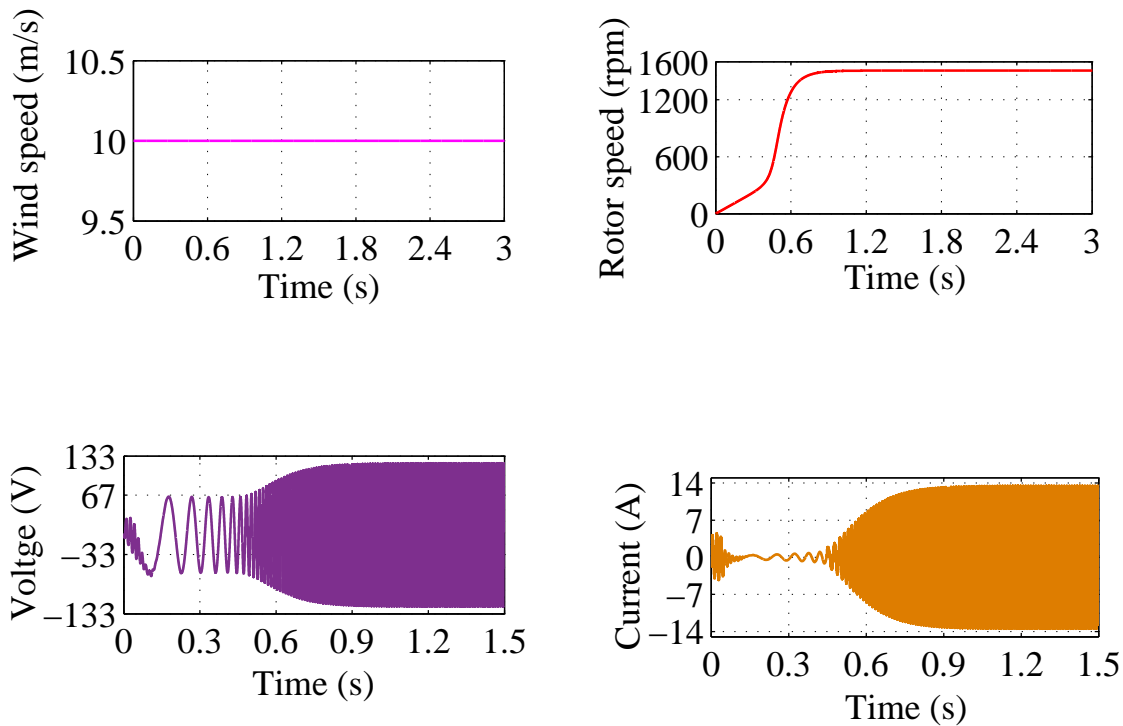


**Figure 3.19:** Wind-driven FM-SRG at constant of  $v_w = 10 \text{ m/s}$  with  $R_L = 250 \Omega$ ,  $L = 30 \text{ mH}$  for  $C = 190 \mu \text{ F}$ .

of the generator rotor speed from the rated values of  $157.08 \text{ rad/s}$  (1500 rpm) to  $67.54 \text{ rad/s}$  (645 rpm), as shown in Fig. 3.20. Under this condition, the generated voltage and current decrease from an initial value of  $121 \text{ V}$  to a new value of  $65.5 \text{ V}$  for the FM-SRG. The current supplied by the machine also decreases. At  $t = 6.5 \text{ s}$ , again, the wind speed is increased to its previous value. The performance of the FM-SRG under the change of load are presented in Fig. 3.21 for FM-SRG. The inductive loads instantly decrease from  $258 \Omega$ ,  $30 \text{ mH}$  to  $150 \Omega$ ,  $10 \text{ mH}$  at  $5 \text{ sec}$ , and then increases back to the initial impedance load values at  $t = 7 \text{ sec}$ . At  $5 \text{ sec}$ , the reduction in both the stator currents and voltages is observed, i.e., the voltage slightly changes from the steady-state value of  $121 \text{ V}$  to  $118 \text{ V}$  for FM-SRG. Similarly, the stator current decreases from  $13.5 \text{ A}$  to  $12.9 \text{ A}$  for FM-SRG. At  $t = 7 \text{ s}$  impedance load value is changed to its previous value. It is observed that the current and voltage increase to the initial values. As the speed of the FM-SRG kept fixed at  $1500 \text{ rpm}$ , and thus the frequency remains the same despite the change in load. This is one of the advantages over the self-excited induction generator, whose frequency and voltage are highly influenced by changing load conditions.

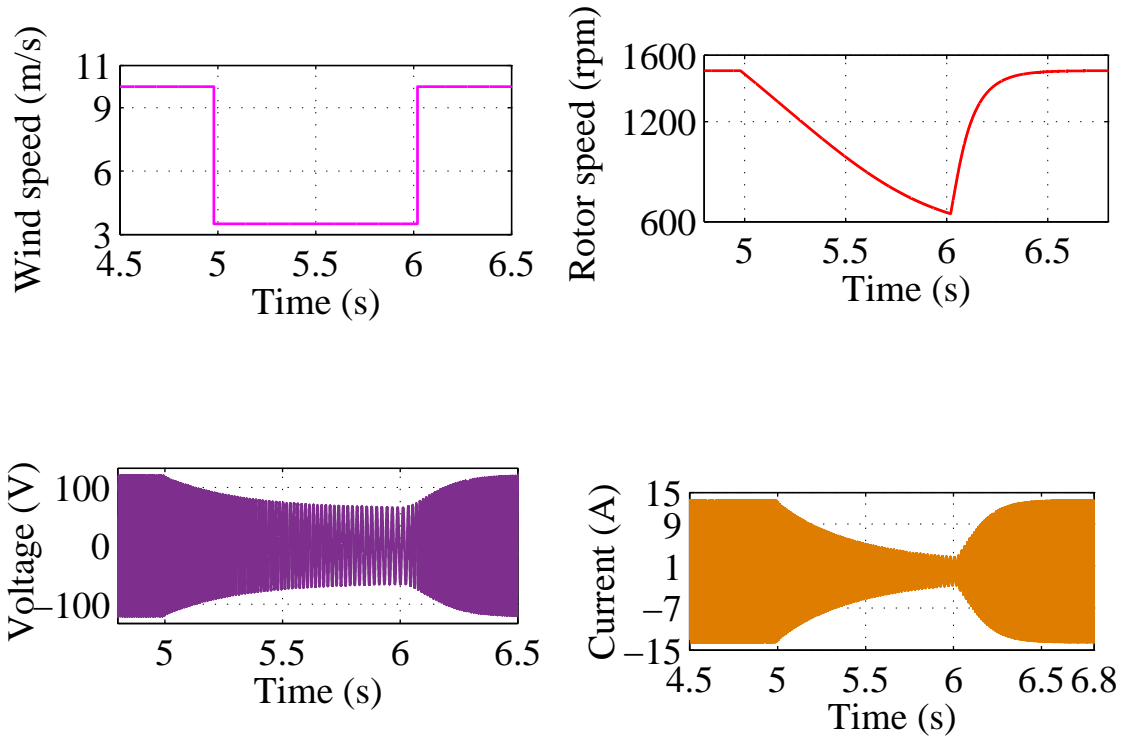


**Figure 3.20:** Wind-driven FM-SRG for falls in speed from  $v_{\omega} = 10 \text{ m/s}$  to  $v_{\omega} = 4.98 \text{ m/s}$  with  $R_L = 250 \Omega$ ,  $L = 30 \text{ mH}$  for  $C = 190 \mu \text{ F}$ .

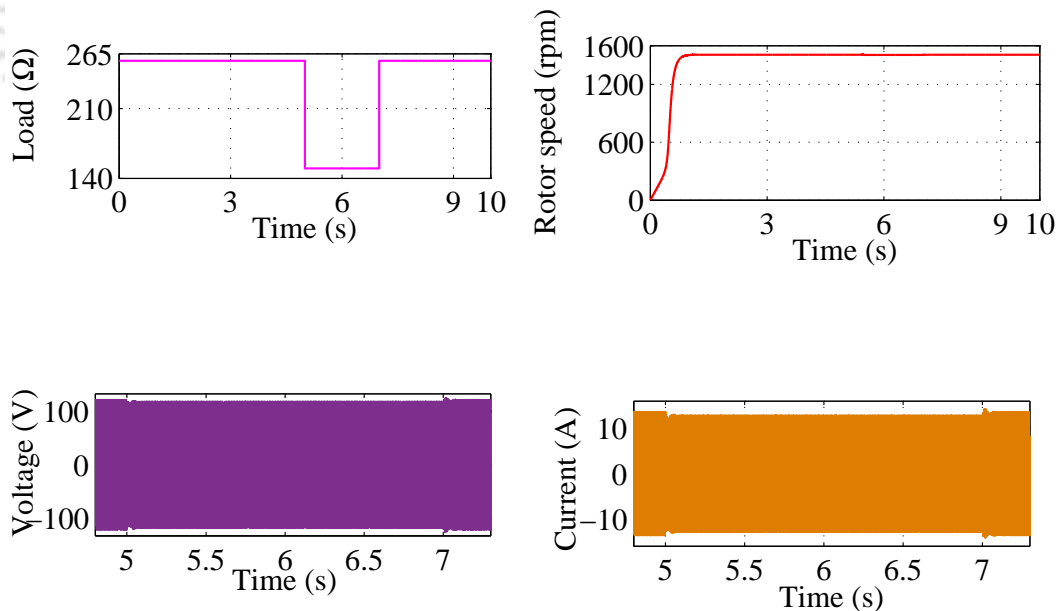


**Figure 3.21:** Wind-driven FM-SRG at constant of  $v_{\omega} = 10 \text{ m/s}$  with  $Z_L = 258 \Omega$  to  $150 \Omega$  for  $C = 190 \mu \text{ F}$ .

From Fig. 3.21, it is observed that the change in load for FM-SRG, slightly changes the current and voltage as compared to the self-excited induction generator.

### 3. ELECTROMAGNETIC TORQUE ANALYSIS OF SRG WITH FERRITE MAGNET FOR WIND ENERGY GENERATION

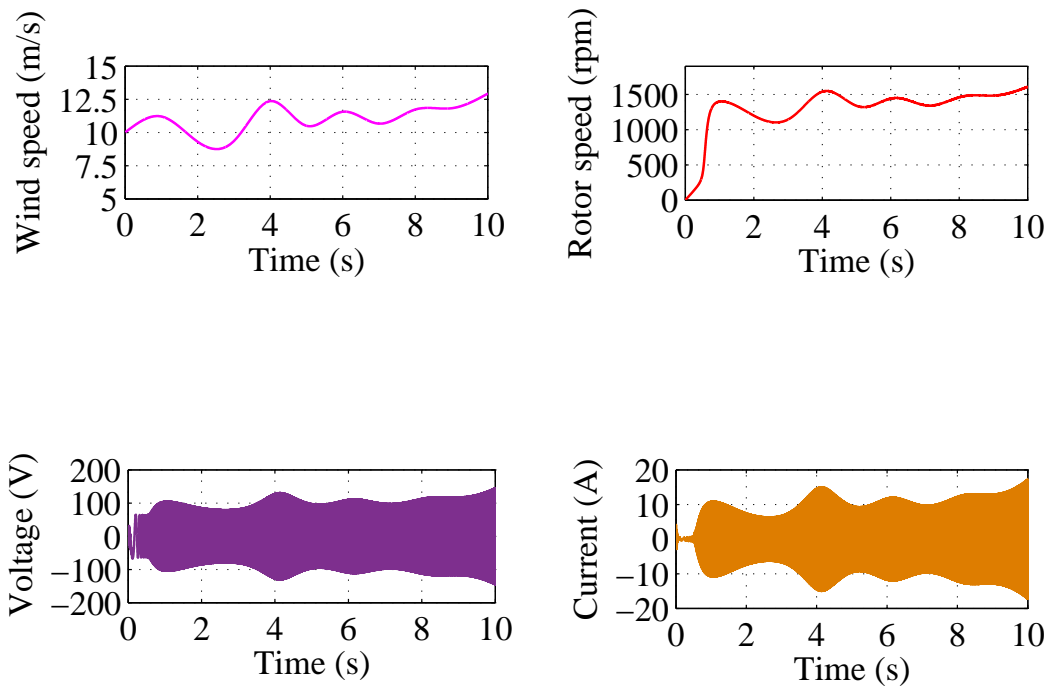


**Figure 3.22:** Wind-driven FM-SRG for variable speed with  $R_L = 250 \Omega$ ,  $L = 30 \text{ mH}$  for  $C = 190 \mu \text{F}$ .

The performance of the FM-SRG under the variable wind speed is shown in Figs. 3.22. The inductive load is kept constant at  $250 \Omega$ ,  $30 \text{ mH}$ , and the wind speed is varied, as shown in Fig. 3.22. This variation of wind speed was observed from a location in India over a period of one hour, forty minutes. But to show the effect of wind variation on the machine's performance, the duration of variation was mapped to a time of 10 sec purely for simulation. Fig. 3.22, shows the variation in the stator current, voltage, and rotor speed. It is observed that the variation in current FM-SRG is slightly more as compared with SRG. But, as the practical generator will have a speed controller, which will regulate the rotor speed, this kind of voltage and current fluctuations will not be observed for a practical FM-SRG.

#### 3.4.4 Performance comparison of SRG and FM-SRG

Using sections 2.3.2 and 3.2 the summarized performance comparison of SRG and FM-SRG are given in Table 3.10. The design performance of SRG and FM-SRG is compared using analytical calculation as shown in Table 3.10. Similarly, the performance of the designed SRG and FM-SRG is compared using FEA. The maximum induced electromotive forces (emfs) in the stator winding of the 2.1 kW SRG and FM-SRG with symmetric design are shown in Figs. 2.5(a)

and 3.13(a). The results obtained through FEA simulation with the same excitation current of the machines is shown in Fig. 2.5(a) and 3.13(a). It could be observed that SRG has more induced emf as compared with FM-SRG as predicted by the voltage equation.

The peak values of back emf produced at 1500 rpm corresponding to different magnetizing currents for both machines are shown in Fig. 2.5(b) and 3.13(b). It is observed that, for SRG, emf starts with zero voltage and the experimental result distinguished by dashed line, whereas for FM-SRG, with zero magnetizing current the induced voltage is approximately 42 volts (peak) due to the presence of magnet. But for FM-SRG, the voltage at saturation is approximately 20 volts less than SRG. Fig.2.5(b) shows experimentally obtained emf by SRG, which is very close to the simulated (FEA) results.

The torque versus power angle curves as shown in Fig. 2.6(a) and 3.14(a) are obtained using FEA. It is observed that the torque produced by the SRG and FM-SRG for  $R_s \neq 0$  are

**Table 3.10:** Evaluated performance parameters of SRG and FM-SRG for 2.1 kW Generators

Parameters	Quantity	
	SRG	FM-SRG
$L_m$	76 mH	58 mH
$L_d$	80.5 mH	69.4 mH
$L_q$	15 mH	11.5 mH
$L_{ls}$	1.15 mH	0.87 mH
$I_m$	13.5 A	13.5 A
$L_s$	65 mm	50 mm
$l_g$	0.5 mm	0.5 mm
$k_u$	0.5	0.5
$R_s$	1.00 $\Omega$	0.70 $\Omega$
$D_r$	104 mm	104 mm
$D_{in}$	105 mm	105 mm
$D_o$	165 mm	165 mm
$h'$	11.811 mm	11.811 mm
$m$	24	24
$E_{ph}$	150 V	125 V
$\eta$	86.5%	90.49%
$W_t$	0.99 kg	0.8 kg
$W_y$	2.7 kg	2.07 kg

### 3. ELECTROMAGNETIC TORQUE ANALYSIS OF SRG WITH FERRITE MAGNET FOR WIND ENERGY GENERATION

**Table 3.11:** Variation of torque ripple with phase currents for SRG and FM-SRG

Maximum currents (A)	Ripple for SRG	Ripple for FM-SRG
0	0	0.126
2.5	0.155	0.307
5	0.430	0.503
7.5	0.668	0.830
10	0.918	1.150
12.5	1.044	1.390
13.5	1.260	1.600

comparable with little variations. The peak torque in generating mode is achieved at an angle close to  $100^\circ$  of power angle for FM-SRG, and near to  $94^\circ$  for SRG as shown in Fig.2.6(a) and 3.14(a).

Further, a comparison of the cogging torque and flux with out excitation for the FM-SRG are shown in Fig.3.14(b) and 3.16. It can be noted that this cogging torque has a negative role in power generation, while SRG does not experience the presence of cogging torque. The machine with less cogging torque is more suitable for wind power generation. It is suitable to have a ferrite-magnet SRG to increase maximum average torque per ampere. However, the strength of the ferrite magnetic is limited by the permissible ripple torque in its design (i.e., nearly  $\leq 12\%$  of rated torque ripple is considered for the design).

Table 3.11, provides a comparative analysis of the presence of ripple torque in SRG and FM-SRG with an increase of stator current. It can be seen that the ripple torque is less in SRG as compared to FM-SRG.

To design the machine, the key parameters such as volume, mass, rated power, and torque of the machines are utilized. For the specific power, torque density, and mass of each components have been evaluated. There are important advantages in applying SRG in terms of machine performance and manufacturing. In Chapter 2, and in this Chapter, SRG and FM-SRG are designed for a power rating of 2.1 kW, respectively. By optimizing the design parameters for the machines, the final design has the stack length of 65 mm for SRG, and 50 mm for FM-SRG. The other initial and final ( i.e., the optimal one) such as power density ( $P_\rho$ ), specific power density ( $P_{sp}$ ), torque density ( $T_\rho$ ), and specific torque ( $T_{sp}$ ) are provided in Tables. 2.8, and 3.8.

### 3.4 Structure and performance evaluations

It can be noted that the performance in terms of torque density ( $T_p$ ) and specific torque ( $T_{sp}$ ) are comparable for the two machines. Moreover, SRG is more robust, and its manufacturing cost is less as compared with FM-SRG, while FM-SRG is more compact for the same rating as shown in Figs. 2.9(b), and 3.18(b), respectively.

**Table 3.12:** Performance comparison of existing machines with up to date SRG, and FM-SRG

Existing Machines [68]			
Performance	IE2 class IM	IE4 <sup>-</sup> class SRM	IE4 <sup>+</sup> class PM – SRM
<i>Power</i>	2.6 kW	2.45 kW	2.4 kW
<i>Speed</i>	1700 rpm	1800 rpm	1800 rpm
<i>Power factor</i>	0.77	0.65	0.71
<i>Torque</i>	12.2 Nm	11.67 Nm	11.67 Nm
<i>Torque ripple</i>	–	11.44%	11.46%
<i>Efficiency(%)</i>	83.89	88.96	90.5
Existing Machines [55]			
Performance	–	–	IE4 <sup>+</sup> class PM – SRM
<i>Power</i>	–	–	1.8 kW
<i>Speed</i>	–	–	1500 rpm
<i>Torque</i>	–	–	11.86 Nm
<i>Torque ripple</i>	–	–	11.25%
<i>Cogging torque</i>	–	–	0.154 Nm
<i>Volume</i>	–	–	2.6 L
Up to date Machines			
Performance	–	IE4 <sup>-</sup> class SRG	IE4 <sup>+</sup> class FM – SRG
<i>Power</i>	–	2.1 kW	2.1 kW
<i>Speed</i>	–	1500 rpm	1500 rpm
<i>Power factor</i>	–	0.69	0.72
<i>Torque</i>	–	12.23 Nm	12.28 Nm
<i>Torque ripple</i>	–	9.7%	11%
<i>Cogging torque</i>	–	–	0.12 Nm
<i>Volume</i>	–	1.4 L	1.07 L
<i>Efficiency(%)</i>	–	86.95	90.49

Further, the performance of the designed FM-SRG, and SRG at such a rated condition is

### 3. ELECTROMAGNETIC TORQUE ANALYSIS OF SRG WITH FERRITE MAGNET FOR WIND ENERGY GENERATION

---

compared with the induction machine obtained from an *IE2* class and reference SRM with similar stators. As observed from Table 3.12 the SRM, and the PM-SRM has higher performances than that of the IM. Furthermore, using proper ferrite magnet arrangement and design algorithm, the performance of the SRG, and FM-SRG achieves the International Electrotechnical Commission (IEC) *IE4+* class as shown in Table 3.12. Moreover, from Table 3.12 it can be observed that performance of SRG and FM-SRG are better compared to the other machines rating. (i.e., the higher power rated, the higher the efficiency) [69].

#### 3.5 Summary

The effect on the performance index for the synchronous reluctance generator (SRG) by placing the low-cost ferrite magnet in the rotor air barrier with suitable location and orientation is presented. The orientation is chosen in such a way as to reduce the q-axis flux. It is observed that as the percentage volume of the ferrite magnet ( $V_{fm}$ ) increases in the air barrier, there is an increase in the performance index of SRG, but it is observed till the  $V_{fm} = 30\%$ . The performance index, and ripple torque changes for  $V_{fm} > 30\%$  have been evaluated. Hence, it can be said that, for this particular design, till  $V_{fm} \leq 30\%$ , there is an improvement in power factor, compactness, and the operational efficiency of FM-SRG. Moreover, the variation of the *d* – axes and *q* – axes flux linkage, and inductances while varying the  $V_{fm}$  are analyzed. Additionally, analytical, finite element analysis, and detail performance comparison of SRG and FM-SRG, are provided in the present work.



### 3. ELECTROMAGNETIC TORQUE ANALYSIS OF SRG WITH FERRITE MAGNET FOR WIND ENERGY GENERATION

---



# 4

## **ELECTROMAGNETIC-MECHANICAL STRESS ANALYSIS OF SRG FOR WIND ENERGY APPLICATION**

### **Contents**

---

<b>4.1</b>	<b>Introduction . . . . .</b>	<b>96</b>
<b>4.2</b>	<b>Machine design parameters and problem statement . . . . .</b>	<b>97</b>
<b>4.3</b>	<b>Analysis of electromagnetic performance . . . . .</b>	<b>99</b>
<b>4.4</b>	<b>Analysis of mechanical performance . . . . .</b>	<b>106</b>
<b>4.5</b>	<b>Summary . . . . .</b>	<b>111</b>

---

### 4.1 Introduction

The design and modeling of SRG and FM-SRG have been discussed in Chapters 2, and 3, respectively. The present Chapter is focused on the electromagnetic and mechanical stress on the rotor of the synchronous reluctance generator (SRG). While improving the electromagnetic performances, the stress on the various components of the rotor of the machine must be simultaneously analyzed. This will ensure the structural stability of the rotor of the machine. The topology associated with the design of SRG rotors are either transversely laminated variant (TLV) or axially laminated variant (ALV) types [14]. However, the TLV design is more commonly used over ALV [15]. Hence, this chapter investigates the rotor of the TLV type. Significant literature is available in the design of the number of flux barriers, and their shape insulation ratio [16,33]. Park *et al.* [70], Mohammadi *et al.* [36], and Di Nardo *et al.* [37] has investigated different computational and analytical barriers optimization methods. Similarly, significant work has been done towards the selection of material grade used in SRG design [38–40]. But, very few and rare studies have been carried out on the analysis and design of electromagnetic-mechanical stress performance with respect to radial and tangential ribs that link the flux lines. The work presented in this Chapter tries to fulfill the gap in the literature.

An SRG design base on a high power factor and high reactance ratio i.e., high  $X_d/X_q$  for better performance is achieved through the high-quality design of the rotor. The design evolves the number of barriers, shape, and the number of poles along with the design of tangential and radial ribs to ensure good performances. The SRG coupled with the wind turbine experiences a wide variation of centripetal or centrifugal force acting on the rotor, and hence, requires the electromagnetic-mechanical stress analysis of the SRG. For low wind speed centripetal load is less, but to have better electromagnetic performance, the design of the rotor should be such that the  $q$  – axis inductance reduces and the  $d$  – axis inductance increase [14], but this can be achieved by a decrease in the thickness of radial and tangential ribs. The design based on the reduced thickness of axial and tangential ribs leads towards high stress on the ribs, and hence, is not suitable for high speed. Hence, a trade-off between electromagnetic and mechanical stress performances with the variation of wind speed is required to validate the design.

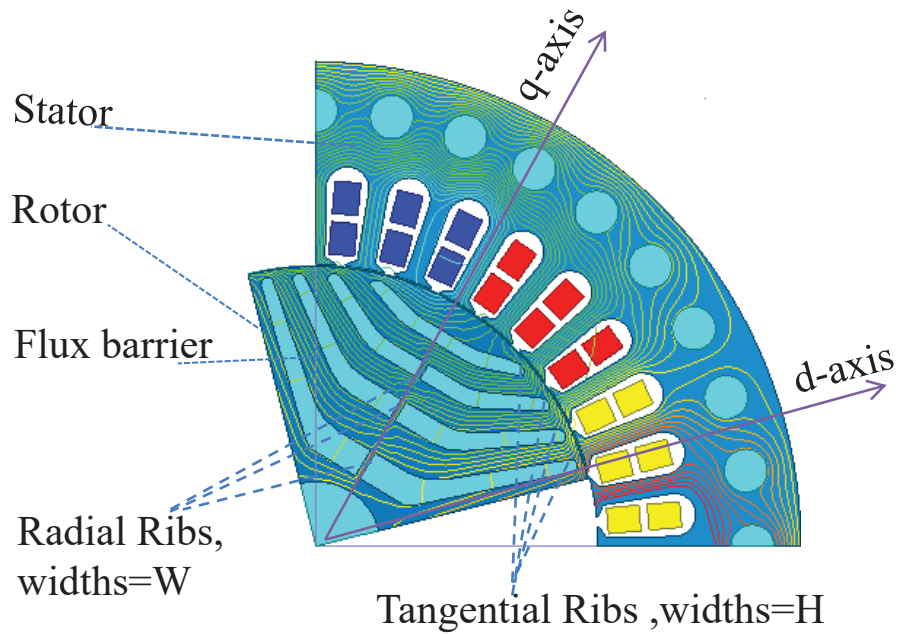


**Figure 4.1:** Structural, cross-section and  $dq$  – axes rotor reference frame of SRG.

It is observed from the literature review that the electromagnetic-mechanical analysis of SRG rotor design with the variation of wind speed in self-excited mode is not covered in the available literature. Therefore, this Chapter focuses on the trade-off between mechanical and electromagnetic performances with the variation of wind speed and thickness of tangential and radial ribs. The finite element analysis (FEA) is used for both mechanical stress analysis and electromagnetic analysis. The considered SRG has been designed for producing  $12.75 \text{ Nm}$  of torque at  $1500 \text{ rpm}$  equal to  $2.1 \text{ kW}$  with the efficiency of  $86.95\%$ , with a stator fill factor of  $50\%$ , is shown in Fig. 4.1.

## 4.2 Machine design parameters and problem statement

### 4.2.1 Design specification and parameters

The geometrical dimension and specifications of the SRG are summarized in Tables 2.1, and 2.4 of Chapter 2. The air gap length is fixed to the range, as allowed by the manufacturer ( $l_g = 0.35$  to  $1.0 \text{ mm}$ ). It is important to note that as the air gap length increases, the torque and power factor decreases ( $l_g \sim 1/L_d$ ) [14, 40]. While designing the machine, it is common to use distributed windings, to reduce the harmonic content of the stator emf, which negatively

#### 4. ELECTROMAGNETIC-MECHANICAL STRESS ANALYSIS OF SRG FOR WIND ENERGY APPLICATION

---

impacts the reluctance torque and the core losses [71]. The present design has four poles, and the design procedure can be extended for more number of poles. For a better design, in terms of iron losses, torque ripple, and mechanical strength, typically the number of flux barrier are approximately half of the number of slots per pole. Hence, the present design uses five flux barriers per pole with 36 stator slots as shown in Fig. 4.1.

The detailed sizing, and design procedure of the SRG start by assigning the initial key parameters of the wind turbine such as speed, and maximum torque. The analysis of the machine and its designed parameters are summarized in Tables 2.1, and 2.4. The present work includes the mechanical stress analysis of the designed machine with varying rotor speeds. It also provides a study on its influence on the rotor design of SRG. Here, the stator is assumed to be fixed in all cases.

##### 4.2.2 Rotor parameterizations

The parameterizations of different kinds of rotor flux barrier have been given in references [48, 72, 73]. All the findings show that the flux barrier and tangential ribs structure plays an important role in torque ripple minimization, and maximization of average torque [74]. Mostly, it is observed that the performances could be improved by using complex design, i.e., increasing the number of bridges, etc, but the complex design significantly increases the cost of production, difficult to manufacture, and also involves a high cost for its design [73, 75]. Hence the present work has used only four poles and few flux barriers as shown in Fig. 4.1. Every flux barrier is consists of trapezoid shape segments and is identified by the tangential thickness  $H$ , radial thickness  $W$ , and the end point angle at the air gap,  $\alpha_m$  which assures the structural integrity at high-speed, as shown in Fig. 4.2. The expression for maximum rotor tips mechanical end point angle  $\alpha_m$ , in terms of number of barriers ( $k_i$ ), poles pair (P) and floating angle ( $\beta$ ) as in equation (2.9) [76].

In spite of the many advantages of SRG, care must be taken while designing the rotor of SRG for high wind speed. It is important to ensure that the machine is mechanically stable, and produces more electromagnetic torque with minimal ripples.

### 4.3 Analysis of electromagnetic performance

The electromagnetic performance of SRG rotor can be improved by minimizing the reluctance of the  $d$ -axis,  $\mathfrak{J}_d$  and maximizing the reluctance of the  $q$ -axis,  $\mathfrak{J}_q$ . The ratio of  $d$ -axis inductance to the  $q$ -axis inductance (saliency ratio) is usually defined using the orthogonal axis inductances,  $L_d \sim 1/\mathfrak{J}_d$  and  $L_q \sim 1/\mathfrak{J}_q$  [48]. This inductance ratio is denoted as  $\xi_1$ , as given below:

$$\xi_1 = \frac{L_d}{L_q} \quad (4.1)$$

or the saliency ratio can be expressed as:

$$\xi_1 = \frac{X_d}{X_q} \quad (4.2)$$

For better electromagnetic performance, this ratio needs to be large. It is observed that by reducing the thickness of ribs (i.e., for both radial and tangential ribs), as shown in Fig. 4.4, 4.5, the inductance ratio ( $\xi_1$ ) tends to increase, but at the same time the mechanical stress tends to increase, hence, a design choice needs to be made between these conflicting objectives. Fig. 2.8(b) and 4.2 show the variation of  $d$  and  $q$ -axes inductances with respect to the change of  $q$  and  $d$ -axes currents and thickness of tangential and radial ribs, respectively. These plots are associated with the rotor cross-section, with the radial rib thickness ( $W = 1 \text{ mm}$ ) and tangential ribs thickness ( $H = 1.2 \text{ mm}$ ), respectively. The curves obtained from the experimental setup and FEA can be distinguished by the smoothed and orange-dotted lines as presented in Fig. 2.8(b). The  $L_d$  of the SRG keeps increasing for low values of current. However, as the current becomes approximately more than  $5 \text{ A}$ , the value of  $L_d$  starts decreasing and attains a constant value because of the magnetic saturation. While the  $L_q$  of SRG is high for the low value of current due to the presence of bridge in  $q$ -axis, it decreases gradually with the increase of current and subsequently becomes constant.

The important point to note that in the designed SRG, the thickness of tangential and radial ribs (see Fig 4.3) plays an important role in controlling the  $q$ - and  $d$ -axis fluxes, hence, control

#### 4. ELECTROMAGNETIC-MECHANICAL STRESS ANALYSIS OF SRG FOR WIND ENERGY APPLICATION

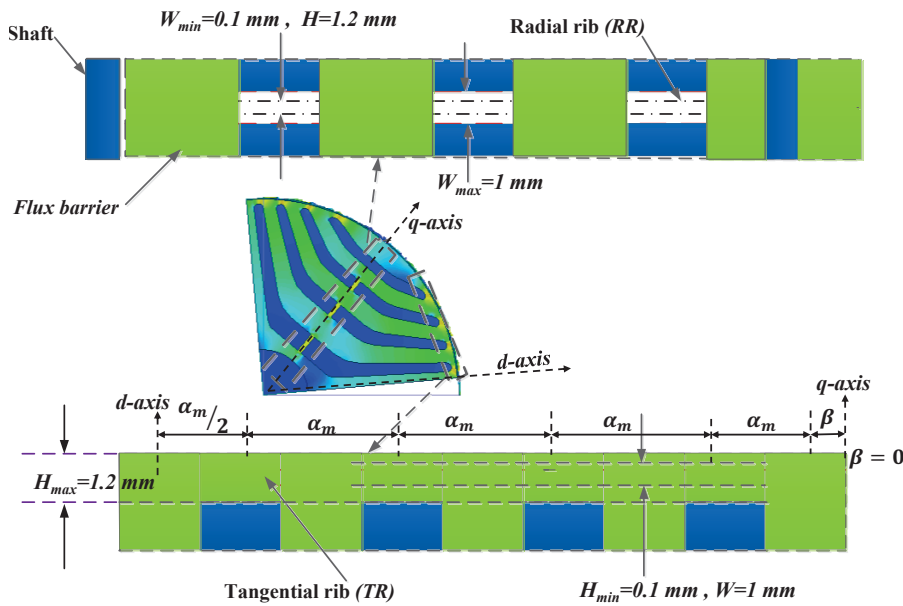


**Figure 4.2:** Rotor cross section view: radial and tangential ribs thickness.

the associated inductances. Fig. 4.4, shows the effect of variation in tangential rib thickness on

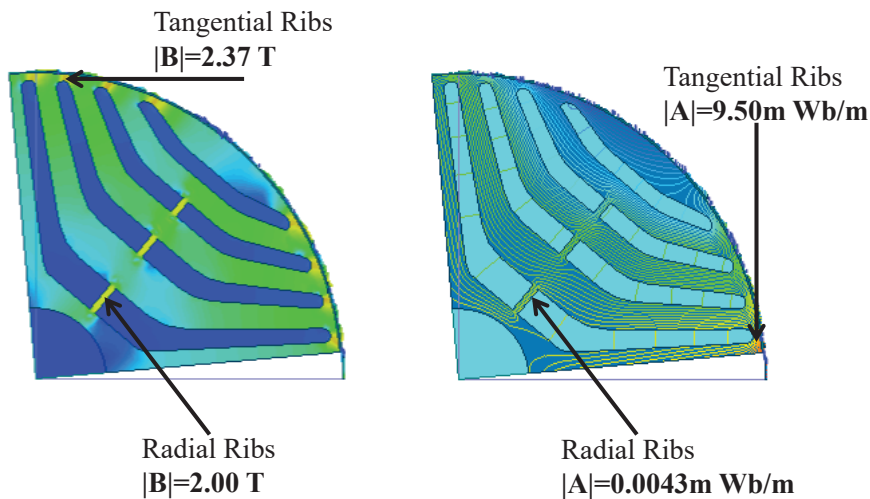
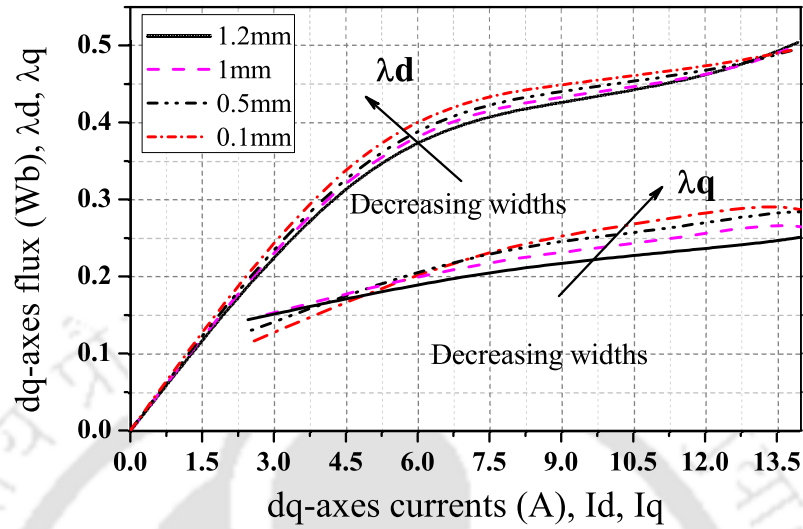


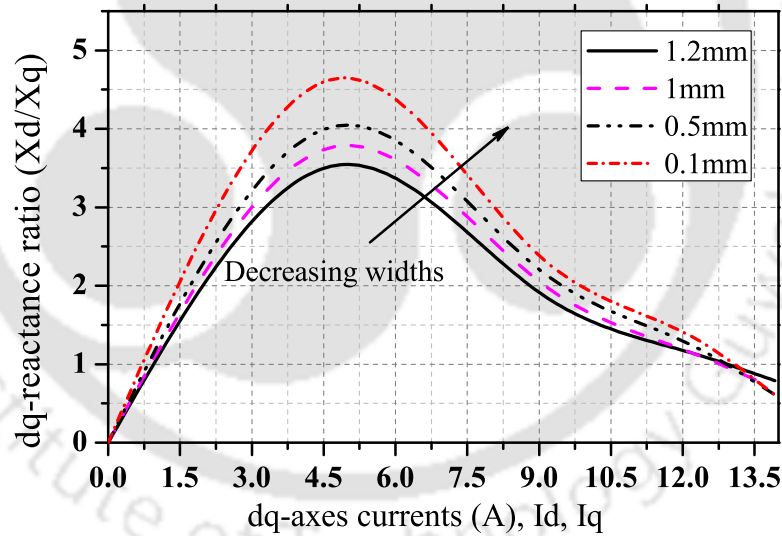
**Figure 4.3:** Magnetic field density and flux lines plot showing ribs saturation.

$d$ - $q$  axis fluxes, the ratio of  $d$  and  $q$ -axis inductances and reactance while keeping the thickness of radial ribs to a value of  $W_{max} = 1 \text{ mm}$ . From Fig. 4.4(a), it is observed that as the thickness of tangential rib is reduced, the value of  $\lambda_d$  slightly increases, whereas, the value of  $\lambda_q$  decrease till the ratio of  $(X_d/X_q)$  is maximum, as shown in Fig. 4.4(b) (i.e., as the core start saturation, the influence of  $I_q$  is more). Similarly, the plot of  $d$  and  $q$  - axis inductances is shown in Fig.

4.5(a). It is also observed that as the core start getting saturated, there is a decrease in  $(X_d/X_q)$



(a)



(b)

**Figure 4.4:** (a)  $d$ - and  $q$ -axes flux linkages magnetizing curve with tangential rib widths. (b)  $d$ - and  $q$ -reactance ratio with tangential rib widths.

ratio. Fig. 4.5(b), and 4.6 show the effect of variation in radial rib thickness on  $d-q$  axis fluxes, the ratio of  $d$  and  $q$  axis inductances and reactants while keeping the thickness of tangential ribs to a value of  $H_{max} = 1.2 \text{ mm}$ . From Fig. 4.5(b), it is observed that as the thickness of radial rib is reduced, the value of  $\lambda_d$  slightly increases, whereas, the value of  $\lambda_q$  decrease till the ratio of  $(X_d/X_q)$  is maximum, as shown in Fig. 4.6(a). Similarly, the plot of  $d$  and  $q$  axis inductances is shown in Fig. 4.6(b). It is also observed from Fig. 4.4, 4.5, 4.6 that the effect of variation

#### 4. ELECTROMAGNETIC-MECHANICAL STRESS ANALYSIS OF SRG FOR WIND ENERGY APPLICATION

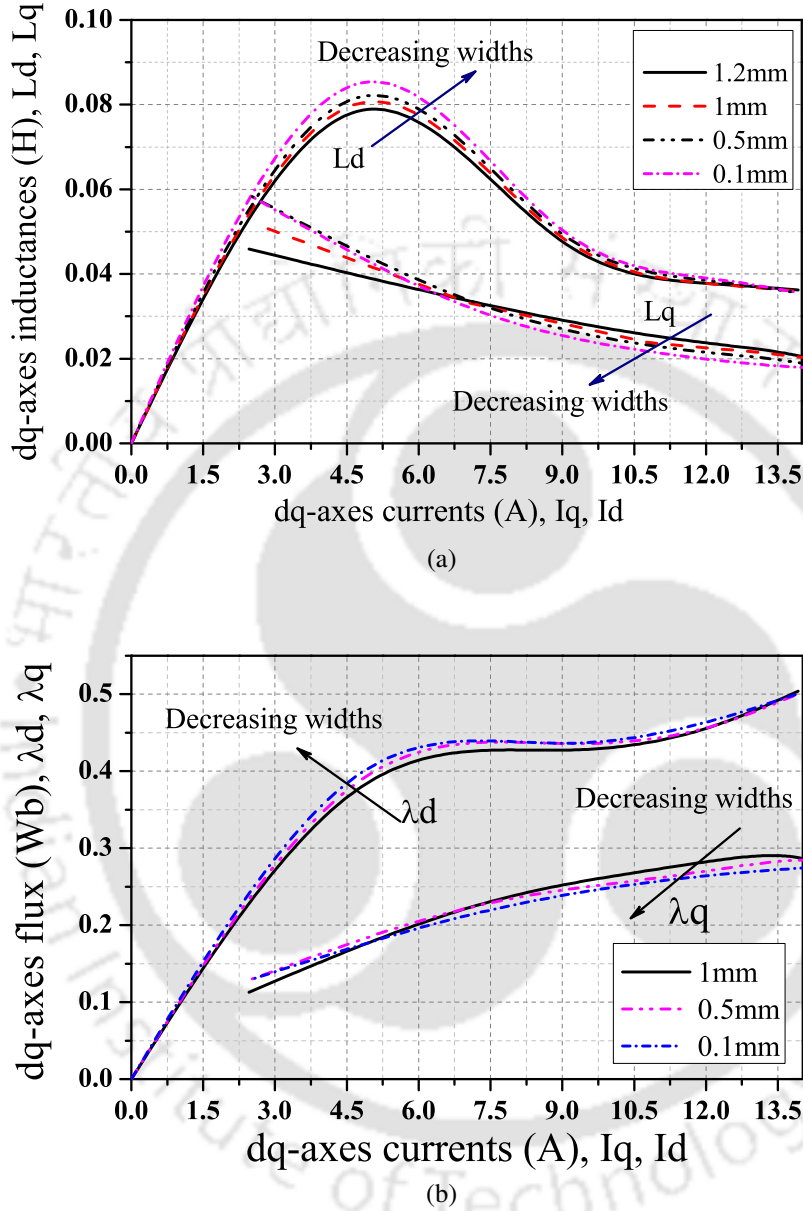
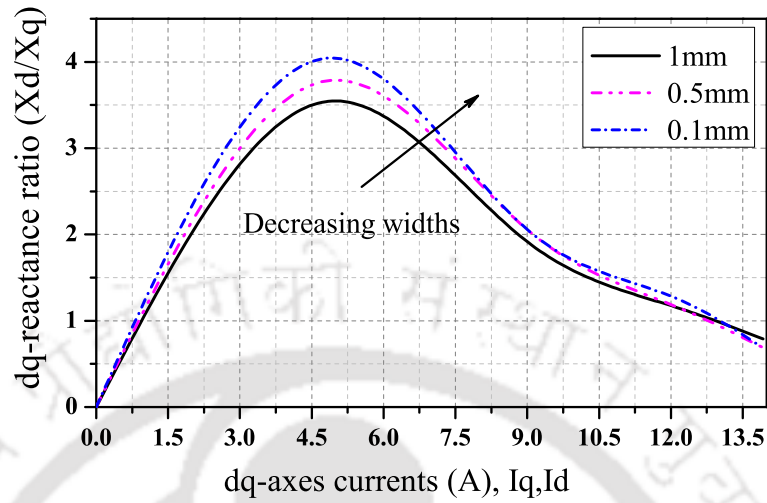


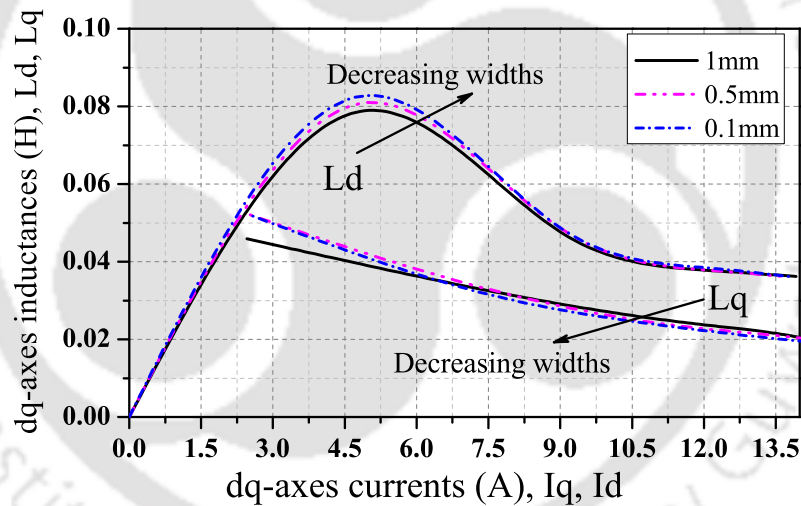
**Figure 4.5:** (a)  $d$ - and  $q$ -inductances with tangential rib widths. (b)  $d$ - and  $q$ -axes flux linkages magnetizing curve with radial rib widths.

on inductance is more with the change in thickness of tangential ribs, as compared with the variation in thickness of radial ribs.

In summary, the tangential and radial ribs should be small enough to produce good electromagnetic performance, i.e., to reduce the  $q$  – axis inductance and maximize the  $d$  – axis inductance (increasing reluctance torque), but the mechanical stress in the ribs should be below the centripetal loading.



(a)

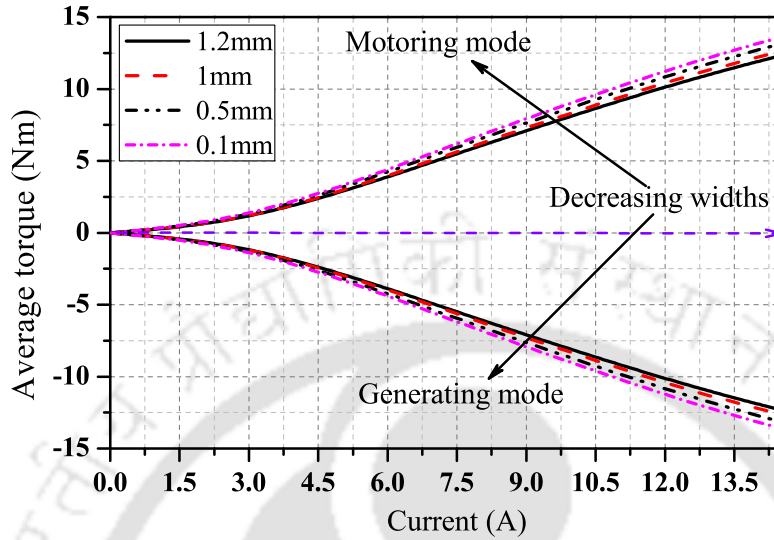


(b)

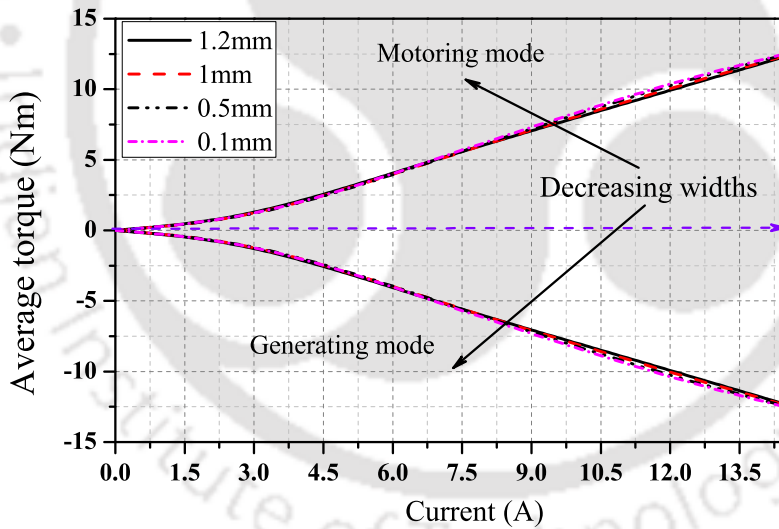
**Figure 4.6:** (a)  $d$ - and  $q$ -reactance ratio with radial rib widths. (b)  $d$ - and  $q$ -inductances with radial rib widths.

Fig. 4.7(a) shows that the performance of machines in motoring and generating mode. Fig. 4.7(a), the effect of reducing tangential rib i.e., with rib thickness 1.2 mm, 1 mm, 0.5 mm and 0.1 mm is shown while keeping the thickness of radial ribs to a value of  $W_{max} = 1$  mm. It is observed that as the thickness of tangential rib reduces, the torque increase in motoring and generating modes, as shown in Fig. 4.7(a), mainly because the magnetic flux flowing outward from the rotor  $q$ -axis reduces, hence, reducing the value of  $L_q$ . Similarly, in Fig. 4.7(b), the effect of reducing radial rib width i.e., with rib thickness 1.2 mm, 1 mm, 0.5 mm and 0.1 mm

#### 4. ELECTROMAGNETIC-MECHANICAL STRESS ANALYSIS OF SRG FOR WIND ENERGY APPLICATION



(a)

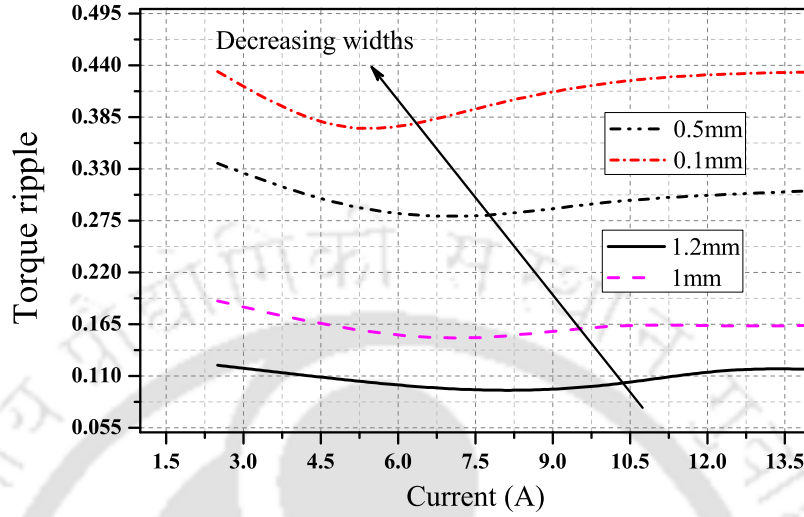


(b)

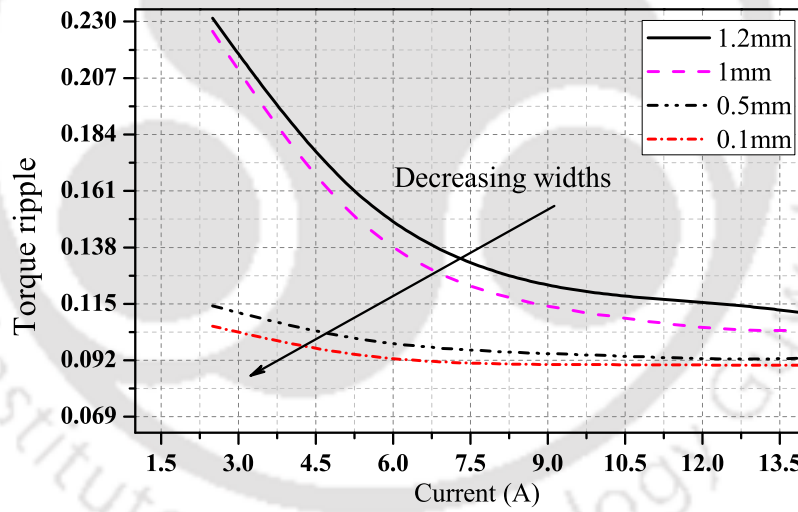
**Figure 4.7:** (a) Average torque-current profile of SRG curve with tangential rib widths. (b) Average torque-current profile of SRG curve with radial rib widths.

is shown while keeping the thickness of tangential ribs to a value of  $H_{max} = 1.2 \text{ mm}$ . It is observed that as the thickness of the radial rib reduces, the torque slightly increase in motoring and generating modes, as shown in Fig. 4.7(b), mainly due to the reduction of magnetic flux in  $q - axis$ . However, it is observed that the effect of radial ribs width variations on torque is not much as compared with the variation of tangential rib widths. From Figs. 4.7(a) and 4.7(b),

it is observed that the average torque is a function of square of stator current till the current



(a)



(b)

**Figure 4.8:** (a) Torque ripple percentage curve with tangential rib widths. (b) Torque ripple percentage curve with radial rib widths.

of the machine is 5A. However, after 5A the difference between  $(L_d - L_q)$  is approximately constant as seen from Fig. 4.7, hence, the variation of average torque is observed to be linear. The influences of the tangential rib width on torque ripple while keeping the thickness of radial ribs to a value of  $W_{max} = 1 \text{ mm}$  are shown in Fig. 4.8(a). From Fig.4.8(a) it can be observed that the torque ripple increases by reducing the tangential rib thickness. Similarly, the effect on torque ripple for the variation of radial rib thickness while keeping the thickness of tangential

## 4. ELECTROMAGNETIC-MECHANICAL STRESS ANALYSIS OF SRG FOR WIND ENERGY APPLICATION

---

ribs to a value of  $H_{max} = 1.2 \text{ mm}$  is shown in Fig. 4.8(b). It is observed, that the torque ripple,  $(T_{max} - T_{min})/T_{av}$ , decrease by reducing the radial rib thickness. When the radial rib width is reduced, both the magnetic and air reluctance layers increase for q-axis flux, that causes  $L_q$  to reduce, while  $L_d$  almost remains constant or slightly change.

### 4.4 Analysis of mechanical performance

From the analysis of electromagnetic performance, as discussed in the previous section, it is observed that for better electromagnetic performance, the thickness of ribs need to be reduced, but as these ribs also provide mechanical strength to the rotor, it is important to know the stress in these ribs, under the influence of centripetal force, and check whether the stress is within the permissible limit.

#### 4.4.1 Centripetal force on flux barriers

It can be seen from Fig. 4.1, that mainly the radial ribs, support the flux barriers together under influence of centripetal force while operating at variable speed. The flux guides lamination has a mass of [40]:

$$M_a = \rho_{ir} L_s \iint dA \quad (4.3)$$

where,  $L_s$  is the stack length,  $\iint dA$  is the cross-section area of the flux barriers, which has a complex shape, and  $\rho_{ir}$  is the density of lamination material. When the generator is operating with the rotational speed of  $\omega$ , the centripetal force acting towards the center of the rotor (i.e., normally) with radius  $R$  at the surface of the rotor is given as:

$$f = M_a R \omega^2 \quad (4.4)$$

The yield strength  $\delta_y$ , is the stress above which the material become plastic, and hence, the stress on a rotor must be below the yield strength of the material used in the design of rotor. From, equation (4.4), it can be observed that the stress on the rotor is a function of  $\omega^2$ . Usually, the stress must be less than yield strength with an acceptable safety factor while designing and/or sizing the tangential and radial ribs.

The lamination material (50C350 – AP)/(M19) is used in the design of the rotor for SRG, which has average yield strength of 310 *Mpa*, and the lamination density of 7600 *kg/m<sup>3</sup>*. The commonly used safety factor  $S_f$  is given as per the equation below:

$$S_f = \frac{\delta_y}{\sigma_p} \quad (4.5)$$

where,  $\delta_y$  is the average yield strength of the material,  $\sigma_p$  is the stress on the rotor. Fig. 4.9 shows the distribution of mechanical stress at different parts of SRG rotor, rotating at 1500 *rpm* using finite element analysis (FEA). The peak stress observed at the critical points of the rotor are reported as in Fig. 4.9, and can be observed that the ribs are highly stressed. To provide the quantitative analysis, Table 4.1, and 4.2 provides the details about peak stress observed in ribs i.e., in tangential ribs indexed as 1,2,3 and 4 i.e.,  $TR_{1,2,3,4}$  and radial ribs index as 1,2, and 3 i.e.,  $RR_{1,2,3}$ . The results shown in Table 4.1 corresponds to the rotor rotating at 1500 *rpm*, with the simultaneous variation in thickness of both tangential ribs (TR) and radial ribs (RR) by same thickness i.e., the thickness of both TR/RR is same and varies from 1.2 *mm* to 0.1 *mm*. The Table also provides a stress factor (SF), centripetal force at the surface of the rotor (f), average torque ( $T_{av}$ ), and percentage torque ripple ( $T_{rip}$ ). Similarly, Table 4.2 provides the similar analysis for rotor rotating at 2500 *rpm*, i.e., 60% over the rated speed of 1500 *rpm*. From Table 4.1 it is observed that the design is suitable for tangential and radial ribs thickness at the rotor speed of 1500 *rpm*. While, Table 4.2 shows the tangential and radial thickness is not suitable at speed of 2500 *rpm* for 0.1 *mm*. The stress factor (SF) on the ribs given as:

$$SF = \sum_{i=1}^{Nb} \left| \sigma_p^i - \sigma_{tar} \right| \quad (4.6)$$

where, Nb is total number of tangential and radial ribs,  $Nb = 7$ ,  $\sigma_p^i$  is peak stress on  $i^{th}$  rotor rib,  $\sigma_{tar}$  is stress target that usually taken to be as 80% of yield strength.

#### 4.4.2 Tangential and radial rib thickness

This section analysis the effect on stresses estimated for SRG with simultaneous variation in thickness of both tangential ribs (TR) and radial ribs (RR) by same thickness. For the estimation of stress, the present work uses finite element analysis (FEA). From Fig. 4.9, it could

#### 4. ELECTROMAGNETIC-MECHANICAL STRESS ANALYSIS OF SRG FOR WIND ENERGY APPLICATION

**Table 4.1:** Mechanical performance (Von Mises stress, centripetal force, stress factor) of peak stress and Electromagnetic performance (torque and ripple) of the designed rotor speed of 1500 rpm

Thickness ( $TR/RR$ ) →	1.2 mm	1 mm	
Parameters	Peak stress	Peak stress	Unit
$TR_{1,2,3,4}$	38	57	$Mpa$
$RR_{1,2,3}$	23	34	$Mpa$
$SF$	1515	1406	$Mpa$
$f$	908	902	$N$
$T_{av}$	12.28	12.63	$Nm$
$T_{rip}(\%)$	11	16	–
Thickness ( $TR/RR$ ) →	0.5 mm	0.1 mm	
Parameters	Peak stress	Peak stress	Unit
$TR_{1,2,3,4}$	72	172	$Mpa$
$RR_{1,2,3}$	65	245	$Mpa$
$SF$	1253	313	$Mpa$
$f$	890	880	$N$
$T_{av}$	13.41	14.08	$Nm$
$T_{rip}(\%)$	26	36	–

**Table 4.2:** Mechanical performance (Von Mises stress, centripetal force and stress factor) of peak stress and Electromagnetic performance (torque and ripple) of the designed rotor speed of 2500 rpm

Thickness ( $TR/RR$ ) →	1.2 mm	1 mm	
Parameters	Peak stress	Peak stress	Unit
$TR_{1,2,3,4}$	98	146	$Mpa$
$RR_{1,2,3}$	69	88	$Mpa$
$SF$	1137	888	$Mpa$
$f$	2323	2310	$N$
$T_{av}$	12.20	12.50	$Nm$
$T_{rip}(\%)$	9	13	–
Thickness ( $TR/RR$ ) →	0.5 mm	0.1 mm	
Parameters	Peak stress	Peak stress	Unit
$TR_{1,2,3,4}$	184	440	$Mpa$
$RR_{1,2,3}$	168	565	$Mpa$
$SF$	496	1719	$Mpa$
$f$	2277	2270	$N$
$T_{av}$	13.40	14.05	$Nm$
$T_{rip}(\%)$	27	37	–

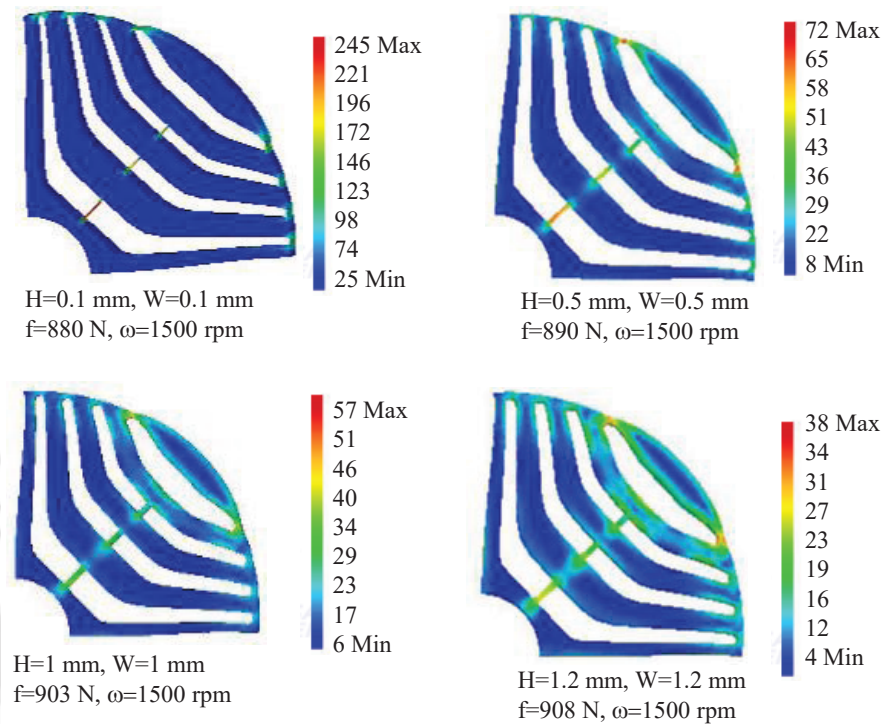


**Figure 4.9:** Von Mises stress distributions (Mpa) of designed rotor with ribs widths variation (minimum=0.1 mm to maximum=1.2 mm)

be observed that ribs i.e., tangential or radial are the ones that are associated with high stress as compared with other parts of the rotor. Hence, this section analyses the stress at tangential and radial ribs in detail. Fig. 4.10(a), show the stress experienced by the tangential rib of different widths with the variation of centripetal force. Similarly, Fig. 4.10(b), shows that the stress observed at the radial rib. From the results, it can be observed that the stress reduced with increasing ribs width. It is also observed that the variation of stress with an increase in centripetal force is approximately linear.

Fig. 4.11(a) provides the plot associated with the stress in tangential ribs of thickness varying from 0.1 mm to 1.2 mm. It is observed that as the ribs thickness decrease, the stress in tangential rib increase. It is also observed that the increase in stress on tangential ribs is approximately quadratic to the variation of rotor speed. Fig. 4.11(b), provides a plot of safety factors in the tangential rib with different widths vs rotor speed. The zoomed version of the plot shows the yield strength line corresponding to the safety factor of 1, but it is common to take a safety factor of 2.5 for most of the design, hence, the present work also uses a safety factor of 2.5, as

**4. ELECTROMAGNETIC-MECHANICAL STRESS ANALYSIS OF SRG FOR WIND ENERGY APPLICATION**

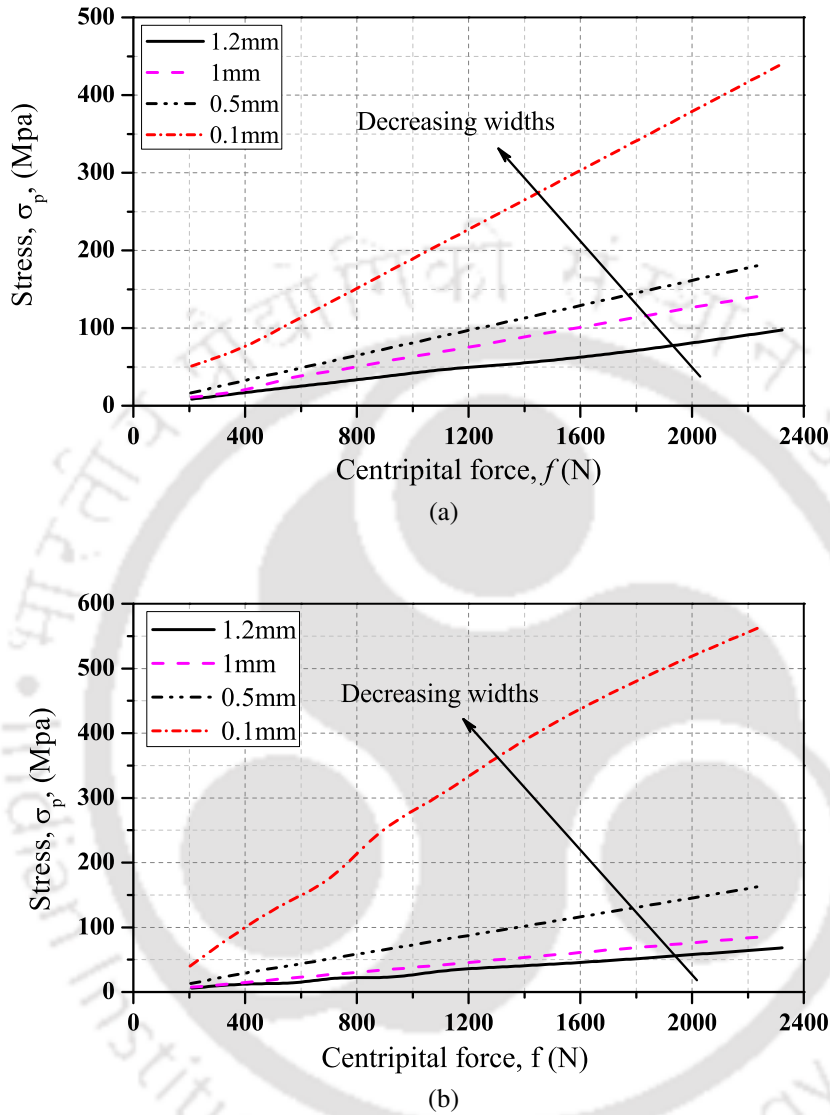


**Figure 4.10:** (a) Stress at tangential rib with different widths vs centripetal force. (b) Stress at radial rib with different widths vs centripetal force.

shown by a dashed line in the plot. It can also be observed that a thickness of 1.2 mm or more is required to provide mechanical stability of the tangential rib.

Similarly, Fig.4.12(a) provides the plot associated with the stress in radial ribs of thickness varying from 0.1 mm to 1.2 mm. It is observed that as the ribs thickness decrease, the stress in radial rib increase. It is also observed that the increase in stress on radial ribs is approximately quadratic to the variation of rotor speed. Fig. 4.12(b), provides a plot of safety factor in the radial rib with different widths vs rotor speed. It can also be observed that a thickness of radial

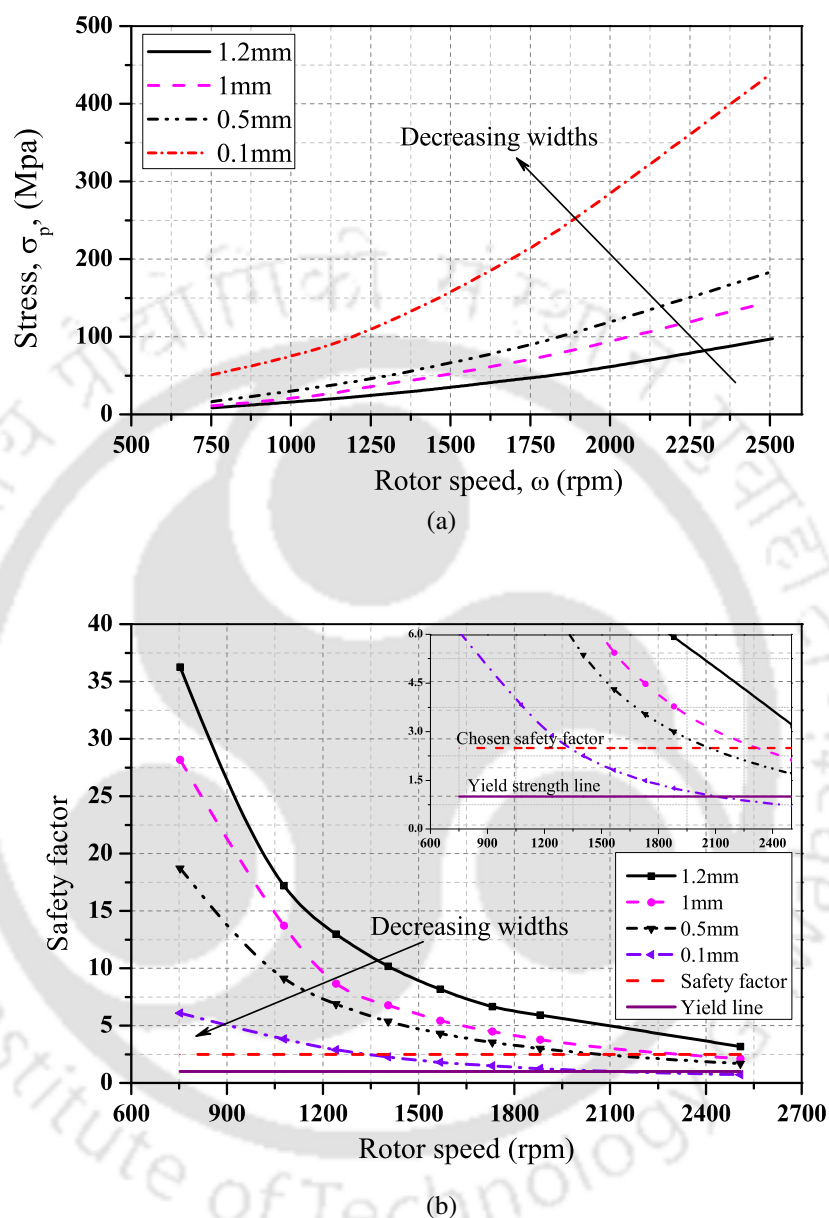


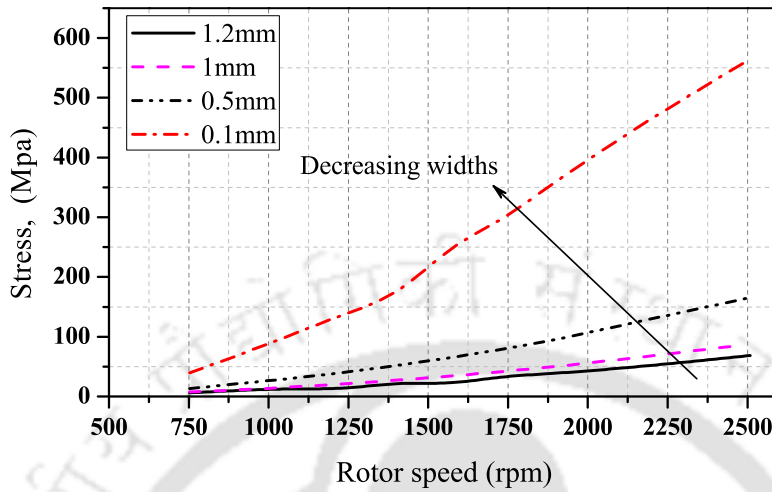
**Figure 4.11:** (a) Stress at tangential rib with different widths vs rotor speed. (b) Safety factor of tangential rib with different widths vs rotor speed

rib should be more or equal to 1.0 mm for ensuring mechanical stability of the ribs.

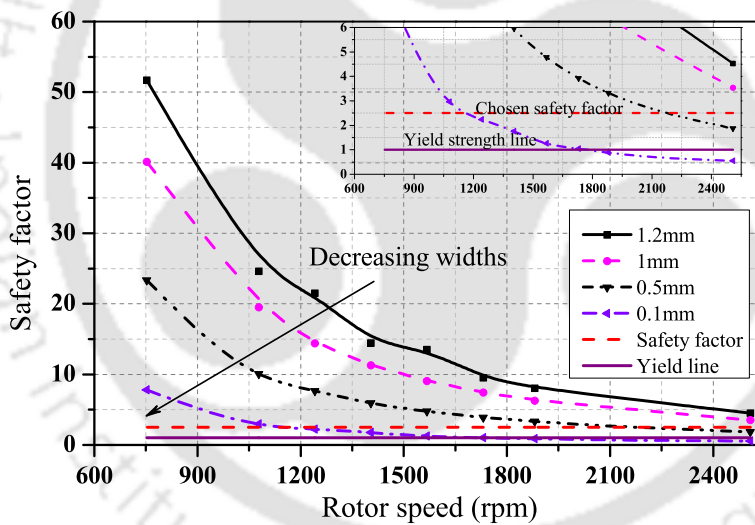
## 4.5 Summary

The electromagnetic-mechanical stress analysis of SRG for a rotor with transverse lamination are evaluated. The work mainly discuss how the thickness of ribs affect the electromagnetic performances of the machine i.e., it is observed that with decrease in the thickness of both radial or tangential ribs, there is an increase in the inductance ratio, which reaches to its peak value

#### 4. ELECTROMAGNETIC-MECHANICAL STRESS ANALYSIS OF SRG FOR WIND ENERGY APPLICATION



(a)



(b)

**Figure 4.12:** (a) Stress at radial rib with different widths vs rotor speed. (b) Safety factor of radial rib with different widths vs rotor speed

near to its rated current, and then there is a decrease in this ratio due to the effect of saturation in the core. Further, the mechanical stress analysis is done to find the minimum thickness of the ribs which could ensure mechanical stability. It is also observed that the maximum stress is either at tangential ribs or radial rib of the SRG rotor. To ensure the mechanical stability, a safety factor of 2.5 is used in the present work while suggesting the minimum thickness of the tangential ribs and radial ribs are 1.2 mm, and 1 mm, respectively.



#### 4. ELECTROMAGNETIC-MECHANICAL STRESS ANALYSIS OF SRG FOR WIND ENERGY APPLICATION

---



# 5

## EFD AND IFD THERMAL MODELING OF SELF-EXCITED SRG FOR WIND ENERGY APPLICATION

### Contents

---

5.1	Introduction . . . . .	116
5.2	Heat sources calculation of SRG . . . . .	117
5.3	Lumped parameter model, and the use of EFD and IFD to estimate the temperature rise. . . . .	118
5.4	Thermal analysis of SRG using 3D FEA . . . . .	141
5.5	Experimental verification of the results . . . . .	143
5.6	Summary . . . . .	149

---

### 5.1 Introduction

In recent times, the literature suggests to use synchronous reluctance generators (SRG) in the wind energy applications because of its ruggedness, no copper loss in the rotor, high power density, compactness, cost-effectiveness, low maintenance and easy to assemble. Even though it has many advantages, some failure is observed due to thermal overloading and insulation breakdown. O'Donnell P. identified that a large number of machine failures are due to the temperature overloading of the various machine components [41]. Nearly, 45% of the induction generator failures are associated with failure of insulation of copper winding and iron core [2, 41–43]. In most cases, the excessive temperature rise is observed at the end region of the copper windings as compared to other parts of the generator. Tallam R.M. et al. reported that the rise in temperature, which slowly degrades the quality of insulation is the main cause of generators failures [44]. These types of failures can severely affect the generation capability of the distributed generation. Moreover, it also increases the financial cost associated with the maintenance and replacement of the machine.

The National Electrical Manufacturers Association (NEMA) provides the allowable temperature range for different types of insulation classes as given in Table 5.1. To prevent the thermal failure of the generator, it is important to appropriately select the insulation class for stator windings. The present design utilizes the insulation of *F* class as the rise of temperature of the component of the machine is less than  $105^{\circ}$ . This class of insulation could be used in generators with ratings in the range of a few kW to MWs. The choice of the class of the insulation may also change based on the atmospheric temperature.

To protect the machine from thermal overloading, a thermal analysis of the machine to know the heat transfer mechanism of different components of the generator is required. The thermal analysis of the generator is as important as its magnetic design and plays an important role in the design of the overload thermal protection system [77]. The previous research work on thermal analysis is mostly related to induction generators and ac synchronous generators. It is observed from the literature review that thermal analysis is based on finite element analysis (FEA) which is highly computational and complex. Therefore, this Chapter provides the thermal analysis of

**Table 5.1:** Limits of temperature for different insulation class in (°C) [1–3]

Insulation T.	Ambient T.	Hot spots tolerance	Allowable T. rise	Insulation Class
105	40	5	60	A
130	40	10	80	B
155	40	10	105	F
180	40	15	125	H
Over 189	40	15	Over 134	C

SRG using 3D time-dependent Finite Element Analysis (FEA), Explicit finite difference (EFD), and Implicit Finite finite difference (IFD) to fill the gap in the available literature.

The EFD and IFD methods are techniques used in numerical analysis to obtain numerical approximations to the solution of time dependent partial differential equations. The EFD method calculate the state of the systems at a later time from the inial condition of the system at the present/current time. It uses forward and central difference, while IFD method find out the solution by solving the equation involving both the later one and the current time of the system. i.e.,it uses backward and central difference [78].

The Chapter, covers the thermal modeling of the 2.1 kW self-excited SRG, which is modeled and designed through a finite element analysis (FEA). The developed models of the designed SRG represented in Fig. 5.1. The losses of different parts of the generator where estimated in Chapter 2, which act as heat sources in the machine. The thermal analysis is done using a explicit and implicit models and compared with 3D time-dependent FEA model. The results are also validated through the experimental test on the developed machine.

## 5.2 Heat sources calculation of SRG

The core loss, copper loss, core weights and detail calculation of parameters are given in Chapter 2, which gives approximate heat source of the SRG. The core losses mainly depend on the magnitude of the stator flux, the rotor flux density, and the frequency of output voltage. It is observed that the stator windings and stator end windings losses are the primary heat sources for the copper losses. These losses are parameterized as the heat sources in the thermal modeling of SRG.

Table 5.2 summarizes various losses of the machine, which are used to approximate the

**5. EFD AND IFD THERMAL MODELING OF SELF-EXCITED SRG FOR WIND ENERGY APPLICATION**

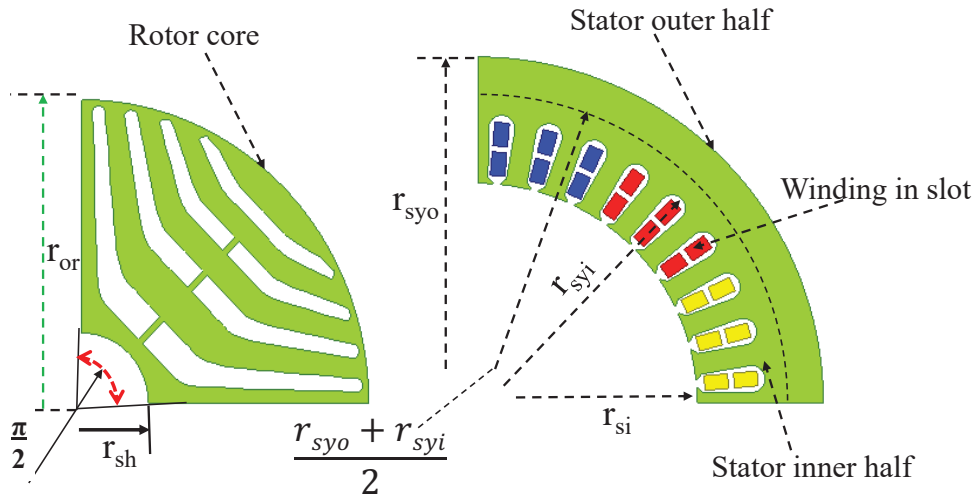


**Figure 5.1:** Rotor and stator structure of SRG.

**Table 5.2:** Loss analysis of the 2.1 kW SRG for rated wind speed

Wind speed (m/s)	Rotor Speed (rpm)	Losses	Watt
10	1500	Stator copper	274.0
		Stator teeth core	3.762
		Stator core	6.480
		Rotor core	3.626
		Total losses	287.868

temperature rise for different nodes of the thermal circuit. For low power rated machine, large eddy current can not be induced in the iron core, as it has very thin laminates. Thus, the core loss could be evaluated from machine parameters, and it is observed that the core losses are small, while copper loss due to the resistance of the wire in stator winding is large as shown in Table 5.2. These copper losses can be reduced by using wire with a large cross-section area in the construction of the coils [48].

**5.3 Lumped parameter model, and the use of EFD and IFD to estimate the temperature rise.**

There is a gap in the literature on the thermal modeling and heat flow modeling of an SRG used in wind energy applications. The widely used machines for thermal modeling are the induction generator and conventional synchronous generator. The present work extends the explicit, and implicit models for SRG. It uses the mesh of thermal resistance along with heat source, to model the various parts of the generator. Moreover, to test the accuracy of the model,

### 5.3 Lumped parameter model, and the use of EFD and IFD to estimate the temperature rise.

---

the results are compared with 3D FEA thermal model, which uses both axial and radial heat flow for various components in the generator [1, 35].

The explicit, the implicit thermal modeling, and 3D FEA are applicable for both steady-state and time-dependent thermal analysis of the machine. The explicit, and implicit consists of thermal capacitances and resistances/conductances. Besides, the thermal mesh model circuit includes the heat sources of the generator. In the model, different parts of the generator are represented as the nodes. And at each node, the presence of capacitance is associated with heat stored in the components of the generator. The presence of resistance in the model symbolizes the thermal resistance associated with the flow of heat between the various parts of the generator. Thus, by solving the explicit, and implicit equations model, it is possible to estimate the temperature rise for various components of the generator.

As the various heat sources and the different parts of the generator are radially placed at equidistant from the shaft of the generator and have laminations in the axial direction, it is reasonable to model only the radial flow of heat to get the temperature rise in the machine (since the difference is negligible, i.e., less than 0.6%). However, to further improve the accuracy of the model, the axial flow of heat for the shaft is also considered in the present work.

All the thermal resistances present in the model correspond to the heat flow by the various process, such as radiation, convection, and conduction in various parts of the generator, which are typically made of different materials.

The temperature at the thermal node of each location is given by  $\theta_a$  to  $\theta_l$ , and the ambient temperature is represented as  $\theta_{am}$ . The capacitors  $C_a$  to  $C_l$ , which are connected to the nodes, are used to represent the heat stored by various components of the machine, as shown in Fig.5.2. The model assumes that the heat is uniformly distributed in the generator from each heat source.

Finally, for each node, the energy balance principle is applied to compute the temperature rise at different locations of generator components. The equation (5.1), and (5.2) are energy balance equations of EFD, and IFD, respectively. The EFD and IFD approaches used to calculate incremental temperature rise for every  $\Delta t$  interval. Equation (5.1) uses direct computation of temperature rise at each node in terms of known quantities, while equation (5.2) find out the

## 5. EFD AND IFD THERMAL MODELING OF SELF-EXCITED SRG FOR WIND ENERGY APPLICATION

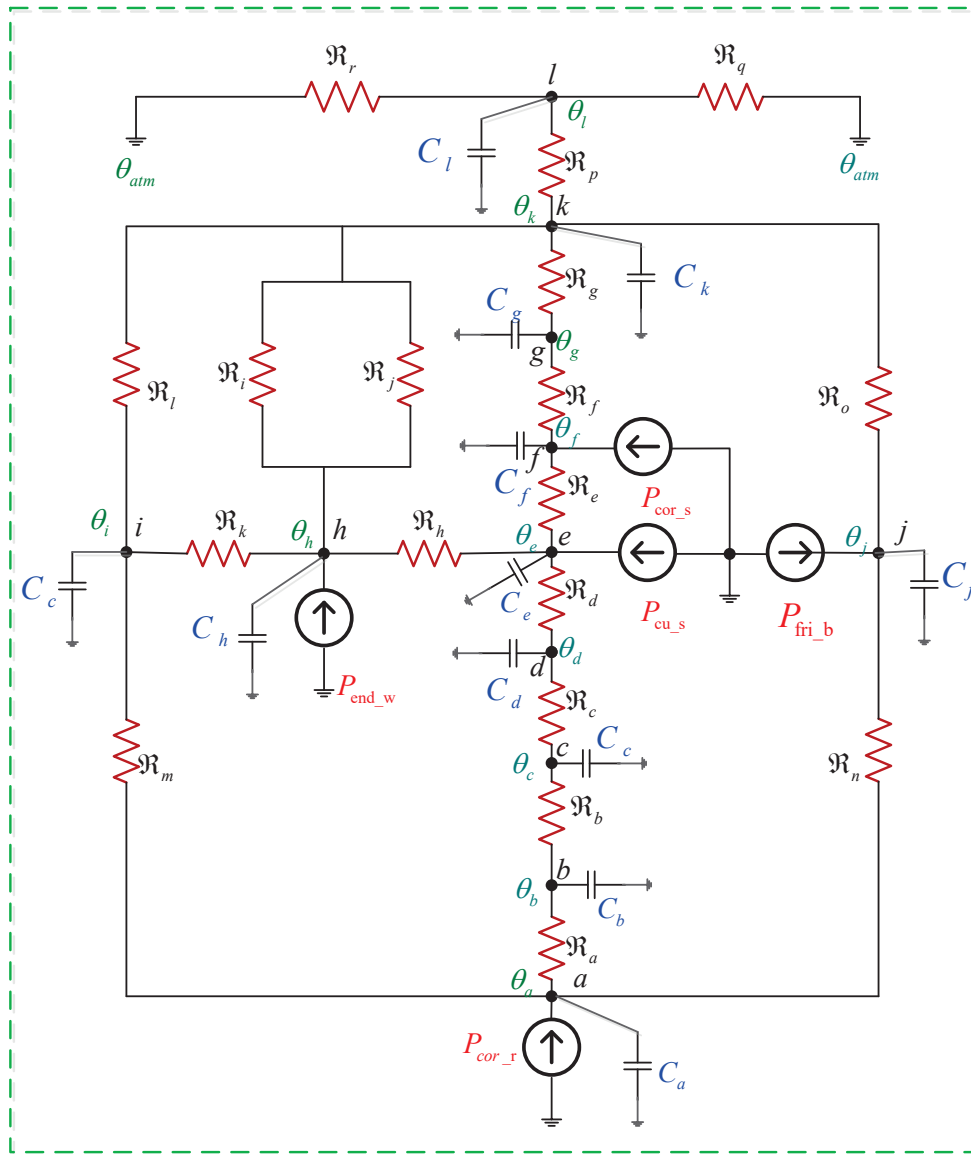


Figure 5.2: Thermal network model of SRG

temperature rise at each nodes by solving equation at current time  $t$  and later time  $t + 1$ . The general form of equations representing the model are as follows [79, 80]:

For explicit,

$$\theta^{p+1} = \theta^p + \frac{\Delta t}{\rho c V_{element}} \left( \sum_{Node} \theta^p + P_{gen-loss}^p \right) \quad (5.1)$$

and for implicit,

$$\theta^{p+1} = \theta^p + \frac{\Delta t}{\rho c V_{element}} \left( \sum_{Node} \theta^{p+1} + P_{gen-loss}^{p+1} \right) \quad (5.2)$$

where, the term  $\rho c V_{element}$  is equal to the thermal capacitance of the material ( $C = \rho c V_{element}$ ).

### 5.3 Lumped parameter model, and the use of EFD and IFD to estimate the temperature rise.

**Table 5.3:** Thermal properties for thermal capacitance and resistance calculation at room temperature [1,2]

Material	Thermal conductivity (W/m °C)	Specific heat capacity (J/kg °C)	Density (kg/m <sup>3</sup> )
<i>Aluminium</i>	202	920.48	2700
<i>Copper</i>	386	383	8954
<i>Iron</i>	73	452	7600
<i>Steel</i>	54	465	7833
<i>Air</i>	0.02624	1005	1.205

Similarly,  $V_{element}$  is the volume of material. The equation (5.1) and (5.2) is used to get the equation corresponding to the change of temperature at a particular node at each iteration, and is given as:

For explicit,

$$\frac{\theta^{p+1} - \theta^p}{\Delta t} = 1/C \left[ P_{gen-loss}^p + \theta_{cnv}^p + \theta_{rad}^p + \theta_{cnd}^p \right] \quad (5.3)$$

and, for implicit,

$$\frac{\theta^{p+1} - \theta^p}{\Delta t} = 1/C \left[ P_{gen-loss}^{p+1} + \theta_{cnv}^{p+1} + \theta_{rad}^{p+1} + \theta_{cnd}^{p+1} \right] \quad (5.4)$$

Here,  $\theta_{cnv}$ ,  $\theta_{cnd}$ ,  $\theta_{rad}$ ,  $\theta^p$ , and  $\theta^{p+1}$  are the temperatures associated with convection, conduction, radiation, temperature at time  $p\Delta t$ ,  $(p+1)\Delta t$ , respectively.

In (5.1) to (5.4),  $\theta_{cnv}$ ,  $\theta_{cnd}$ , and  $\theta_{rad}$ , are used to get the updated of  $\theta$ . Equation (5.3) and (5.4) represent a general equation to get an update of  $\theta$ , i.e., is used to get the updated value of  $\theta_a$  to  $\theta_i$ . Generator loss  $P_{gen-loss}$  in (5.1), is used to refer the losses, such as stator winding loss, rotor core loss, stator core loss, and other loss as given in Table 5.2. These losses are modeled as the thermal injection at nodes  $\theta_a$ ,  $\theta_e$ ,  $\theta_f$ ,  $\theta_h$ , and  $\theta_j$ , as shown in Fig.5.2. To evaluate, the temperature rise at a specific node, it is required to estimate the heat flow coefficient corresponding to the radiation, convection, and conduction for various components of the generator. The thermal parameters and material dimension of various parts of the generator are summarized in Tables 5.3, and 5.4, respectively. Here, emissivity ( $\epsilon$ ) of Iron and Aluminum is taken as 0.72, and 0.25, respectively.

## 5. EFD AND IFD THERMAL MODELING OF SELF-EXCITED SRG FOR WIND ENERGY APPLICATION

**Table 5.4:** Generator physical dimension data

Parts of the Generator	Values(mm)
Inner diameter of stator	105
Outer diameter of stator	165
Outer diameter of rotor	104
End winding outer radius	40.6
End winding inner radius	37
End winding axial length	127
Stack length	65
Air gap length	0.5
Shaft length	250
Air thickness between rotor and end caps	92.5
Frame fins length	84.5
Frame fins width	5.67
Lamination thickness	0.35
Frame length	84.5
Stator slot height	11.811
Frame fins height	7.45
Operating parameters of the generator	
Rated current (A)	9.5
Output Power (kW)	2.1
Phase voltage (V)	150
Stator winding resistance ( $\Omega$ )	1.0

### 5.3.1 Analytical solution of thermal conductance, capacitance, EFD and IFD methods

The temperature rises for a different section of the generator can be estimated by selecting the suitable modeling method (i.e., radial or combined radial-axial methods) and by calculating the thermal resistance and capacitance. The radial method provides a negligible difference compared to combined radial-axial method [2, 3, 81]. The error introduced by radial method is below 0.6% compared to combined radial-axial method. Hence, the simplified radial axis model is reasonably accurate and it involves less computational complexity.

The developed analytical model based on radial axis heat flow uses the following assumptions to simplify the calculation of parameters:

### 5.3 Lumped parameter model, and the use of EFD and IFD to estimate the temperature rise.

---

- Neglecting percentage increase for the field harmonics in stator, rotor, and mechanical losses.
- The thermal and electrical properties of the iron steel of different grades are assumed to be the same.
- The magnitude of flux density is assumed to be constant for the stator core, stator tooth, and the ribs of the rotor. i.e., each of these parts has different flux density, but for a particular region, the flux density is assumed to be constant.
- The effects of some variation in frequency due to the changing load are neglected.
- A generator symmetry is assumed cylindrical around the shaft, and radial plane via center.
- Each cylinder thermal is symmetrical in the radial direction.
- The heat flow in the axial direction is considered only in the shaft and is neglected in other parts of the machine.
- The calculated heat sources (losses) are uniformly distributed via the machine body.

#### 5.3.1.1 Estimation of temperature rise using calculated thermal conductance and capacitance

This subsection explains how the estimate of the temperature rise at each node is obtained using the calculated thermal conductance, and thermal capacitance (i.e, the temperature rise at assign nodes are evaluated from the thermal equivalent circuit as shown in Fig.5.2). The calculation of the thermal conductance and thermal capacitance is based on the parameter of the machine.

*a) Node a,  $\theta_a$ : Temperature rise in rotor core:* The temperature rise,  $\theta_a^{p+1}$  in rotor core can be estimated using the parameters  $K_a$ ,  $K_m$ ,  $K_n$ , and  $P_{cor-r}$ . The thermal capacitance,  $C_a$  in rotor core can be determine from machine parameters. Rotor core loss  $P_{cor-r}$  act as the heat source for the rotor which flows radially, i.e., from rotor core  $\rightarrow$  air gap  $\rightarrow$  stator lamination  $\rightarrow$  generator frame  $\rightarrow$  atmosphere, and axially from rotor end surface to central air. Henec, the  $\theta_a$  i.e., the

## 5. EFD AND IFD THERMAL MODELING OF SELF-EXCITED SRG FOR WIND ENERGY APPLICATION

temperature at the core can be expressed using the references [2, 3, 81, 82]. Using equations (5.1), and (5.2) an explicit and implicit temperature equations for each nodes ( $a$  to  $l$ ) is derived, and the final results are as follow:

$$\begin{cases} \theta_a^{p+1} = \theta_a^p \left[ 1 - \Delta t \varepsilon_a (K_a + K_m + K_n) \right] + \Delta t \varepsilon_a (P_{cor-r})^p \\ + \Delta t \varepsilon_a \left[ K_a \theta_b^p + K_m \theta_i^p + K_n \theta_j^p \right] \end{cases} \quad (5.5)$$

For an explicit equation (5.5), from the von Neumann stability condition,  $|\xi| \leq 1$  it found that:

$$\begin{cases} 0 < \Delta t \varepsilon_a \leq \frac{1}{\left( \frac{1}{2}(K_a + K_m + K_n) - 1 \right)} \\ or \\ 0 < \Delta t \frac{1}{C_a} \leq \frac{1}{\left( \frac{1}{2}(K_a + K_m + K_n) - 1 \right)} \end{cases} \quad (5.6)$$

whereas, the implicit equation is given as:

$$\begin{cases} \theta_a^{p+1} \left[ 1 + \Delta t \varepsilon_a (K_a + K_m + K_n) \right] = \theta_a^p + \Delta t \varepsilon_a (P_{cor-r})^{p+1} \\ + \Delta t \varepsilon_a \left[ K_a \theta_b^{p+1} + K_m \theta_i^{p+1} + K_n \theta_j^{p+1} \right] \end{cases} \quad (5.7)$$

while, all the implicit equations are inherently stable.

where,  $\varepsilon_{a...l} = 1/C_{a...l}$ ,  $\theta_a^{p+1}$  is temperature rise of rotor core,  $K_{a...r} = 1/\mathfrak{R}_{a...r}$ , is thermal conductance of the network. The thermal conductance,  $K_a$  and capacitance,  $C_a$  respectively, can be expressed as :

$$K_a = \frac{1}{q_a \ln \left( \frac{r_{or}}{r_{sh}} \right)} \quad (5.8)$$

and,

$$C_a = c_i \rho_i L_s A_{r-end} / 2 \quad (5.9)$$

Here,  $q_a = 1/(2\pi k_{ir} L_s)$ ,  $L_s$  is stack length which equal to rotor length,  $r_{or}$  is rotor outer

### 5.3 Lumped parameter model, and the use of EFD and IFD to estimate the temperature rise.

radius,  $r_{sh}$  is rotor shaft radius, and  $k_{ir}$  is conductivity of the lamination.

The thermal conductance  $K_m$  is:

$$K_m = A_{r-end} h_{ria} \quad (5.10)$$

where  $A_{r-end}$  is the area of rotor end surface that has been computed by applying FEA. The FEA is used to evaluate the rotor end surface due to its very complex geometry.  $h_{ria}$  is the convection heat flow coefficients in the region between the inner air and rotor end, which includes both the forced and free flow of air. The values of  $h_{ria}$  is calculated using Schubert expression (5.52).

The thermal conductance of  $K_n$  is:

$$K_n = \frac{1}{q_n \ln\left(\frac{r_{or}}{r_{ir}}\right) + q_{sh} + q_{she}} \quad (5.11)$$

The equation is the sum of three thermal resistance,  $q_n = 1/(2\pi k_{ir} L_s)$ , the 1<sup>st</sup> one is the radial thermal resistance because of rotor core,  $q_{sh} = 0.5L_s/\pi k_{ir} r_{sh}^2/4$ , the 2<sup>nd</sup> thermal resistance due to the shaft part which is under the rotor core, and  $q_{she} = 0.5(L_{sh} - L_s)/2\pi k_{ir} r_{sh}^2$ , the 3<sup>rd</sup> is the equivalent axial thermal resistance because of the shaft part which is external to rotor core. Where  $L_{sh}$  is the shaft length, and  $r_{sh}$  is the shaft radius, which is same as the inner core radius ( $r_{ir}$ ).

b) Node b,  $\theta_b$ : Temperature rise on rotor surface: The thermal conductance,  $K_b$  thermal capacitance,  $C_b$  and temperature rise on rotor surface,  $\theta_b^{p+1}$  calculated as follow: For explicit the result is:

$$\theta_b^{p+1} = \theta_b^p \left[ 1 - \Delta t \varepsilon_b (K_a + K_b) \right] + \Delta t \varepsilon_b \left[ K_a \theta_a^p + K_b \theta_c^p \right] \quad (5.12)$$

That gives:

$$\left\{ \begin{array}{l} 0 < \Delta t \varepsilon_b \leq \frac{2}{(K_a + K_b + 1)} \\ or \\ 0 < \Delta t \frac{1}{C_b} \leq \frac{2}{(K_a + K_b + 1)} \end{array} \right. \quad (5.13)$$

## 5. EFD AND IFD THERMAL MODELING OF SELF-EXCITED SRG FOR WIND ENERGY APPLICATION

and, for implicit the final result given as:

$$\theta_b^{p+1} \left[ 1 + \Delta t \varepsilon_b (K_a + K_b) \right] = \theta_b^p + \Delta t \varepsilon_b \left[ K_a \theta_a^{p+1} + K_b \theta_c^{p+1} \right] \quad (5.14)$$

where,  $\theta_b^{p+1}$  is temperature rise of rotor surface. The thermal conductance  $K_b$ , and capacitance  $C_b$ :

$$\begin{cases} K_b = A_{rs} h_{airgp} \\ \text{and,} \\ C_b = c_i \rho_i L_s A_{rs} / 2 \end{cases} \quad (5.15)$$

Here,  $A_{rs} = 2\pi r_{or} L_s$  is the area of rotor surface,  $h_{airgp}$  is air gap forced convection heat coefficient which depends on air gap length, rotor speed and viscosity of the fluid, and is given as:

$$h_{airgp} = N_u k_{air} / l_g \quad (5.16)$$

Here,  $k_{air}$  is thermal conductivity of air,  $N_u$  is the Nusselt number, and  $l_g$  is the length of the air gap. Using Becker and Kaye and equation (5.20), the Nusselt number associated with to air gap convection force coefficient is given as: [1, 2]

$$\begin{cases} Nu = 2; \text{ for } T_a < 1700 \\ Nu = 0.128 T_a^{0.367}; \text{ for } 1700 < T_a < 10,000 \\ Nu = 0.409 T_a^{0.241}; \text{ for } 10,000 < T_a < 100,000,000 \end{cases} \quad (5.17)$$

$T_a$  is the modified Taylor number and found from the equation:

$$T_a = T_{an} / F_g \quad (5.18)$$

where,  $F_g$  is the geometry factor given as:

### 5.3 Lumped parameter model, and the use of EFD and IFD to estimate the temperature rise.

$$F_g = \frac{\pi^4 (2r_a - 2.304l_g) \left/ \left( (2r_a - l_g) \right) \right.}{1679 \left[ 0.0056 + 0.057 \left( (2r_a - 2.304l_g) \left/ \left( (2r_a - l_g) \right) \right)^2 \right] \left( 1 - \frac{l_g}{2r_a} \right)} \quad (5.19)$$

where,  $l_g$  is the air gap length. Since,  $l_g \ll r_{or}$ , neglecting it,  $F_g \approx 1$ , and  $T_a$  and  $T_{an}$  are nearly equal.

The Taylor number  $T_{an}$  can be computed using the equation, as given below

$$T_{an} = \rho \omega^2 r_a l_g \left/ \mu^2 \right. \quad (5.20)$$

Here,  $r_a$ ,  $\omega$ ,  $\rho$ ,  $l_g$  and  $\mu$  are the average radius of the stator inner yoke, and outer rotor radius, the rotor angular speed, density of coolant material, air gap length, and the dynamic viscosity cooling material, respectively. The value of  $T_{an}$  is found to be 13136, approximately.

c) Node c,  $\theta_c$ : Temperature rise in the air gap: The thermal conductance, thermal capacitance, and temperature rise in the air gap,  $K_c$ ,  $C_c$ , and  $\theta_c^{p+1}$ , respectively, can be evaluated. And the results for explicit, and implicit method are given below:

For explicit:

$$\theta_c^{p+1} = \theta_c^p \left[ 1 - \Delta t \varepsilon_c (K_b + K_c) \right] + \Delta t \varepsilon_c \left[ K_b \theta_b^p + K_c \theta_d^p \right] \quad (5.21)$$

For implicit, it gives:

$$\left\{ \begin{array}{l} 0 < \Delta t \varepsilon_c \leq \frac{2}{(K_c + K_b + 1)} \\ or \\ 0 < \Delta t \frac{1}{C_c} \leq \frac{2}{(K_c + K_b + 1)} \end{array} \right. \quad (5.22)$$

and for implicit,

$$\theta_c^{p+1} \left[ 1 + \Delta t \varepsilon_c (K_b + K_c) \right] = \theta_c^p + \Delta t \varepsilon_c \left[ K_b \theta_b^{p+1} + K_c \theta_d^{p+1} \right] \quad (5.23)$$

## 5. EFD AND IFD THERMAL MODELING OF SELF-EXCITED SRG FOR WIND ENERGY APPLICATION

The thermal conductance and capacitance  $K_c, C_c$ :

$$\left\{ \begin{array}{l} K_c = A_s h_{airgp} \\ \text{and,} \\ C_c = c_i \rho_i A_{si} L_s \end{array} \right. \quad (5.24)$$

where,  $\theta_c^{p+1}$  is temperature rise of air gap,  $r_{si}$  is inner radius of the stator,  $A_s = 2\pi r_{si} L_s$  is stator inner surface area, and  $h_{airgp}$  is given in (5.16), and energy stored in stator tooth is assumed to be same as energy stored in air gap.

d) Node d,  $\theta_d$ : Temperature rise in stator tooth: The values of thermal conductances, capacitance, and temperature rise at the stator tooth,  $K_d, K_h, C_d$ , and  $\theta_d^{p+1}$  given as:

$$\left\{ \begin{array}{l} \theta_d^{p+1} = \theta_d^p \left[ 1 - \Delta t \varepsilon_d (K_c + K_d) \right] + \Delta t \varepsilon_d (P_{teeth})^p \\ + \Delta t \varepsilon_d \left[ K_c \theta_c^p + K_d \theta_e^p \right] \end{array} \right. \quad (5.25)$$

Which result for stability condition:

$$\left\{ \begin{array}{l} 0 < \Delta t \varepsilon_d \leq \frac{1}{\left( \frac{1}{2}(K_c + K_d) - 1 \right)} \\ \text{or} \\ 0 < \Delta t \frac{1}{C_d} \leq \frac{1}{\left( \frac{1}{2}(K_c + K_d) - 1 \right)} \end{array} \right. \quad (5.26)$$

and,

$$\left\{ \begin{array}{l} \theta_d^{p+1} \left[ 1 + \Delta t \varepsilon_d (K_c + K_d) \right] = \theta_d^p + \Delta t \varepsilon_d (P_{teeth})^{p+1} \\ + \Delta t \varepsilon_d \left[ K_c \theta_c^{p+1} + K_d \theta_e^{p+1} \right] \end{array} \right. \quad (5.27)$$

$$K_d = \frac{1}{q_d \ln \left( \frac{r_{syi}}{r_{si}} \right)} \quad (5.28)$$

### 5.3 Lumped parameter model, and the use of EFD and IFD to estimate the temperature rise.

and,

$$C_d = c_i \rho_i \pi L_s S \phi_e \left( r_{ysi}^2 - r_{si}^2 \right) / 2 \phi_p \quad (5.29)$$

Here,  $q_d = \pi k_{ir} L_s P_t / 2$ ,  $S$ , is lamination stacking factor,  $\theta_d^{p+1}$  is temperature rise of stator teeth,  $r_{ysi}$  is the stator yoke inner radius, and  $P_t$  is percentage volume of a teeth to the entire volume of teeth and slot. The thermal conductance,  $K_h$  depends on slot area and insulating material property, and is given as:

$$K_h = \frac{1}{(\Delta y_{insu} q_h)} \quad (5.30)$$

Here,  $q_h = 1/A_{slot} k_{insu}$ ,  $\Delta y_{insu}$  is thickness of insulation material,  $k_{insu}$  is the conductivity of insulating material,  $A_{slot}$  is the slot area.

e) Node e,  $\theta_e$ : Temperature rise on stator winding: The thermal conductance, thermal capacitance, temperature rise in the stator winding,  $K_e$ ,  $C_e$ ,  $\theta_e^{p+1}$ , respectively, are given as:

$$\begin{cases} \theta_e^{p+1} = \theta_e^p \left[ 1 - \Delta t \varepsilon_e (K_d + K_e + K_h) \right] + \Delta t \varepsilon_e P_{cu-s}^p \\ + \Delta t \varepsilon_e \left[ K_d \theta_d^p + K_e \theta_f^p + K_h \theta_h^p \right] \end{cases} \quad (5.31)$$

result in:

$$\begin{cases} 0 < \Delta t \varepsilon_e \leq \frac{1}{\left( \frac{1}{2}(K_d + K_e + K_h) - 1 \right)} \\ or \\ 0 < \Delta t \frac{1}{C_e} \leq \frac{1}{\left( \frac{1}{2}(K_d + K_e + K_h) - 1 \right)} \end{cases} \quad (5.32)$$

and,

$$\begin{cases} \theta_e^{p+1} \left[ 1 + \Delta t \varepsilon_e (K_d + K_e + K_h) \right] = \theta_e^p + \Delta t \varepsilon_e P_{cu-s}^{p+1} \\ + \Delta t \varepsilon_e \left[ K_d \theta_d^{p+1} + K_e \theta_f^{p+1} + K_h \theta_h^{p+1} \right] \end{cases} \quad (5.33)$$

$$K_e = \frac{1}{q_e \ln \left( \frac{(r_{ysi} + r_{syo})/2}{r_{ysi}} \right)} \quad (5.34)$$

## 5. EFD AND IFD THERMAL MODELING OF SELF-EXCITED SRG FOR WIND ENERGY APPLICATION

and,

$$C_e = c_c \rho_c A_c L_s Q_s / 2 \quad (5.35)$$

Here,  $q_e = 1/(2\pi k_{ir} L_s P_s)$ ,  $\theta_e^{p+1}$  is temperature rise of stator winding,  $K_e$  is radial conduction conductance of stator inner yoke,  $C_e$  is stator winding capacitance,  $r_{syo}$  is outer radius of stator yoke, and  $P_s$  is percentage volume of a slot to the entire volume of teeth and slot.

f) Node f,  $\theta_f$ : Temperature rise in stator yoke inner half: Expression for temperature in the stator yoke inner half,  $\theta_f^{p+1}$  using explicit and implicit methods at node f is evaluated. Thus, the final results of  $K_f$ ,  $C_f$ ,  $\theta_f^{p+1}$  are given as:

$$\begin{cases} \theta_f^{p+1} = \theta_f^p \left[ 1 - \Delta t \varepsilon_f (K_e + K_f) \right] + \Delta t \varepsilon_f (P_{cor-s})^p \\ + \Delta t \varepsilon_f \left[ K_e \theta_e^p + K_f \theta_g^p \right] \end{cases} \quad (5.36)$$

gives:

$$\begin{cases} 0 < \Delta t \varepsilon_f \leq \frac{1}{\left( \frac{1}{2}(K_e + K_f) - 1 \right)} \\ \text{or} \\ 0 < \Delta t \frac{1}{C_f} \leq \frac{1}{\left( \frac{1}{2}(K_e + K_f) - 1 \right)} \end{cases} \quad (5.37)$$

and,

$$\begin{cases} \theta_f^{p+1} \left[ 1 + \Delta t \varepsilon_f (K_e + K_f) \right] = \theta_f^p + \Delta t \varepsilon_f (P_{cor-s})^{p+1} \\ + \Delta t \varepsilon_f \left[ K_e \theta_e^{p+1} + K_f \theta_g^{p+1} \right] \end{cases} \quad (5.38)$$

$$K_f = \frac{1}{q_f \ln \left( \frac{(r_{syi} + r_{syo})/2}{r_{syo}} \right)} \quad (5.39)$$

and,

$$C_f = c_i \rho_i \pi L_s S \left( \left( (r_{syi} + r_{syo})/2 \right)^2 - r_{syi}^2 \right) / 2 \quad (5.40)$$

Here,  $q_f = 1/(2\pi k_{ir} L_s)$ .

### 5.3 Lumped parameter model, and the use of EFD and IFD to estimate the temperature rise.

g) Node g,  $\theta_g$ : Temperature rise in stator yoke outer half : The parameters,  $K_g$ ,  $C_g$ ,  $\theta_g^{p+1}$ , i.e., thermal conductance, thermal capacitance and temperature rise at the stator yoke for the outer half at node g are determined as below: For explicit:

$$\theta_g^{p+1} = \theta_g^p \left[ 1 - \Delta t \varepsilon_g (K_f + K_g) \right] + \Delta t \varepsilon_g \left[ K_f \theta_f^p + K_g \theta_k^p \right] \quad (5.41)$$

$$\left\{ \begin{array}{l} 0 < \Delta t \varepsilon_g \leq \frac{2}{(K_f + K_g + 1)} \\ \text{or} \\ 0 < \Delta t \frac{1}{C_g} \leq \frac{2}{(K_f + K_g + 1)} \end{array} \right. \quad (5.42)$$

and, for implicit:

$$\theta_g^{p+1} \left[ 1 + \Delta t \varepsilon_g (K_f + K_g) \right] = \theta_g^p + \Delta t \varepsilon_g \left[ K_f \theta_f^{p+1} + K_g \theta_k^{p+1} \right] \quad (5.43)$$

letting:

$$\left\{ \begin{array}{l} K_g = \frac{1}{l_{ig} q_g} \\ \text{and,} \\ C_g = c_i \rho_i \pi L_s S \left( r_{syo}^2 - \left( (r_{ysi} + r_{syo}) / 2 \right)^2 \right) / 2 \end{array} \right. \quad (5.44)$$

Here,  $q_g = 1/2\pi k_{air} r_{syo} L_s$ ,  $\theta_g^{p+1}$  is temperature rise of outer stator yoke,  $K_f$  is radial conduction conductance between stator and frame,  $C_f$  is capacitance of outer yoke,  $l_{ig}$  is the air gap length between the interfaces (i.e., the small gap due to roughness between the frame and outer stator core) which is assumed in the range of 0.05 to 0.08 mm,  $k_{air}$  is the conductivity of inner air.

h) Node h,  $\theta_h$ : Temperature rise in stator end winding : The end winding temperature rise,  $\theta_h^{p+1}$ , can be evaluated at node, h. Moreover, the parameters  $K_i$ ,  $K_j$ ,  $K_k$ ,  $C_h$  can be calculated and

## 5. EFD AND IFD THERMAL MODELING OF SELF-EXCITED SRG FOR WIND ENERGY APPLICATION

given as:

$$\begin{cases} \theta_h^{p+1} = \theta_h^p \left[ 1 - \Delta t \varepsilon_h (K_h + K_i + K_j + K_k) \right] + \Delta t \varepsilon_h (P_{end-w})^p \\ + \Delta t \varepsilon_h \left[ K_h \theta_e^p + K_i \theta_k^p + K_j \theta_k^p + K_k \theta_i^p \right] \end{cases} \quad (5.45)$$

then,

$$\begin{cases} 0 < \Delta t \varepsilon_h \leq \frac{1}{\left( \frac{1}{2} (K_h + K_i + K_j + K_k) - 1 \right)} \\ or \\ 0 < \Delta t \frac{1}{C_h} \leq \frac{1}{\left( \frac{1}{2} (K_h + K_i + K_j + K_k) - 1 \right)} \end{cases} \quad (5.46)$$

and,

$$\begin{cases} \theta_h^{p+1} \left[ 1 + \Delta t \varepsilon_h (K_h + K_i + K_j + K_k) \right] = \theta_h^p + \Delta t \varepsilon_h (P_{end-w})^{p+1} \\ + \Delta t \varepsilon_h \left[ K_h \theta_e^{p+1} + K_i \theta_k^{p+1} + K_j \theta_k^{p+1} + K_k \theta_i^{p+1} \right] \end{cases} \quad (5.47)$$

$$K_i = \frac{1}{q_i \ln \left( \frac{r_{ewo}}{r_{ewi}} \right)} \quad (5.48)$$

and,

$$C_h = c_c \rho_c (1 - \beta) v_c / 2\chi \quad (5.49)$$

and here,

$$\begin{cases} K_j = \delta \varepsilon A_{ew} b_t \\ here, \\ b_t = \left( \theta_k^p + \theta_h^p \right) \left( (\theta_k^2)^p + (\theta_h^2)^p \right) \end{cases} \quad (5.50)$$

Here,  $q_i = 1/(2\pi k_{air} l_{ew})$ ,  $\theta_h^{p+1}$  is temperature rise of stator end winding,  $A_{ew}$  is the end-winding area, and  $\varepsilon$  is the emissivity of the material.

$$K_k = h_{ew} A_{ew} \quad (5.51)$$

### 5.3 Lumped parameter model, and the use of EFD and IFD to estimate the temperature rise.

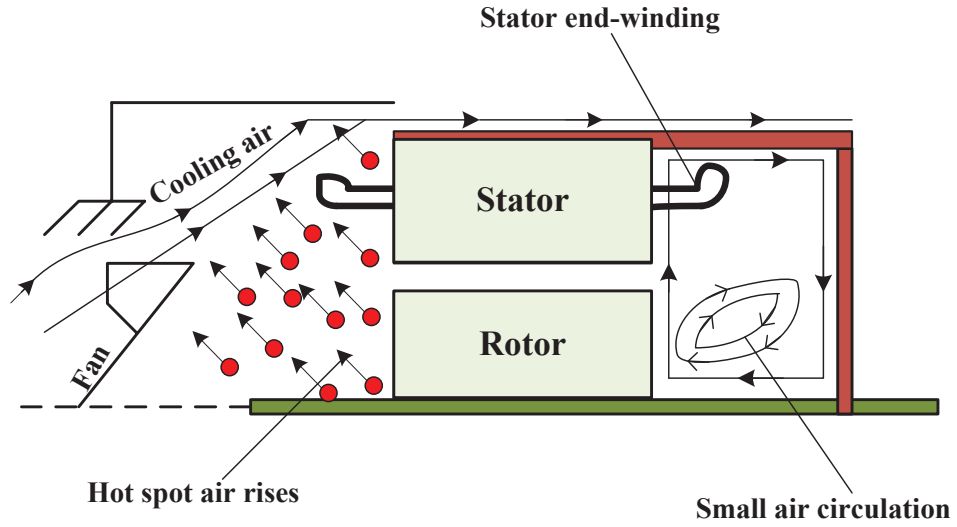


**Figure 5.3:** Air circulation, combined forced and free convection between end winding and end cap in a SRG.

Here,  $h_{ew}$  is the free and forced heat coefficient between the inner air and the stator winding. The estimation of  $h_{ew}$  is quite complex since it requires to know the heat flow under the influence of temperature at the end region. The stator end-winding gap of the generator is classified into two regions. One of them is the gap between the stator end winding and the generator frame, and the other between the rotor end and the stator end winding. The air circulates in the end space due to the rotation of the rotor, but the flow of air is negligible in SRG as compared with the squirrel-cage induction machine due to the presence of a smooth surface at the rotor end which is shown in Fig.5.3. Hence, mainly, the heat transfer takes place in the stator end winding region by the forced and combined free convection. It is quite complex to estimate the velocity of inner airflow, due to the presence of end winding structure. Hence, the present work uses the rotor peripheral speed to estimate inner airflow speed. Among many models, Schubert's model is commonly applied to calculate the convection heat transfer coefficient. The equation for Schubert's modeling is [49]:

$$\begin{cases} h_{ew} = 15.5 \times \left[ 1 + (0.4\vartheta_a)^{0.9} \right] \\ \vartheta_a = r_{or}\omega\eta_{ef} \end{cases} \quad (5.52)$$

Here,  $\vartheta_a$  is the air speed in the stator end winding region,  $\omega$  is the angular speed of the rotor

## 5. EFD AND IFD THERMAL MODELING OF SELF-EXCITED SRG FOR WIND ENERGY APPLICATION

(1500 rpm), and  $\eta_{ef}$  is fan factor (i.e., fan efficiency of the end ring fans) which are used to estimate inner airflow speed. In general, the fan efficiency is assumed to be less than or equal to 60%.

i) Node  $i$ ,  $\theta_i$ : Temperature rise of inner air: The parameters  $K_l$ , and  $\theta_i^{p+1}$  that represented the thermal conductance, and temperature rise of the inner air of generator, respectively, are given as:

$$\begin{cases} \theta_i^{p+1} = \theta_i^p \left[ 1 - \Delta t \varepsilon_i (K_l + K_k + K_m) \right] \\ + \Delta t \varepsilon_i \left[ K_l \theta_k^p + K_k \theta_h^p + K_m \theta_a^p \right] \end{cases} \quad (5.53)$$

as,

$$\begin{cases} 0 < \Delta t \varepsilon_i \leq \frac{2}{(K_l + K_k + K_m + 1)} \\ \text{or} \\ 0 < \Delta t \frac{1}{C_i} \leq \frac{2}{(K_l + K_k + K_m + 1)} \end{cases} \quad (5.54)$$

and,

$$\begin{cases} \theta_i^{p+1} \left[ 1 + \Delta t \varepsilon_i (K_l + K_k + K_m) \right] = \theta_i^p \\ + \Delta t \varepsilon_i \left[ K_l \theta_k^{p+1} + K_k \theta_h^{p+1} + K_m \theta_a^{p+1} \right] \end{cases} \quad (5.55)$$

$$\begin{cases} K_m = h_{inair} A_{encap} \\ \text{and} \\ C_i = c_a \rho_a V_{aspc} / 2 \end{cases} \quad (5.56)$$

Here,  $\theta_i^{p+1}$  is temperature rise of inner air,  $V_{aspc}$ ,  $h_{inair}$  are inner volume, and the convection coefficient for the region between the machine end cap and inner air respectively, and  $A_{encap}$  is end cap surface area. Since the value of the convection coefficient ( $h_{inair}$ ) is similar to the value of the convection coefficient of  $h_{ew}$ . Hence, the present work assumes that both are the same.

j) Node  $j$ ,  $\theta_j$ : Temperature rise in the bearing: At node  $j$  the  $K_o$ , and  $\theta_j^{p+1}$ , the thermal

### 5.3 Lumped parameter model, and the use of EFD and IFD to estimate the temperature rise.

conductance, and temperature rise in the bearing is given as:

$$\begin{cases} \theta_j^{p+1} = \theta_j^p \left[ 1 - \Delta t \varepsilon_j (K_o + K_n) \right] \\ + \Delta t \varepsilon_j \left[ K_o \theta_k^p + K_n \theta_a^p \right] \end{cases} \quad (5.57)$$

$$\begin{cases} 0 < \Delta t \varepsilon_j \leq \frac{2}{(K_o + K_n + 1)} \\ \text{or} \\ 0 < \Delta t \frac{1}{C_j} \leq \frac{2}{(K_o + K_n + 1)} \end{cases} \quad (5.58)$$

and,

$$\begin{cases} \theta_j^{p+1} \left[ 1 + \Delta t \varepsilon_j (K_o + K_n) \right] = \theta_j^p \\ + \Delta t \varepsilon_j \left[ K_o \theta_k^{p+1} + K_n \theta_a^{p+1} \right] \end{cases} \quad (5.59)$$

while,

$$K_o = \frac{1}{q_o \ln \left( \frac{r_{encap}}{r_{sh}} \right)} \quad (5.60)$$

where,  $q_o = 1/(2\pi k_{ir} \Delta y_{encap})$ ,  $\theta_j^{p+1}$ ,  $\Delta y_{encap}$ ,  $k_{ir}$ , and  $r_{encap}$  are temperature rise of bearing, the thickness of the end cap, the conductivity of end cap material, and the radius of the end cap respectively.

*k) Node k,  $\theta_k$ : Temperature rise at the frame:* Thermal conductances and temperature rise at the frame  $K_p$ ,  $K_q$ ,  $K_r$ , and  $\theta_k^{p+1}$  are evaluated as:

$$\begin{cases} \theta_k^{p+1} = \theta_k^p \left[ 1 - \Delta t \varepsilon_k (K_g + K_i + K_j + K_o + K_l + K_p) \right] \\ + \Delta t \varepsilon_k \left[ K_g \theta_g^p + K_i \theta_h^p + K_j \theta_h^p + K_o \theta_j^p + K_l \theta_i^p + K_p \theta_l^p \right] \end{cases} \quad (5.61)$$

## 5. EFD AND IFD THERMAL MODELING OF SELF-EXCITED SRG FOR WIND ENERGY APPLICATION

with,

$$\left\{ \begin{array}{l} 0 < \Delta t \varepsilon_k \leq \frac{2}{(K_g + K_i + K_j + K_o + K_l + K_p + 1)} \\ or \\ 0 < \Delta t \frac{1}{C_k} \leq \frac{2}{(K_g + K_i + K_j + K_o + K_l + K_p + 1)} \end{array} \right. \quad (5.62)$$

and,

$$\left\{ \begin{array}{l} \theta_k^{p+1} \left[ 1 + \Delta t \varepsilon_k (K_g + K_i + K_j + K_o + K_l + K_p) \right] = \theta_k^p \\ + \Delta t \varepsilon_k \left[ K_g \theta_g^{p+1} + K_i \theta_h^{p+1} + K_j \theta_h^{p+1} + K_o \theta_j^{p+1} + K_l \theta_i^{p+1} + K_p \theta_l^{p+1} \right] \end{array} \right. \quad (5.63)$$

$$K_p = \frac{1}{(q_p \Delta y_f)} \quad (5.64)$$

where,  $q_p = 1/A_f k_{al}$ ,  $\theta_k^{p+1}$  is temperature rise of frame,  $A_f$  is the fins area,  $\Delta y_f$  is the height of the fins, and  $k_{al}$  is the conductivity of fin material.

1) Node  $l$ ,  $\theta_l$ : Temperature rise at the fins: While temperature rise at the fins node,  $\theta_l^{p+1}$ , thermal conductances  $K_q$ , and  $K_r$  are given as:

For explicit:

$$\left\{ \begin{array}{l} \theta_l^{p+1} = \theta_l^p \left[ 1 - \Delta t \varepsilon_l (K_q + K_r) \right] + \Delta t \varepsilon_l \left[ K_p (\theta_k^p \right. \\ \left. - \theta_g^p) + K_q \theta_{atm}^p + K_r \theta_{atm}^p + K_o (\theta_j^p - \theta_k^p) \right] \end{array} \right. \quad (5.65)$$

implies,

$$\left\{ \begin{array}{l} 0 < \Delta t \varepsilon_l \leq \frac{1}{\left( \frac{1}{2} (K_q + K_r) - 1 \right)} \\ or \\ 0 < \Delta t \frac{1}{C_l} \leq \frac{1}{\left( \frac{1}{2} (K_q + K_r) - 1 \right)} \end{array} \right. \quad (5.66)$$

### 5.3 Lumped parameter model, and the use of EFD and IFD to estimate the temperature rise.

and, for implicit:

$$\begin{cases} \theta_l^{p+1} \left[ 1 + \Delta t \varepsilon_l (K_q + K_r) \right] = \theta_l^p + \Delta t \varepsilon_l \left[ K_p (\theta_k^{p+1} \right. \\ \left. - \theta_g^{p+1}) + K_q \theta_{atm}^{p+1} + K_r \theta_{atm}^{p+1} + K_o (\theta_j^{p+1} - \theta_k^{p+1}) \right] \end{cases} \quad (5.67)$$

$$\begin{cases} K_q = \delta \varepsilon A_{ra} d_t \\ \text{where,} \\ d_t = \left( \theta_{atm} + \theta_l^p \right) \left( \theta_{atm}^2 + (\theta_l^p)^2 \right) \end{cases} \quad (5.68)$$

where,  $A_{ra}$  is the radiation surface area.

$$K_r = h_f A_{fra} \quad (5.69)$$

where  $\theta_l^{p+1}$  is temperature rise of fins,  $A_{fra}$  is the generator frame surface area, and  $h_f$  is the forced convection coefficient for the region between the generator frame to the atmosphere.

$$\begin{cases} h_f = \frac{\rho_f c_f Q \vartheta_f}{4L_f} \times \left( 1 - e^{-m_a} \right) \\ \text{where,} \\ m_a = 0.1448 \left( L_f^{0.946} / Q^{1.16} \right) \left( \frac{k_f}{\rho_f c_f \vartheta_f} \right)^{0.214} \end{cases} \quad (5.70)$$

where,  $k_f$ ,  $\rho_f$  and  $c_f$  are thermal conductivity, density and specific heat capacity of fins respectively.

#### 5.3.1.2 Solution of the developed lumped parameter based thermal model using explicit and implicit methods

The explicit and implicit thermal network equations corresponding to each nodes are presented (i.e., utilizing the matrix representation) as the equation below, respectively.

$$\begin{cases} Y_t = U_t + \Delta t Q_t D_t^p + \Delta t Q_t K_t U^p \\ Y_t = U_t + \Delta t Q_t D_t^{p+1} + \Delta t Q_t K_t U^{p+1} \end{cases} \quad (5.71)$$

Where, the matrix  $Y_t$ ,  $U_t$ ,  $Q_t$ ,  $D_t^p$ ,  $K_t$ ,  $D_t^{p+1}$ ,  $U^{p+1}$  and  $U^p$  given as:

**5. EFD AND IFD THERMAL MODELING OF SELF-EXCITED SRG FOR WIND ENERGY APPLICATION**

$$Y_t = \begin{bmatrix} \theta_a^{p+1} \\ \theta_b^{p+1} \\ \theta_c^{p+1} \\ \theta_d^{p+1} \\ \vdots \\ \theta_l^{p+1} \end{bmatrix}, U_t = \begin{bmatrix} \theta_a^p \\ \theta_b^p \\ \theta_c^p \\ \theta_d^p \\ \vdots \\ \theta_l^p \end{bmatrix}, Q_t = \begin{bmatrix} \varepsilon_a & 0 & 0 & 0 & \cdots & 0 \\ 0 & \varepsilon_b & 0 & 0 & \cdots & 0 \\ 0 & 0 & \varepsilon_c & 0 & \cdots & 0 \\ 0 & 0 & 0 & \varepsilon_d & \cdots & 0 \\ \vdots & \vdots & \vdots & \vdots & \ddots & \vdots \\ 0 & 0 & 0 & 0 & \cdots & \varepsilon_l \end{bmatrix}^{12 \times 12} \quad (5.72)$$

$$K_t = \begin{bmatrix} -K_{am} & K_a & 0 & 0 & \cdots & 0 \\ K_a & -K_{ab} & K_b & 0 & \cdots & 0 \\ 0 & K_b & -K_{bc} & K_c & \cdots & 0 \\ 0 & 0 & K_c & -K_{ed} & \cdots & 0 \\ \vdots & & & & \ddots & \\ 0 & 0 & K_e & -K_{ef} & \cdots & -K_{qr} \end{bmatrix}^{12 \times 12} \quad (5.73)$$

$$D_t^p = \begin{bmatrix} P_{core-r}^p \\ 0 \\ 0 \\ P_{teeth}^p \\ P_{cu-s}^p \\ P_{cor-s}^p \\ 0 \\ P_{end-w}^p \\ 0 \\ 0 \\ 0 \\ 0 \\ 0 \end{bmatrix}, D_t^{p+1} = \begin{bmatrix} P_{core-r}^{p+1} \\ 0 \\ 0 \\ P_{teeth}^{p+1} \\ P_{cu-s}^{p+1} \\ P_{cor-s}^{p+1} \\ 0 \\ P_{end-w}^{p+1} \\ 0 \\ 0 \\ 0 \\ 0 \\ 0 \end{bmatrix} \quad (5.74)$$

### 5.3 Lumped parameter model, and the use of EFD and IFD to estimate the temperature rise.

$$, U^p = \begin{bmatrix} \theta_a^p \\ \theta_b^p \\ \theta_c^p \\ \theta_d^p \\ \vdots \\ \theta_l^p \end{bmatrix}, U^{p+1} = \begin{bmatrix} \theta_a^{p+1} \\ \theta_b^{p+1} \\ \theta_c^{p+1} \\ \theta_d^{p+1} \\ \vdots \\ \theta_l^{p+1} \end{bmatrix} \quad (5.75)$$

The entry thermal conductance  $K_t$  matrix are specified as:

$$K_{amn} = K_a + K_m + K_n, K_{ab} = K_a + K_b, K_{bc} = K_b + K_c$$

$$K_{cd} = K_c + K_d, K_{deh} = K_d + K_e + K_h, K_{ef} = K_e + K_f$$

$$K_{fg} = K_f + K_g, K_{hijk} = K_h + K_i + K_j + K_k$$

$$K_{ij} = K_i + K_j, K_{ikm} = K_i + K_k + K_m, K_{on} = K_o + K_n$$

$$K_{gijolp} = K_g + K_i + K_j + K_o + K_l + K_p, K_{qr} = K_q + K_r$$

Here,  $K_{a...r} = 1/\mathfrak{R}_{a...r}$ ,  $K_t$ ,  $U^p$ ,  $D_t^p$ , and  $Q_t$  are thermal conductance at each mesh, thermal conductance matrix, temperature rise, power loss matrix, thermal capacitance matrix respectively.

In similar manner, the steady state, at  $(Y_t - U_t)/\Delta t=0$ , temperature rise for the SRG is given by:

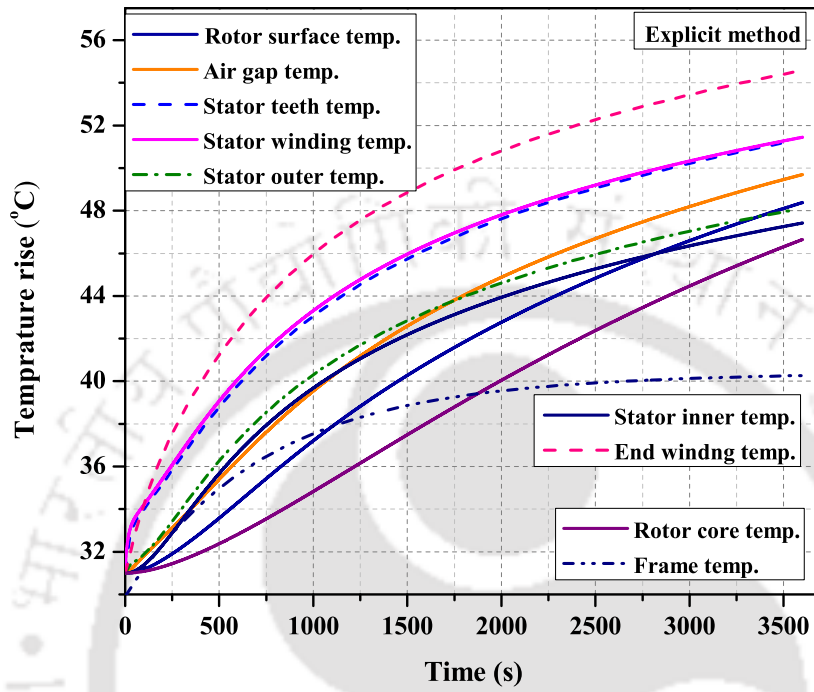
$$\begin{cases} U^p = K_t^{-1} D_t^p + \theta_{atm} \\ U^{p+1} = K_t^{-1} D_t^{p+1} + \theta_{atm} \end{cases} \quad (5.76)$$

Where,  $D_t^p$ ,  $D_t^{p+1}$ ,  $U^p$ ,  $U^{p+1}$ , and  $K_t^{-1}$  are defined in equations (5.72) to (5.75).

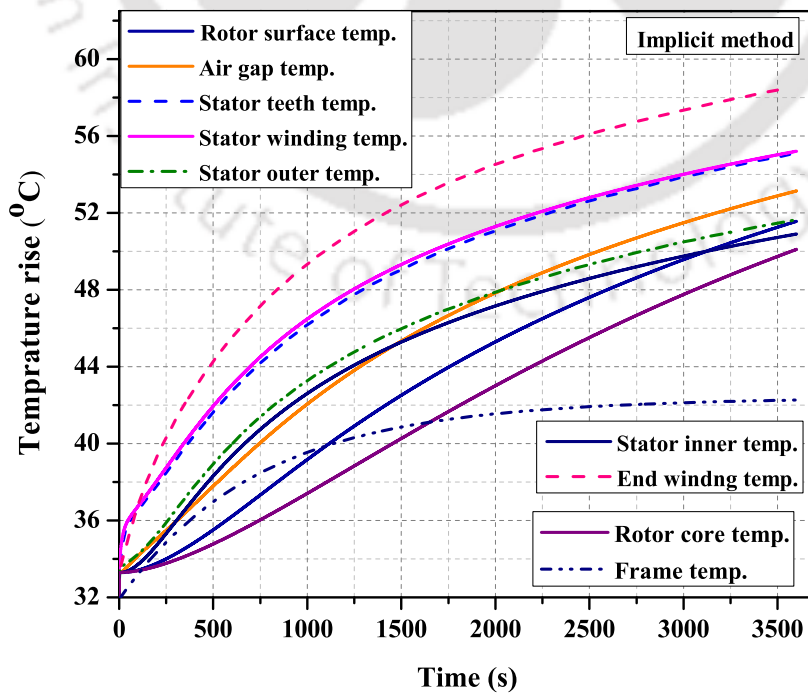
The values of thermal capacitance and resistance are evaluated/calculated with the help of given equations. The summarized capacitance and resistance values are shown as in Table 5.5.

Fig. 5.4(a) and 5.4(b) show the estimated temperature rise at the rotor core, rotor surface, air gap, stator inner core, stator outer core, stator teeth, stator end winding and stator windings in the slot determine by implicit and explicit finite difference. It could be observed that the

5. EFD AND IFD THERMAL MODELING OF SELF-EXCITED SRG FOR WIND ENERGY APPLICATION



(a)



(b)

Figure 5.4 (a) Temperature rise curve using explicit method. (b) Temperature rise curve using implicit method.

**Table 5.5:** Calculated thermal capacitance and resistance

Thermal capacitance $C_{a...f}, (J/K)$	Thermal capacitance $C_{g...l}, (J/K)$	Thermal resistance $\mathfrak{R}_{a...i}, (K/W)$	Thermal resistance $\mathfrak{R}_{j...r}, (K/W)$
$C_a = 904.5$	$C_g = 3442.4$	$\mathfrak{R}_a = 0.46$	$\mathfrak{R}_j = 0.0067$
$C_b = 724$	$C_h = 3090.3$	$\mathfrak{R}_b = 0.231$	$\mathfrak{R}_k = 0.533376$
$C_c = 801.3$	$C_i = 4543$	$\mathfrak{R}_c = 0.222$	$\mathfrak{R}_l = 0.479$
$C_d = 368.5$	$C_j = 5897$	$\mathfrak{R}_d = 0.018$	$\mathfrak{R}_m = 1.083$
$C_e = 6320.4$	$C_k = 679.6$	$\mathfrak{R}_e = 0.0142$	$\mathfrak{R}_n = 0.014$
$C_f = 315$	$C_l = 4928$	$\mathfrak{R}_f = 0.002875$	$\mathfrak{R}_o = 0.05692$
–	–	$\mathfrak{R}_g = 0.068$	$\mathfrak{R}_p = 0.016572$
–	–	$\mathfrak{R}_h = 0.0553$	$\mathfrak{R}_q = 0.095$
–	–	$\mathfrak{R}_i = 0.24$	$\mathfrak{R}_r = 0.0232$

temperature rise limitation in the rotor core, rotor surface, air gap, stator inner core, stator outer core, stator teeth, stator end winding and stator windings as shown in Table 5.7. The result from explicit and implicit methods show that the end winding temperature rise to 54.58187°C, and 58.58268°C, respectively. With these results, it can be observed that maximum temperature rise at different parts of the machine is well below the safety limits of the insulation class of the material type.

#### 5.4 Thermal analysis of SRG using 3D FEA

The 3D comsol multiphysics is also used to carry the thermal analysis of the SRG. Here, in this section, comsol multiphysics is used to obtain the temperature distribution of the SRG. Further, in the next section, the result obtained with FEA, experimental, implicit and explicit are compared. The main drawback of FEA based thermal analysis is its high computational time in the case of 3D modeling.

A finite element meshing of the SRG region is done using a physics-controlled sequence type with an element size finer. The triangular mesh of quarter consists of 32296 numbers of the degree of freedom (DOF) as shown in Fig. 5.5(a). The boundary conditions and domain are specified, such as initial temperature, heat source or heat fluxes, and symmetry. The rotor motion is considered by setting the prescribed rotational velocity of the rotating domain (band). The constant angular velocity is set in rpm, with a small initial angle, and rotation axis base point. The results are observed as depicted in Fig. 5.5(a), and Fig.5.5(b). Fig. 5.5(a), shows

## 5. EFD AND IFD THERMAL MODELING OF SELF-EXCITED SRG FOR WIND ENERGY APPLICATION

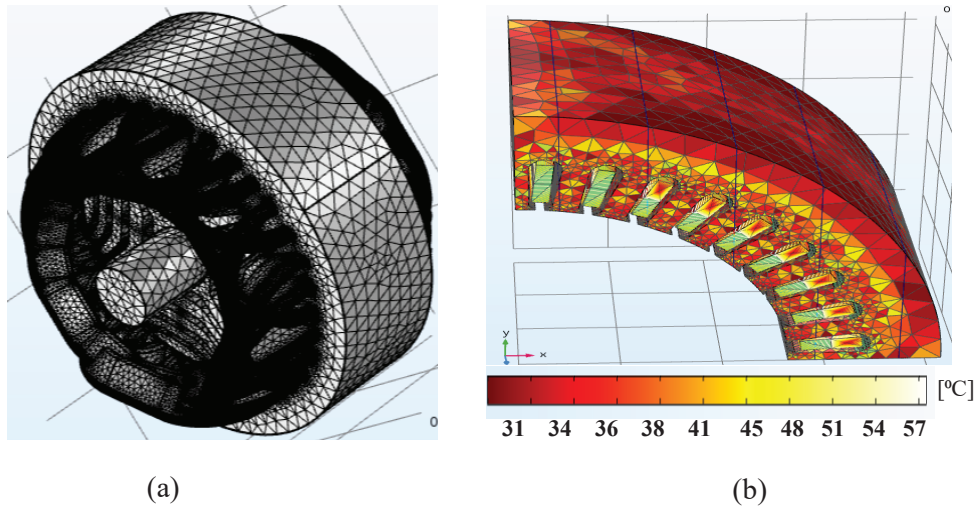


**Figure 5.5:** Three-dimensional mesh analysis and thermal distribution rise ( $^{\circ}\text{C}$ ) of SRG for  $t = 3600 \text{ sec}$ . the finite element meshing of the machine, while Fig. 5.5(b) shows thermal analysis of stator with its mesh. i.e., it shows that the temperature spread in different layers of stator yoke. From Fig.5.5(b) it is found that maximum temperature distribution is observed in the stator winding part/layer. It is also observed that the temperature distribution in the inner layer of the stator yoke is less than the temperature in stator winding and is slightly higher than the temperature in the stator outer yoke layer.

The basic equation that relates the thermal distribution of  $\theta$  at different section of the generator and heat flow is given by the differential equation:

$$\rho C_p \frac{\partial \theta}{\partial t} - P_{gen} = \nabla(\kappa \nabla \theta) \quad (5.77)$$

where  $C_p$  is specific heat capacity, and  $P_{gen}$  represents generator losses.

From Fig.5.5(b) it can be observed that, the distribution of surface temperature rise as the function of time (i.e., for  $t = 0$  to  $t = 3600 \text{ sec}$ ). It is also clear that the initially rate of increase in surface temperature is more and settles to near constant value in 3600 sec.

Fig. 5.6 shows the 3D temperature analysis at the stator inner core, stator outer core, and stator winding end edge. It could be observed that the temperature rise in stator inner core, stator outer core and, stator winding end edge are limited to  $50.40130^{\circ}\text{C}$ ,  $49.91401^{\circ}\text{C}$ , and  $57.15210^{\circ}\text{C}$ , respectively, as shown in Fig. 5.6.

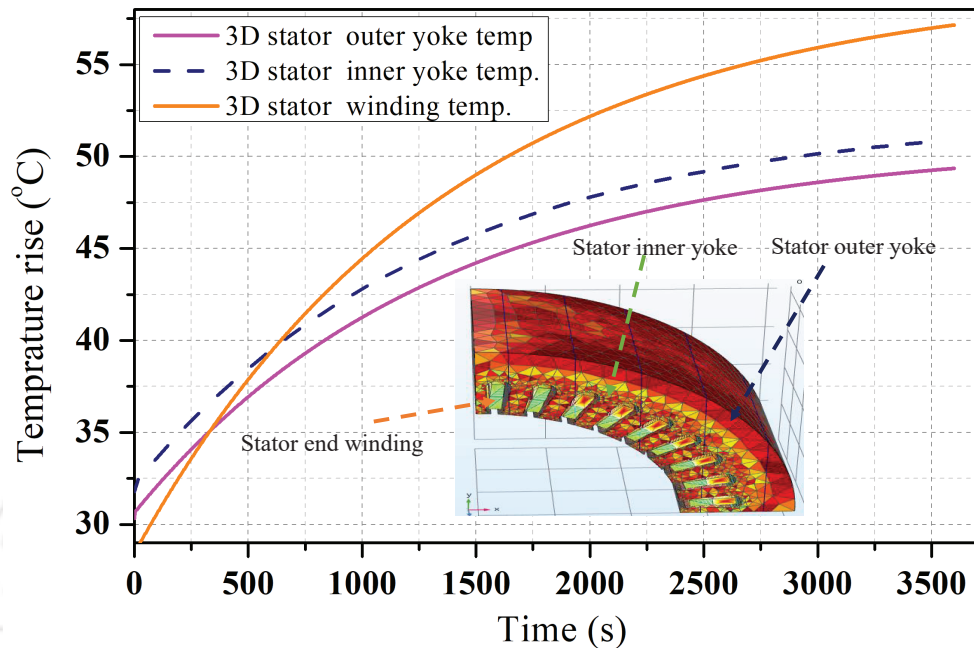


**Figure 5.6:** Three-dimensional stator core and stator end winding thermal distribution ( $^{\circ}\text{C}$ ) of SRG for  $t = 3600 \text{ sec}$ .

## 5.5 Experimental verification of the results

This section compares the temperature rise in SRG with different thermal analysis methods. The thermal analysis of the machine is evaluated for the explicit method, the implicit method, and is compared with the 3D FEA. Further, the results are also compared with the experimental results obtained by operating the SRG with the temperature sensor placed at various locations of the machine.

The accuracy of the thermal analysis through the explicit and implicit thermal modeling is compared with the developed experimental setup in the laboratory with the rating of 2.1 kW SRG, whose design parameters are given in Table 5.4. Fig. 5.7(a) show the experimental bench, where the test generator was driven by a DC motor for 3600 s as the prime mover. A torque sensor is used through the coupling between the test generator and a DC motor as the prime mover. For sensing the temperature, five thermistors were used in the experimental setup. Three thermistor temperature sensors were inserted into the stator end-winding near the stator surface per phase. The remaining two temperature sensors are inserted into the stator

## 5. EFD AND IFD THERMAL MODELING OF SELF-EXCITED SRG FOR WIND ENERGY APPLICATION

**Table 5.6:** Instruments used in the Experimental setup

Instrumentation	Model	Specification	Accuracy
<i>Torque indicator</i>	VTI01	Max., 100 kg.m	±0.2%
<i>Thermistors</i>	KTY84130	Max., 300°C	±0.5%
<i>Tachometers</i>	NCTM1000	Max. output ± 5 mW	–
<i>Exp. torque</i>	SRG	Measured, 12.17 Nm	-
<i>Exp. resistance</i>	-	Measured, 0.995 Ω	-

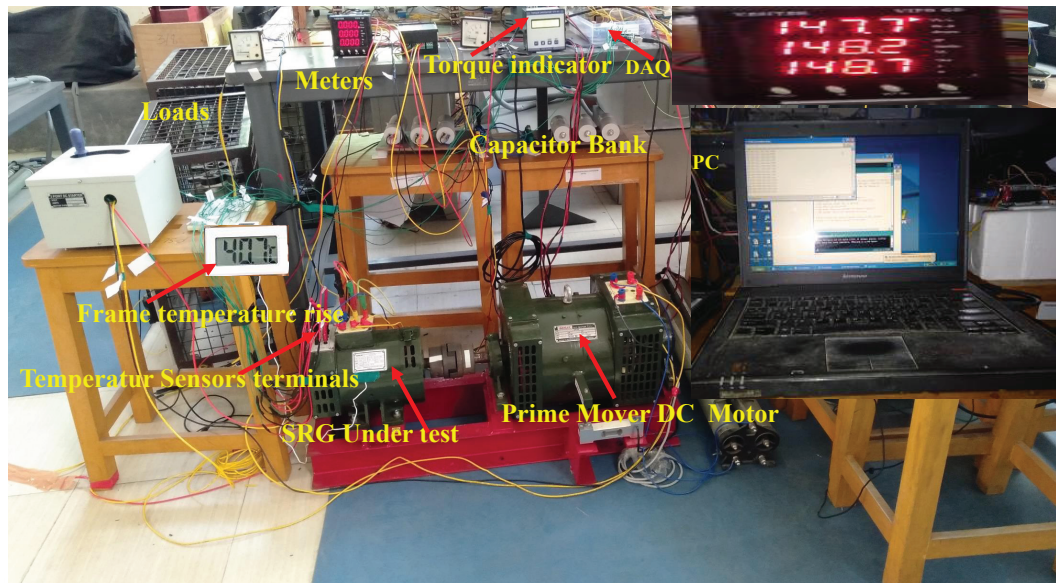
inner yoke and stator outer yoke through small holes on the stator core. A tape is used to keep the thermistors in the coil and core. During the test, the result from the sensor was recorded using an interfacing circuit with a PC and Arduino. Table 5.6 shows the specification of the instrumentations. Fig.5.7(b) shows the schematic diagram of mentioned experimental setup.

### 5.5.1 Comparison of EFD, IFD, 3D FEA with the experimental results

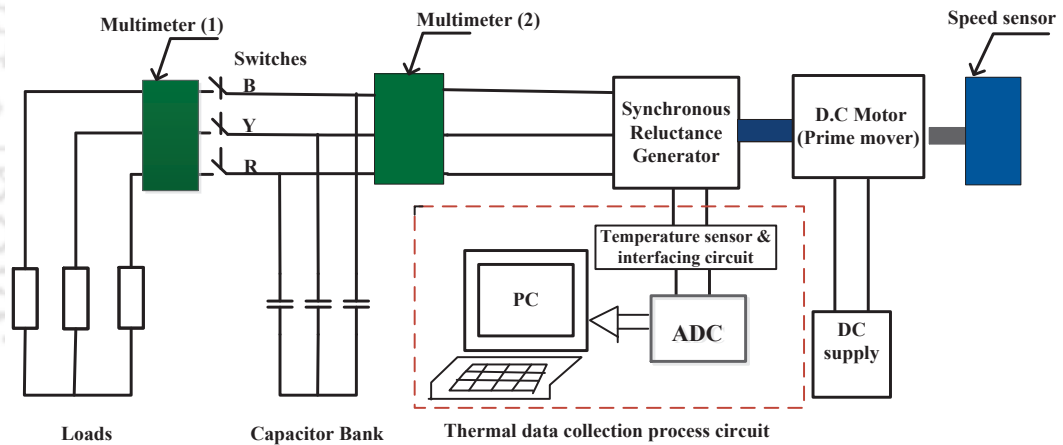
Fig. 5.8, and 5.9 show the comparison between the estimated temperature of SRG obtained using the explicit, implicit, 3D FEA, and experimental setup for the wind turbine which runs at a mean wind speed of 10 m/s, i.e., the SRG rotating at 1500 rpm at the rated stator current. The result indicates that there is a negligible difference between the predicted temperature by the explicit, implicit, 3D FEA and experimental setup.

The 3D FEA model has modeled the machine in much more details with a more accurate parameters, and the results are very close to the one which are obtained from the explicit, implicit, and through the experimental setup. The proposed methods (IFD and EFD) used the numerical solution of equations (5.1), and (5.2), which uses forward and backward difference to solve the partial differential equation respectively. The 3D FEA also apply the partial differential equation of (5.77) in dynamic condition. It is observed that for both methods the temperature rise time to reach steady-state depends on the values of the thermal capacitance of the materials. The thermal capacitance is based on the specific capacity, density, and volume of the material. Therefore, the shape/pattern of the temperature rise curve in all methods is found to be similar.

In this Chapter, the effects of some variation in frequency due to the change of load are neglected in evaluating the temperature rise (i.e., the SRG output frequency is not affected by load change).



(a)

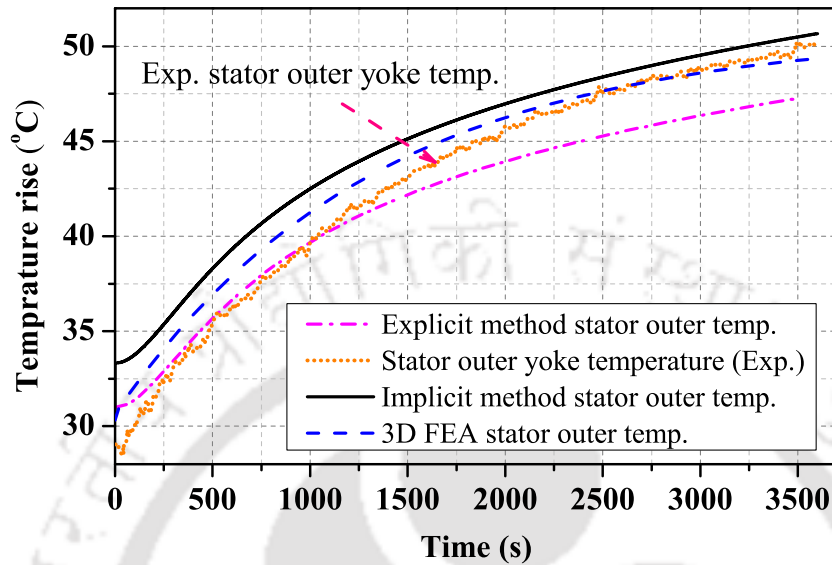


(b)

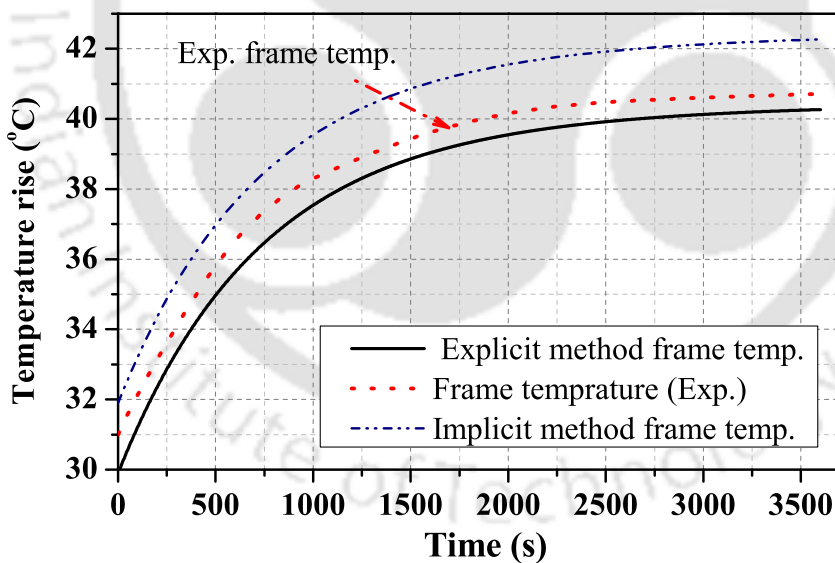
**Figure 5.7:** TEFC SRG: (a) Thermal experimental setup. (b) Schematic diagram of the test bench.

Fig. 5.8(a), and 5.8(b) represents the temperature of the stator outer yoke, and frame as estimated by the explicit, implicit, and 3D FEA. Further, the estimated results are verified through the experimental test. The results indicate that the nature of temperature rise at different location is observed to be exponential. While doing the experimental test, the ambient temperature was 30°C, hence, the explicit, implicit and 3D FEA are also done with the initial temperature of 30°C. From Fig. 5.8(a), it could be observed that the estimated temperature of the stator outer by explicit method is slightly less than FEA, and great than implicit method, but results from both method are very close to the result obtained from the experimental setup. It can also be observed that temperature rise settles to its final value in about 3000 sec. Similarly, Fig. 5.8(b)

**5. EFD AND IFD THERMAL MODELING OF SELF-EXCITED SRG FOR WIND ENERGY APPLICATION**



(a)

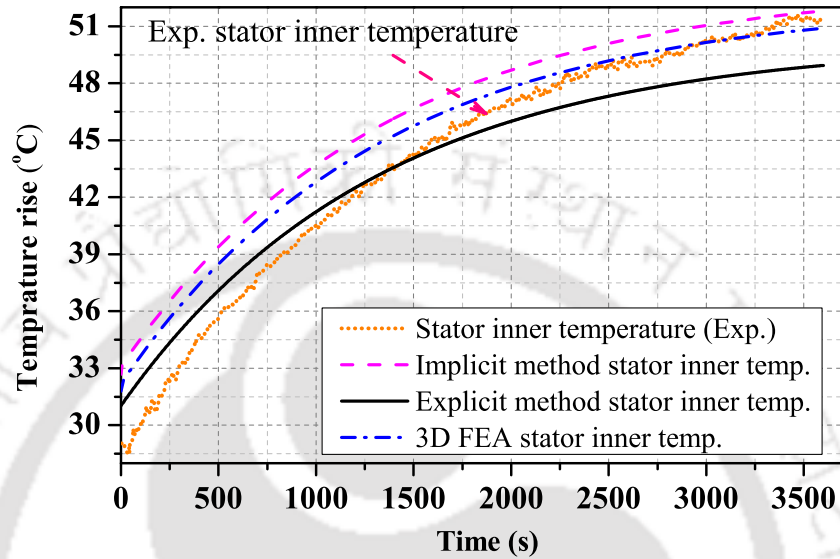


(b)

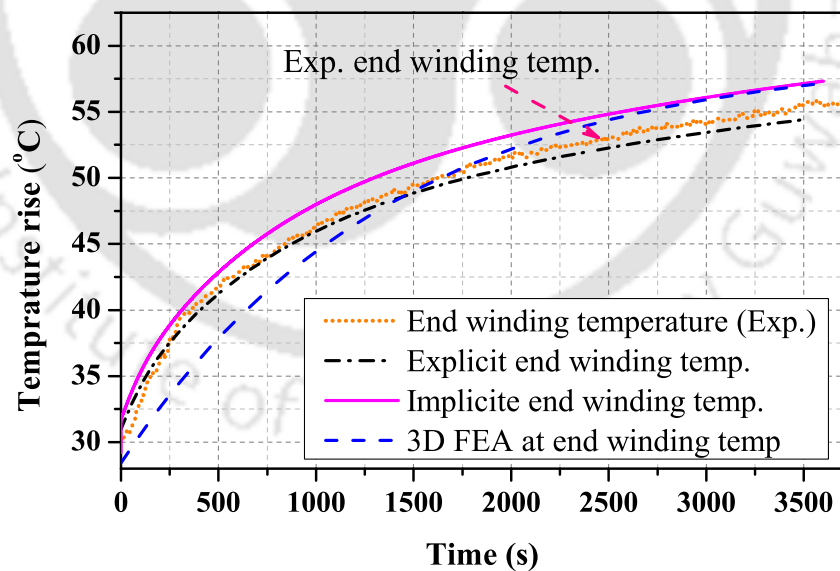
**Figure 5.8:** (a) Stator outer yoke temperature rise comparisons using 3D-FEA, IFD, EFD and Experimental. (b) Frame temperature rise comparisons using IFD, EFD and Experimental.

shows the rise in the temperature of the stator frame. It is observed that the results obtained by both of the models are approximately the same. Further, it also compares the temperature rise obtained through the explicit, implicit and through experimental setup. It is observed that the results of stator frame are very close to the experimental results for explicit and implicit

methods with a maximum deviation of  $0.43231^{\circ}\text{C}$ , and  $1.56876^{\circ}\text{C}$ , respectively.



(a)



(b)

**Figure 5.9:** (a) Stator inner yoke temperature rise comparisons using 3D FEA, explicit, implicit, and Experimental. (b) End winding temperature rise comparisons using 3D FEA, explicit, implicit, and Experimental.

Fig. 5.9(a), and 5.9(b) represents the temperature of stator inner yoke and end winding.

Here, the estimated temperature are given by the explicit, implicit, and 3D FEA. Further, the

## 5. EFD AND IFD THERMAL MODELING OF SELF-EXCITED SRG FOR WIND ENERGY APPLICATION

---

estimated results are verified through the experimental test. While performing the experimental test, the ambient temperature was about  $30^{\circ}\text{C}$ , hence, it is also used as the initial temperature of the explicit, implicit and 3D FEA.

From Fig. 5.9(a), it could be observed that the estimated temperature of the stator inner yoke by explicit method is slightly less than that of FEA while slightly more for the implicit method, but the results from all the methods are very close to the result as obtained from the experimental setup. It can also be observed that the rise in temperature settles to its final value in about 3000 s with a maximum deviation of  $3.15351^{\circ}\text{C}$ ,  $0.37738^{\circ}\text{C}$ , and  $0.86898^{\circ}\text{C}$  for explicit, implicit, and 3D FEA, respectively, as compared with the experimental result.

From Fig. 5.9(a), it can be observed that the temperature rise in stator inner yoke is limited to  $48.11677^{\circ}\text{C}$ ,  $51.64766^{\circ}\text{C}$ ,  $50.40130^{\circ}\text{C}$  and  $51.27028^{\circ}\text{C}$  for explicit, implicit, 3D-FEA, and experimental test, respectively.

Similarly, Fig. 5.9(b), shows the rise in the temperature of the stator end winding. It could be observed that the estimated temperature of the stator end winding by implicit method is slightly higher than FEA while for the explicit method it is slightly less, but the results obtained from all the methods are very close to the result obtained from the experimental setup i.e., with a maximum deviation of  $1.58121^{\circ}\text{C}$ ,  $2.4196^{\circ}\text{C}$ , and  $0.98902^{\circ}\text{C}$  for explicit, implicit and 3D FEA, respectively. Moreover, the temperature rise in end winding is limited to  $54.58187^{\circ}\text{C}$ ,  $58.58268^{\circ}\text{C}$ ,  $57.15210^{\circ}\text{C}$  and  $56.16308^{\circ}\text{C}$  for explicit, implicit, 3D-FEA, and experimental setup, respectively. Further, it also observed that the temperature rise in stator end winding is high as expected compared to other parts of the generator.

In summary, we observed that the highest temperature rise is seen at the stator end winding. Its maximum value is limited to  $\approx 56.16308^{\circ}\text{C}$  as per the experiment. From the experimental result, it can be seen that the stator outer yoke, and stator inner yoke temperature are limited to  $50.12790^{\circ}\text{C}$ , and  $51.27028^{\circ}\text{C}$ , respectively. The estimated and experimentally measured steady temperature for SRG at the rotor speed of 1500 rpm are summarized in Table 5.7.

**Table 5.7:** Explicit, implicit, FEA calculated and Experimental temperature at steady state

Components	Explicit (°C)	Implicit (°C)	3D FEA (°C)	Experimental (°C)
<i>Rotor core</i>	46.64943	50.10467	46.01390	--
<i>Rotor surface</i>	48.38283	51.56792	47.33711	--
<i>Air gap</i>	49.59510	53.14581	51.04108	--
<i>Stator inner yoke</i>	48.11677	51.64766	50.40130	51.27028
<i>Stator outer yoke</i>	47.42241	50.90403	49.91401	50.12790
<i>Stator teeth core</i>	51.36191	55.10828	49.8793	--
<i>Stator winding</i>	51.44554	55.21230	49.89515	--
<i>End winding</i>	54.58187	58.58268	57.15210	56.16308
<i>Frame</i>	40.26769	42.26876		40.7000

## 5.6 Summary

The thermal analysis of self-excited synchronous reluctance generator (SRG) is presented for wind energy application. The heat sources of different components of the generator, i.e., the electrical losses and core losses, are presented. Three methods are used to perform thermal analysis, i.e., FEA based, explicit and implicit methods. The work includes a comparative analysis of the estimated temperature rise by the three methods. It is observed that the estimated temperature is nearly the same for all methods. But, the computational complexity of the explicit, implicit is significantly less as compared with FEA based thermal analysis. Moreover, the estimated results are also very close to the results obtained through the experimental setup developed in the laboratory on the developed SRG.

From the thermal analysis of the SRG, it is observed that the maximum temperature rise of various components such as stator end winding (56.16308°), stator outer yoke (50.12790°), and stator inner (51.27028°) are within the acceptable limit of the machine as per the experimental test. It could also be concluded that the machine is safe from thermal overloading.

**5. EFD AND IFD THERMAL MODELING OF SELF-EXCITED SRG FOR WIND ENERGY APPLICATION**

---



# 6

## CONCLUSION AND FUTURE WORK

### Contents

---

6.1 Conclusions . . . . .	152
---------------------------	-----

---

### 6.1 Conclusions

Design and modeling of electric machine from wind turbine models is essential for the analysis and control purpose. There are several works reported in the literature on design of synchronous reluctance motors/generators. To improve the performance and efficiency of the machine, some rotor shape design are done. There is still some scope to extend the design of synchronous reluctance generator. The key findings of the study are explored in this section.

#### (i) Design and Modeling of Self-excited SRG for Wind Energy Application

The present thesis includes the design and modeling of reluctance generator. The performance of the machine, including the  $d$  and  $q$ -axes saturation effects has been evaluated to observe the merits and demerits of its use in rural area electrification. The compactness, reliable and efficiency of this generator have been evaluated. Considering inductive load, a simple formulae to calculate the required minimum excitation capacitance is developed. The effects of stator resistance on electromagnetic torque with variation of power angle have been evaluated. The work also include, how the generated voltage changes with the change of capacitor. It also verify that if the value of capacitor is less than minimum value of the capacitor, the generator is not able to generate the voltage. The analysis carried out in this section also includes, the effects of residual flux linkage on the excitation of reluctance generator. The performance of the machine for change of load, and speed is also determined. The results indicate that the generated current and voltage slightly decrease with decrease in load impedance. To keep the voltage constant, with change of load, it is important to continuously vary reactive power support i.e., to dynamically vary the capacitance of the capacitor. It is observed that if the wind-driven SRG operate at constant speed, the frequency remains constant despite the change in load. The above advantages, clearly show that designed SRG can effectively used for rural electrification.

#### (ii) Design and Modeling of Self-excited FM-SRG for Wind Energy Application

The effects on the performance index for the synchronous reluctance generator (SRG) by placing the low-cost ferrite magnet in the rotor air barrier with suitable location and orientation are presented. The orientation is chosen in such a way as to reduce the  $q$ -axis flux. It is observed that as the percentage volume of the ferrite magnet ( $V_{fm}$ ) increases in the air barrier, there is an increase in the performance index of SRG, but it is observed till the  $V_{fm} = 30\%$  for this particular design. For  $V_{fm} > 30\%$ , the performance index decrease, as there is a significant increase in the ripple torque. Hence, it can be said that till  $V_{fm} \leq 30\%$ , there is an improvement in power factor, compactness, and the operational efficiency of FM-SRG.

Moreover, the analysis in variation of the  $d$ -axes and  $q$ -axes flux linkage and inductances while varying the  $V_{fm}$  is evaluated. It also links this variation to the improved performance of the machine. Further, analytical, finite element analysis, and detail performance comparison of SRG and FM-SRG, are provided in the present work.

### (iii) Electromagnetic-mechanical Stress Analysis of Wind-Driven Self Excited SRG

The electromagnetic-mechanical stress analysis of SRG for a rotor with transverse lamination have been presented. How the thickness of ribs affects the electromagnetic performances of the machine have been discussed i.e., it is observed that with decrease in the thickness of both radial or tangential ribs, there is an increase in the inductance ratio ( $L_d/L_q$ ), which reaches to its peak value near to its rated current, and then there is a decrease in this ratio due to the effect of saturation in the core. Further, the mechanical stress analysis is done to find the minimum thickness of the ribs which could ensure mechanical stability. It is also observed that the maximum stress is either at tangential ribs or radial rib of the SRG rotor. To ensure the mechanical stability, a safety factor of 2.5 is used in the present work. It also suggest the minimum thickness of the ribs.

### (iv) Thermal Analysis of Wind Driven Self Excited SRG

The lumped parameter model of the self excited synchronous reluctance generator (SRG)

## 6. CONCLUSION AND FUTURE WORK

---

is used to evaluate the thermal analysis. In the developed model, the losses of different components of the generator, i.e., the electrical losses and core losses, are represented as heat sources. The lumped parameter model uses explicit, and implicit methods to estimate the temperature of various components of SRG. The results are compared with the finite element method based thermal analysis. It is observed that the estimated temperature is nearly the same for all methods. But, it is observed that in the explicit, and implicit finite difference the analysis is simple and fast compared to Finite Element Analysis (FEA). Moreover, the explicit, and implicit results are very close to the results obtained through the experimental setup developed in the laboratory, which includes the developed SRG. From the thermal analysis of the SRG, it is observed that the maximum temperature rise of various components such as stator end winding ( $56.16308^\circ$ ), stator outer yoke ( $50.12790^\circ$ ), and stator inner ( $51.27028^\circ$ ) are within the acceptable limit of the machine as per the experimental test. It could also be concluded that the machine is safe from thermal overloading.

### 6.1.1 Scope for further work

In this thesis, some design algorithms are given. These can be extended as further work;

- It is observed that the generated voltage varies with the change of capacitors, load, and rotor speed. Therefore, a capacitor with variable capacitance is needed at the terminal of the generator. Current work does not include how it can be achieved, hence, the work can be extended to include it.
- The work does not include its performance when connected to a Micro-grid, hence, the present work can be extended with the study on its impact on the microgrid.
- The present work does not include the experimental verification of FM-SRG. The work can be extended with its inclusion.



## 6. CONCLUSION AND FUTURE WORK

---





# A

## **SUPPLEMENTARY MATERIALS**

**Contents**

---

<b>A.1</b>	<b>Some important design equations are placed as:</b>	<b>158</b>
<b>A.2</b>	<b>Stator and Rotor Details:</b>	<b>158</b>
<b>A.3</b>	<b>The Impedance load detail derivation</b>	<b>159</b>
<b>A.4</b>	<b>The steady state torque derivation of SRG</b>	<b>168</b>

---

**A.1 Some important design equations are placed as:**

$$L_{md} = k_d L_m, L_{mq} = k_q L_m$$

$$\xi_1 = \frac{L_d}{L_q} = \frac{(k_d + k_q)}{2k_q}$$

where,  $\xi_1$  is power factor.

$$L_s = \tau \left( \frac{L_s}{\tau} \right)$$

$$\tau_s = \frac{\tau}{3q}, q = \frac{Q_s}{6P}$$

$$A_s = \frac{mI_m}{k_u J}$$

where,  $A_s$ ,  $\tau_s$  and  $k_u$  are slot area, slot pitch, and slot filling factor respectively.

$$L_d = L_{md} + L_{ls}, L_q \simeq 2L_{mq}$$

$$e_s = \frac{2h'}{3(b_1 + b_2)} + \frac{2h_2}{(b_1 + b)} + \frac{h_1}{b}$$

$$e_a = \frac{5l_g}{(5b + 4l_g)}, e_e = \frac{0.34q}{L_s(L_e - 0.64\tau)}$$

$$k_c = \frac{\tau(5l_g + b)}{\tau(5l_g + b) - b^2}, k_s = \frac{B_m}{B_a}$$

where,  $B_a$  is average air gap flux density

**A.2 Stator and Rotor Details:**

**A.2.1 Stator and slot details design:**

Fig.A.1 shows that the detail design of stator structure.

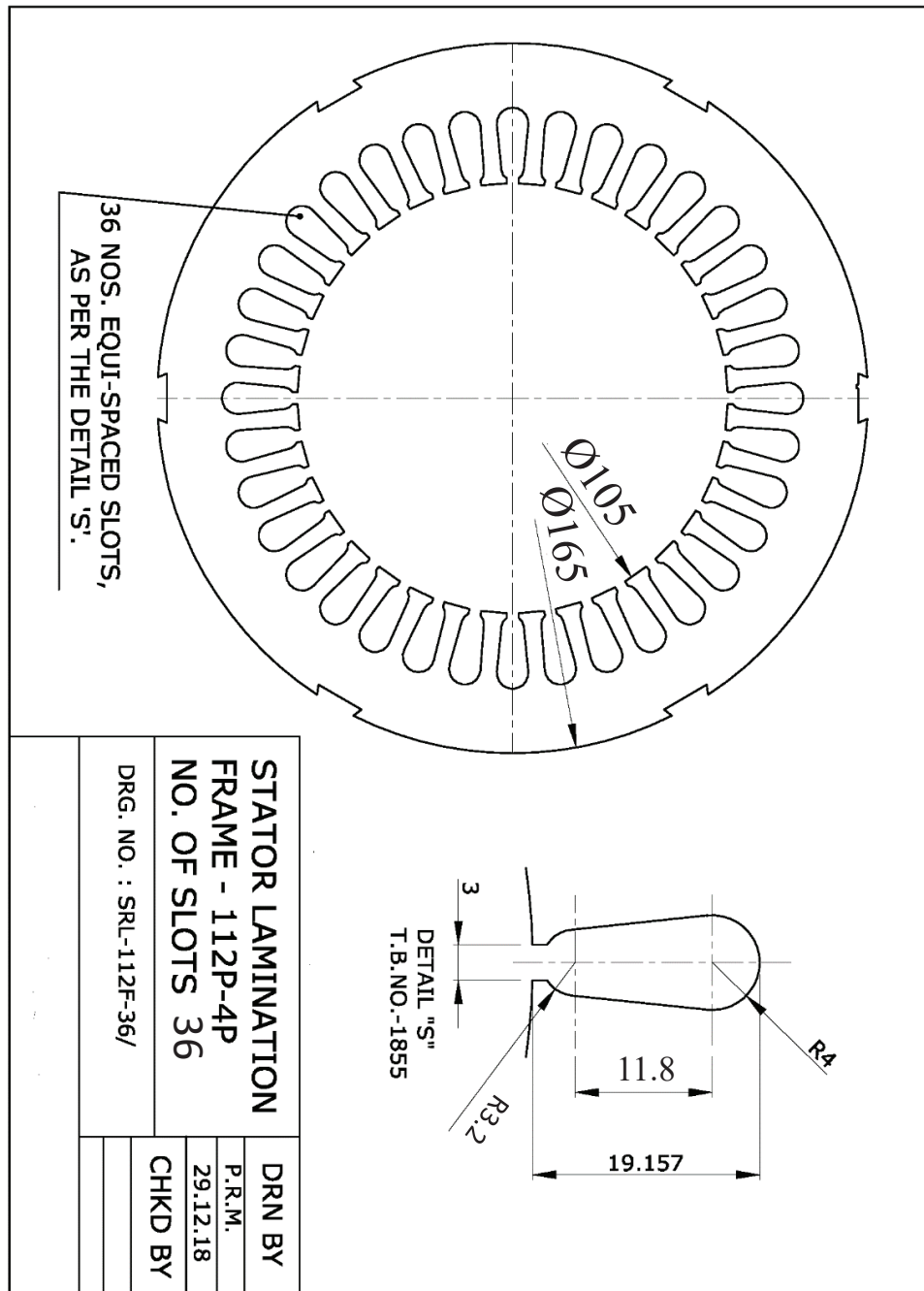


Figure A.1: Stator structure design

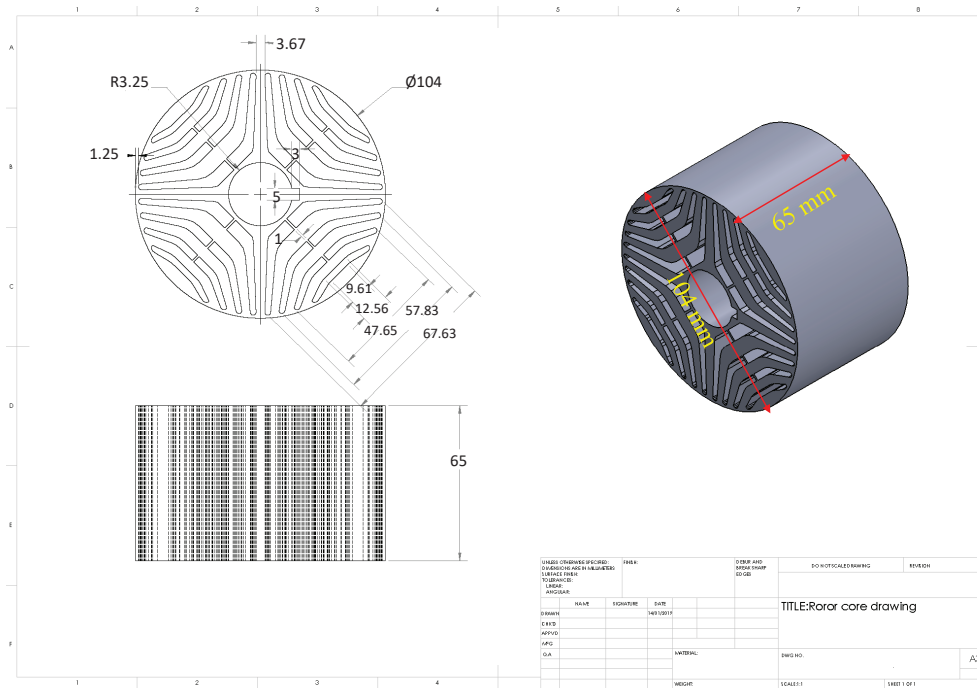
### A.2.2 Complete rotor lamination:

Fig.A.2 shows that different view of rotor structure.

## A.3 The Impedance load detail derivation

The equivalent circuit shown in Fig.A.3 has the voltage, current, and flux equations. To derive the dynamic equations, the d- q-axes components of the variable V, I and  $\Lambda$  are utilized.

## A. SUPPLEMENTARY MATERIALS



**Figure A.2:** Rotor structure design view

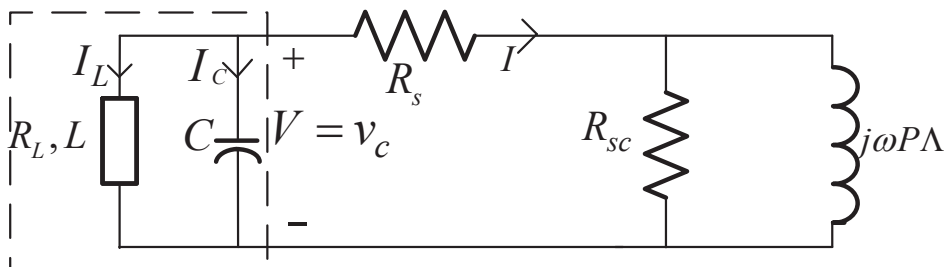


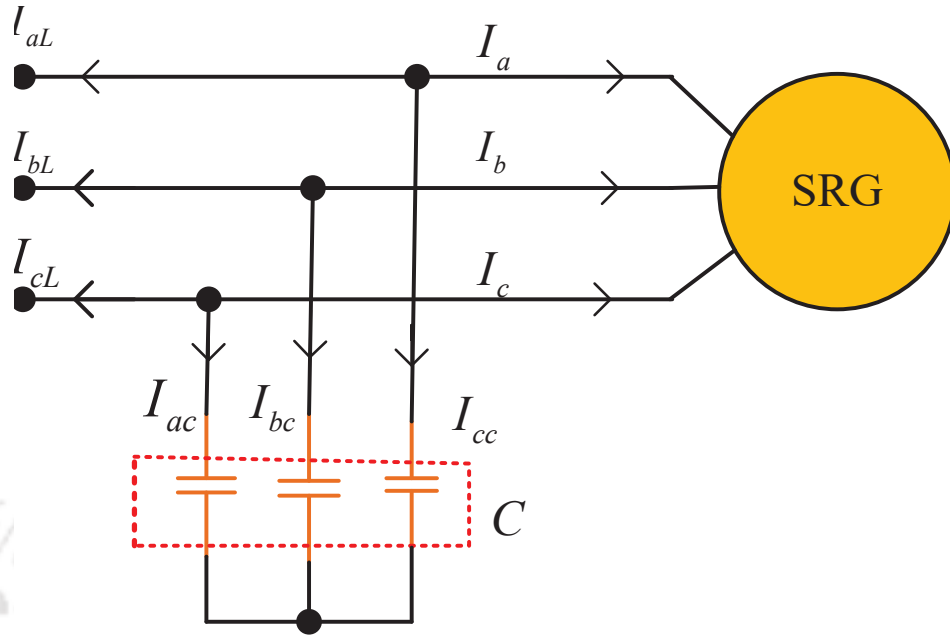
**Figure A.3:** Circuit of the synchronous reluctance generator with capacitor  $C$ , resistive  $R_L$  and inductive  $X_L$  loads

The  $d$ - and  $q$ -axes components of circuit shown in Fig.A.3 the equations are obtained as:

$$V = V_d + jV_q \quad (\text{A.1})$$

$$I = I_d + jI_q \quad (\text{A.2})$$

$$\Lambda = \lambda_d + j\lambda_q \quad (\text{A.3})$$



### Capacitors Bank

Figure A.4: Synchronous reluctance generator with required capacitor C

#### A.3.1 Excitation Capacitors Modeling

For the capacitor component the current for three-phase stated as:

From Fig.A.4 the currents through the capacitors can be obtained as:

$$I_{acbcc} = \rho q_{acbcc} \quad (A.4)$$

where  $q_{acbcc}$  is charge in the capacitance phase  $a$ ,  $b$ , and  $c$ . The  $\rho$  is operator, and given as

$$\rho = \frac{d}{dt}.$$

Thus,

$$I_{acbcc} = \frac{d}{dt} q_{acbcc} \quad (A.5)$$

The transformation of variables yields:

$$I_{dqo} = k_s \rho \left[ k_s^{-1} q_{dqo} \right] \quad (A.6)$$

Where,  $k_s$  can be expressed as:

## A. SUPPLEMENTARY MATERIALS

---

$$k_s = \frac{2}{3} \begin{bmatrix} \cos\theta & \cos(\theta - 2\pi/3) & \cos(\theta + 2\pi/3) \\ \sin\theta & \sin(\theta - 2\pi/3) & \sin(\theta + 2\pi/3) \\ 1/2 & 1/2 & 1/2 \end{bmatrix} \quad (\text{A.7})$$

and,  $\frac{d\theta}{dt} = \omega_e$

From the inverse transformation,  $k_s^{-1}$  given as:

$$k_s^{-1} = \frac{1}{\det(k_s)} \text{adj}(k_s) \quad (\text{A.8})$$

yields

$$k_s^{-1} = \begin{bmatrix} \cos\theta & \sin\theta & 1 \\ \cos(\theta - 2\pi/3) & \sin(\theta - 2\pi/3) & 1 \\ \cos(\theta + 2\pi/3) & \sin(\theta + 2\pi/3) & 1 \end{bmatrix} \quad (\text{A.9})$$

and,

$$I_{dqo} = k_s \rho \left[ k_s^{-1} q_{dqo} \right] \quad (\text{A.10})$$

can be written as:

$$I_{dqo} = k_s \rho \left[ k_s^{-1} \right] q_{dqo} + k_s k_s^{-1} \rho q_{dqo} \quad (\text{A.11})$$

Therefore,

$$\rho \left[ k_s^{-1} \right] = \begin{bmatrix} -\sin\theta \frac{d\theta}{dt} & \cos\theta \frac{d\theta}{dt} & 0 \\ -\sin(\theta - 2\pi/3) \frac{d\theta}{dt} & \cos(\theta - 2\pi/3) \frac{d\theta}{dt} & 0 \\ -\sin(\theta + 2\pi/3) \frac{d\theta}{dt} & \cos(\theta + 2\pi/3) \frac{d\theta}{dt} & 0 \end{bmatrix} \quad (\text{A.12})$$

But,  $\frac{d\theta}{dt} = \omega_e$

implies that:

$$\rho \left[ k_s^{-1} \right] = \omega_e \begin{bmatrix} -\sin\theta & \cos\theta & 0 \\ -\sin(\theta - 2\pi/3) & \cos(\theta - 2\pi/3) & 0 \\ -\sin(\theta + 2\pi/3) & \cos(\theta + 2\pi/3) & 0 \end{bmatrix} \quad (\text{A.13})$$

From equations A.7 and A.13

$$k_s \rho \begin{bmatrix} k_s^{-1} \end{bmatrix} = \frac{2}{3} \begin{bmatrix} \cos\theta & \cos(\theta - 2\pi/3) & \cos(\theta + 2\pi/3) \\ \sin\theta & \sin(\theta - 2\pi/3) & \sin(\theta + 2\pi/3) \\ 1/2 & 1/2 & 1/2 \end{bmatrix} \times \omega_e \begin{bmatrix} -\sin\theta & \cos\theta & 0 \\ -\sin(\theta - 2\pi/3) & \cos(\theta - 2\pi/3) & 0 \\ -\sin(\theta + 2\pi/3) & \cos(\theta + 2\pi/3) & 0 \end{bmatrix} \quad (\text{A.14})$$

As per trigonometric ratio it yields:

$$k_s \rho \begin{bmatrix} k_s^{-1} \end{bmatrix} = \frac{2}{3} \omega_e \begin{bmatrix} 0 & 3/2 & 0 \\ -3/2 & 0 & 0 \\ 0 & 0 & 0 \end{bmatrix} = \omega_e \begin{bmatrix} 0 & 1 & 0 \\ -1 & 0 & 0 \\ 0 & 0 & 0 \end{bmatrix} \quad (\text{A.15})$$

thus,

$$I_{dqo} = k_s \rho \begin{bmatrix} k_s^{-1} \end{bmatrix} q_{dqo} + k_s k_s^{-1} \rho q_{dqo}; k_s k_s^{-1} = 1 \quad (\text{A.16})$$

The stored charge on capacitance given as:

$$q_{dqo} = CV_{dqo}; \quad (\text{A.17})$$

for capacitor,

$$q_{dcqoc} = CV_{dcqoc} \quad (\text{A.18})$$

and

$$V_{dcqoc} = V_{dLqLoL} \quad (\text{A.19})$$

then,

$$I_{dcqoc} = \begin{bmatrix} 0 & \omega_e & 0 \\ -\omega_e & 0 & 0 \\ 0 & 0 & 0 \end{bmatrix} \times \begin{bmatrix} q_{dc} \\ q_{qc} \\ q_{oc} \end{bmatrix} + \rho q_{dcqoc} \quad (\text{A.20})$$

Consequently,

## A. SUPPLEMENTARY MATERIALS

---

$$\begin{bmatrix} I_{dc} \\ I_{qc} \end{bmatrix} \begin{bmatrix} 0 & \omega_e C V_{qL} & 0 \\ -\omega_e C V_{dL} & 0 & 0 \\ 0 & 0 & 0 \end{bmatrix} + \begin{bmatrix} C \rho V_{dL} \\ C \rho V_{qL} \end{bmatrix} \quad (\text{A.21})$$

$$I_{dc} = \omega_e C V_{qL} + C \rho V_{dL} \quad (\text{A.22})$$

$$I_{qc} = -\omega_e C V_{qL} + C \rho V_{qL} \quad (\text{A.23})$$

By applying Kirchoff's current law (KCL), the capacitors  $d$ - and  $q$  - axes current can be obtained as:

$$I_{dc} = -I_d - I_{dL} \quad (\text{A.24})$$

$$I_{qc} = -I_q - I_{qL} \quad (\text{A.25})$$

From equations A.22, A.23, A.24 and A.25 we have:

$$\rho V_{qL} = \omega_e \rho V_{dL} + \frac{-I_q - I_{qL}}{C} \quad (\text{A.26})$$

$$\rho V_{dL} = -\omega_e \rho V_{qL} + \frac{-I_d - I_{dL}}{C} \quad (\text{A.27})$$

### A.3.2 Resistive and Inductive loads Modeling

The detail derivation of expression in (2.27) obtained from resistive and inductive can be explained as:

For a three phase resistive, the transformation of:

$$V_{abc} = R_L I_{abc} \quad (\text{A.28})$$

transformation of  $V_{abc}$ , will be

$$V_{dgo} = k_s R_L k_s^{-1} I_{dgo} \quad (\text{A.29})$$

From equation A.16,  $k_s k_s^{-1} = 1$

Therefore, equation A.29 becomes

$$V_{dqo} = R_L I_{dqo} \quad (\text{A.30})$$

Or

$$\begin{bmatrix} V_d \\ V_q \end{bmatrix} = \begin{bmatrix} R_L & 0 \\ 0 & R_L \end{bmatrix} \begin{bmatrix} I_d \\ I_q \end{bmatrix} \text{ i.e., } V_d = R_L I_d, V_q = R_L I_q \quad (\text{A.31})$$

For a three phase inductive, the transformation of:

$$V_{abc} = \rho \lambda_{abc} = \frac{d}{dt} \lambda_{abc} \quad (\text{A.32})$$

can be expressed as:

$$V_{dqo} = \rho k_s \left[ k_s^{-1} \lambda_{dqo} \right] \quad (\text{A.33})$$

equation A.33, can be written as:

$$V_{dqo} = k_s \rho \left[ k_s^{-1} \lambda_{dqo} \right] + k_s k_s^{-1} \rho \lambda_{dqo} \quad (\text{A.34})$$

for steady state,

$$\rho \lambda_{dqo} = 0 \quad (\text{A.35})$$

and for dynamic state,

$$\rho \lambda_{dqo} \neq 0 \quad (\text{A.36})$$

From equation A.13:

$$\rho \left[ k_s^{-1} \right] = \omega_e \begin{bmatrix} -\sin\theta & \cos\theta & 0 \\ -\sin(\theta - 2\pi/3) & \cos(\theta - 2\pi/3) & 0 \\ -\sin(\theta + 2\pi/3) & \cos(\theta + 2\pi/3) & 0 \end{bmatrix} \quad (\text{A.37})$$

## A. SUPPLEMENTARY MATERIALS

---

and

$$k_s \rho \begin{bmatrix} k_s^{-1} \end{bmatrix} = \begin{bmatrix} 0 & \omega_e & 0 \\ -\omega_e & 0 & 0 \\ 0 & 0 & 0 \end{bmatrix} \quad (\text{A.38})$$

thus for inductive load,

$$V_{dqo} = \begin{bmatrix} 0 & \omega_e & 0 \\ -\omega_e & 0 & 0 \\ 0 & 0 & 0 \end{bmatrix} \begin{bmatrix} \lambda_d \\ \lambda_q \\ \lambda_o \end{bmatrix} + \rho \lambda_{dqo} \quad (\text{A.39})$$

Implies,

$$\begin{bmatrix} V_d \\ V_q \\ V_o \end{bmatrix} \begin{bmatrix} 0 & \omega_e & 0 \\ -\omega_e & 0 & 0 \\ 0 & 0 & 0 \end{bmatrix} \begin{bmatrix} \lambda_d \\ \lambda_q \\ \lambda_o \end{bmatrix} + \begin{bmatrix} \rho \lambda_d \\ \rho \lambda_q \\ \rho \lambda_o \end{bmatrix} \quad (\text{A.40})$$

Or, for balanced load equation A.40 can be expressed as:

$$\begin{bmatrix} V_d \\ V_q \end{bmatrix} \begin{bmatrix} 0 & \omega_e & 0 \\ -\omega_e & 0 & 0 \end{bmatrix} \begin{bmatrix} \lambda_d \\ \lambda_q \end{bmatrix} + \begin{bmatrix} \rho \lambda_d \\ \rho \lambda_q \end{bmatrix} \quad (\text{A.41})$$

i.e.,

$$V_d = \omega_e \lambda_q + \rho \lambda_d \quad (\text{A.42})$$

and,

$$V_q = -\omega_e \lambda_d + \rho \lambda_q \quad (\text{A.43})$$

But,

$$\lambda_d = L_d I_d \quad (\text{A.44})$$

and

$$\lambda_q = L_q I_q \quad (\text{A.45})$$

From equations A.43, A.44 and A.45 the  $d$ - and  $q$ - axes voltage can be written as:

$$V_q = -\omega_e \lambda_d + L_q \rho I_q \quad (\text{A.46})$$

$$V_d = \omega_e \lambda_q + L_d \rho I_d \quad (\text{A.47})$$

The voltage across the load is the sum of voltage drop across the resistance and inductance loads. Thus, from equations A.31, A.46, and A.47, the  $q$ - and  $d$ - axes load voltages obtained as:

$$V_{dL} = V_d(\text{inductive}) + V_d(\text{resistive}) \quad (\text{A.48})$$

$$V_{qL} = V_q(\text{inductive}) + V_q(\text{resistive}) \quad (\text{A.49})$$

As shown in Fig.A.5, we have inductive load  $L$  and resistive load  $R_L$  for  $d$ - and  $q$ -axes equivalent circuit.

Provided that:

$$\begin{cases} V_{qL} = -\omega_e L I_{dL} + R_L I_{qL} + L \rho I_{qL} \\ V_{dL} = \omega_e L I_{qL} + R_L I_{dL} + L \rho I_{dL} \end{cases} \quad (\text{A.50})$$

Equation A.50, yields:

$$\begin{cases} I_{qL} = \int \frac{1}{L} (V_{qL} - I_{qL} R_L + \omega P L I_{dL}) dt \\ I_{dL} = \int \frac{1}{L} (V_{dL} - I_{dL} R_L - \omega P L I_{qL}) dt \end{cases} \quad (\text{A.51})$$

Where,  $\omega P = \omega_e$

Finally, the  $d$ - and  $q$ - axes load modeling with capacitors, inductor and resistor shown in

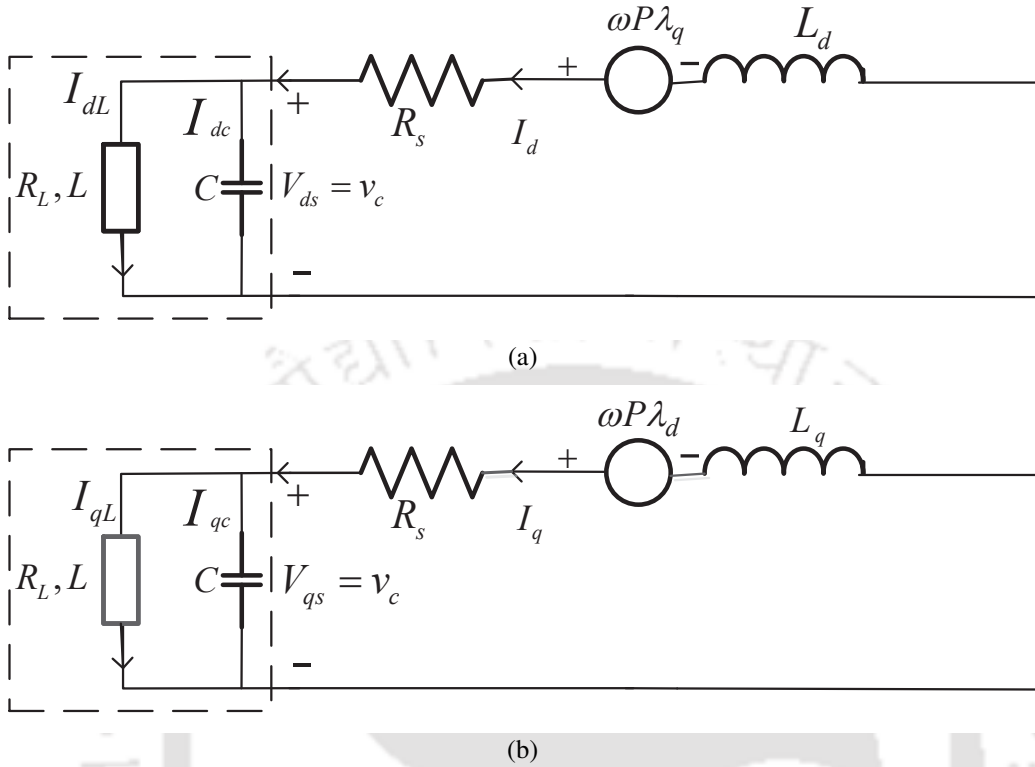


**Figure A.5:** (a) Rotor reference frame equivalent circuit of a self excited reluctance generator (d-axis). (b) Rotor reference frame equivalent circuit of a self excited reluctance generator (q-axis).

Fig. A.5(a) and A.5(b) respectively.

#### A.4 The steady state torque derivation of SRG

For steady state the stator voltages are symmetric and sinusoidal quantities and the speed is constant. The voltages equation can be written as:

$$V_{a,b,c} = V_{max} \cos(\omega_e t - (j-1)\frac{2\pi}{3}); j = 1, 2, 3 \quad (A.52)$$

Using the Park, transformation of  $V_{abc}$  to  $V_{dq}$

$$V_d = V_{max} \cos(\theta_1), \quad V_q = V_{max} \sin(\theta_1), \quad V_o = 0 \text{ (symmetry)}, \quad \text{and} \quad \frac{d}{dt} = 0 \quad (A.53)$$

The actual stator current,  $I_{abc}$  are also symmetric quantities with frequency,  $P\omega$ . But lag the phase voltage by  $\theta_1$ . Therefore,

$$I_d = I_{max} \cos(\theta_1 - \theta_1), \quad I_q = I_{max} \sin(\theta_1 - \theta_1), \quad I_o = 0 \text{ (symmetry)}. \quad (A.54)$$

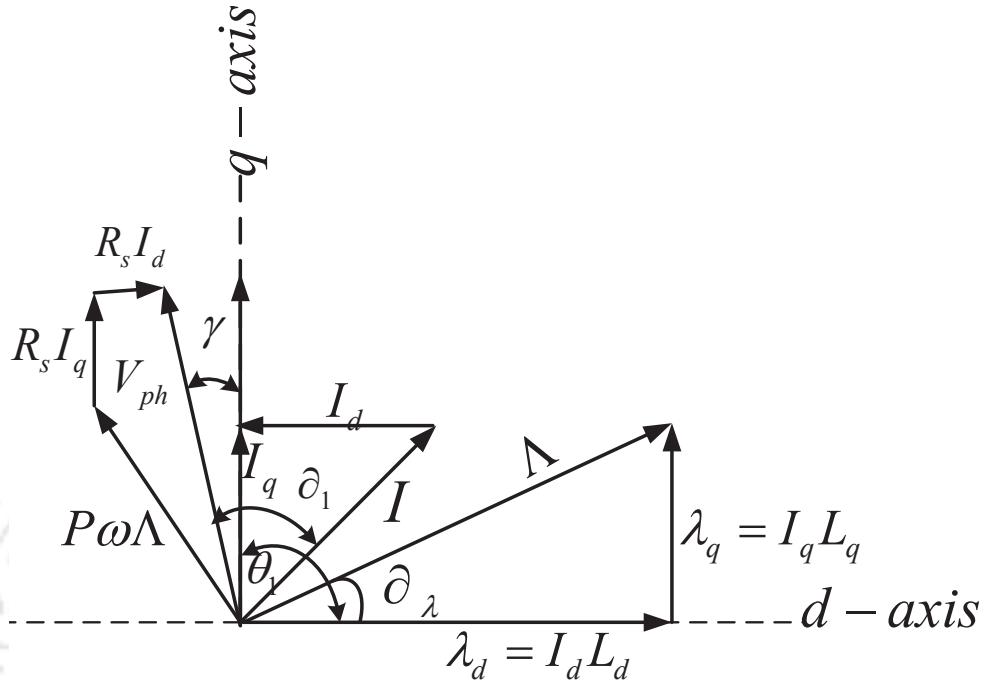


Figure A.6: The vector diagram of SRG (motor convection)

where,

$$I = I_d + jI_q, \quad V_{ph} = V_d + jV_q, \quad \Lambda = \lambda_d + j\lambda_q. \quad (\text{A.55})$$

$$V_{ph} = IR_s + jP\omega\Lambda, \quad T_e = \frac{3}{2}P\text{Re}j(\Lambda I^*) = \frac{3P}{2}(L_d - L_q)I_dI_q \quad (\text{A.56})$$

and,

$$\Lambda = L_dI_d + jL_qI_q \quad (\text{A.57})$$

The vector diagram for steady state as shown in Fig.A.6 a space electric angle (power angle) shift between  $q$  – axis and stator voltage,  $V_{ph}$ .

$$\theta_1 = \pm\left(\frac{\pi}{2} + \gamma\right) \quad (\text{A.58})$$

While, +, – are for motoring and generating modes respectively. Using the above equations, and substituting in to A.56, it yields:

$$\begin{cases} V_d + jV_q = IR_s + jP\omega\Lambda \\ V_d + jV_q = (I_d + jI_q)R_s + jP\omega(L_dI_d + jL_qI_q) \\ V_{max}\cos(\theta_1) + jV_{max}\sin(\theta_1) = (I_d + jI_q)R_s + jP\omega(L_dI_d + jL_qI_q) \end{cases} \quad (\text{A.59})$$

## A. SUPPLEMENTARY MATERIALS

---

Equation A.59, is true if the left side and right side imaginary and real parts are equal. Therefore,

$$\begin{cases} V_{max}\cos(\theta_1) = I_d R_s - P\omega L_q I_q \\ V_{max}\sin(\theta_1) = I_q R_s + P\omega L_d I_d \end{cases} \quad (\text{A.60})$$

From A.60, solve for  $I_d$  as:

$$\frac{V_{max}\cos(\theta_1) + P\omega L_q I_q}{R_s} = I_d \quad (\text{A.61})$$

$$\frac{V_{max}\sin(\theta_1) - I_q R_s}{P\omega L_d I_d} = I_d \quad (\text{A.62})$$

Equating equations A.61 and A.62, applying,  $\theta_1 = \pm(\frac{\pi}{2} + \gamma)$ , it provides that:

$$\frac{V_{max}[\cos(\gamma)R_s - P\omega L_d \sin(\gamma)]}{(P\omega)^2 L_q L_d + R_s^2} = I_q \quad (\text{A.63})$$

Similarly,  $I_d$  obtained as:

$$\frac{V_{max}[\cos(\gamma)R_s + P\omega L_q \sin(\gamma)]}{(P\omega)^2 L_q L_d + R_s^2} = I_d \quad (\text{A.64})$$

Substituting equations A.63 and A.64 in to equation A.56, And defining,  $\beta = R_s/(P\omega L_d)$ ,  $\varphi = L_q/L_d$ , it provides:

$$T_e = \frac{3P}{(2(P\omega)^2 L_d)(\varphi + \beta^2)^2} V_{max}^2 (1 - \varphi) \left[ (\varphi - \beta^2) \sin(2\gamma) - 2\beta(1 + \varphi) \sin^2(\gamma) + 2\varphi\beta \right] \quad (\text{A.65})$$

### A.4.1 Effects of ferrite-magnet on $q$ – axis flux

The vector diagram for FM-SRG is shown in Fig.A.7,  $I$ ,  $I_q$ , and  $I_d$  are stator current and its  $q$ – and  $d$ – axes components respectively. Similarly,  $L_q$  and  $L_d$  are  $q$ – and  $d$ – axes inductances. The  $\Lambda$  is the flux linkage of the SRG, when ferrite-magnet are inserted in the rotor, the FM-SRG flux linkage along the negative  $q$ -axis,  $\Lambda_m$  is added. Then, the flux becomes  $\Lambda'_m$

Therefore, using the torque relation,  $T_{em} = T_e + \frac{3P}{2} \Lambda_m I_d$ , the electromagnetic torque of a FM-

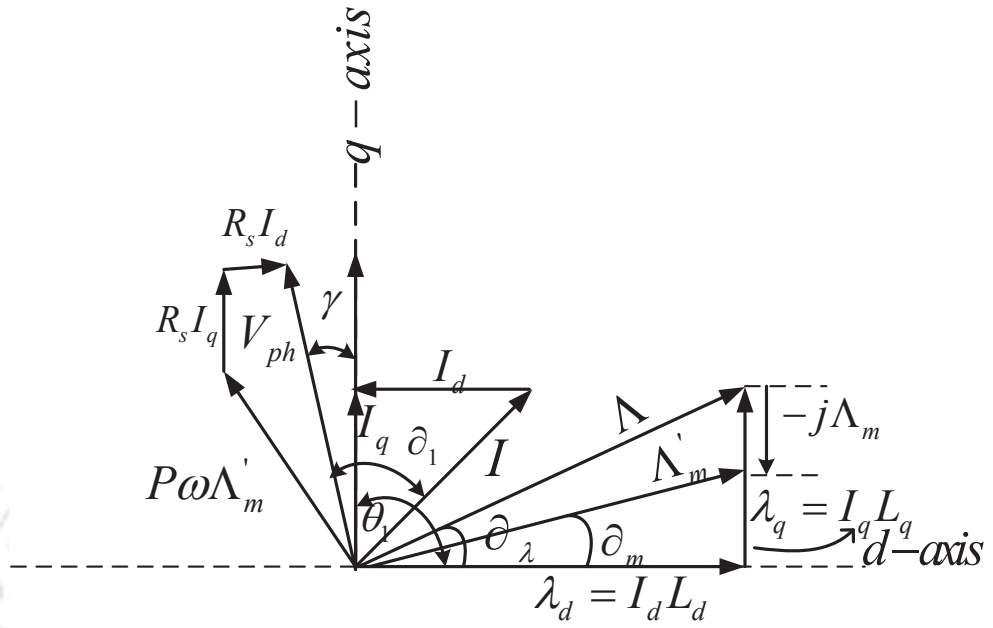


Figure A.7: The vector diagram of FM-SRG (motor convection)

SRG without neglecting stator resistance effects, can be expressed as:

$$T_{em} = \frac{3P}{2} \left[ I_d \Lambda_m + \frac{1}{((P\omega)^2 L_d)(\varphi + \beta^2)^2} V_{max}^2 (1 - \varphi) \left[ (\varphi - \beta^2) \sin(2\gamma) - 2\beta(1 + \varphi) \sin^2(\gamma) + 2\varphi\beta \right] \right] \quad (A.66)$$



## Bibliography

- [1] R. Shafaie, M. Kalantar, and A. Gholami, "Thermal analysis of 10-mw-class wind turbine hts synchronous generator," *IEEE Transactions on Applied Superconductivity*, vol. 24, no. 2, pp. 90–98, 2014.
- [2] F. Ahmed and N. C. Kar, "Analysis of end-winding thermal effects in a totally enclosed fan-cooled induction motor with a die cast copper rotor," *IEEE Transactions on Industry Applications*, vol. 53, no. 3, pp. 3098–3109, 2017.
- [3] A. Boglietti, A. Cavagnino, M. Lazzari, and A. Pastorelli, "A simplified thermal model for variable speed self cooled industrial induction motor," in *Conference Record of the 2002 IEEE Industry Applications Conference. 37th IAS Annual Meeting (Cat. No. 02CH37344)*, vol. 2. IEEE, 2002, pp. 723–730.
- [4] T. Ayodele and A. Ogunjuyigbe, "Wind energy resource, wind energy conversion system modelling and integration: a survey," *International Journal of Sustainable Energy*, vol. 34, no. 10, pp. 657–671, 2015.
- [5] S. Alghuwainem, "Steady-state analysis of an isolated self-excited induction generator driven by regulated and unregulated turbine," *IEEE transactions on energy conversion*, vol. 14, no. 3, pp. 718–723, 1999.
- [6] B. Wu, Y. Lang, N. Zargari, and S. Kouro, *Power conversion and control of wind energy systems*. John Wiley & Sons, 2011, vol. 76.
- [7] I. Boldea, *The Electric Generators Handbook-2 Volume Set*. CRC Press, 2005.
- [8] K. Idjdarene, D. Rekioua, T. Rekioua, and A. Tounzi, "Performance of an isolated induction generator under unbalanced loads," *IEEE Transactions on energy conversion*, vol. 25, no. 2, pp. 303–311, 2010.
- [9] T. Ayodele, A. Ogunjuyigbe, and O. Akinola, "Optimal location, sizing, and appropriate technology selection of distributed generators for minimizing power loss using genetic algorithm," *Journal of Renewable Energy*, vol. 2015, 2015.
- [10] A. Alolah, "Capacitance requirements for three phase self-excited reluctance generators," in *IEE Proceedings C-Generation, Transmission and Distribution*, vol. 138, no. 3. IET, 1991, pp. 193–198.
- [11] S.-C. Kuo and L. Wang, "Analysis of isolated self-excited induction generator feeding a rectifier load," *IEE Proceedings-Generation, Transmission and Distribution*, vol. 149, no. 1, pp. 90–97, 2002.
- [12] Y. Rahim, J. Fletcher, and N. Hassanain, "Performance analysis of salient-pole self-excited reluctance generators using a simplified model," *IET Renewable Power Generation*, vol. 4, no. 3, pp. 253–260, 2010.

## BIBLIOGRAPHY

---

- [13] F. El-Khouly and A. Osheiba, "Brushless induction and reluctance generators with dc excitation: experimental verification," *Electric Power Components and Systems*, vol. 32, no. 8, pp. 839–853, 2004.
- [14] C. M. Donaghy-Spargo, "Electromagnetic–mechanical design of synchronous reluctance rotors with fine features," *IEEE Transactions on Magnetics*, vol. 53, no. 11, pp. 1–8, 2017.
- [15] T. Matsuo and T. A. Lipo, "Rotor design optimization of synchronous reluctance machine," *IEEE Transactions on Energy Conversion*, vol. 9, no. 2, pp. 359–365, 1994.
- [16] E. Obe, "Calculation of inductances and torque of an axially laminated synchronous reluctance motor," *IET electric power applications*, vol. 4, no. 9, pp. 783–792, 2010.
- [17] L. Wang, J. Wei, X. Wang, and X. Zhang, "The development and prospect of offshore wind power technology in the world," in *2009 World Non-Grid-Connected Wind Power and Energy Conference*. IEEE, 2009, pp. 1–4.
- [18] R. G. Sullivan, J. Cothren, S. L. Winters, C. Cooper, M. Williamson, and D. Ball, "An assessment of offshore wind turbine visibility in the united kingdom," in *2012 Oceans*. IEEE, 2012, pp. 1–9.
- [19] F. Abdel-Kader, "The reluctance machine as a self-excited reluctance generator," *Electric machines and power systems*, vol. 10, no. 2-3, pp. 141–148, 1985.
- [20] Y. Wang and N. Bianchi, "Investigation of self-excited synchronous reluctance generators," *IEEE Transactions on Industry Applications*, vol. 54, no. 2, pp. 1360–1369, 2018.
- [21] C.-T. Liu, T.-Y. Luo, C.-C. Hwang, and B.-Y. Chang, "Field path design assessments of a high-performance small-power synchronous-reluctance motor," *IEEE Trans. Magn.*, vol. 51, no. 11, 2015.
- [22] T. Chan, "Steady-state analysis of a three-phase self-excited reluctance generator," *IEEE transactions on energy conversion*, vol. 7, no. 1, pp. 223–230, 1992.
- [23] S. S. Maroufian and P. Pillay, "Self-excitation criteria of the synchronous reluctance generator in stand-alone mode of operation," *IEEE Transactions on Industry Applications*, vol. 54, no. 2, pp. 1245–1253, 2018.
- [24] N. Bianchi, S. Bolognani, D. Bon, and M. Dai Pre, "Rotor flux-barrier design for torque ripple reduction in synchronous reluctance and pm-assisted synchronous reluctance motors," *IEEE Transactions on Industry Applications*, vol. 45, no. 3, pp. 921–928, 2009.
- [25] M. Ibrahim and P. Pillay, "The loss of self-excitation capability in stand-alone synchronous reluctance generators," *IEEE Transactions on Industry Applications*, vol. 54, no. 6, pp. 6290–6298, 2018.
- [26] Y. Wang and N. Bianchi, "Analysis of self-excited pm-assisted reluctance generators," *IEEE Transactions on Energy Conversion*, vol. 33, no. 2, pp. 877–885, 2018.
- [27] N. Bianchi, E. Fornasiero, M. Ferrari, and M. Castiello, "Experimental comparison of pm-assisted synchronous reluctance motors," *IEEE Transactions on Industry Applications*, vol. 52, no. 1, pp. 163–171, 2016.
- [28] Y. Wang, G. Bacco, and N. Bianchi, "Geometry analysis and optimization of pm-assisted reluctance motors," *IEEE Transactions on Industry Applications*, vol. 53, no. 5, pp. 4338–4347, 2017.

- [29] M. Ferrari, N. Bianchi, and E. Fornasiero, "Analysis of rotor saturation in synchronous reluctance and pm-assisted reluctance motors," *IEEE Trans. Ind. Appl.*, vol. 51, no. 1, pp. 169–177, 2015.
- [30] M. S. Camara, M. B. Camara, B. Dakyo, and H. Gualous, "Permanent magnet synchronous generator for offshore wind energy system connected to grid and battery-modeling and control strategies," *International Journal of Renewable Energy Research (IJRER)*, vol. 5, no. 2, pp. 386–393, 2015.
- [31] K. Latoufis, G. Messinis, P. Kotsampopoulos, and N. Hatziargyriou, "Axial flux permanent magnet generator design for low cost manufacturing of small wind turbines," *Wind engineering*, vol. 36, no. 4, pp. 411–431, 2012.
- [32] A. G. Aissaoui and A. Tahour, "Wind turbines-design, control and applications," 2016.
- [33] R.-R. Moghaddam and F. Gyllensten, "Novel high-performance synrm design method: An easy approach for a complicated rotor topology," *IEEE Transactions on Industrial Electronics*, vol. 61, no. 9, pp. 5058–5065, 2014.
- [34] D. Bang, H. Polinder, G. Shrestha, and J. A. Ferreira, "Review of generator systems for direct-drive wind turbines," in *European wind energy conference & exhibition, Belgium*, vol. 31, 2008.
- [35] G. Klaus, M. Wilke, J. Fraunhofer, W. Nick, and H.-W. Neumuller, "Design challenges and benefits of hts synchronous machines," in *2007 IEEE Power Engineering Society General Meeting*. IEEE, 2007, pp. 1–8.
- [36] M. Mohammadi, T. Rahman, R. Silva, M. Li, and D. Lowther, "A computationally efficient algorithm for rotor design optimization of synchronous reluctance machines," *IEEE Transactions on Magnetics*, vol. 52, no. 3, pp. 1–4, 2016.
- [37] M. Di Nardo, G. L. Calzo, M. Galea, and C. Gerada, "Design optimization of a high speed synchronous reluctance machine," *IEEE Transactions on Industry Applications*, vol. 54, no. 1, pp. 233–243, 2018.
- [38] M. Ibrahim, P. Sergeant, and E. M. Rashad, "Synchronous reluctance motor performance based on different electrical steel grades," *IEEE Transactions on Magnetics*, vol. 51, no. 11, pp. 1–4, 2015.
- [39] S. Taghavi and P. Pillay, "A novel grain-oriented lamination rotor core assembly for a synchronous reluctance traction motor with a reduced torque ripple algorithm," *IEEE Transactions on Industry Applications*, vol. 52, no. 5, pp. 3729–3738, 2016.
- [40] C. M. Spargo, B. C. Mecrow, J. D. Widmer, C. Morton, and N. J. Baker, "Design and validation of a synchronous reluctance motor with single tooth windings," *IEEE transactions on energy conversion*, vol. 30, no. 2, pp. 795–805, 2015.
- [41] M. R. W. Group *et al.*, "Report of large motor reliability survey of industrial and commercial installations, part i," *IEEE Trans. Industrial Applications*, vol. 1, no. 4, pp. 865–872, 1985.
- [42] M. Group *et al.*, "Report of large motor reliability survey of industrial and commercial installations, part ii," *IEEE Trans. Ind. Appl.*, vol. 21, no. 4, pp. 865–872, 1985.
- [43] P. Albrecht, J. Appiarius, R. McCoy, E. Owen, and D. Sharma, "Assessment of the reliability of motors in utility applications-updated," *IEEE transactions on Energy Conversion*, no. 1, pp. 39–46, 1986.

## BIBLIOGRAPHY

---

- [44] R. M. Tallam, S. B. Lee, G. C. Stone, G. B. Kliman, J. Yoo, T. G. Habetler, and R. G. Harley, "A survey of methods for detection of stator-related faults in induction machines," *IEEE Transactions on Industry Applications*, vol. 43, no. 4, pp. 920–933, 2007.
- [45] D. A. Staton and A. Cavagnino, "Convection heat transfer and flow calculations suitable for electric machines thermal models," *IEEE transactions on industrial electronics*, vol. 55, no. 10, pp. 3509–3516, 2008.
- [46] M. Nagrial and M. Rahman, "Operation and characteristics of self-excited reluctance generator," in *Industry Applications Society Annual Meeting, 1988., Conference Record of the 1988 IEEE*. IEEE, 1988, pp. 55–58.
- [47] J. Elder, J. Boys, and J. Woodward, "The process of self excitation in induction generators," in *IEE Proceedings B-Electric Power Applications*, vol. 130, no. 2. IET, 1983, pp. 103–108.
- [48] I. Boldea, "Reluctance synchronous machines and drives (monographs in electrical and electronic engineering)," 2002.
- [49] S. Murthy, O. Malik, and A. Tandon, "Analysis of self-excited induction generators," in *IEE Proceedings C (Generation, Transmission and Distribution)*, vol. 129, no. 6. IET, 1982, pp. 260–265.
- [50] S. Stipetic, D. Zarko, and M. Kovacic, "Optimised design of permanent magnet assisted synchronous reluctance motor series using combined analytical–finite element analysis based approach," *IET Electric Power Applications*, vol. 10, no. 5, pp. 330–338, 2016.
- [51] A. Mohamadein, Y. Rahim, and A. Al-Khalaf, "Steady-state performance of self-excited reluctance generators," in *IEE Proceedings B-Electric Power Applications*, vol. 137, no. 5. IET, 1990, pp. 293–298.
- [52] H. Holttinen, E. Peltola, and S. Tuhkanen, "Renewable energy sources and distributed energy production," *Technology and Climate Change CLIMTECH 1999–2002*, p. 5.
- [53] J. Juergens, A. Fricasse, L. Marengo, J. Gragger, M. De Gennaro, and B. Ponick, "Innovative design of an air cooled ferrite permanent magnet assisted synchronous reluctance machine for automotive traction application," in *2016 XXII International Conference on Electrical Machines (ICEM)*. IEEE, 2016, pp. 803–810.
- [54] G. Liu, X. Du, W. Zhao, and Q. Chen, "Reduction of torque ripple in inset permanent magnet synchronous motor by magnets shifting," *IEEE Transactions on Magnetics*, vol. 53, no. 2, pp. 1–13, 2016.
- [55] C.-T. Liu, T.-Y. Luo, P.-C. Shih, S.-C. Yen, H.-N. Lin, Y.-W. Hsu, and C.-C. Hwang, "On the design and construction assessments of a permanent-magnet-assisted synchronous reluctance motor," *IEEE Transactions on Magnetics*, vol. 53, no. 11, pp. 1–4, 2017.
- [56] H. Huang, Y.-S. Hu, Y. Xiao, and H. Lyu, "Research of parameters and antidemagnetization of rare-earth-less permanent magnet-assisted synchronous reluctance motor," *IEEE Transactions on Magnetics*, vol. 51, no. 11, pp. 1–4, 2015.
- [57] Y. Wang, D. Ionel, D. G. Dorrell, and S. Stretz, "Establishing the power factor limitations for synchronous reluctance machines," *IEEE Transactions on Magnetics*, vol. 51, no. 11, pp. 1–4, 2015.

- [58] M. Obata, S. Morimoto, M. Sanada, and Y. Inoue, "Performance of pmasynrm with ferrite magnets for ev/hev applications considering productivity," *IEEE Transactions on Industry Applications*, vol. 50, no. 4, pp. 2427–2435, 2013.
- [59] N. Bianchi, H. Mahmoud, and S. Bolognani, "Fast synthesis of permanent magnet assisted synchronous reluctance motors," *IET Electric Power Applications*, vol. 10, no. 5, pp. 312–318, 2016.
- [60] Y. Wang, D. M. Ionel, M. Jiang, and S. J. Stretz, "Establishing the relative merits of synchronous reluctance and pm-assisted technology through systematic design optimization," *IEEE Transactions on Industry Applications*, vol. 52, no. 4, pp. 2971–2978, 2016.
- [61] C.-T. Liu, H.-Y. Chung, and S.-Y. Lin, "On the electromagnetic steel selections and performance impact assessments of synchronous reluctance motors," *IEEE Transactions on Industry Applications*, vol. 53, no. 3, pp. 2569–2577, 2017.
- [62] K. Tefera, P. Tripathy, and R. Adda, "Electromagnetic and mechanical stress analysis of wind-driven synchronous reluctance generator," *CES Transactions on Electrical Machines and Systems*, vol. 3, no. 1, pp. 107–114, 2019.
- [63] I.-H. Lin, M.-F. Hsieh, H.-F. Kuo, and M.-C. Tsai, "Improved accuracy for performance evaluation of synchronous reluctance motor," *IEEE Transactions on Magnetics*, vol. 51, no. 11, pp. 1–4, 2015.
- [64] J. H. Lee, "Efficiency evaluations of synchronous reluctance motor using coupled fem and preisach modeling," *IEEE transactions on magnetics*, vol. 39, no. 5, pp. 3271–3273, 2003.
- [65] ———, "Design solutions to minimize iron core loss in synchronous reluctance motor using preisach model and fem," *IEEE transactions on magnetics*, vol. 38, no. 5, pp. 3276–3278, 2002.
- [66] P. Roshanfekar, S. Lundmark, T. Thiringer, and M. Alatalo, "A synchronous reluctance generator for a wind application-compared with an interior mounted permanent magnet synchronous generator," 2014.
- [67] V. Mukherjee, M. Sokolov, J. Pippuri, M. Hinkkanen, and A. Belahcen, "Comparative study of inner and outer rotor bearingless synchronous reluctance motors," *The Journal of Engineering*, vol. 2019, no. 17, pp. 4375–4379, 2019.
- [68] H.-C. Liu, I.-G. Kim, Y. J. Oh, J. Lee, and S.-C. Go, "Design of permanent magnet-assisted synchronous reluctance motor for maximized back-emf and torque ripple reduction," *IEEE Transactions on Magnetics*, vol. 53, no. 6, pp. 1–4, 2017.
- [69] ABB, "Iec 60034-30-1 standard on efficiency classes for low voltage ac motors."
- [70] J. M. Park, S. I. Kim, J. P. Hong, and J. H. Lee, "Rotor design on torque ripple reduction for a synchronous reluctance motor with concentrated winding using response surface methodology," *IEEE Transactions on Magnetics*, vol. 42, no. 10, pp. 3479–3481, 2006.
- [71] C. M. Spargo, B. C. Mecrow, and J. D. Widmer, "A seminumerical finite-element postprocessing torque ripple analysis technique for synchronous electric machines utilizing the air-gap maxwell stress tensor," *Magnetics, IEEE Transactions on*, vol. 50, no. 5, pp. 1–9, 2014.
- [72] D. Staton, T. Miller, and S. Wood, "Maximising the saliency ratio of the synchronous reluctance motor," in *IEE Proceedings B-Electric Power Applications*, vol. 140, no. 4. IET, 1993, pp. 249–259.

## BIBLIOGRAPHY

---

- [73] A. Saleem, N. Alatawneh, R. R. Chromik, and D. A. Lowther, "Effect of shear cutting on microstructure and magnetic properties of non-oriented electrical steel," *IEEE Transactions on Magnetics*, vol. 52, no. 5, pp. 1–4, 2016.
- [74] R. I. Stephens, A. Fatemi, R. R. Stephens, and H. O. Fuchs, *Metal fatigue in engineering*. John Wiley & Sons, 2000.
- [75] J. Ikaheimo, J. Kolehmainen, T. Kansakangas, V. Kivela, and R. R. Moghaddam, "Synchronous high-speed reluctance machine with novel rotor construction," *IEEE Transactions on Industrial Electronics*, vol. 61, no. 6, pp. 2969–2975, 2014.
- [76] M. R., *Synchronous reluctance machine (SynRM) design*. KTH Royal Institute of Technology, 2007.
- [77] M. NEMA, "Information guide for general purpose industrial ac small and medium squirrel-cage induction motor standards," 2007.
- [78] L. Lapidus and G. F. Pinder, *Numerical solution of partial differential equations in science and engineering*. John Wiley & Sons, 2011.
- [79] R. Schneider, "Explicit and implicit finite-difference methods for the diffusion equation in two dimensions," Forschungszentrum Karlsruhe GmbH Technik und Umwelt (Germany). Inst. fuer , Tech. Rep., 2003.
- [80] S. Reza-E-Rabbi, S. Arifuzzaman, T. Sarkar, M. S. Khan, and S. F. Ahmmed, "Explicit finite difference analysis of an unsteady mhd flow of a chemically reacting casson fluid past a stretching sheet with brownian motion and thermophoresis effects," *Journal of King Saud University-Science*, vol. 32, no. 1, pp. 690–701, 2020.
- [81] J. Nerg, M. Rilla, and J. Pyrhonen, "Thermal analysis of radial-flux electrical machines with a high power density," *IEEE Transactions on industrial electronics*, vol. 55, no. 10, pp. 3543–3554, 2008.
- [82] P. Mellor, D. Roberts, and D. Turner, "Lumped parameter thermal model for electrical machines of tefc design," in *IEE Proceedings B (Electric Power Applications)*, vol. 138, no. 5. IET, 1991, pp. 205–218.

## List of Publications

### Journal Publications

- (i) Tefera K. Praveen T. and Ravindranath A., “Design and modeling of self-excited SRG and FM-SRG for wind energy generation”, ”in *IET Renewable power generation,1898-1914*, 2021.
- (ii) Tefera K. Praveen T. and Ravindranath A., “Electromagnetic Torque Analysis of wind-driven SRG with Ferrite Magnet”, *CES Transactions and Electrical machines and systems (IEEE index)*, vol. 4(3), 172-179, 2020.
- (iii) Tefera K. Praveen T. and Ravindranath A., “Electromagnetic and Mechanical Stress Analysis of Wind-Driven Synchronous Reluctance Generator”, *CES Transactions on Electrical machines and systems (IEEE index)*, vol. 3(1), 107-114, 2019.
- (iv) Tefera K. Praveen T. and Ravindranath A., “Implicit and explicit thermal analysis of synchronous reluctance generator for wind energy application”, *Under Second Review ” recommended for publication.*



---

## **Curriculum Vitae**

*Tefera Kitaba Tolesa*

### **Educational Qualifications**

- (i) Doctor of Philosophy (Ph.D)[Currently Pursuing]: From the Department of Electronics and Electrical Engineering, Indian Institute of Technology Guwahati India. Thesis submission: July, 2021, Cumulative Performance Index (CPI):7.5.
- (ii) Masters of Engineering (M.E): In Power Electronics and drives, Anna University College of Engineering, Guindy Campus, Chennai, India. Year of Completion: April, 2012, Cumulative Performance Index (CPI):7.47.
- (iii) Bachelor of Technology (B.Tech): In Electrical Power Engineering, Defense University College of Engineering , Bishoftu, Ethiopia. Year of Completion: April, 2007, Cumulative Performance Index (CPI):7.40.

### **Research Paper (Published)**

#### **Referred Journal:**

- (i) Tefera K., Praveen T., and Ravindranath A., “Design and modeling of self-excited SRG and FM-SRG for wind energy generation”, *in IET Renewable power generation, 1898-1914, 2021.*
- (ii) Tefera K., Praveen T., and Ravindranath A., “Electromagnetic Torque Analysis of wind-driven SRG with Ferrite Magnet”, *CES Transactions and Electrical machines and systems (IEEE index), vol. 4(3), 172-179, 2020.*
- (iii) Tefera K., Praveen T., and Ravindranath A., “Electromagnetic and Mechanical Stress Analysis of Wind-Driven Synchronous Reluctance Generator”, *CES Transactions on Electrical machines and systems (IEEE index), vol. 3(1), 107-114, 2019.*

**Manuscript Communicated:**

- (i) Tefera K., Praveen T., and Ravindranath A., “Implicit and explicit thermal analysis of synchronous reluctance generator for wind energy application”, *Under Second Review* ” recommended for publication.



